DEVELOPMENT OF A MICRO CRYSTALLISATION SYSTEM FOR THE PRODUCTION OF SUB-MICRON PARTICULATES WITH NARROW-SIZE-DISTRIBUTION

NABEEL KADHIM ABBOOD ALGHAFFARI

Thesis submitted to the University of Nottingham for the degree of Doctor of Philosophy

FEBRUARY 2015

Abstract

Recent advancements in applied, medical materials engineering sciences and micro/nano technology have stimulated increasing demand for novel, high quality and precisely-shaped particles. As most of the materials that are used by these scientific fields are in crystalline forms, it is evident that crystallization, in particular micro-scale crystallisation is a very useful tool to satisfy this demand. This research charts the investigation and optimisation of micro-scale continuous crystallisation of a fine and commonly used compound, i.e. paracetamol, with attempts to overcome the limitations of such process, for instance to produce particles with narrow particle size distribution and maintain a smooth and continuous operation without microchannel blockage. In this thesis, efforts have been directed to design and test a micro scale continuous crystalliser using two different crystallisation techniques; namely: cooling down of saturated solution and adding antisolvent agent. The former technique was not so successful due to the difficult thermal control of such microfluidic system with available resources, as well as due to the inherent nature of such crystallisation mode, which required long induction time to start crystallisation. The latter technique, on the other hand, was successful due to the short induction time required to drive crystallisation and it does not require any thermal management, as it is performed at ambient temperature. Using the antisolvent technique require very short mixing time to mix the mother liquor with an antisolvent agent to produce supersaturated solution. This was achieved by proposing a novel microfluidic design consisting of baffled microchannel devices operated by superimposing a fully reverse oscillatory flow to facilitate fast non-axial mixing regardless of the very low axial flow rate that is typical to microfluidic devises. Computational fluid dynamics simulations in addition to microfluidic flow visualisation experiments were carried out to examine the non-axial mixing performance for the proposed

design. Subsequently, the proposed design was tested as a continuous crystalliser and showed very good performances by producing sub-micrometre particles with a very narrow particle size distribution. Finally, the performance of the micro scale continuous crystalliser was optimised to produce particle with minimum particle size using custom design of experiment technique. Results of this optimisation process were successful and produced paracetamol particles having average Z-Ave = 99.89 nm with standard deviation equivalent to 7.315 nm. Finally, this thesis shows a successful demonstration of a simple yet versatile microcrystallisation system capable of producing particles of consistent size by utilising fully reverse oscillatory flow into baffled microchannel.

For my wife, son, daughter, and all of my family for your dedicated support and patient.

Acknowledgements

In the name of Allah, the most beneficent and the most merciful. All praises to Allah the almighty for giving me the strength, guidance, and patience in completing this thesis. With His blessing, this thesis is finally accomplished. First of all, I would like to express my genuine gratitude to my beloved family for their endless love, prayers, and tolerance. To my wife, Mrs. Haneen Faris, thank you for your persevering support and encouragement. In particular, I wish to express my sincere appreciation to my earlier supervisor Dr David Hassell, current supervisor Dr Phei Li Lau for their support, guidance and critics during the period of my research. Your practical view and guidance on my research work were of utmost importance. Thank you very much for the unending help and support throughout the course of my research. I am also indebted to Universiti of Nottingham Malaysia campus, academics, senior staff, staff, and technician, for the excellent work to make my research journey in Malaysia such a successful mission. My fellow postgraduate students and friends, thank you for your help and sharing your time with me. Thank you for your friendship.

Contents

List of Figures

List of Tables

Nomenclatures

A	Cross-section area, m^2
$A_{Inter-baffle}$	Area of single inter-baffle cavity, mm^2
D	Diameter, mm
D_h	Hydraulic diameter, mm
f	Oscillation frequency, Hz
Q_n	Net volumetric flow rate, $mm^3\ s^{-1}$
Q_o	Oscillatory volumetric flow rate, $mm^3\ s^{-1}$
Re_n	Net flow Reynolds number
Re_o	Oscillatory flow Reynolds number
St	Strouhal number
Sto	Stokes number
U_o	Mean oscillatory fluid velocity, $m\ s^{-1}$
U_{red}	Reduced oscillatory velocity
Z-Ave	Intensity based hydrodynamic average particle size

Greek Symbols

μ	Viscosity, Pa.s
ρ	Density, $kg\ m^{-3}$
α	Statistical significance level
β	Mathematical model parameter
∇	Error due to lack of fit
ε	Te pure error

Abbreviations

2D	Two-dimensional
3D	Three-dimensional
CFD	Computational fluid dynamics
DoF	Degree of freedom
DPS	Differential pressure sensor
NoE	Number of elements
OBM	Oscillatory baffled microchannel
OFR	Oscillatory flow reactor
PDMS	Polydimethylsiloxane
PMMA	Poly(methyl methacrylate)
PV	Particle-based flow visualization
VA	Vortices area
VAR	Vortices area ratio

Chapter 1

Crystallisation

1.1 Introduction

Solid materials in crystalline form, such as salt, sugar, marble, precious stones, pharmaceutical products, pigments, etc. have been used by humans since the early stages of civilization. Early historical records show that salt, sugar, and other medicine related material were produced artificially in crystalline form in; Egypt about 1500 B.C.; India about 327 B.C.; and Arabia about 1000 A.D. respectively (Schoen et al., 1956). In modern times it has been estimated that the majority of the chemical and pharmaceutical materials that are used by various human activities are in the crystalline form (Leubner, 2010). Generally, crystallisation can be achieved through a number of techniques; namely, cooling down a saturated solution, precipitation of a chemical reaction product, removal of solvent, adding an antisolvent agent, or a combination of these techniques (Jones, 2002). The selection of crystallisation route and whether the operation is continuous or batch depends on; the nature of the final product and initial feed solution; the required quality of the crystals; and the economical feasibility of the process. Fundamentally, the crystallisation occurs in two phenomenon steps known as *nucleation* and *growth*. Within the modern chemical industries, it is important to control these two phenomenon steps in order to produce a high degree of quality chemicals or pharmaceutical products in crystalline form.

Crystal quality plays an important role in the fine chemical and pharmaceutical industries, and while numerous methods and techniques can be employed to categorise it the common assessment techniques are:

Crystal morphology and habit: This is the physical shape of the crystals. Many of the materials in the crystalline form have different

morphologies and habits. While both crystal morphology and habit depend on many factors, the main ones include; the material and feed solvent; crystallisation temperature; the crystallisation process technique and type. Figure (1.1) shows a typical morphology and habit for a crystal. Crystal morphology and habit have a direct and important effect on the volumetric properties of a crystalline materials such as, among others, density, solubility and dissolution rate.

Crystal size distribution: This is the quantitative measurement of the crystal sizes along with its respective quantity within a large crystal population. A narrow crystal size distribution is a key quality criterion as it provides consistency in the size and density of a crystal material as this results in good packing and free flow of a bulk material. Furthermore, this is important for areas of drug dosing and delivery where consistency in product quantity is crucial.

Inclusion phenomenon: This is the presence of mother liquor solution within the crystal structure once they have been formed (McNaught and Wilkinson, 1997). This will lead to further process complications due to either; partial crystal dissolution back into the included solution due to the event that elevated temperatures are experienced by the crystal; cake formation where crystal fracture around the included solution leads to subsequent solvent evaporation and agglomeration between adjacent crystals.

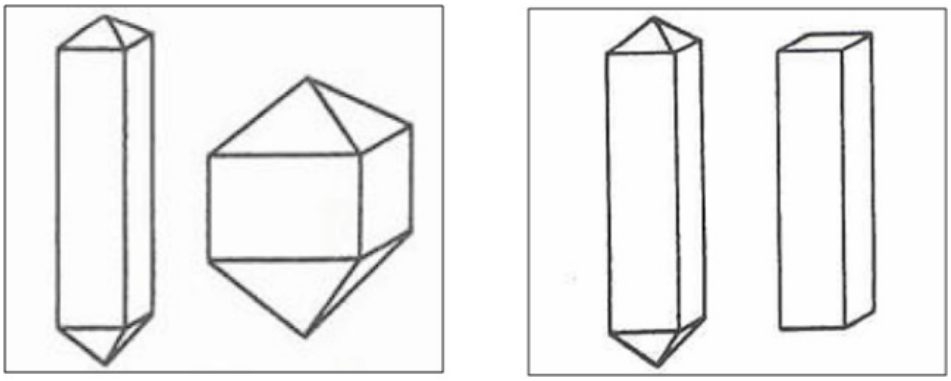

Figure 1.1: Morphology and habit of crystals, (a) same morphology different habit and (b) different morphology same habit. (source: Mullin (2001)).

1.2 Issues with current approaches

Current industrial scale crystallisation takes place in both batch and continuous unit operations. In its nature, crystallisation phenomenon is very sophisticated and required a higher level of understanding on aspects such as (Tung, 2009):

1. Inherited material properties such as solubility, morphology and habit
2. Crystallisation fundamentals such as nucleation rate, induction time, and growth rate.
3. Crystallisation units operation condition such as mixing rate, cooling rate and/or antisolvent adding rate.

As an example for one of the crystallisation issues is the inclusion phenomenon. Many researchers suggest that the inclusion phenomenon occurs due to the irregularity in the mixing profile across crystallises domains (Chew et al., 2004). Therefore, in this research, the use of microchannels is evaluated as the crystallisation domain, with specific attention paid to:

1. Providing better control of the hydrodynamics profile of the crystallisation domain. This will ensure homogeneous physical and chemical properties throughout the crystallisation domain which will lead to unified crystals quality as well as eliminate the irregularities in the mixing profile that cause the inclusion phenomena.
2. Producing a very narrow crystal size distribution due to the constrained growing domain that the microchannel provided to the crystals to grow (Myerson, 2003; Su et al., 2007; Sultana, 2010).

1.3 Microcrystallisers

Recently, there has been a great amount of interest in developing crystallisation in micro scale crystallizers (see Figure (1.2)). This is driven by the fact that current industrial crystallizers, in spite of their many advantages, still have issues when it comes to the final crystalline-product properties e.g. obtaining the crystals size distribution, shape and quality that is required both by the downstream processes and market demand (Jones, 2002). Crystallising in a microdomain for instance in microreactors or microchannes with a characteristic length of 50–1000 micrometre has great potential to rectify the issues which affect current crystallisers

(cf. §1.2) since they prove a stable, homogeneous and domain-controlled environment for crystals to nucleate and grow.

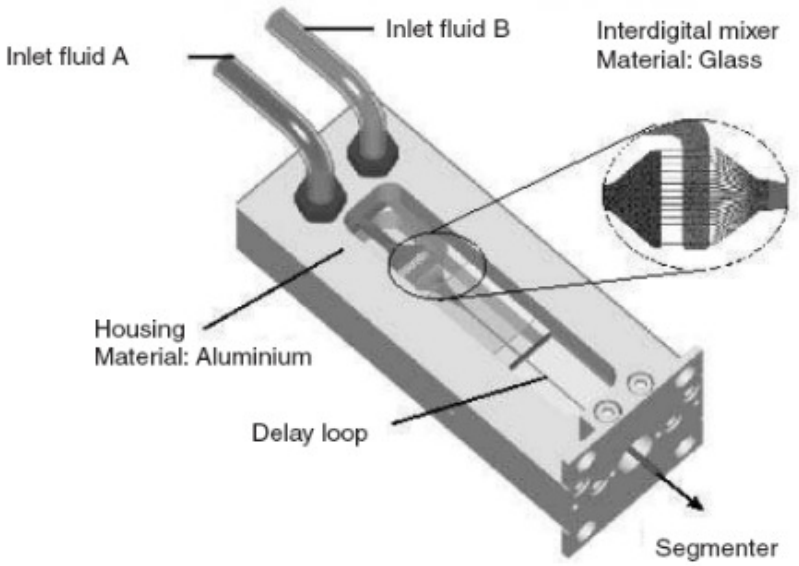

Figure 1.2: Microcrystalliser produced by Schenk et at.(See Jones (2002)).

Despite the advantages that microchannels have when applied to the field of crystallisation, some difficulties need to be dealt with before they can be successfully applied to continuous crystallisation production. These difficulties are:

A. Blockage: Continuous microcrystallisers have a high tendency to be blocked by the formation of crystals inside their micro-channels. In their review, Chen et al. (2011) indicate that passage blockage is a major obstruction to the application of microcrystallisers, and eliminating this problem would lead to further development of this concept.

B. Increasing throughput: In macro-scale processes, after bench studies are performed, the process is scaled-up to a size suitable to achieve the required production rate. This concept is not applicable for micro-scale applications, due to the fact their design concept relies in part on the large surface area to volume ratios which is reduced should scaling-up principles and rules be applied. The new concept of scale-out needs to be applied and accepted by the wider industrial community to bring micro crystalliser plants to production rates required by industry.

C. Limited downstream process equipment: In a technology vendors review carried out by Chen et al. (2011), small-scale continuous filters (less than 4 liter of slurry per minute) are unavailable in the industrial and scientific equipment supply market. This issue will lead to significant lag in developing continuous crystallisers for practical usage in the industry.

Thus, for any research on microcrystallisers, points (A) to (C) above need to be addressed thoroughly to achieve a functional microcrystalliser.

1.4 Problem statement

Current industrial crystallizers, in spite of their many advantages, still have issues when it comes to the produced crystalline-product properties such as obtaining a narrow crystals size distribution with high quality crystals and with minimum variation between batches as most of the current crystallisation processes operated in large vessels and in batch operation mode. Continuous crystallisation in a microdomain for instance in microreactors or microchannes with a characteristic length of 50-1000 micrometre has great potential to rectify these issues which affect current crystallisers since they prove a stable, homogeneous and domain-controlled environment for crystals to nucleate and grow to produced a high quality crystalline product with a narrow particle size distribution. In addition to that, the operation in a continuous manner will minimised the variation of properties of the produced crystalline product.

Given these issues, it is enquired to design,evaluate and optimise a micro-scale continuous crystalliser

1.5 Objectives

The objective of this work is to propose a design and operation method for a continuous micro-scale crystalliser to produce a fine active pharmaceutical ingredient with a very narrow particle size distribution. It also aims to provide a new insight for the design and operation of such micro-scale for a smooth and continuous operation for the micro-scale crystalliser without any blockage of the microchannels used.

The thesis work will comprise the following objectives:

1. To determine the usability of continuous crystallisation by cooling in a micro-scale crystalliser.

2. To examine and quantify the non axial mixing of the proposed oscillatory baffled microchannel at different operation conditions by means of computational fluid dynamics simulations in addition to micro-flow visualisation technique

3. By means of design of experiments methodology, the performance of the proposed oscillatory baffled microchannels need to be modelled for continuous antisolvent crystallisation at different operation conditions and then optimised to produce fine particle with a very narrow particle size distribution.

1.6 Thesis organisation

The thesis are organised as follows: Section 2 gives an introduction to the crystallisation process followed by a literature review on crystallisation at micro-scale domain and then gives a brief introduction to the methodology of oscillatory flow in baffled channels. Section 3 demonstrates the experimental works carried out to achieve continuous crystallisation in a micro-scale crystalliser by utilising solution-cooling technique as crystallisation mode. In Section 4, a proposal for a novel continuous micro crystallisation technique is presented followed by an evaluation for the proposed technique by means of computational fluid dynamics modelling and micro-flow visualisation technique. Section 5 shows the experimental works preformed to evaluate the performance the proposed continuously operated oscillatory flow baffled micro crystalliser at different operation conditions in addition to at an optimal condition. The conclusion as well as some thoughts for future study is given in the last section.

References

Jie Chen, Bipul Sarma, James M. B. Evans, and Allan S. Myerson. Pharmaceutical crystallization. *Crystal Growth & Design*, 11(4):887–895, 2011. 4, 5

C. M. Chew, R. I. Ristic, R. D. Dennehy, and J. J. De Yoreo. Crystallization of paracetamol under oscillatory flow mixing conditions. *Crystal Growth & Design*, 4(5):1045–1052, 2004. 851VL Times Cited:11 Cited References Count:33. 3

Alan G. Jones. *Crystallization process systems*. Butterworth-Heinemann, Oxford; Boston, 2002. ix, 1, 3, 4

Ingo H. Leubner. *Precision crystallization: theory and practice of controlling crystal size*. CRC Press/Taylor & Francis, Boca Raton, 2010. 1

A. D. McNaught and A. Wilkinson. *IUPAC Compendium of Chemical Terminology*. Blackwell Scientific Publications, Oxford, 1997. 2

J. W. Mullin. *Crystallization*. Butterworth-Heinemann, Oxford; Boston, 2001. ix, 2

Allan S. Myerson. Molecular crystals of controled size, 2003. 3

Herbert M. Schoen, C. S. Grove, and Joseph A. Palermo. The early history of crystallization. *Journal of Chemical Education*, 33(8):373–null, 1956. doi: 10.1021/ed033p373. 1

Y. F. Su, H. Kim, S. Kovenklioglu, and W. Y. Lee. Continuous nanoparticle production by microfluidic-based emulsion, mixing and crystallization. *Journal of Solid State Chemistry*, 180(9):2625–2629, 2007. 3

Mahmooda Sultana. *Microfluidic systems for continuous crystallization of small organic molecules*. PhD thesis, 2010. 3

H.H. Tung. *Crystallization of organic compounds: an industrial perspective*. Wiley, 2009. 3

Chapter 2

Literature review

2.1 Introduction

This chapter discusses works published in the literature on crystallisation in microfluidics devises, oscillatory flow reactors and baffled oscillatory flow reactor. A general introduction is made to crystallisation, defining and describing the characteristics of this widely known phenomenon. A description of oscillatory flow in baffled channels is given and published experimental and computational effects of helical flow are reviewed and discussed.

2.2 Crystallisation background

Early historical records show that commodity materials such as salt, sugar, and other medicine related material were produced artificially in crystalline form in; Egypt from 1500 B.C.; India from 327 B.C.; and Arabia from 1000 A.D. respectively (Schoen et al., 1956). Since these pioneering periods of production, more and more products are generated in crystalline form, and used in many aspects of our modern life. Examples include the food, pigment, fine and specialty chemical, and the pharmaceutical and cosmetic industries. This great focus on crystallisation as a modern industrial process resulted due to the wide range of materials which can be produced in a highly purified crystalline form, the lower energy consumption and operational temperatures required when compared to other separation processes, and its production scale versatility, which can vary from grams per day to thousands of tons per day (Genck et al., 2008).

The properties of a crystal, such as crystal size, shape and form, play a very important role as it is further pressed in downstream operations

such as filtration, washing, drying and milling. They also affect the manner in which the final product performs, where crystal properties such as bioavailability, solubility and dissolution rate play important roles (Chen et al., 2011). Thus, it is essential to control these properties within the crystallisation process, before any further downstream processes, to reduce production cost and waste in these subsequent operations.

This chapter briefly introduces the fundamental principles of crystallisation from solution, a process which is essentially a liquid-solid separation process. It then provides a review which highlights the benefits of using micro processes, i.e. microcrystallisers, for crystallisation and provides examples of there use within the literature.

2.3 Solid-Liquid System

As most of the crystalline products are crystallised from a solid-liquid systems, it is important here to generally describe this system and its crystallisation related terminology. Figure 2.1 shows a typical representation of a solid-liquid system where the sold curve represent the equilibrium state of the solid-liquid system (Jones, 2002). This equilibrium state that known as solubility is defied as the maximum amount of the solid phase that can be dissolved in a known amount of the liquid phase to form a thermodynamically homogeneous solution at a particular temperature and pressure. As can be seen from Figure 2.1, the equilibrium state divides the solid-liquid system into a lower and an upper region, know as undersaturation and supersaturation regions respectively. In nature as well as in man-made-processes, solid dissolution is represented by moving from the undersaturated region toward the saturation curve and, conversely, crystallisation or precipitation is represented by moving from the supersaturated region toward the saturation curve.

The characteristics of the equilibrium state for any solid-liquid system are controlled by the system condition, e.g. temperature, pressure, pH, and/or nature of the solid and liquid phases. For instance, Solubility of a typical solid-liquid system (most of substances) can be;

1. increases with temperature increasing and vice versa, and

2. decrease with pressure increasing and vice versa. At this point, it is worth to indicate that pressure effect on solid-liquid systems is very little compared the temperature effect (Mersmann, 2001).

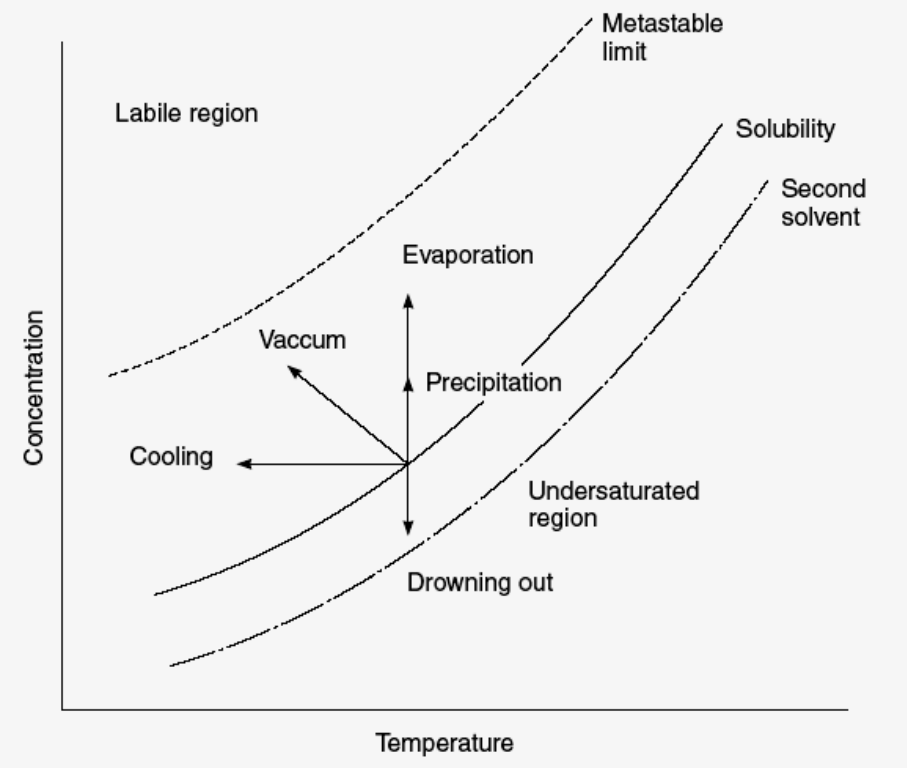

Figure 2.1: Typical phase equilibrium of a solid-liquid system (source: Jones, 2002)

Practically, the saturation curve of any solid-liquid system is known as the solubility curve or diagram which can be produced by plotting solubilises for a certain solid-liquid system at various temperatures. Solubility diagrams give a very clear picture on the solubility behaviour of a particular solid-liquid system. Figure 2.2 shows, as an example, a typical solubility diagram for some different compounds in water where it can be observed that for some compounds the solubility is increased with increasing temperature while for few other compounds it decreased. Furthermore, it can be observed that for each compound there is a different rate of solubility change with respect to temperature change. This rate can be estimated by calculating the slope of the curve at two different temperatures. The saturation concentration often depends strongly on temperature but only slightly on pressure (Mersmann, 2001). Solubility in the solubility diagrams can be quantified in mole fraction, weight fraction, or more commonly as solute weight per a give weight of solvent or solution. Solubility of any solid-liquid system can be obtained by laboratory experiments as descried next or by the means of computational chemistry science which is out of scope of this research.

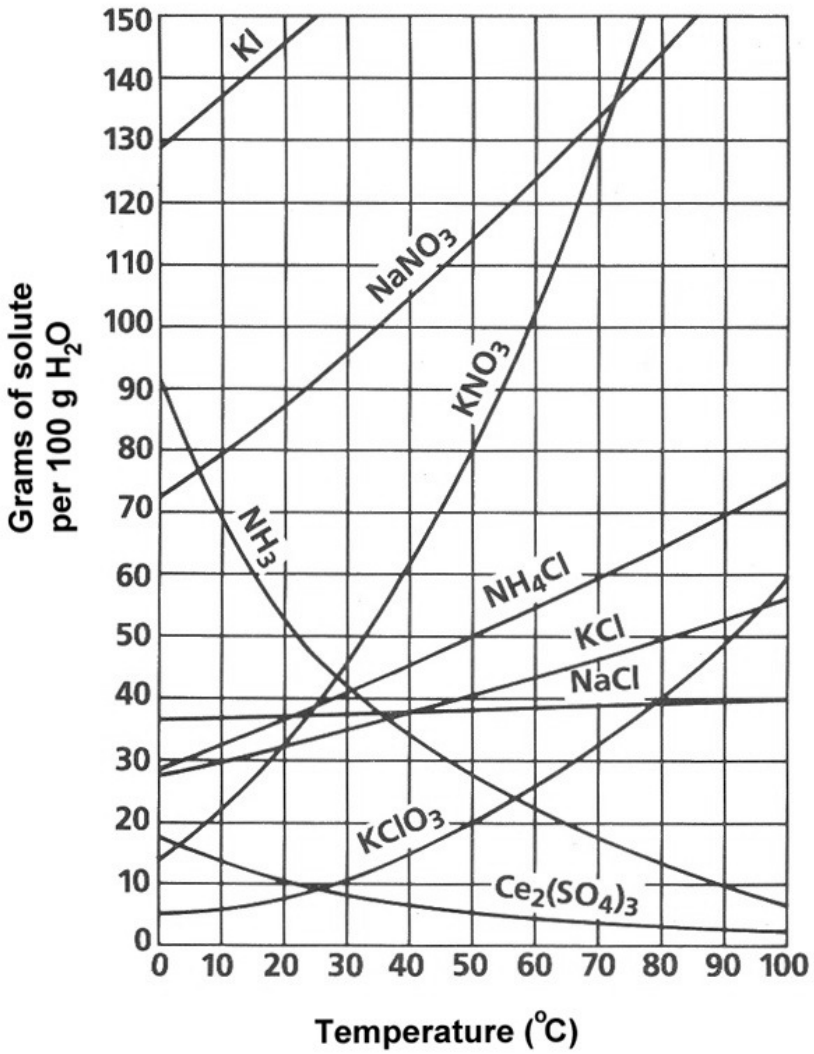

Figure 2.2: Solubility curves for different compounds in water.

2.4 Solubility Measurement

There are many techniques that can be used for measurement of solubility of a solid-liquid system. Choosing which particular technique to use depends on many factors e.g. nature of the solid-liquid system, cost and availability of the solute and the solvent, apparatuses and expertise available and the required degree of accuracy (Mullin, 2001). Generally, solubility measurement techniques can be classified into two main branches; direct and indirect. The direct techniques can be further divided into two more branches known as analytical and synthesis techniques. At the analytical technique, a saturated solution, prepared by stirring an access solute with a known amount of solvent at a constant temperature, is physically or chemically analyzed to determine the solute concentration which is represent the solubility. At the synthesis techniques, however, no analysis is

requires. Solubility is determined by gradually adding small amount of solvent in a time intervals manner to a known amount of solute at constant temperature till the entire dissolution of the solute (Mullin, 2001; Hefter and Tomkins, 2003). In the indirect techniques, the solubility of a solid-liquid system are deduced from the solubility product of that system (Hefter and Tomkins, 2003). In this research the isothermal method reported by Mullin and Slpek (1981) was chosen to determine the solubility of a Paracetamol-Water system at various temperatures. This technique involves, visual monitoring of the disappearance (dissolution) of a predetermine amount of solute by adding a controlled amount of solvent in timely manner at a constant temperature. Factors behind this choice were:

1. Simple setup (with some modification),
2. Reasonably low cost and time consuming,
3. No solution concentration assessment is required, and
4. Acceptable precision of at least 0.5%.

2.5 Supersaturation

Prior to any crystallisation process, a saturated solution should be brought to a supersaturated state. As can be seen from Figure 2.1 above, supersaturation state can be achieved by different techniques known as crystallisation modes such as:

1. Gradually cooling the solution temperature,
2. Adding second solvent (antisolvent),
3. Solvent removing, or
4. Reducing system pressure.

In Practice, one or more of these techniques is used depending on the solid-liquid system characteristics. For instance, solubility of solid-liquid systems that are highly dependent on temperature, i.e. have a high solubility change rate with temperature increment, are more likely moved to the supersaturation state by cooling. On the other hand, systems that show relatively low dependency on temperature, i.e. have relatively flat solubility curve, are more likely to be in the supersaturation state by solvent removing e.g. production of table salt by evaporation (Jones, 2002).

Equations (2.1) to (2.3) show the common quantitative expression of the supersaturation state where C, C^*, ΔC, S, and σ are concentration, saturation concentration, concentration driving force, supersaturation ratio, and relative supersaturation respectively (Mullin, 2001; Mersmann, 2001).

$$\Delta\, C = C - C^* \tag{2.1}$$

$$S = \frac{C}{C^*} \tag{2.2}$$

$$\begin{aligned} \sigma &= \frac{C - C^*}{C^*} \\ &= \frac{\Delta C}{C^*} \\ &= S - 1 \end{aligned} \tag{2.3}$$

2.6 Crystallisation

Crystallisation can be achieved through a number of techniques know as crystallisation modes. These modes are aimed to accomplish one goal which is achieving a supersaturated solution state. Major crystallisation modes are: cooling down a saturated solution, precipitation of a chemical reaction product, removal of solvent, adding an antisolvent agent, or a combination of these techniques (Jones, 2002).

2.6.1 Crystal Formation

Crystal formation is controlled by two consecutive phenomena known as nucleation and growth. Crystal growth will be the second step after nucleation occurs. Nucleation can be divided into two categories which are primary which occur at high supersaturation solution, and secondary nucleation that formed within the metastable zone. Primary nucleation is said to be homogeneous if the nuclei formed simultaneously, whereas it is called heterogeneous if foreign particles is used to induce the nuclei formation. Moreover, it does not involve the product crystal. On the other hand, secondary nucleation involves the presence of the crystalline product ,which commonly known as seeds, whereby contacts by crystal with each other, agitator and mechanical parts in the crystallisation domain may induce the nuclei formation (Genck et al., 2008). Without nuclei formation, it is hard to get the crystals to form and grow though the system has been put under supersaturation condition. At the growth stage, diffusion of solute particles from mother liquor to crystal interface (nuclei interface) and the

incorporation of the diffused solute into crystal lattice are two important growth processes for crystal formation whereby the slower among them will control the crystals growth rate (Mullin, 2001). The presence of impurities or variation and/or inhomogeneity in mass transfer rate can disturb the growth process which may allows inclusion to occur at the crystal lattice which affects the final product purity. Moreover, bridging of crystal can take place when another layer of crystal is actually formed before the layer below it fully covers the crystal interface.

2.6.2 Primary Nucleation

A rapid primary nucleation which occurs at high supersaturation is very unstable due to the fact the crystal will redissolve back, but it will be stable under a condition when the particle grow exceeding its critical size. The critical size of nuclei (see Figure 2.3 and Equation (2.5)) can be estimated from the overall free energy, ΔG, as follows based on the assumption that the particle is of a spherical shape (Mullin, 2001).

$$\Delta\ G = \Delta\ G_S - \Delta\ G_V \tag{2.4}$$

$$\Delta G_{crit} = \frac{4}{3}\pi\gamma r_c^2 \tag{2.5}$$

Where ΔG_S, ΔG_V, ΔG_{crit}, γ, and r_c are surface free energy, volume free energy, critical free energy, the interfacial tension and critical nucleus radios respectively.

2.6.3 Secondary Nucleation

In contrast to primary nucleation which may take very long time to form a critical nucleus especially for low-to-moderate supersaturation solutions, secondary nucleation occurs at a lower supersaturation instantaneously with the presence of initial crystal in the solution. Moreover, it can also occur within the metastable zone, where the growth is encouraged (Genck et al., 2008). There are many methods that can be used to cause secondary nucleation (Jones, 2002) such as:

1. Contact between crystals and/or crystalliser mechanical pats,
2. Shear forces due to fluid flow and mixing,
3. Fracture due to crystals impact,

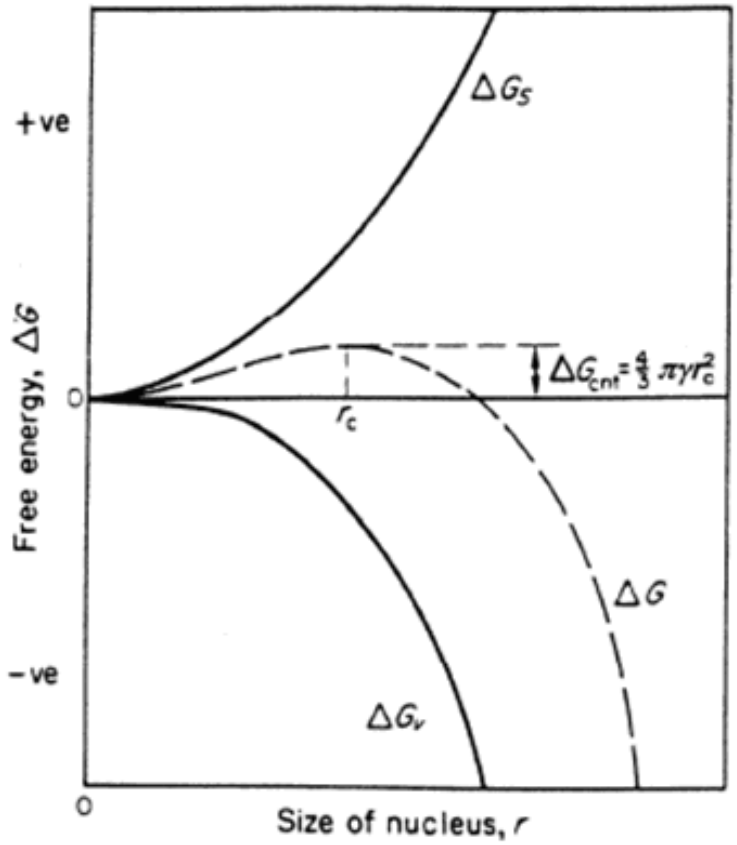

Figure 2.3: Free energy diagram for nucleation explaining the existence of a critical nucleus (source: Mullin, 2001, p.183).

4. Attrition between crystals or fluid flow and

5. Needle as a result of crystals disruption.

Furthermore, work done by Powers H.E.C (See Mullin, 2001, p.195) shows that crystal does nucleate when the supersaturated solution flow passing the stationary crystal formation which act as the seed. Growing crystal by seeding a supersaturated solution has an advantage in controlling the crystal size distribution.

2.6.4 Growth of crystals

Growth is the next step after formation of stable nuclei has occurred. Many theories have been developed to discuss the growth process of crystal, which includes surface energy theories, adsorption layer theories, kinematic theories, and diffusion-reaction theories (Mullin, 2001). At the growth stage, diffusion of solute molecules from mother liquor to crystal interface and the incorporation of the diffused solute molecules into crystal surface are two important growth processes for crystal formation whereby the slower

among them will control the crystals growth rate (Mullin, 2001). Figure 2.4 shows the growth rate at the crystal-solution interface.

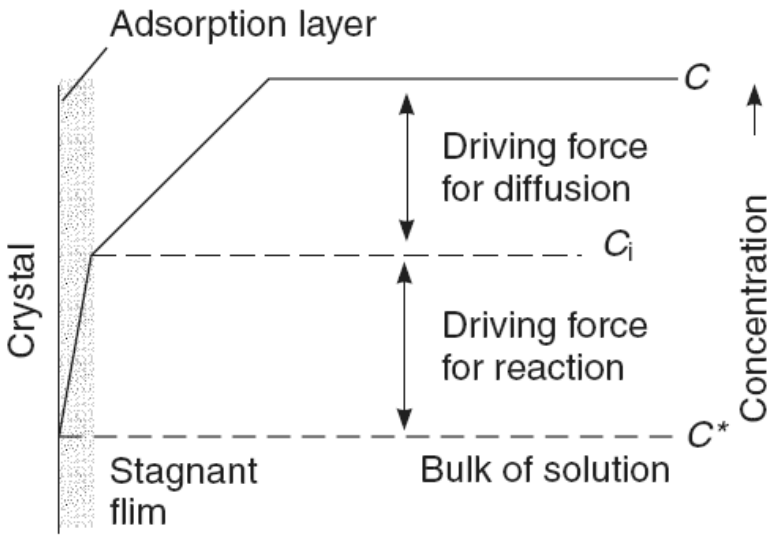

Figure 2.4: Concentration profile at crystal-solution interface (Jones, 2002, p.126).

2.7 Crystallisation Processes

As other chemical processing equipments, crystallisers come in deferent shapes, sizes and operating modes i.e. batch or continuous. Generally, crystallisers operating modes is the basic classification criteria yet it has a certain degree of consideration. Choosing which operation mode depends on many factors (Jones, 2002; Genck et al., 2008; Myerson, 2002) for instance:

1. Production rate: commonly, batch crystallizers used for small production rates e.g. up to 10000 tonnes per year ($\approx$ 27 ton/day).

2. Operating costs: continues crystallizers have a lower energy, labour and capital coats comparing with batch crystallizers with the same production rates.

3. Operating periods: continues crystallizers have long operating time comparing with batch crystallizers.

4. Material handling: Batch crystallizers have a degree of difficulties when it comes to handling wet or semidry crystallises materials.

5. Material cost: Batch crystallizers are preferred for the production of expensive crystalline materials such as pharmaceutical, fine chemical and specialty products.

6. Industrial regulations: As in the pharmaceutical industry, which is a highly regulated industrial sector, batch crystallisers are the major crystallisation process permitted to be used as primary process (McKeown et al., 2010).

Whether a crystallizers is batch or continues, its size and shape will be mainly determine by factors such as: (i) production rates, (ii) supersaturation achieving mode, (iii) feed and product materials properties, and (iv) final crystalline product characteristics requirements.

2.8 Microfluidics

Microfluidic devices are characterised as such by their sub-millimeter scale features, and have been widely used in many chemistry and/or engineering fields such as micro reactors, micro separator, micro chromatography, micro heat exchangers and microanalysis (Ehrfeld et al., 2000; Jones, 2002; Hartman et al., 2011; Tabeling, 2010; van der Woerd et al., 2003). For particle synthesis, microfluidics have been broadly used over the last few years to produced particles either as a primary process i.e. precipitator or as a secondary process where the desire product of a chemical reaction is separated by means of crystallisation (Lemaitre et al., 2002; Myerson, 2003; Schiewe and Zierenberg, 2007; Ehrfeld et al., 2000; Moschou et al., 2014). The application of microfluidics for organic molecules, however, have mostly been used as a high throughput tool for protein crystallization and have focused on droplet based methods where droplets are used as micro-batch-crystallisation units (Hansen et al., 2002; Allen, 2003). This interest in using microfluidics in chemistry and engineering fields is related to the many advantages that microfluidics provide such as (Ehrfeld et al., 2000):

1. Better heat and mass transfer rates and response time compared to macro-scale equipment duo to its high surface-to-volume ration.

2. Safety issues where work done on a very small amount of material which reduces the potential risk in case of leak or reaction run-out.

3. Low cost duo to the small amount of materials and equipments used to fabricate and operate the initial microfluidics devises.

2.9 Small Scale Microchannel Crystallisation

Recently, there has been a great amount of interest in developing crystallisation in micro-scale crystallisers. This is due to the fact that current industrial crystallisers, in spite of their many advantages, still have issues when it comes to the final crystalline-product properties e.g. obtaining the desired crystals size distribution, shape and quality that is required both by the recent downstream processes and market demand (Jones, 2002). Crystallising in a microdomain has great potential to rectify these issues (see 1.2.) since they prove a stable, homogeneous and domain-controlled environment for crystals to nucleate and grow. In addition to the advantages that the microcrystallisers can provide (Jones, 2002; Su et al., 2007; Sultana, 2010) many researchers were used similar techniques, i.e. crystallisation in micro-domain, to investigate crystallisation-related-fields such as: aggregation (Hounslow and Pitt, 2011), crystals nucleation and growth kinetics (Ildefonso et al., 2011), sold form screening i.e. crystal crystallography and habit (Thorson et al., 2010) and solubility measurement (Laval et al., 2007). Despite the advantages that microchannels have when applied to the field of crystallisation, there are some difficulties which need to be dealt with before they can be successfully be applied to continuous crystallisation production. These difficulties are:

a) Blockage:

Continuous microcrystallisers have a high tendency to be blocked by the formation of crystals inside their micro-channels. In their review, Chen et al. (2011) and Moschou et al. (2014) indicate that passage blockage is a major obstruction to the application of microcrystallisers, and eliminating this problem would lead to further development of this concept.

b) Numbering-up:

In macro-scale processes, after bench studies are performed, the process is scaled-up to a size suitable to achieve the required production rate. This concept is not applicable for micro-scale applications, due to the fact their design concept relies in part on the large surface area to volume ratios which is reduced should scaling-up principles and rules be applied. The new concept of scale-out needs to be applied and accepted by the wider industrial community to bring micro crystalliser plants to production rates required by industry. Fig-

ure 2.5 illustrates the conceptual differences between the scaling-up and numbering-up principles.

c) Limited downstream process equipment:

In a technology vendors review carried out by Chen et al. (2011), small scale continuous filters (less than 4 l of slurry per minute) are unavailable in the industrial and scientific equipment supply market. This issue will lead to significant lag in developing continuous crystallisers for practical usage in the industry. Thus, for any research on microcrystallisers, points (a) to (c) above need to be addressed thoroughly to achieve a functional microcrystalliser.

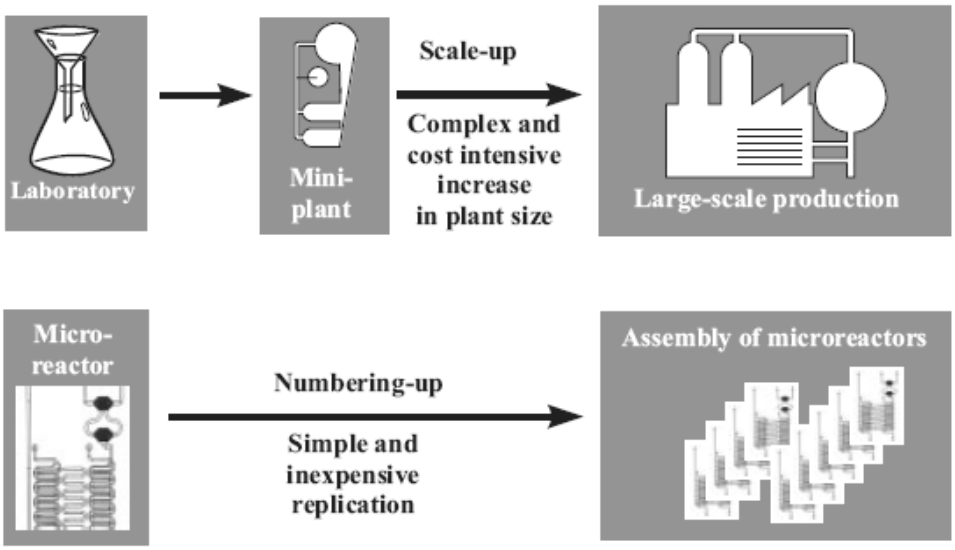

Figure 2.5: Generic scheme illustrating scale-up vs. numbering-up concepts (Source: Ehrfeld et al., 2000, p.9).

A review on the recent published works on the field of microcrystallisation (see Table 2.1) shows that all of the microcrystallisation experiments were carried out as a continuous operation. This operational manner can be further classified into a (i) plug flow regime and (ii) segmented flow regime where the crystallisation process occurs inside a droplet. In contrast, micro-batch crystallisation was performed to evaluate material related crystallisation properties and/or screening such as crystals nucleation and growth kinetics (Ildefonso et al., 2011), crystallography and habit (Thorson et al., 2010) and solubility (Laval et al., 2007). In term of crystallisation mode, most of the continuous microcrystallisation reported experiments were done using precipitation (Su et al., 2007; Scargiali et al., 2009; Jongen et al., 2003) or antisolvent (Ferguson et al., 2011; Thorson

et al., 2010; Sultana, 2010; Schiewe and Zierenberg, 2007; Myerson, 2003) as mode of crystallisation. This is because the straightforwardness of these two crystallisation modes compared to cooling crystallisation mode, which required extra equipments such as thermostatic water bathes in addition to the present of additional process variables such as temperature and cooling rate that need to be estimated, simulated, measured and controlled. Due to the lack in research for continuous microcrystallisation adopting cooling as a crystallisation mode, this research will study this fairly covered topic using the mostly used medicine of Paracetamol as model system.

Table 2.1: Summary of works done on crystallisation and related topics related to this research.

#	Author and year	Crystalliser dimension*	Crystallization mode	Operation mode	Objective
1	Yamazaki et al. 2011	h≤1 mm, l = 25 cm	Shear effect	Continuous	Investigation of optimum operation condition
2	Hounslow and Pitt 2011	Capillary tube	Cooling	Continuous	Aggregation characterisation
3	Ildefonso et al. 2011	Droplet vol. 250 nL	Cooling	Batch	Nucleation kinetics study
4	Ferguson et al. 2011	d = 3 mm	Antisolvent	Continuous	Design and optimisation study
5	Eder et al. 2010	d = 2.0 mm, l = 15 m	Cooling and Seeded	continuous	Continuously operated tubular crystalliser
6	Thorson et al. 2010	d = 60 micrometer	Antisolvent, cooling and evaporation	Batch	Solid form screening
7	Sultana 2010	h = 250m, w = 250m and l = 1.5 m	Antisolvent and supercritical	Continuous and segmented flow	Demonstration of continuous crystallisation in a microfluidics device
8	Scargiali et al. 2009	Taylor-Couette reactor	Precipitation	Continuous	Nano particle Precipitation
9	Schiewe and Zierenberg 2007	d = 1–2 mm and l = 1–25 m	Antisolvent	segmented	Producing inhalable Medicaments
10	Su et al. 2007	d = 500 micrometers	Precipitation	Segmented flow	Continuous nanoparticle production
11	Laval et al. 2007	d = 500 micrometer	Cooling	Batch	Solubility screening
12	Jongen et al. 2003	Microchannel	Precipitation	Continuous segmented flow	Narrow particle size distribution and scale-out
13	Myerson 2003	d = 250 micrometer	Seeding, cooling,andantisolvent	Continuous	Controlled crystals size production
14	Lemaitre et al. 2002	d = 100 µm–10 mm and l = 5–7.5 m	Precipitation	Segmented flow	Controlled crystals size production

* d = diameter, l = length, h = height and w = width

2.10 Oscillatory Flow Mixer/Reactor

The application of external mechanical energy in the form of pulsation has been a common practice to improve chemical process performance, in term of mass and heat transfer rates. Theses processes were commonly known among other as oscillatory flow units such as oscillatory flow mixer (OFM) and oscillatory flow reactor (OFR). This external energy can be applied on a process mainly by two means such as:

1. Alternating motion of some built-in-parts of a process column or vessel e.g. trays in which an oscillatory flow within the contained materials is generated. Such alternating motion will increase the contact areas between the materials phases within the vessel which enhanced the mass, heat or reaction rates depending on the process type.

2. Oscillation inside a process unit is generated by the oscillatory hydraulic transmission of a perturbation to the liquid contained in the column or vessel. This perturbation is typically generated by positive displacement pumps with a plug or membrane at the inlet section.

A typical OFR can be achieved by the application of an oscillatory flow to a cylindrical column or pipe containing periodically spaced orifice baffles. Figure 2.6 shows a schematic representation of an OFR. This OFR can be operated in a batch or continuous manner and in a horizontal or vertical orientation. Liquids or multiphase fluids are typically oscillated in the axial direction by means of diaphragms, or pistons, at one or both ends of the tube (Caldeira and Ni).

2.10.1 Oscillatory flow mixing in baffled tubes

Figure 2.7 shows the mechanism of oscillatory flow mixing in baffled tubes or channels. By the present of baffles perpendicular to an oscillatory flow direction, the flow patterns between two baffles exhibit a complicated eddy mixing pattern due to the presence of baffles walls. Two half cycles can be identified, each containing flow infusion (forward stroke) and withdraw (backward stroke), corresponding to a sinusoidal velocity-time function (see Figure 2.8. On each infusion, vortex rings are formed downstream of the baffles. A peak velocity is reached and then as the flow reversed, the vortices are swept into the bulk, and consequently unravel with bulk flow acceleration in the opposite (axial) direction. It is the radial velocities, arising from the repeating cycles of vortex formation, and of similar magnitude of the axial ones, which create a uniform mixing in each inter-baffle

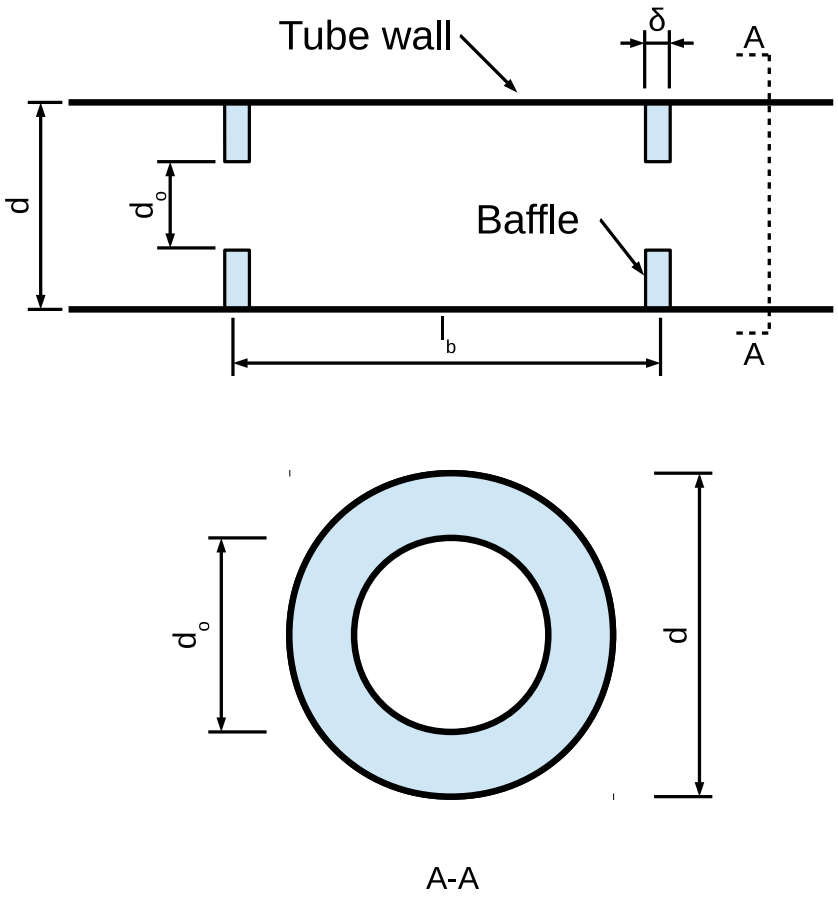

Figure 2.6: schematic diagram shows a typical baffled tube along with its geometrical basis.

zone (Brunold et al., 1989; Mackley and Ni, 1993; Howes et al., 1991; Reis, 2006).

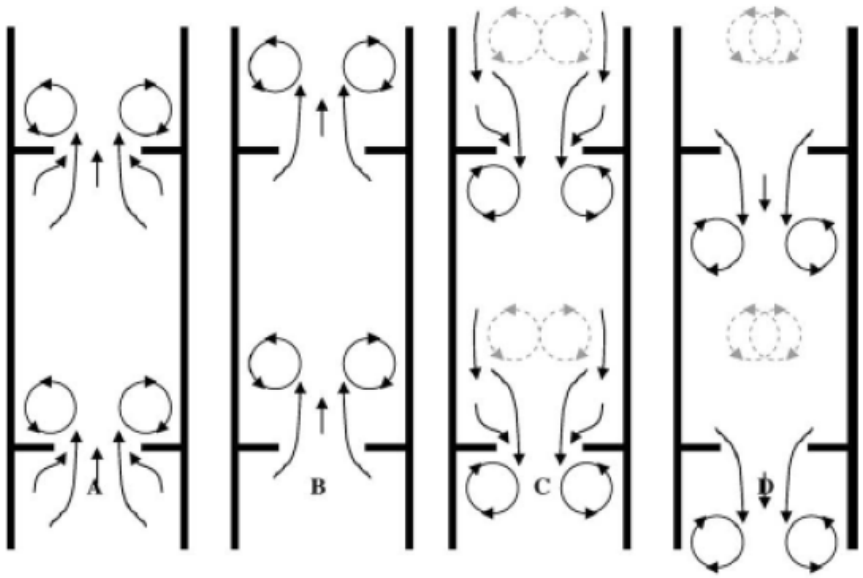

Figure 2.7: Mechanism of oscillatory flow mixing (OFM) in an OFR. (A) Start of infusion. (B) Peak velocity in forward stroke. (C) Start of backward stroke. (D) peak velocity in backward stroke (source: Reis, 2006).

2.10.2 Parameters governing the OFR

The dynamical nature of OFR had been characterised by a few fundamental dimensionless groups, i.e. the classical Reynolds number, Re_n, the oscillatory Reynolds number, Re_o, and the Strouhal number, St. Furthermore, two dimensionless geometrical parameters can be used to link the fluid mechanics within OFR with its geometry: the baffle spacing defined as l_b/d, the baffle free area, a, defined as: d_o/d. A brief definition of each dimensionless group is presented in the following sections.

2.10.2.1 Net-flow Reynolds number, Re_n

In flow in pipes the Reynolds number, Re_n, is the dimensionless number used as the indicator of the type of flow which is defined as follows

$$Re_n = \frac{\rho DU}{\mu} \tag{2.6}$$

where D is the tube diameter, μ the viscosity of fluid and U the mean superficial flow velocity.

2.10.2.2 The oscillatory Reynolds number, Re_o

When an oscillatory motion is introduced onto the net flow, an additional dimensionless group is often needed to characterise such oscillatory motion, in conjunction with the above defined Re_n.

$$Re_o = \frac{\rho D U_o}{\mu} \tag{2.7}$$

where D is the tube diameter, μ the viscosity of fluid and U_o the maximum oscillatory flow velocity. Recent studies have been show that in an OFR operated at low Re_o e.g.$\tilde{1}$00–300, it exhibits plug flow characteristics and the generated vortices are axisymmetrically within each baffled cavity. When Re_o increases further, the symmetry is broken and flow becomes intensely mixed and chaotic (Stonestreet and Van Der Veeken, 1999; Ni and Pereira, 2000). Figure 2.8 shows an arbitrary oscillatory flow at different Re_o generated from a syringe pump with a sinusoidal pumping program. These different Re_o were generated from different pumping frequencies with constant amplitude.

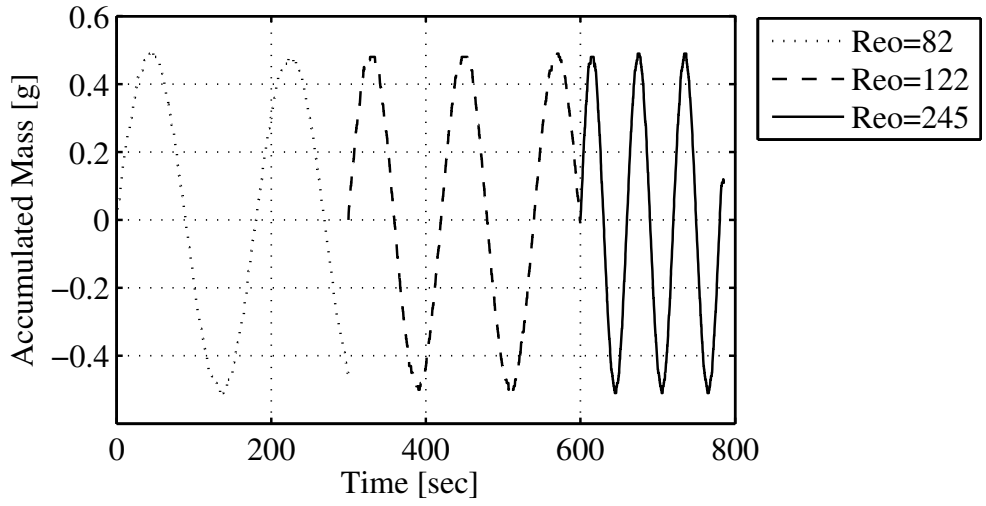

Figure 2.8: Sinusoidal oscillatory flow generated using the syringe pump with a 1 ml syringe for different oscillatory Reynolds number, Re_o. Mass flow rate were recorded using an on-line digital balance connected to a computer.

2.10.2.3 The Strouhal number, St

The description of OFR/OFM develops further when tube inserts or varying tube shapes are incorporated. Sobey (1982) introduced another dimensionless number, when working in a flow through a furrowed channel to account for the additional parameters involved. This was named the Strouhal number,

$$St = \frac{fh}{U_o} \tag{2.8}$$

where h is the half channel width and U_o is the maximum oscillatory velocity at the maximum channel width. The physical meaning of such dimensionless group was just given in Sobey's later work of flow past an indentation in a channel (Sobey, 1985) as the ratio of the channel length scale to the scale of the fluid particle displacement. Brunold et al. (1989) followed Sobey's examples and definitions and reported the second dimensionless group to define the fluid mechanics in OFR's, referring to it as the Strouhal number, St. It represents a measure of the effective eddy propagation and is defined as the ratio of column diameter to the stroke length:

$$St = \frac{d}{4\pi x_o} \tag{2.9}$$

where d is the tube diameter and x_o is the oscillatory pump stroke length. This re-definition of St is actually the most used. Although it was indicated by Ni and Gough (1997) that the St numbers was originally developed for Von Karman vortex street phenomenon, which is the development of an oscillatory vortices behind a cylindrical object in a flowing fluid, which later used by oscillatory baffled flow (OBF) researches. It is worth to indicate that it would be better to use the Keulegan-Carpenter number which is originally developed to study the fluid flow behind object subjected to oscillatory flow.

References

T. Allen. *Powder sampling and particle size determination*. Elsevier, 2003. 18

C. R. Brunold, J. C. B. Hunns, M. R. Mackley, and J. W. Thompson. Experimental observations on flow patterns and energy losses for oscillatory flow in ducts containing sharp edges. *Chemical Engineering Science*, 44 (5):1227–1244, 1989. U4289 Times Cited:100 Cited References Count:12. 25, 27

R. Caldeira and X.W. Ni. Continuous manufacturing of multi-products using a continuous oscillatory baffled reactor. 23

Jie Chen, Bipul Sarma, James M. B. Evans, and Allan S. Myerson. Pharmaceutical crystallization. *Crystal Growth & Design*, 11(4):887–895, 2011. 10, 19, 20

Rafael J. P. Eder, Stefan Radl, Elisabeth Schmitt, Sabine Innerhofer, Markus Maier, Heidrun Gruber-Woelfler, and Johannes G. Khinast. Continuously seeded, continuously operated tubular crystallizer for the production of active pharmaceutical ingredients. *Crystal Growth & Design*, 10(5):2247–2257, 2010. 22

W. Ehrfeld, V. Hessel, and H. Lwe. *Microreactors: new technology for modern chemistry*. Wiley-VCH, 2000. ix, 18, 20

S. Ferguson, G. Morris, M. Barrett, H. Hao, and B. Glennon. Design and optimization of plug flow crystallizers, August 4th, 2011 2011. 20, 22

Wayne J. Genck, David S. Dickey, Frank A. Baczek, Daniel C. Bedell, Kent Brown, Wu Chen, Daniel E. Ellis, Peter Harriott, Tim J. Laros, Wenping Li, James K. McGillicuddy, Terence P. McNulty, James Y. Oldshue, Fred Schoenbrunn, Julian C. Smith, Donald C. Taylor, Daniel R. Wells, and Todd W. Wisdom. *Liquid-Solid Operations and Equipment*, chapter 18, pages 1922–2074. McGraw-Hill, New York, 8th edition, 2008. 9, 14, 15, 17

Carl L. Hansen, Emmanuel Skordalakes, James M. Berger, and Stephen R. Quake. A robust and scalable microfluidic metering method that allows protein crystal growth by free interface diffusion. *Proceedings of the National Academy of Sciences of the United States of America*, 99(26): 16531–16536, 2002. 18

R. L. Hartman, J. P. McMullen, and K. F. Jensen. Deciding whether to go with the flow: evaluating the merits of flow reactors for synthesis. *Angew Chem Int Ed Engl*, 50(33):7502–19, 2011. Hartman, Ryan L McMullen, Jonathan P Jensen, Klavs F P50 GM067041/GM/NIGMS NIH HHS/ Germany International ed. in English Angew Chem Int Ed Engl. 2011 Aug 8;50(33):7502-19. doi: 10.1002/anie.201004637. Epub 2011 Jun 27. 18

G. T. Hefter and R. P. T. Tomkins. *The experimental determination of solubilities*. J. Wiley & Sons, Chichester, West Sussex, England; Hoboken, NJ, 2003. 13

M. J. Hounslow and K. Pitt. Poiseuille flow crystallizer a novel device in which to characterise crystal aggregation during precipitation from solution, August 4th, 2011 2011. 19, 22

T. Howes, M. R. Mackley, and E. P. L. Roberts. The simulation of chaotic mixing and dispersion for periodic flows in baffled channels. *Chemical Engineering Science*, 46(7):1669–1677, 1991. 25

M. Ildefonso, N. Candoni, and S. Veesler. Using microfluidics for fast, accurate measurement of lysozyme nucleation kinetics. *Crystal Growth & Design*, 11(5):1527–1530, 2011. 19, 20, 22

Alan G. Jones. *Crystallization process systems*. Butterworth-Heinemann, Oxford; Boston, 2002. ix, 10, 11, 13, 14, 15, 17, 18, 19

Nathalie Jongen, Marcel Donnet, Paul Bowen, Jacques Lemaître, Heinrich Hofmann, Rainer Schenk, Christian Hofmann, Montaha Aoun-Habbache, Sophie Guillemet-Fritsch, Joseph Sarrias, et al. Development of a continuous segmented flow tubular reactor and the scale-out concept–in search of perfect powders. *Chemical engineering & technology*, 26(3):303–305, 2003. 20, 22

Philippe Laval, Nicolas Lisai, Jean-Baptiste Salmon, and Mathieu Joanicot. A microfluidic device based on droplet storage for screening solubility diagrams. *Lab on a Chip*, 7(7):829–834, 2007. 19, 20, 22

Jacques Lemaitre, Nathalie Jongen, Robert Vacassy, and Paul Bowen. Production of powders, 2002. 18, 22

M. R. Mackley and X. Ni. Experimental fluid dispersion measurements in periodic baffled tube arrays. *Chemical Engineering Science*, 48(18): 3293–3305, 1993. Lt797 Times Cited:56 Cited References Count:16. 25

Robert Rahn McKeown, James T. Wertman, and Philop C. Dell'Orco. *Crystallization design and scale-up*, chapter 13. John Wiley & Sons, New Jersey, 2010. 18

Alfons Mersmann. *Crystallization technology handbook*. Marcel Dekker, New York, 2 edition, 2001. 10, 11, 14

Parthena Moschou, Mart HJM de Croon, John van der Schaaf, and Jaap C Schouten. Advances in continuous crystallization: toward microfluidic systems. *Reviews in Chemical Engineering*, 30(2):127–138, 2014. 18, 19

J. W. Mullin. *Crystallization*. Butterworth-Heinemann, Oxford; Boston, 2001. ix, 12, 13, 14, 15, 16, 17

J. W. Mullin and M. Slpek. Solubility and density isotherms for potassium aluminum sulfate water alcohol systems. *Journal of Chemical and Engineering Data*, 26(2):164–165, 1981. Lk186 Times Cited:9 Cited References Count:4. 13

Allan S. Myerson. Molecular crystals of controled size, 2003. 18, 21, 22

A.S. Myerson. *Handbook of industrial crystallization*. Butterworth-Heinemann, 2nd edition, 2002. 17

X. Ni and P. Gough. On the discussion of the dimensionless groups governing oscillatory flow in a baffled tube. *Chemical Engineering Science*, 52 (18):3209–3212, 1997. Xu013 Times Cited:32 Cited References Count:45. 27

Xiongwei Ni and Nitin E. Pereira. Parameters affecting fluid dispersion in a continuous oscillatory baffled tube. *AIChE Journal*, 46(1):37–45, 2000. 26

N. Reis. *Novel oscillatory flow reactors for biotechnological applications*. PhD thesis, 2006. ix, 25

F. Scargiali, A. Busciglio, F. Grisafi, and A. Brucato. On the performance of a taylor-couette reactor for nanoparticle precipitation, June 14, 2011 2009. 20, 22

Joerg Schiewe and Bernd Zierenberg. Process and apparatus for producing inhalable medicaments, 2007. 18, 21, 22

Herbert M. Schoen, C. S. Grove, and Joseph A. Palermo. The early history of crystallization. *Journal of Chemical Education*, 33(8):373–null, 1956. doi: 10.1021/ed033p373. 9

Ian J Sobey. Observation of waves during oscillatory channel flow. *Journal of Fluid Mechanics*, 151:395–426, 1985. 27

I.J. Sobey. Oscillatory flows at intermediate strouhal number in asymmetric channels. *Journal of Fluid Mechanics*, 125(1):359–373, 1982. 27

P. Stonestreet and P. M. J. Van Der Veeken. The effects of oscillatory flow and bulk flow components on residence time distribution in baffled tube reactors. *Chemical Engineering Research and Design*, 77(8):671–684, 1999. 26

Y. F. Su, H. Kim, S. Kovenklioglu, and W. Y. Lee. Continuous nanoparticle production by microfluidic-based emulsion, mixing and crystallization. *Journal of Solid State Chemistry*, 180(9):2625–2629, 2007. 19, 20, 22

Mahmooda Sultana. *Microfluidic systems for continuous crystallization of small organic molecules*. PhD thesis, 2010. 19, 21, 22

P. Tabeling. *Introduction to Microfluidics*. Oxford University Press, Oxford, 2010. 18

Michael R. Thorson, Sachit Goyal, Yuchuan Gong, Geoff G.Z. Zhang, Charles F. Zukoski, and Paul J.A. Kenis. Microfluidic platforms for the screening of solid forms of candidate drugs, October 2010 2010. 19, 20, 22

Mark van der Woerd, Darren Ferree, and Marc Pusey. The promise of macromolecular crystallization in microfluidic chips. *Journal of Structural Biology*, 142(1):180–187, 2003. 18

Yasuo Yamazaki, Takahiro Nishita, Sun Lee, and Woo-Sik Kim. Strategic design of micro-crystallizer for industrial applications, August 4th, 2011 2011. 22

Chapter 3

Metastable zone width measurement

3.1 Introduction

This chapter discusses an experimental study of crystallisation of model component in a microchennel device by means of cooling a saturated solution of that component. The goal of this experiment was to produce fine crystals of the model component with a very narrow particle size distribution and high crystalline quality as well.

3.2 Nucleation measurement

Formation of stable nucleuses is crucial for any seedless crystallization process. These stable nucleuses will be further grow and may aggregate to form the final crystalline product. In this study and in order to achieve these stable nucleuses, it is important to study the affecting factors on this process such as supersaturation degree that required to initiating the crystals nucleation process. Solution supersaturation degree inside the microchannel will be controlled by cooling a saturated solution using a substrate thermal management block (STMB) wherein the temperature of the micro crystallizer can be contorted by setting the temperature of the STMB to the desired value. Solution supersaturation degree will be indicated as the difference between the equilibrium temperature of the initial Paracetamol solution inside the syringe and the microcrystallizer's temperature, ($\Delta T > 0$).

3.3 Methodology

In order to start a continuous homogeneous and primary crystallisation process within a micro-reactor domain from solution by means of cooling, it is important to know the time width of the metastable zone for a particular set of supersaturation conditions. Once this width is known, a suitable set of experimental conditions can be chosen for specific reactor geometries to ensure a suitable density of stable nucleus that will grow to the desired size within the reactor.

The Metastable zone width can be measured by two different methods (Garside et al., 2002):

Isothermal: where the mother liquor is rapidly cooled to a predetermined temperature, after which the time taken from reaching the saturation state to the appearance of the first detectable crystal is measured.

Polythermal: where the mother liquor is progressively cooled at a certain cooling rate, after which the elapsed time from reaching the saturation state to the appearance of the first detectable crystal is measured.

With the current experimental apparatus available in the lab, the isothermal technique was used to measure the metastable zone width for Paracetamol solutions with different initial concentrations.

3.3.1 Isothermal metastable zone width measurement procedure

The experiment was carried out in the flowing steps:

1. Paracetamol solutions with different initial concentrations were prepared at temperature above the lab temperature e.g. 40–70 ℃. These solutions were prepared by dissolving a known amount of Paracetamol solute into water at a temperature 5 ℃ above its saturation temperature. All Paracetamol solutions were kept for 15 min at these elevated temperatures to ensure the total dissolution of the Paracetamol solutes in the water. This step is very important to eliminate any secondary crystallisation on the surface of any none-completely dissolved particles of Paracetamol.

2. Once the solution is loaded into the syringe pump and the pump connected to the microcrystalliser, the pump is activated to provide

a flow of the Paracetamol solution through the micro-reactor. This is initially at a temperature above its saturation temperature by at lest 5 ℃.

3. The solution inside the microcrystalliser is then cooled rapidly to a certain temperature below the saturation temperature and the elapsed time from reaching this temperature until the appearances of the first crystal is recorded.

4. The above procedure is repeated for different temperatures to produce the metastable zone width for that particular solution.

By repeating steps (1) throughout (4) for different Paracetamol solution concentrations, it is possible to produce the metastable zone width for Paracetamol solution at different concentrations.

3.4 Experiment setup

The microchannel system used to measure the metastable zone consists of a PID temperature controller, a heat sink and fan module, a thermoelectric module, syringe pump and microcrystalliser. Figures 3.1 and 3.2 illustrate schematically and show the arrangement of these parts. A more detailed description of each unit and their usage is given below:

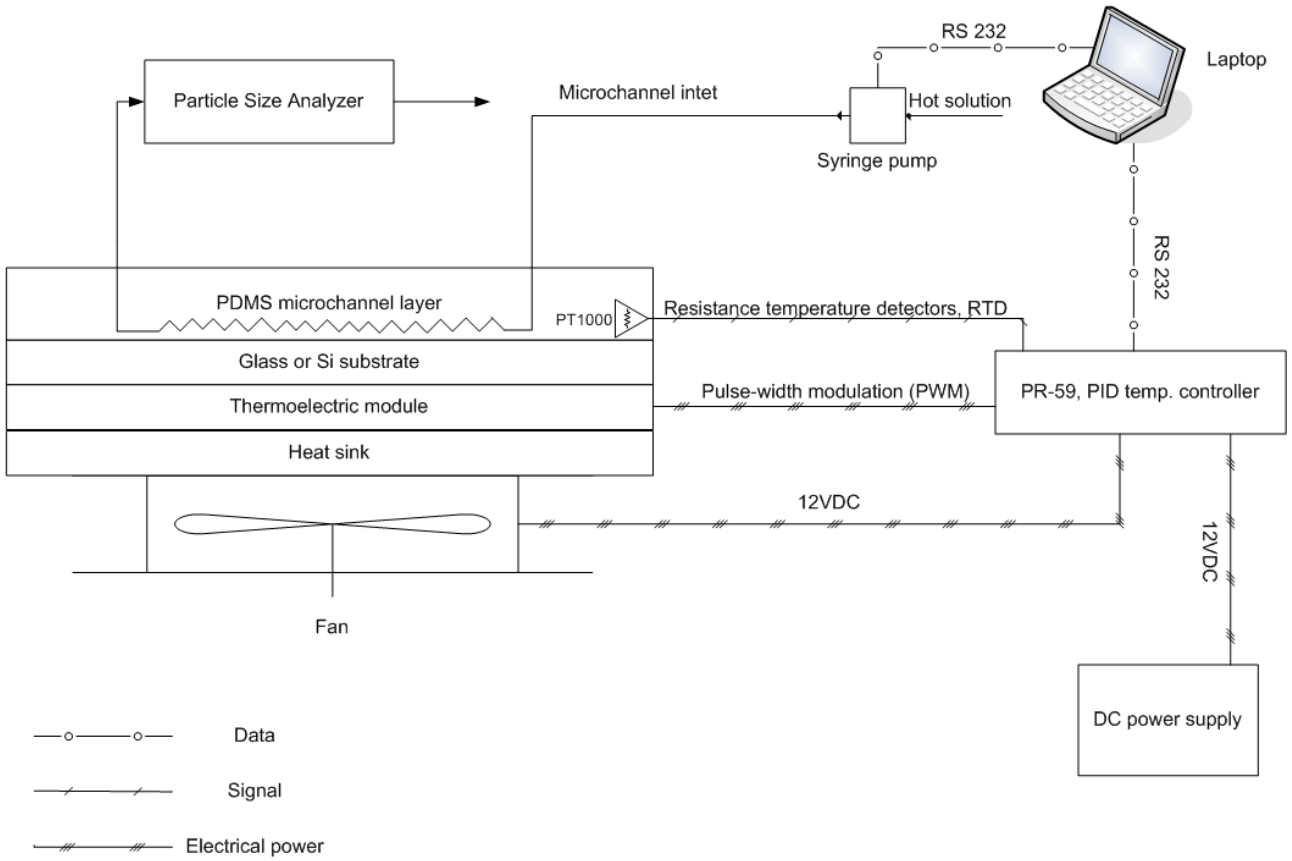

Figure 3.1: Schematic diagram of the Paracetamol crystallisation nucleus detecting experiment.

PID temperature controller: this unit (Laird Technologies S-41451 Gteborg, Sweden, Part# TC-XX-PR-59) controls the substrate temperature by altering the supplied power to the thermoelectric modules. The desired temperature setting can be achieved by communicating to the controller via an RS-232 communication protocol using a specialized software (Seiberlich and Oskarsson, 2008). The real-time data can be retrieved and stored for the purpose of post processing. Using this temperature controller will allow to achieve a working temperature ranges from 10 to 80 ℃ in addition to maintain a constant substrate temperature with a margin of ±0.05 ℃, See Figure 3.3.

Heat sink and fan module: this is to dissipate the heat generated from the thermoelectric modules during the cooling or heating operation modes. Fan operation is controlled via the PR-59 controller as well.

Thermoelectric modules: these are used for heat pumping to achieve the desired substrate temperature and were controlled by the PR-59 controller. This is achieved in conjunction with the temperature feedback signal sent by the resistance temperature detectors (RTD), PT100. In this experiment, two of these thermoelectric modules were electrically connected in series to provide working area of 4×8 cm^2 which is comfortably enough for a microscope-slide-sized microfluidic device.

Syringe pump module: this controls the flow rate of the mother liquor that feed to the microcrystalliser. The flow rate is controlled by means of either directly keying-in the required flow rate on the syringe pump keypad or by an on-line command from a master computer which can control the substrate temperature and the mother liquor flow rate simultaneously. Syringes that used to hold the initial Paracetamol solution were thermally insulated to keep the Paracetamol solution at the desired temperature.

Particle size analyser: This instrument (Zetasizer Nano ZS90, Malvern Instruments) was used to measure the size of the Paracetamol crystals that nucleated inside the micro crystallizer. This Particle size analyzer (PSA) had a particle size detecting range of 0.3–10000 nanometre. The Zetasizer Nano is a two angle particle analyzer for the enhanced detection and measurement of small or dilute samples, and samples at very low or high concentration using dynamic light scattering. Using the flow mode option enables the system to be connected

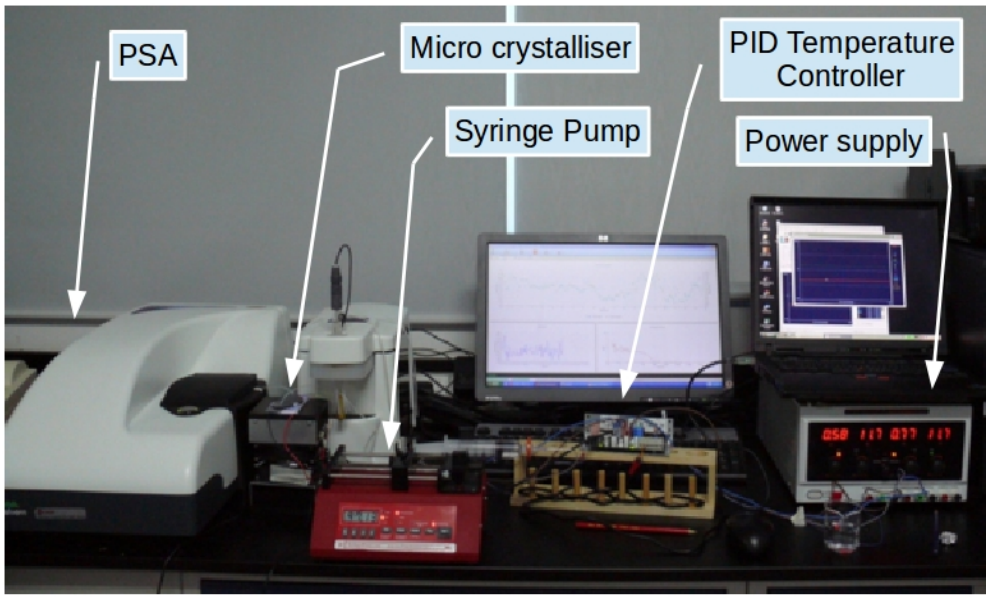

Figure 3.2: A photo showing the metastable zone width measurement experiment.

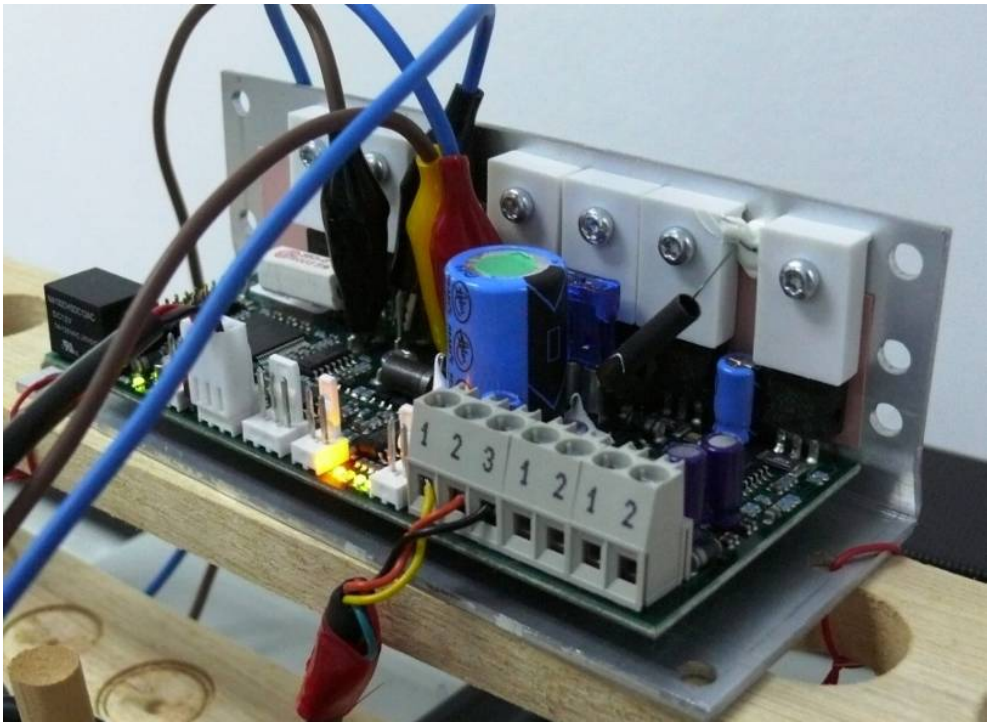

Figure 3.3: A photo for the PR-59 PID temperature controller.

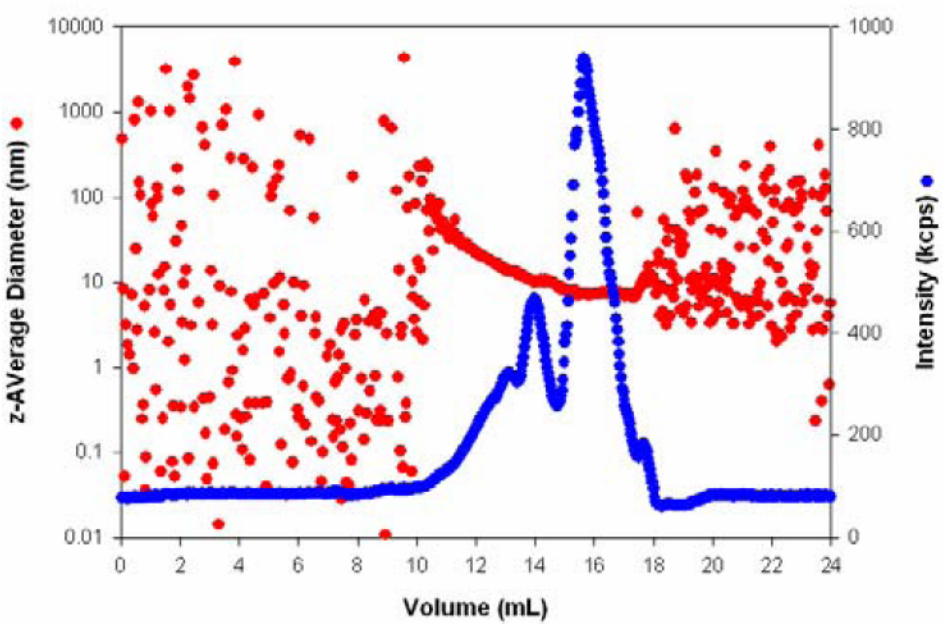

Figure 3.4: Typical raw particle size data obtained from a flow mode from the Zetasizer particle size analysis instrument (source: Malvern Instruments Ltd., 2007).

to the output of the microcrystalliser to be use as a size detector for any nucleated Paracetamol particles. Figures 3.4 and 3.5 show a typical particle size trace obtained from a flow measurement mode from the Zetasizer particle size analysis instrument (Malvern Instruments Ltd., 2007). The blue and red dots in Figures 3.4 and 3.5 represent the reflected light intensity that reflected from the sample and its correspondent particle size respectively. The region of interest is the region where the scattered intensity is significantly higher than a baseline, and the particle size varies smoothly. Therefore, a method is needed to filter the particle size trace and remove the meaningless data. This data filtration and base line estimation was done automatically by the instrument software (Malvern Instruments Ltd., 2012). The output of the microcrystalliser was analysed directly without any further treatment or dilution.

The microcrystalliser device: this microfluidic devise consists of 32 parallel microchannels with dimensions; 350 micrometre in width (W), 100 micrometre in height (H) and 5 cm in length (L) which shown in Figure 3.6. The use of 32 parallel channels was to enable a relatively large amount of Paracetamol mother solution to flow (1 to 3 ml/min) in attempt to prevent it from being cooled down before reaching the

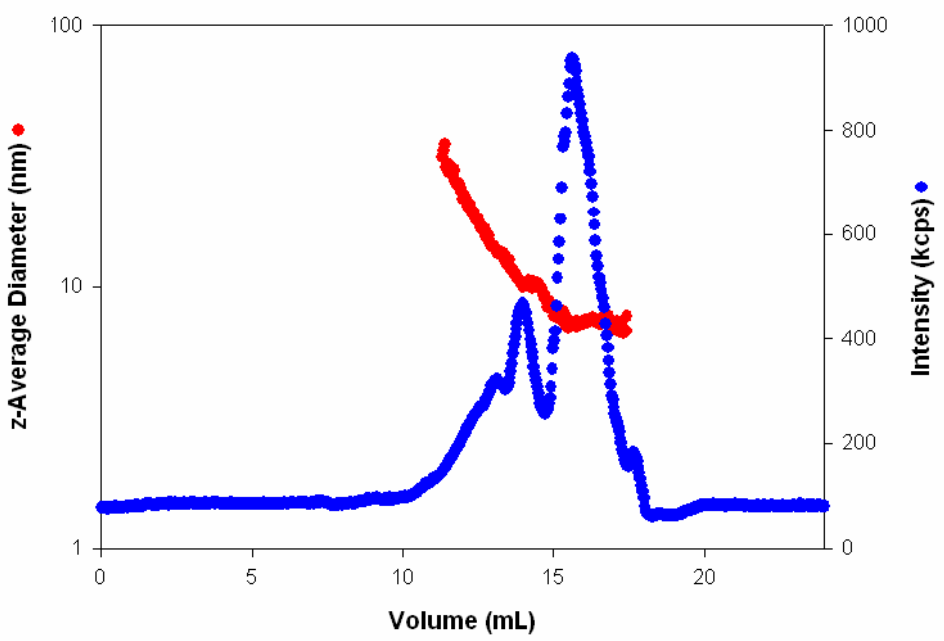

Figure 3.5: Typical particle size data obtained from a flow mode from the Zetasizer particle size analysis instrument after data filtration and setting the intensity base line (source: Malvern Instruments Ltd., 2007).

inlet of the microcrystalliser. At the same time, the use of parallel channels will maintain a low flow rate within each individual channel. Furthermore, this will (1) minimize the pressure drop across the device (2) ensures a suitable flow rate for the particle size analyser to prevent any crystals sedimentation inside the measurement cuvette, (3) minimise the required time for the Paracetamol solution to move from the outlet of the microcrystalliser to the inlet of the PSA. The microcrystalliser was casted in PDMS and hydrophilically bounded to a Silicon wafer.

3.5 Results and discussions

Using the above described experiment setup and procedure; three experiments were conducted with (i) a 1.4% Paracetamol solution (ii) a 2.35% Paracetamol solution and (iii) a 5.0% Paracetamol solution at different temperatures below their solubility temperature. Results from these experiments were summarised in Table 3.1.

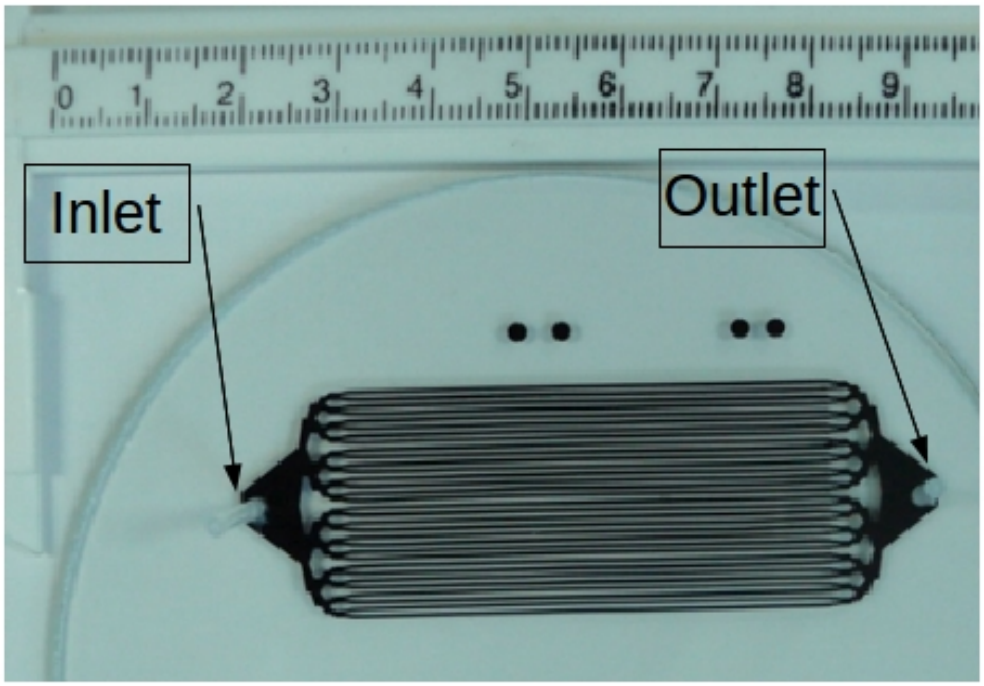

Figure 3.6: Image showing the microchannel geometry used, consisting of 32 parallel-microchannels with the dimensions of 350W×100H×5cmL.

Table 3.1: Summary of the saturated Paracetamol nucleation deducting experiments

#	**Paracetamol initial concentration [g /100 g of water]**	**Equilibrium temp. [℃]**	**Substrate temp. [℃]**	**Super cooling degree [℃]**	**Supersaturation ratio,** $S = \frac{C}{C^*}$**[-]**	**Remarks**
1	1.4	25	23	2	1.02	No nucleation observe
2	1.4	25	8	15	1.62	No nucleation observe
3	2.4	41	29	12	1.52	No nucleation observe
4	2.4	41	28	13	1.56	No nucleation observe
5	2.4	41	27	14	1.6	No nucleation observe
6	2.4	41	26	15	1.62	No nucleation observe
7	2.4	41	25	16	1.65	No nucleation observe
8	2.4	41	24	17	1.67	No nucleation observe
9	2.4	41	23	18	1.69	No nucleation observe
10	2.4	41	22	19	1.74	No nucleation observe
11	2.4	41	21	20	1.8	No nucleation observe
12	2.4	41	20	21	1.9	No nucleation observe
13	2.4	41	19	22	2	No nucleation observe
14	2.4	41	18	23	2.08	No nucleation observe
15	2.4	41	17	24	2.18	No nucleation observe
16	2.4	41	16	25	2.28	No nucleation observe
17	2.4	41	15	26	2.37	No nucleation observe
18	5	59	40	19	2.13	No nucleation observe
19	5	59	39	20	2.13	No nucleation observe
20	5	59	35	24	2.6	No nucleation observe
21	5	59	34	25	2.7	Nucleation observe
22	5	59	33	26	2.8	Nucleation observe

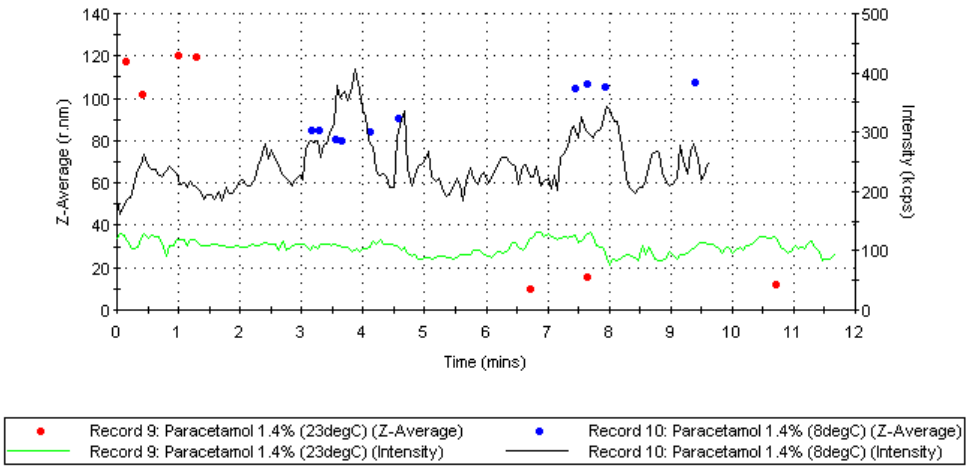

Figure 3.7: Particle size data obtained from a flow mode for 1.4% saturated Paracetamol solution undergoes two different super cooling degrees. Saturation temperature for the 1.4% Paracetamol solution was 25 ℃ and the experiment flowrate was 1.5 ml/min.

Results from the 1.4% Paracetamol solution trial and for two different supersaturation degrees, S=1.02 and S=1.62 (run#1 and 2) are shown in Figure 3.7 which represent measured scattered light intensity in kilo cycle per second (kcps) and particle size (Z-Ave) in nm verses experiment time in min. Conclusion from this figure was there was no singe of any nucleation within the microcrystalliser at these particular supersaturation levels. These results were expected in view of the fact that the supersaturation degrees that achieved were low which lead to a relatively long induction period. Particle size reading given by the PSA were not considered as the intensity reading for both supersaturation degrees did not show a significant rising as required to determined the intensity base line. Furthermore, Paracetamol crystals ware observed approximately one hour later after the end of these two runs in the product collecting tubes.

For the 2.45% initial saturated Paracetamol solution which undergoes different supersaturation degrees, S, rangeed from 1.52 to 2.37, results were similar to the previous trials especially for the ones with relatively low supersaturation degrees. Figures 3.8 to 3.10 show measured light intensity and particle size for the 2.45% initial saturated Paracetamol solution with $S = 1.52-1.9$ at which there were no sign of any particle nucleation. Again, reasons behind that were the same as the supersaturation degrees were low which required a longer induction time for Paracetamol crystals to be nucleated and grow within the microcrystalliser domain. Apparently, this

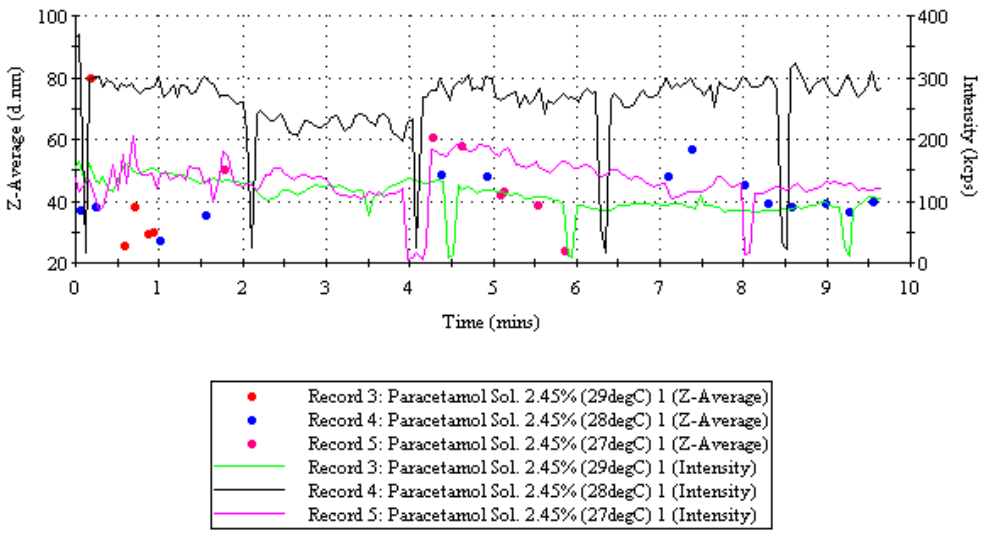

Figure 3.8: Particle size data obtained from a flow mode for 2.45% saturated Paracetamol solution undergoes three different super cooling degrees. Saturation temperature for the 2.45% Paracetamol solution was 41 ℃ and the experiment flowrate was 1.5 ml/min.

induction time still larger than the resident time of the microcrystallizer so that no crystallisation was detected within it.

In Figures 3.10 to 3.12 the reflected light intensity level for the saturated Paracetamol solutions were decline after few minutes from the start of the experiment for substrate temperature of 20 ℃ and below (run # 12–17). This is mainly because the first few millilitres that flown in the system were pure water used to flush the microcrystalliser which have a different reflective index compared with saturation Paracetamol solution which affects the measured reflected light intensity. This decline in the reflected light intensity will not be considered as a base line for the reflected light intensity required for the flow mode measurement.

Particles size results for the 2.45% saturated Paracetamol solution which shown in Figures 3.8 to 3.12 (run # 3-17) were disregarded as its reflected light intensity did not show the anticipated behaviour of having a base line followed by a significant rise in the level of the reflected light intensity (see Figure 3.5). For these experiments runs, Paracetamol crystals were observed in the product collecting tubes within 15–30 min after the end of each run. Here the time taken to observe crystal formation in the collecting tubes after the end of each experiment run were about 50% less than time taken in run # 1–3. This indicates a reduction the induction time as the supersaturation degree increases. Figure 3.13 shows a typical Paracetamol

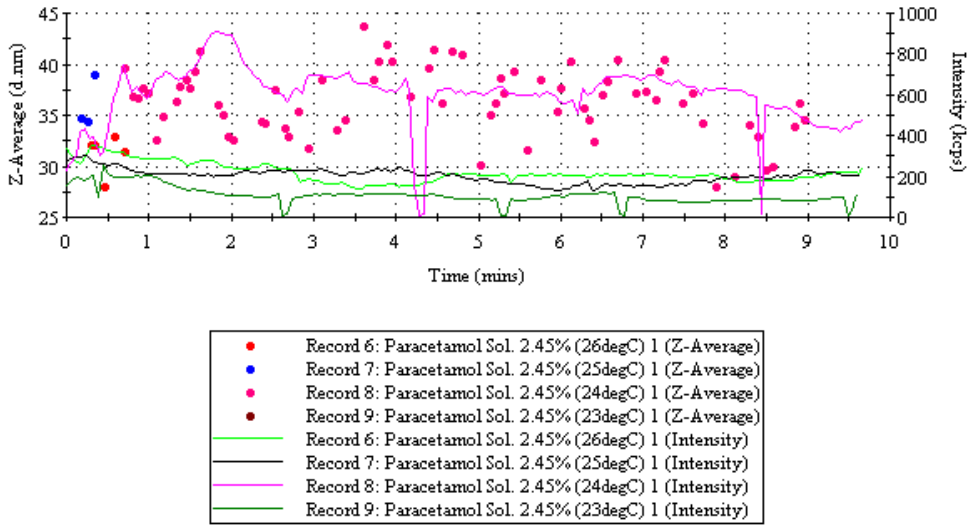

Figure 3.9: Particle size data obtained from a flow mode for 2.45% saturated Paracetamol solution undergoes four different super cooling degrees. Saturation temperature for the 2.45% Paracetamol solution was 41 ℃ and the experiment flowrate was 1.5 ml/min.

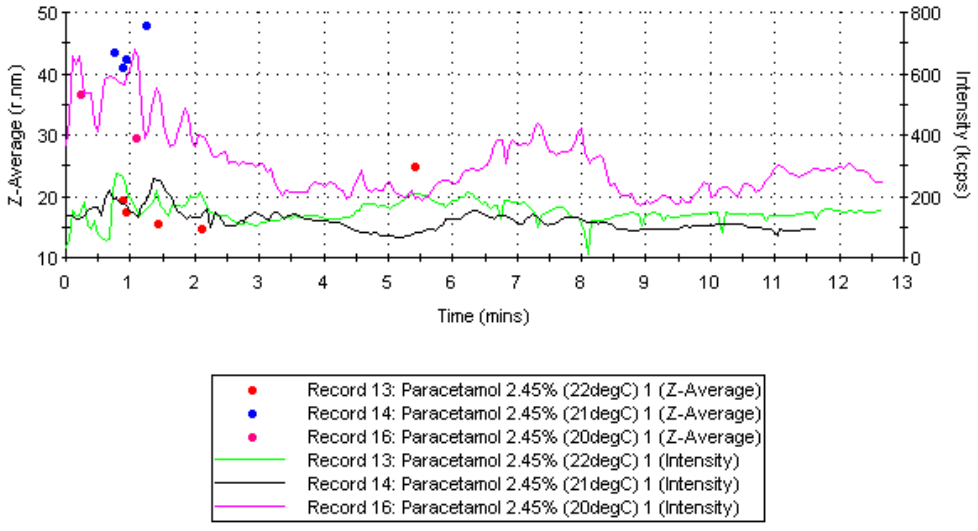

Figure 3.10: Particle size data obtained from a flow mode for 2.45% saturated Paracetamol solution undergoes four different super cooling degrees. Saturation temperature for the 2.4% Paracetamol solution was 41 ℃ and the experiment flowrate was 1.5 ml/min.

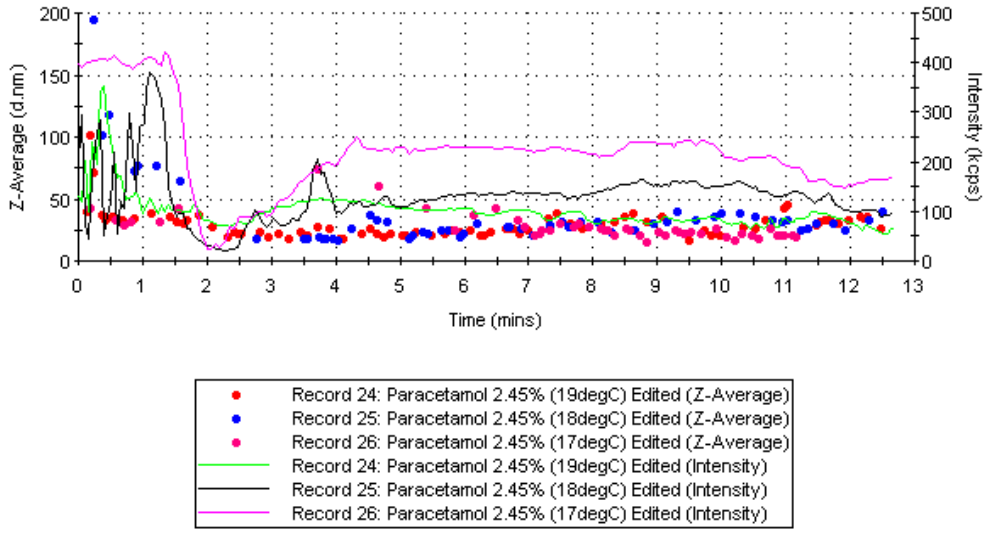

Figure 3.11: Particle size data obtained from a flow mode for 2.45% saturated Paracetamol solution undergoes three different super cooling degrees. Saturation temperature for the 2.45% Paracetamol solution was 41 ℃ and the experiment flowrate was 1.5 ml/min.

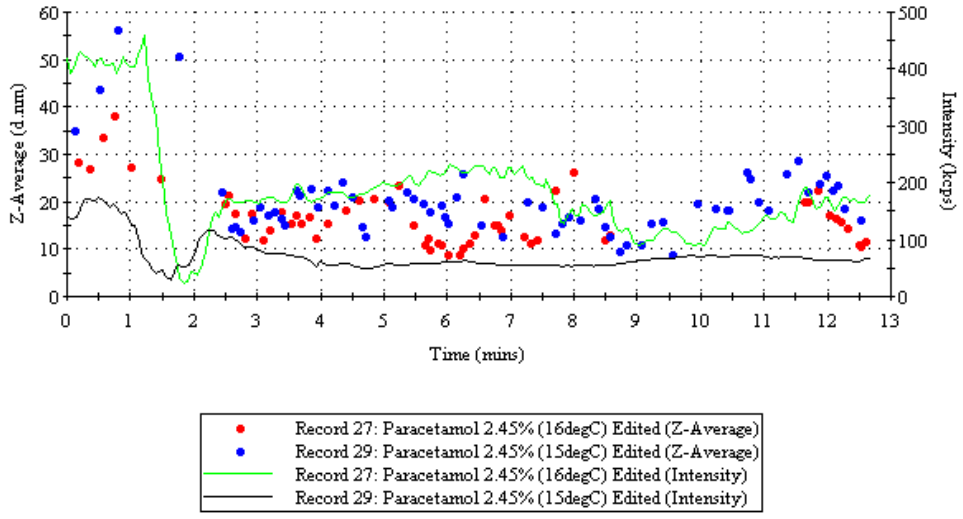

Figure 3.12: Particle size data obtained from a flow mode for 2.45% saturated Paracetamol solution undergoes two different super cooling degrees. Saturation temperature for the 2.45% Paracetamol solution was 41 ℃and the experiment flowrate was 1.5 ml/min.

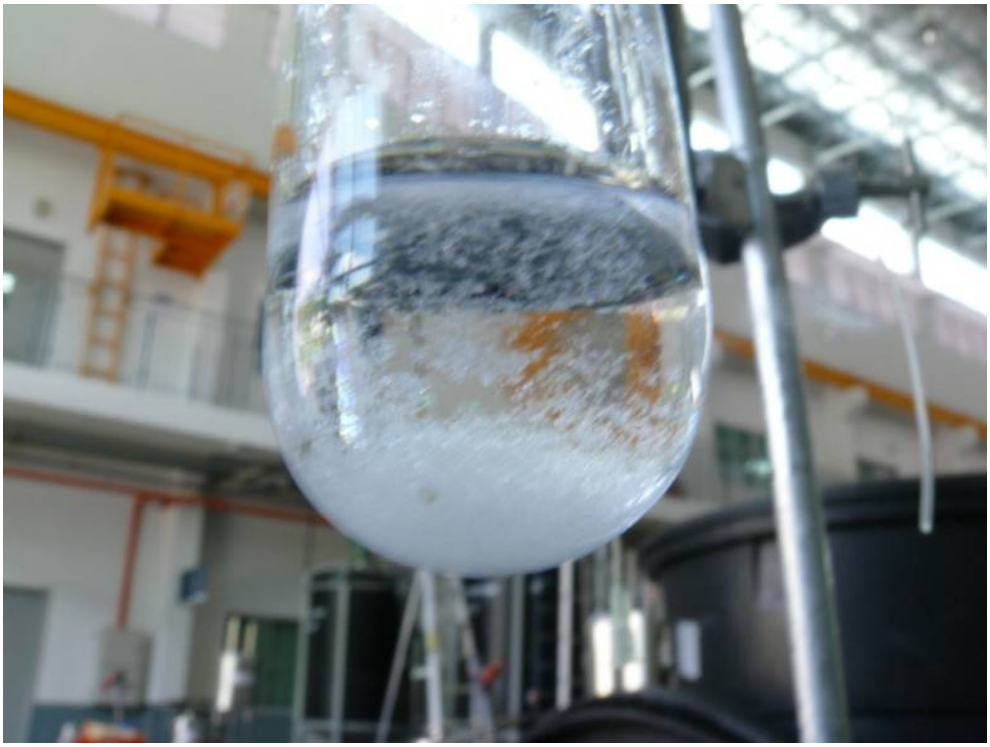

Figure 3.13: A typical Paracetamol crystals formation observed after 15–30 min after the end of nucleation measurement experiment of 2.45% saturated Paracetamol solution.

crystals formation observed after 15-30 min after the end of nucleation measurement experiment for runs # 3–17.

For the 5% saturated Paracetamol solution with a 59 ℃ equilibrium temperature, a nucleation was occurred within the microcrystalliser domain. That was achieved for supersaturation degrees, S, of 2.7 and above. As shown in Figures 3.14 and 3.15 a significant raises in the reflected light intensity levels were achieved for runs # 21 and 22, supersaturated degree of 2.7–2.80. This is a clear indication for the present of particles within the system, which led to an increase the reflected light levels. The average nucleated particle diameter measured was about 10 nm. In addition to that, Paracetamol crystals were observed at the end of the product tube during the experiment running time, which indicate that the nucleated Paracetamol particles were growing within the system and flow out of it.Figure 3.16 shows the Paracetamol crystals flowing out at the end of the output tube for experiment run # 22.

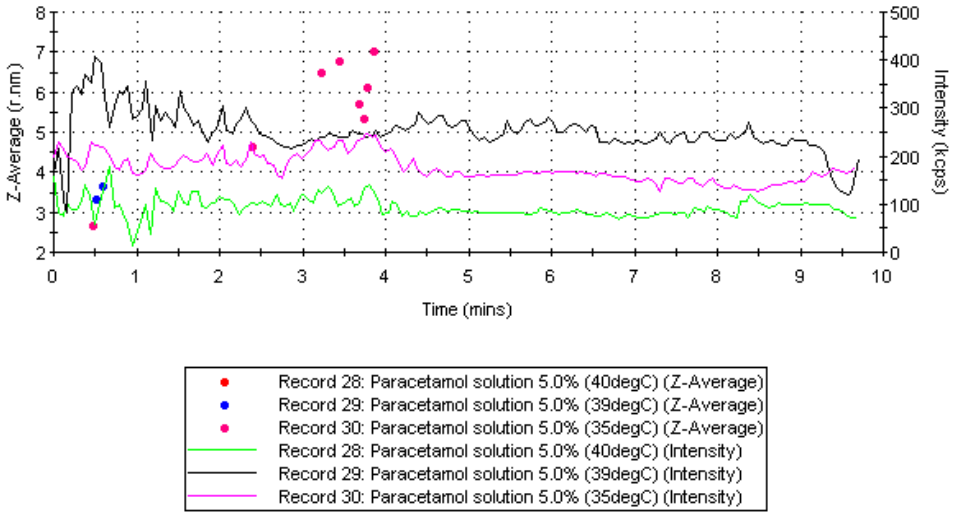

Figure 3.14: Particle size data obtained from a flow mode for 5.0% saturated Paracetamol solution undergoes three different super cooling degrees. Saturation temperature for the 5.0% Paracetamol solution was 59 ℃ and the experiment flowrate was 1.5 ml/min.

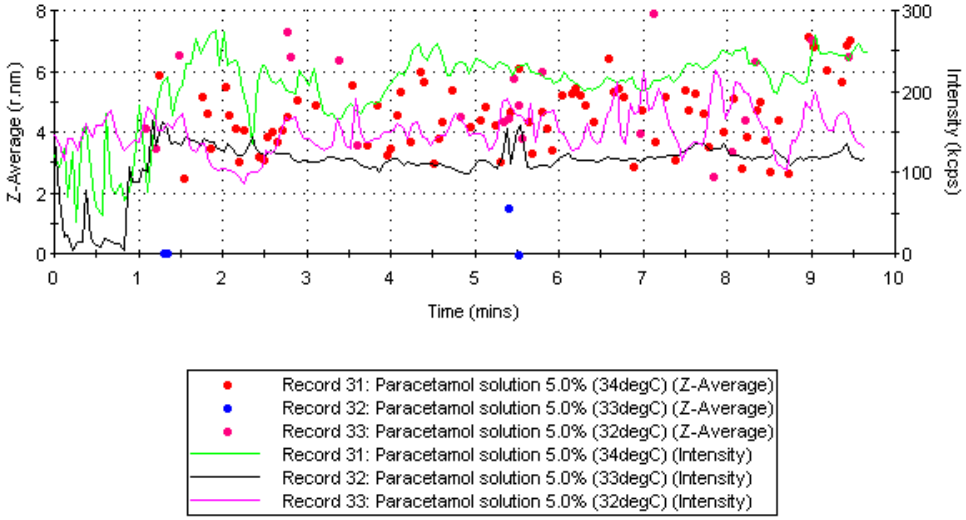

Figure 3.15: Particle size data obtained from a flow mode for 5.0% saturated Paracetamol solution undergoes three different super cooling degrees. Saturation temperature for the 5.0% Paracetamol solution was 59 ℃ and the experiment flowrate was 1.5 ml/min.

Figure 3.16: Crystal observation at the end of the output tube for 5.0% Saturated Paracetamol nucleation measurement experiments.

3.6 Conclusions and future work

Experiment trials conducted to investigate the possibility of nucleus formation by means of analyzing the particle size for a continuous flow of a saturated Paracetamol solution which undergoes a rapid cooling in thermally controlled microchannels were not consistence, did not show any degree of repeatability and very hard to carry out. The possible reasons for these drawbacks could be:

1. The limitation in the experiment trial's time such that each experiment run usually take 10–15 min and then stopped to refill the syringe with a saturated Paracetamol solution. Any attempts to increase the experiment time by lowering the flow rate was led to another conscience which addressed in the next point.

2. Any attempts to lower the experiment flow rate will lead to tubing blockage by the growing crystals because any formed and growing crystals will have longer time inside the system to grow enough and accumulated to block the tubing. In addition to that, lower flow rate will make the Paracetamol saturated solution get colder which

increases the formation and the growing of the crystals and again block the channels.

3. The inconsistency of the initial saturated Paracetamol solution temperature due to the batch and manual nature of syringe refilling process. Furthermore, the saturated Paracetamol solution temperature inside the syringe was dropped till it reached the room temperature which will force the Paracetamol to be crystallised inside the syringe and block the syringe needle.

4. Air trapping inside the microchannel array due to the dismantling and reassembling of the experiment tubing to refill the empty syringe, This will affect the ability to have smooth and consistence flow inside the microchannels, tubing and the size measurement cuvette.

Apart from the above mentioned limitations, it was very hard to maintain the Paracetamol saturated solution at elevated temperature prior to the inlet of the microcrystalliser without having the saturated solution losing heat and start crystallisation. Therefore and in order to eliminate these problems associated with cooling crystallisation, antisolvent crystallisation mode will be used as an alternative to the cooling mode, which can be done at lab temperature, for the rest of this research.

As the antisolvent crystallisation required mixing of a saturated solution with an antisolvent to drive crystallisation, mixing inside micochannels will be the critical part of the process to achieve fast mixing. Therefore, in the next chapters, mixing inside microchannels and continuous antisolvent crystallisation will be investigated using periodically baffled microchannels with superimposed oscillatory flow as a novel approach.

References

John Garside, Alfons Mersmann, Jaroslav Nvlt, Engineers Institution of Chemical, and Crystallization European Federation of Chemical Engineering. Working Party on. *Measurement of crystal growth and nucleation rates*. Institution of Chemical Engineers, Rugby, 2002. (Great Britain). 34

Malvern Instruments Ltd. Data analysis used in flow measurements, 2007. x, 39, 40

Malvern Instruments Ltd. Zetasizer software, 2012. 39

Johan Seiberlich and Thomas Oskarsson. Sc interface 1.1.22, 2008. 37

Chapter 4

The novel oscillatory baffled microreactor

4.1 Introduction

In the previous chapter, continuous crystallisation in microchannel by mean of rapid cooling of a saturation solution was investigated. Results were not consistence, did not show any degree of repeatability and the experimentations were very hard to carry out due to the difficulties in maintaining different parts of the microfluidic setup at different temperature levels and microchannels blockage by uncontrolled crystal growth. Therefore and in order to eliminate these problems, antisolvent crystallisation mode will be used as an alternative to the cooling mode. This can be done at lab temperature, using periodically baffled microchannels with superimposed oscillatory flow as a novel approach to promote mixing within micro domain crystalliser.

Introducing of an oscillatory flow within periodically baffled flowing channels which are known as oscillatory flow reactors, OFR, has been previously shown to be enhanced mass and heat transfer rates in larger systems (Zheng and Mackley, 2008; Harvey et al., 2001; Lawton et al., 2009) and to enhance crystal quality (Chew et al., 2004) because it increases the non axial mixing within the baffled channels. Therefore, it is possible that by applying the same methodology on a microchannel reaction domain which usually runs on very low Reynolds number of magnitude of 1, an encasement can be achieved in terms of good degree of mixing. In addition, superimposing oscillatory flow may assist in preventing microchannel blockage.

The dynamical nature of OFR is normally characterised using the following dimensionless groups, net flow Reynolds number, Re_n, oscillatory flow Reynolds number, Re_o, and Strouhal number, St. The Re_n and Re_o are calculated as shown in Equations 4.1 and 4.2 based on the net flow rate and the maximum oscillatory flow rate respectively. The Strouhal number is evaluated based on work adapted from (Sobey, 1982) and (Brunold et al., 1989) and it represents a measure of the effective eddy propagation and is defined as the ratio of column diameter to the stroke length.

$$Re_n = \frac{\rho D_h Q_n}{\mu A} \tag{4.1}$$

$$Re_o = \frac{\rho D_h Q_o}{\mu A} \tag{4.2}$$

$$\begin{aligned} St &= \frac{f D_h}{U_o} \\ &= \frac{1}{U_{red}} \end{aligned} \tag{4.3}$$

$$\begin{aligned} Sto &= \frac{\rho f D_h^2}{\mu} \\ &= St \times Re_o \end{aligned} \tag{4.4}$$

Figure 4.1 shows a drawing of an OBM, where the only differences between it and a common microchannel device are the presence of periodical baffles within the microchannel and an extra port to introduce the oscillation to the device. This OBM has D_h equal to 553.86 micrometre.

This chapter discussed (a) experimental setup to drive oscillatory flow, its performance and oscillatory flow profile, (b) computational fluid dynamics study to evaluate mixing in OBM, and (c) micro-flow visualisation technique to evaluate OBM.

4.2 Oscillatory flow profile

Initial experimental runs to drive oscillatory flow into OBM using New Era NE-1000 and NE-4000 syringe pumps (Figure 4.2) were unsuccessful mainly because of mechanical difficulties and limitation, which resulted into a poor and most of the times null oscillation flow inside the OBM. These difficulties and limitations were:

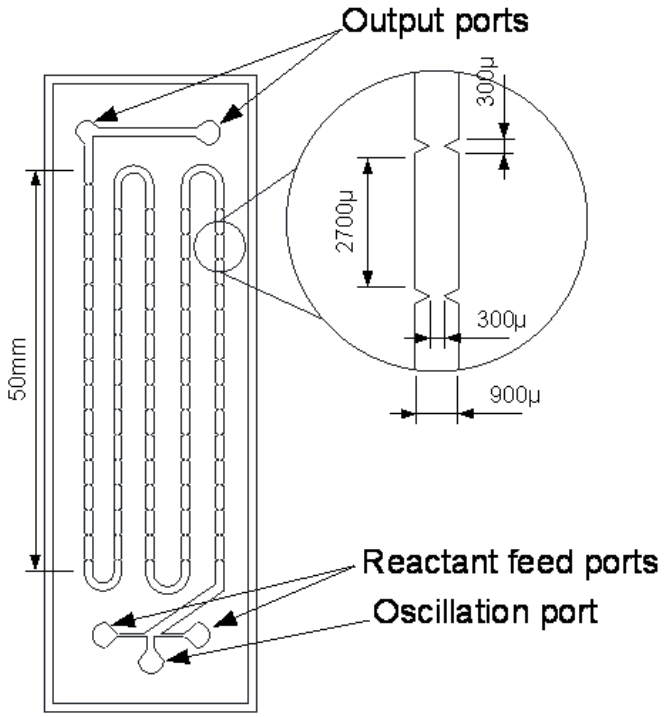

Figure 4.1: Detailed schematic for the OBM used in the experimentation of this chapter. This OBM has D_h equal to 553.86 Micrometres.

1. The relatively large mechanical play in the syringe-bump-carriage mechanism which affect the quality of the oscillatory flow especially at the upper range of f and the lower range of Re_o which required relatively small carriage reciprocating motion.

2. The rubbery-nature of the syringe plunger tip works as mechanical absorber to the small reciprocating movements of syringe plunger as well as it absorbed the oscillatory fluid kinetic energy that led to null oscillatory fluid movement in the OBM.

3. The presence of air pockets at the tip of the syringes which work as fluid kinetic energy absorber. These air pockets were hard to purge out of the system and it is easily introduced to the system whenever a manual refilling is required.

To overcome these limitations, a new set of syringe pumps with advanced features were acquired. These advanced features are:

- Programmable compensation to compensate the mechanical play in the system.

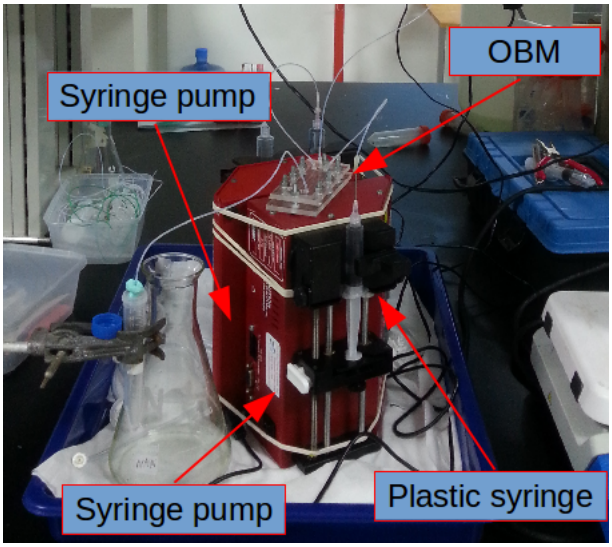

Figure 4.2: Initial oscillation flow experimentation. Syringe pumps were kept in vertical orientation in attempt to purge air pockets present at the tip of the plastic syringes.

- High-resolution plunger movement ranging from 1000 to 12000 steps per full stroke of three cm.
- Glass syringes with solid plunger tip.
- Electrical plunger hold-up mechanism to prevent back flow at high back pressure.
- Integrated selectable valve with several ports to ease the refilling and purging processes of the system that will eliminate the introduction of air in the system.

4.2.1 Experiment setup

Figure 4.3 shows a diagram of the experiment used to capture the oscillatory flow profile and to measure the performance of the newly acquired syringe pumps at different ranges of Re_o and f. This experiment setup consisted of CAVRO XE-1000 valve integrated syringe pump, OBM (Figure 4.1), a differential pressure sensor (DPS) (Freescale semiconductor, Inc., Integrated Silicon Pressure Sensor MPX4250DP) and an oscilloscope. The required oscillatory flow amplitude was controlled using CAVRO pump programming protocol by setting the plunger linear motion speed to deliver a flow rate with oscillatory Reynolds number equivalent to the required Re_o. While the oscillatory flow frequency, f, was controlled by setting the

amount of plunger reciprocal movement in term of steps to achieve a full oscillation cycle.

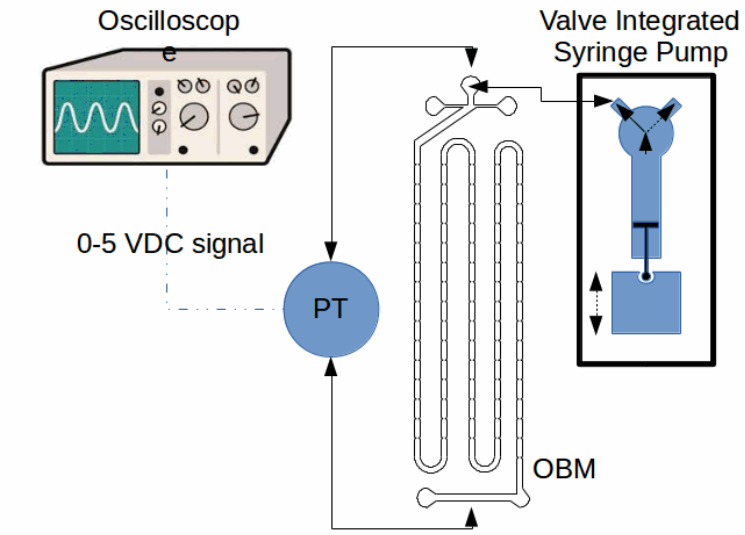

Figure 4.3: Diagram of the oscillatory flow qualifying experiment setup. Here, the valve integrated syringe pump was CAVRO XE-1000 and it is programmed using CAVRO pumps programming protocol.

4.2.2 Methodology

After filling the system with water and purging any trapped air pockets, syringe pump was programmed using CAVRO pump programming protocol to deliver an oscillatory flow with predetermined values of Re_o and f. For each combination of Re_o and f, the trends of differential pressure across the OBM were captured using an oscilloscope (Figure 4.4). The captured differential pressure trends will indicate the quality of the oscillatory flow.

4.2.3 Results and discussion

Figure 4.5 shows a captured oscilloscope screen showing pressure drop trend across the OBM measured in mV on the y-axis with a time interval of one second on the x-axis. Table 4.1 summarised the results obtained from the captured oscilloscope screens for each combination of Re_o and f. These results were measured pressures drop in mV, and oscillation frequency and a descriptive comment on the shape and quality of captures pressure drop trend. These were obtained from a full set of captured oscilloscope measurement screens listed in Appendix A.

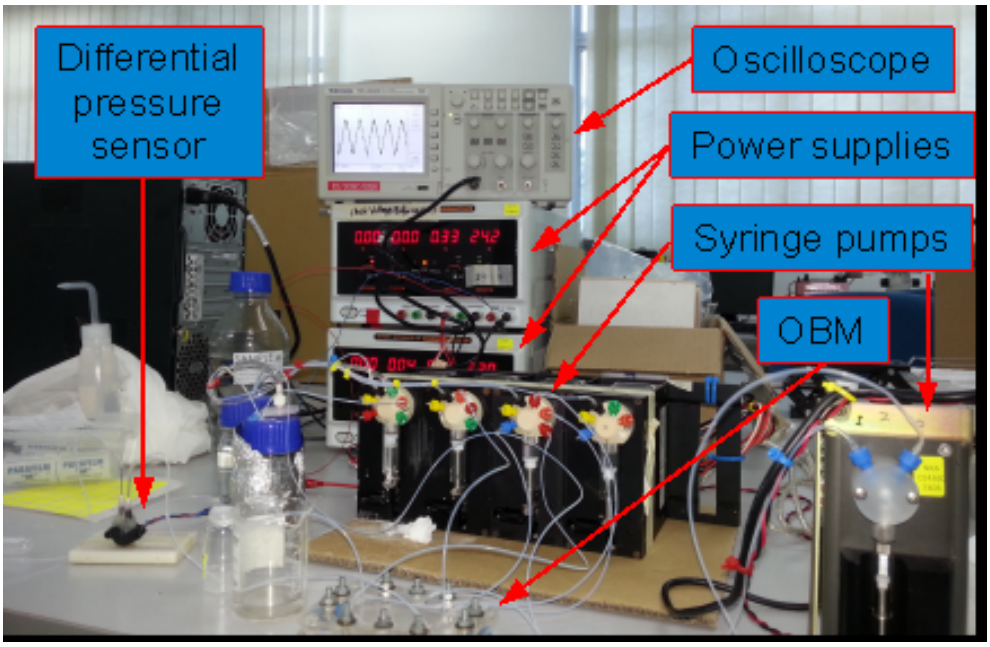

Figure 4.4: Photo illustrating the oscillatory flow generation using the valve-integrated syringe pumps. Oscillatory flow profiles and quality were captured using DPS and oscilloscope at different Re_o and f combinations.

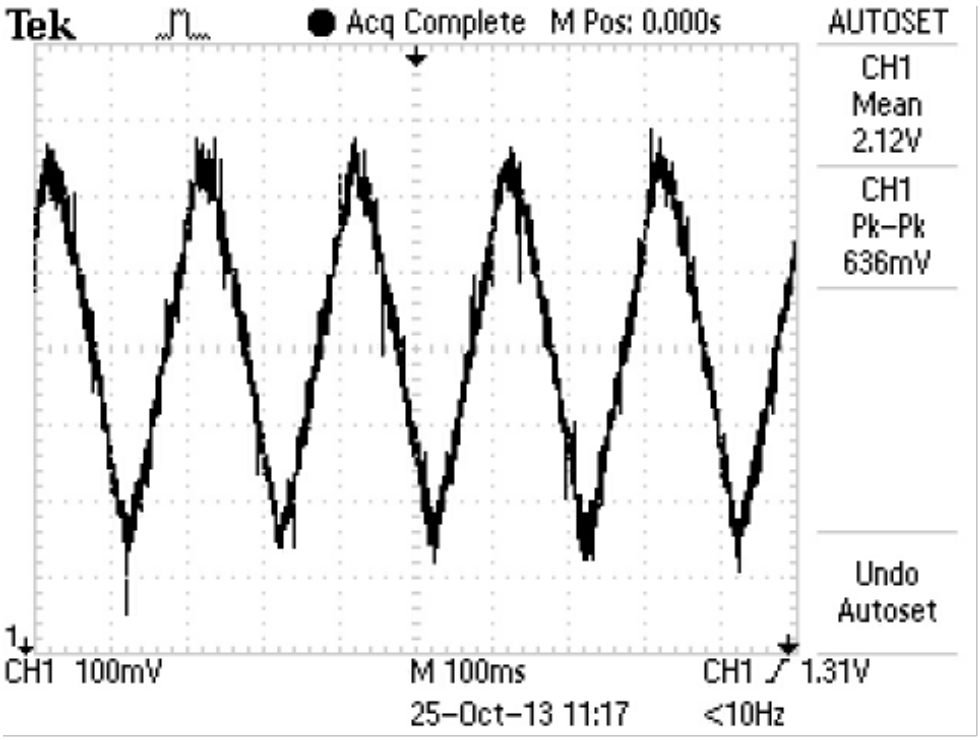

Figure 4.5: Captured oscilloscope screen depecting pressure drop trend across OBM. Here the x-axis represent time interval of 1 s and y-axis represent pressure drop measured in mV.

Table 4.1: The measured pressure drop and oscillation frequency at different programmed Re_o and f.

Syringe pump setting		**Measurements**		
Re_o	**f [Hz]**	**DP pk-pk [mV]**	**f [Hz]**	**Oscillation flow profile/quality**
100	5	200	4.25	Triangular
	10	100	9.5	Triangular
	15	80	14	Weak Triangular
	20	60	16	Very weak Triangular
	25	40	N/A	Not clear
200	5	300	4.75	Triangular
	10	150	9	Triangular
	15	100	14	Triangular
	20	75	17	Weak Triangular
	25	60	19	Very Weak triangular
300	5	400	5	Triangular
	10	200	10	Triangular
	15	150	15	Triangular
	20	100	17	Weak Triangular
	25	75	22	Very weak triangular
385	5	600	5	Triangular
	10	300	9.5	Triangular
	15	200	14	Triangular
	20	100	18	Triangular
	25	80	24	Weak Triangular
	30	60	28	Weak Triangular

Figure 4.6 shows the measured fluid oscillation frequency vs the required, programmed, oscillation frequency at different Re_o. At this figure, measured fluid oscillation frequencies become less than the required oscillation frequency when the required oscillation frequency increased. Furthermore, this reduction is inversely proportional to the Re_o level. This indicates that this valve integrated syringe pump tend to start to operate relatively inefficiently at higher oscillation frequency range, i.e. f >20 Hz.

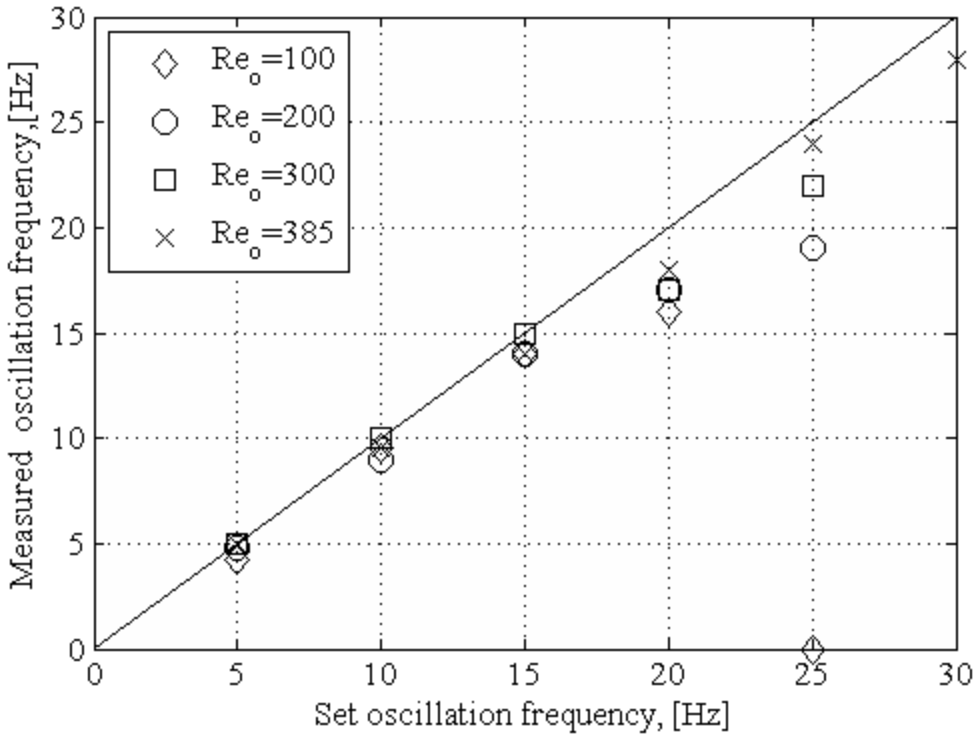

Figure 4.6: comparison between achieved fluid oscillation frequency and programmed oscillation frequency for different Re_o. The estimated error for each measurement is about 5% of its value.

Furthermore, as shown in Figure 4.7 the pressure drop trends were falling to about 100 mV as the required fluid oscillation frequency is greater than 15 Hz regardless of the Re_o. Reasons for this performance is because the syringe pump do not have enough time to accelerate to the required plunger speed as the required oscillation frequency become higher, i.e. this syringe pump will have less time to deliver the required fluid oscillation amplitude.

As a conclusion to this section, the use of this valve integrated syringe pump was better than the previously used syringe pumps e.g. New Era syringe pumps. In addition to that, the valve integrated syringe pump was capable to generate a good oscillatory flow at fluid oscillation ranged from 1 to 20 Hz and it performed better at higher Re_o. Finally and for the

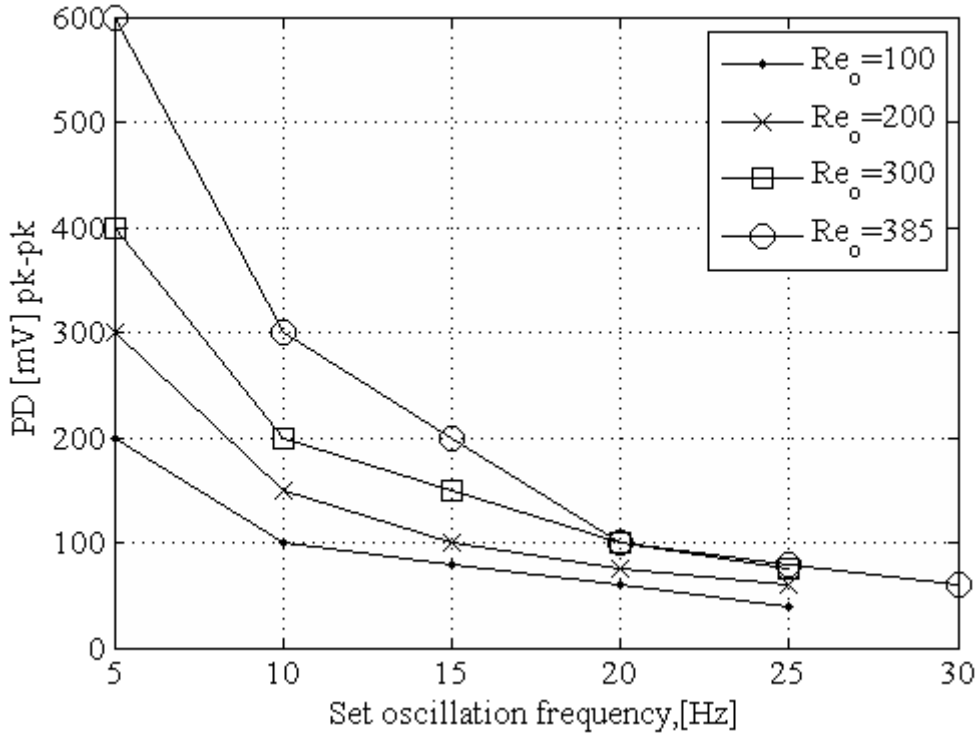

Figure 4.7: Pressure drop (PD) as function of oscillation frequency for different Re_o. The estimated error for each measurement is about 5% of its value.

purpose of computational fluid dynamics, the fluid oscillation function will be a triangular function as shown from the pressure drop trends obtained from this experiment.

4.3 Computational fluid dynamics modelling

Before crystallisation experiments were performed, initial computational fluid dynamics (CFD) modelling was undertaken using COMSOL Multiphysics finite element analysis, solver and simulation software. This modelling study was intended to quantify the non-axial mixing in the OBM by measuring the instantaneous total area of the generated vortices behind the baffles in the oscillatory flow direction at different predetermined values of Re_o and f.

4.3.1 Single inter-baffle cavity modelling

CFD simulations were performed using two-dimensional (2D) geometry of a single inter-baffle cavity with additional inlet and outlet zones to simulate oscillatory flow in a long OBM, see Figure 4.8. Governing equations

were time dependant incompressible Navier-Stokes equations with shallow channel approximation, Equations 4.5 to 4.7. The use of shallow channel approximation in this model will help to account for the drag force term, Equation 4.6, as a volume force to the fluid-flow equation. This drag force is not typically included in a 2D model because they exclude the walls heights boundaries heights which have greater effect on the flow. Boundary conditions were no-slip boundary conditions at the OBM walls and periodic oscillatory flow at the inlet and outlet of a baffled microchannel, as shown in Figure 4.9. Inlet and outlet periodic velocities were forced to be identical to simulate the spatial and temporal periodicity nature of the OBM. Working fluid was water at 25℃.

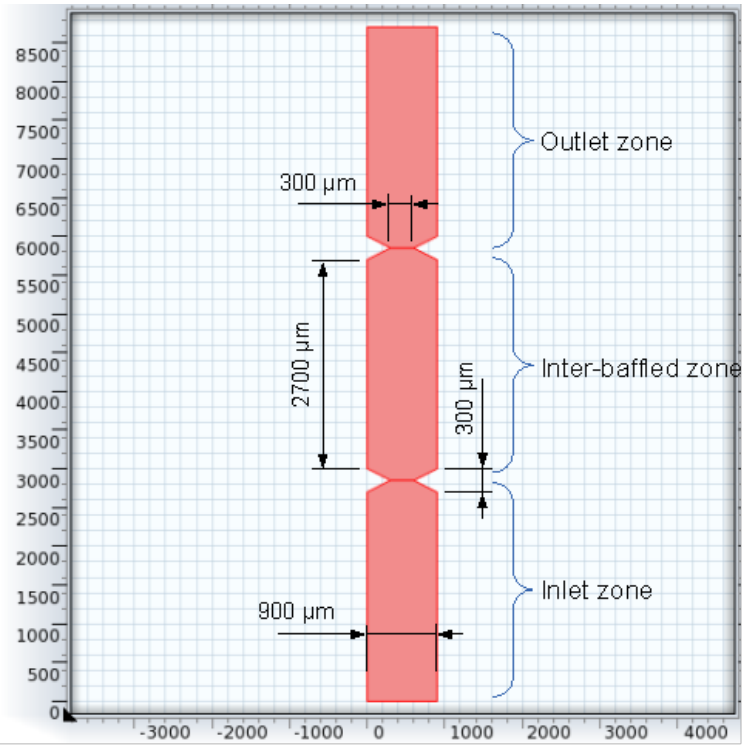

Figure 4.8: 2D geometry of single inter-baffled cavity with additional inlet/outlet zones used in the CFD study.

$$\rho\frac{\partial u}{\partial t}+\rho\left(u\cdot\bigtriangledown\right)u=\bigtriangledown\cdot\left[-PI+\mu\left(\bigtriangledown u\right)+\left(\bigtriangledown u\right)^{T}\right]+F \tag{4.5}$$

$$F_{\mu}=-12\frac{\mu u}{h^{2}} \tag{4.6}$$

$$\rho\bigtriangledown\cdot u=0 \tag{4.7}$$

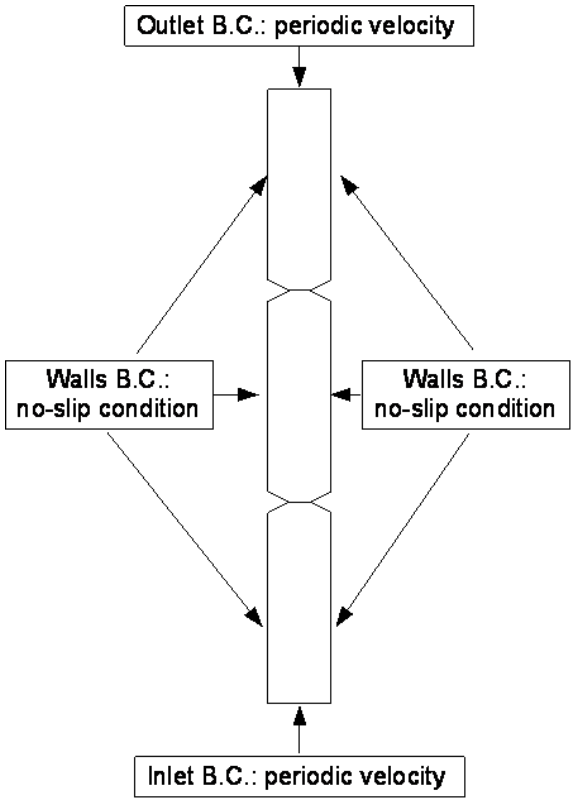

Figure 4.9: Boundary conditions (B.C.) used in the CFD studies for a single inter-baffled area with inlet and outlet zones. Inlet and outlet periodic velocities and mesh configuration were forced to be identical to simulate the spatial and temporal periodicity nature of the OBM.

4.3.2 Oscillatory flow

Previous studies dealing with CFD modelling of oscillatory baffled reactors or channels were without clear reasons using sinusoidal oscillatory function to model the periodically inlet and outlet flow boundary conditions (Hamzah et al., 2012; Zheng and Mackley, 2008; Jian and Ni, 2005; Reis et al., 2005). However, in this CFD modelling, as shown through experimentation detailed in §5.2 inlet and outlet boundary conditions were triangular oscillatory flow. Figure 4.10 shows an arbitrary oscillation function used in this fluid dynamics modelling. Here, Re_o represents the oscillatory flow intensity and f represents the oscillation frequency in Hz.

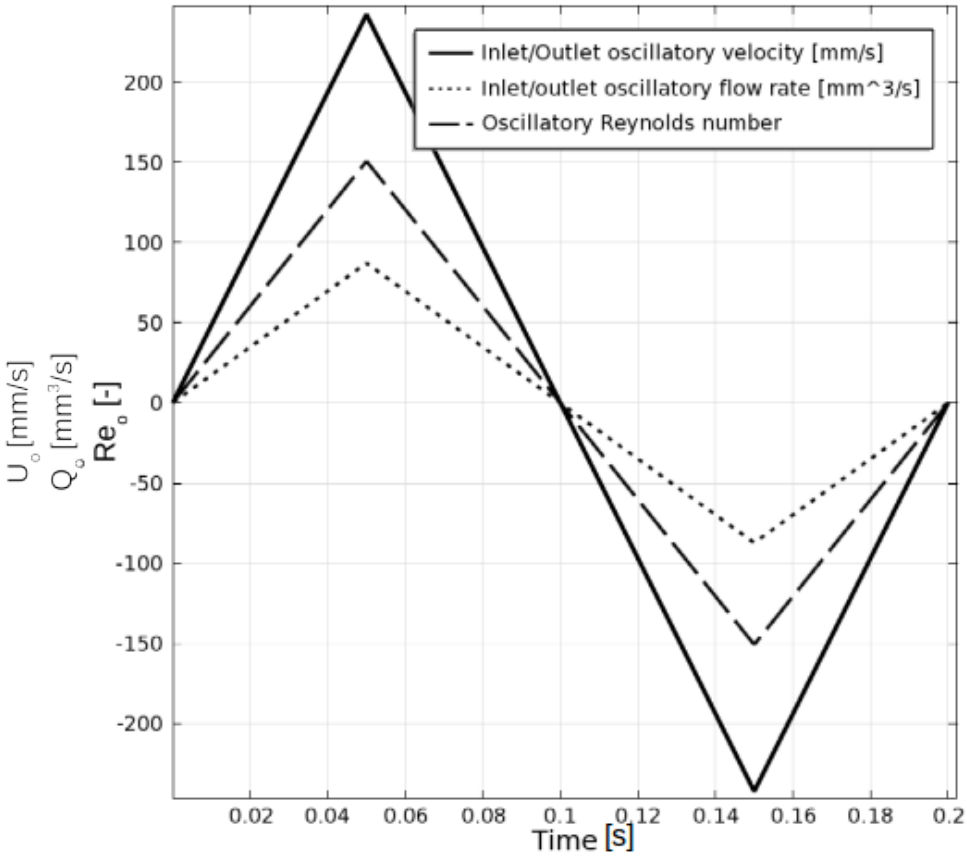

Figure 4.10: Example of the inlet/outlet periodic flow boundary condition. Here it is a triangular wave with maximum Re_o equal to 150.83 and oscillation frequency of 5 Hz. The time scale is in seconds.

4.3.3 Time dependent solver

In this CFD study, the time stepping method was backward differentiation formula with intermediate control over the time stepping. Here, the time

stepper solver was forced to limit its maximum time step to be 0.01 second. This will prevent the time stepping solver to take relatively large time steps which will not help to simulate oscillatory flow with a decent resolution as oscillatory flow changes amplitude with time in a periodic manner. In other parts of this CFD study, maximum time step was set to be 0.001 second for modelling of oscillatory flow with f greater than 20 Hz.

4.3.4 Meshing and mesh conversion study

Mesh generation for this study was mapped using quadrilateral elements optimised for fluid dynamics finite elements method using COMSOL Multiphysics. Mapped meshes were deliberately used to ensure solution stability and to simulate the spatial and temporal periodicity nature of the OBM.

Initial mesh independence studies were performed to ensure that the oscillatory flow fields obtained were independent of the mesh density used. For quantitative comparison, Table 4.2 shows the spatial and temporal average velocity magnitude at different mesh densities and maximum time stepping limits in addition to the computational solving time for each combination. General observation from this table is that time required for the simulation to be completed, which known as computational time or cost, is exponentially proportional to degree of freedom (DoF).

As shown in Figure 4.11, for both 2D mesh conversion studies with maximum time stepping of 0.01 and 0.005 second, the results were independent of the used maximum time stepping and were independent of mesh size at number of element (NoE) of 5226 which equivalent to 48352 degree of freedom (DoF). Here, the maximum time stepping of 0.01 second and DoF of 48352 was chosen for meshing and solve the CFD studies as it requires the latest amount of computational time with a reasonably close result to the solution with higher DoF. As for the three-dimensional (3D) modelling mesh conversion study, it is clear that it required relatively large amount of computational time compare to the 2D modelling, e.g. for a DoF about 500×103, the computational time required for a 3D modelling–about four hours–was about four times greater than the time required for the 2D modelling with the same maximum time step limit. In addition, the 3D modelling did not show the same level of conversion compared to the 2D modelling keeping in mind that the 2D modelling has take into account the drag force of the microchannel's walls. Table 4.3 and Figure 4.12 show the final mesh properties and mesh quality map that adapted in this CFD modelling study respectively.

Table 4.2: Spatial and temporal average velocity magnitude at different mesh densities and maximum time stepping limits.

Average Velocity magnitude (m/s)	**NoE**	**DoF**	**Solving time** [s]
2D with maximum time stepping of 0.005 s			
0.0569	63	710	37
0.0583	252	2551	70
0.0606	648	6300	193
0.0622	1470	13928	448
0.0628	2295	21538	664
0.0633	5226	48352	1479
0.0634	8256	75977	4611
0.0635	12960	118743	7704
0.0637	58212	528376	38774
2D with maximum time stepping of 0.01 s			
0.06334	5226	48352	482
0.06346	8256	75977	588
0.06355	12960	118743	966
0.06367	58212	528376	4601
3D with maximum time stepping of 0.01s			
0.03536	396	2952	30
0.04465	1296	8112	71
0.05003	3564	20000	236
0.05415	8820	45080	636
0.0568	24960	119700	2285
0.05822	51480	237996	6948
0.05899	81432	368680	26679
0.05935	106080	475552	10509
0.05962	127092	565680	13658

Table 4.3: The final mesh properties and statistics.

Mesh statistics Property	**Value**
Minimum element quality	0.8826
Average element quality	0.9594
Quadrilateral elements	5226
Edge elements	542
Vertex elements	16
Maximum element size, m	40.5
Minimum element size, m	18
Resolution of curvature	0.3
Maximum element growth rate	1.15

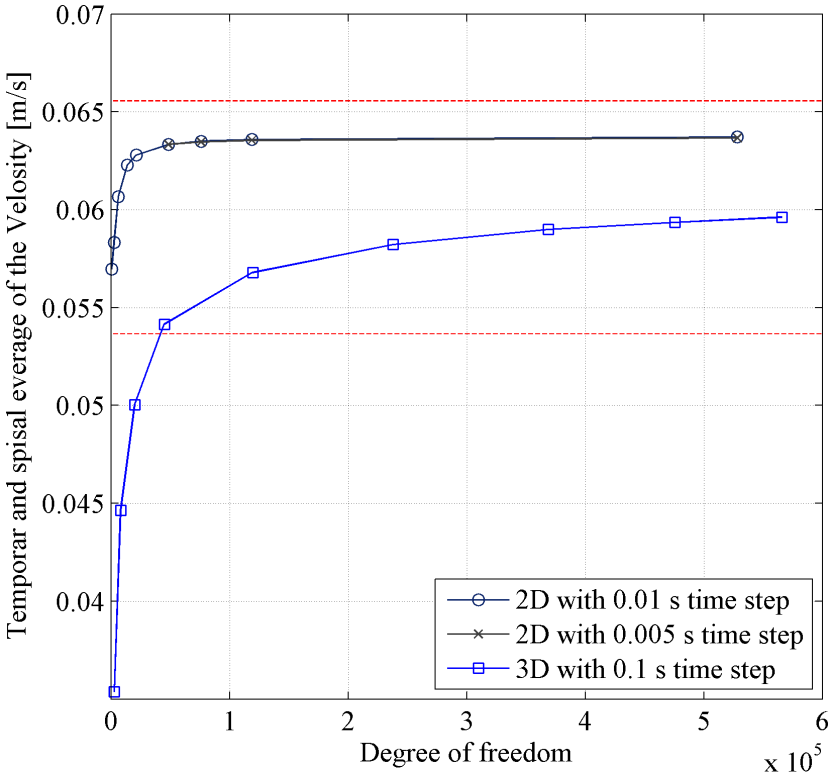

Figure 4.11: Mesh conversion study. Red-dashed lines represent a ±10% of the maximum velocity obtained from the 3D mesh study.

4.3.5 Results and discussion

It is important to identify a quantifiable property for the oscillatory flow through a baffled microchannel to be used to measure the performance of the OBM at different combination of Re_o and f and to be later evaluated against results obtained from particle-based oscillatory flow visualisation experimentation. Such property is the instantaneous total vortices area (VA) which is the total area occupied by vortices at a given instant throughout an oscillation cycle (Reis et al., 2005). This VA is a direct measurement of the non-axial mixing intensity in individual baffled cavity represented by the formation of the vortices behind the baffled area in the direction of an oscillatory flow (See §2.10). For illustration, Figure 4.13 shows an instantaneous oscillatory flow velocity magnitude and field streamline from which two vortices can be identified and then measured its areas. The total sum of These measured areas is representing the VA value.

For the sake of easing the comparison between CFD simulation results, another useful version of the VA is used, which is the percentage VA ratio

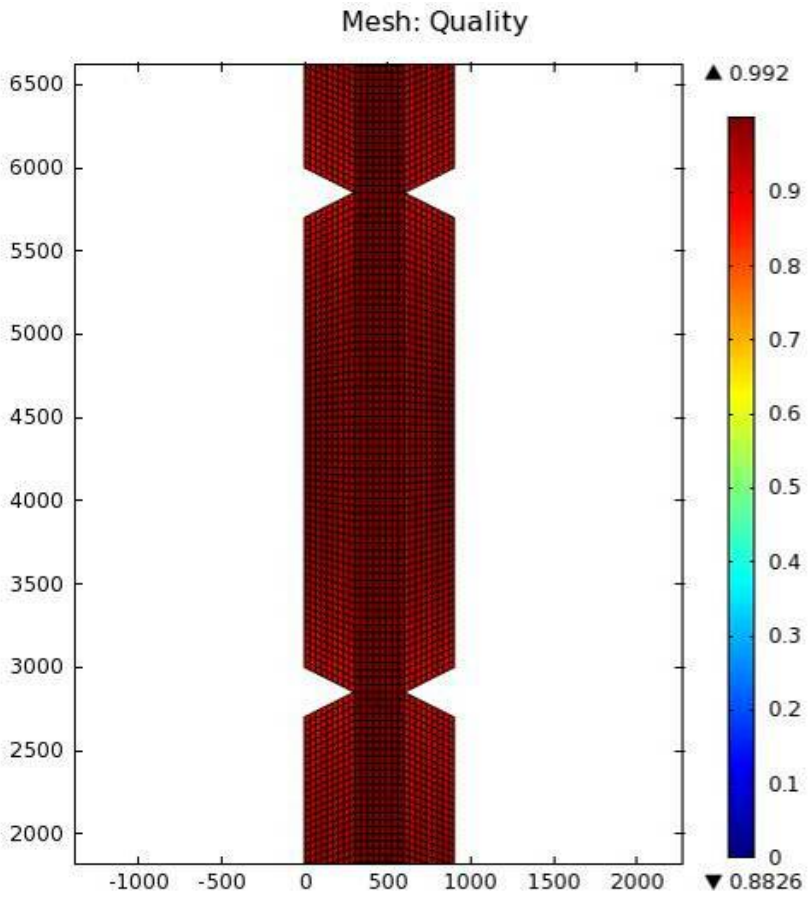

Figure 4.12: The final mesh density and its elements quality.

to the area of one inter-baffle cavity, $A_{inter-baffle}$, which is equal to 2.6 mm^2, see Eq. 4.8.

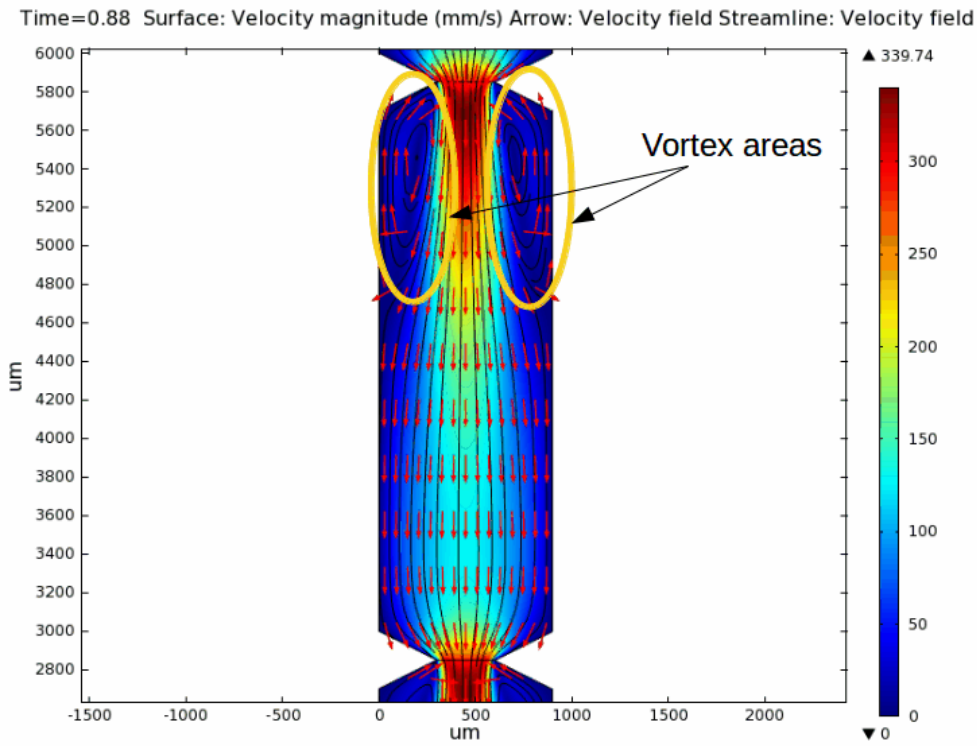

Figure 4.13: Simulated vortices formation after a baffled area generated by sinusoidal oscillating flow at Re_o of 55 and f of 2 Hz. Here, the total VA is 0.273 mm^2.

$$\%VAR = \frac{VA}{A_{Inter-baffle}} \times 100 \tag{4.8}$$

Table 4.4 summarise the results obtained from the CFD simulations for different combination of Re_o ranged from 15.38 to 150.83 and fluid oscillation frequency ranged from 1 to 70 Hz. VA values were obtained by measuring the total area of the vortices using image processing software (Abramoff et al., 2004). These measurements were done in following approach:

1. Loading image represents an instantaneous oscillatory flow velocity magnitude and field streamline at peak value of Re_o.

2. Loaded image were spatially calibrated using OBM width as a reference width.

3. Areas with vortices were selected and saved as region of interest (ROI).

4. Area of each vortex was calculated using the measurement feature of the image processing software for the saved ROI.

5. Total VA was calculated by summing the individual areas of each vortex.

6. The above steps were repeated for each combination of Re_o and f.

The complete list of the instantaneous velocity magnitude and streamline results were listed in Appendix B.

For the purpose of comparison, Figure 4.14 shows the $\%VAR$ as function of Re_o and f. At any fluid oscillation frequency, $\%VAR$ were increasing as the Re_o increasing and this observation is more obvious in the lower rage of f e.g. 1–10 Hz compared with the f greater than 10 Hz. Furthermore, for any Re_o value, the $\%VAR$ values were relatively constant for f ranged from 1 to 10 Hz while the $\%VAR$ start to decrease as f increased further. Initial reasoning for this observation could be related to fluid oscillation frequency as oscillation time which become smaller as f increase.

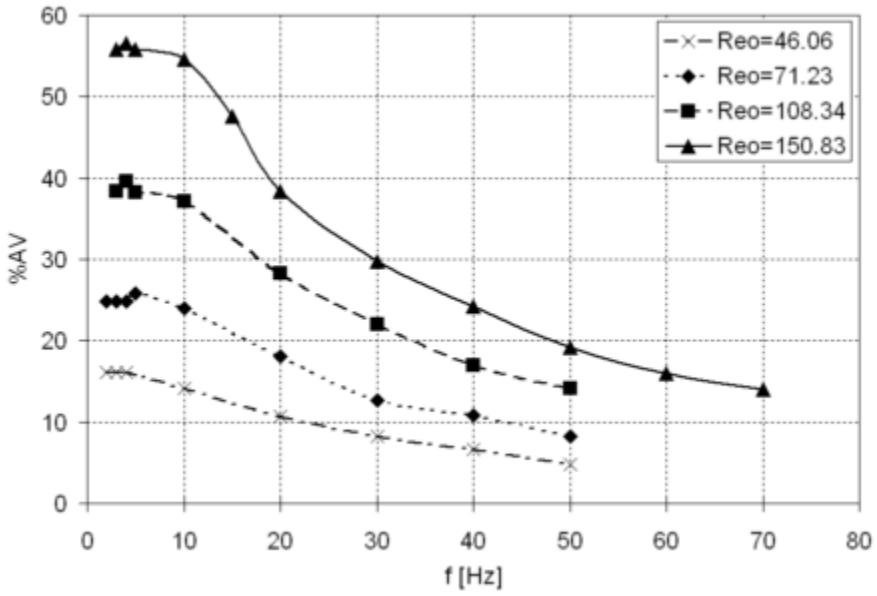

Figure 4.14: $\%VAR$ as function of f for different Re_o values.

Figure 4.15 shows that Re_o and $\%VAR$ are in direct variation for any given f. Furthermore, the slope for this linear relation was relatively similar for f ranged from 2 to 10 Hz and it is decreasing as f increases. Again,

Table 4.4: Percent vortices area ratio for the generated vortices with respect to inter-baffle area for different combinations of Re_o and f obtained from the CFD study.

#	Re_o	f **[Hz]**	Q_o **[mm3/min]**	U_{red}	Sto	VA **[mm2]**	$\%VAR$
1	15.38	1	534.03	44.6	0.34	0.045	3.46
2	15.38	2	534.03	22.3	0.69	0.045	3.46
3	24.65	1	855.9	71.6	0.34	0.093	7.15
4	24.65	2	855.9	35.8	0.69	0.093	7.15
5	36.98	1	1284.03	107.3	0.34	0.162	12.46
6	36.98	2	1284.03	53.7	0.69	0.162	12.46
7	36.98	3	1284.03	35.8	1.03	0.152	11.69
8	46.06	2	1599.31	66.8	0.69	0.209	16.08
9	46.06	3	1599.31	44.6	1.03	0.209	16.08
10	46.06	4	1599.31	33.4	1.38	0.209	16.08
11	46.06	10	1599.31	13.4	3.45	0.183	14.08
12	46.06	20	1599.31	6.7	6.89	0.139	10.69
13	46.06	30	1599.31	4.5	10.34	0.107	8.23
14	46.06	40	1599.31	3.3	13.78	0.086	6.62
15	46.06	50	1599.31	2.7	17.23	0.063	4.85
16	55.34	2	1921.53	80.3	0.69	0.273	21
17	55.34	3	1921.53	53.5	1.03	0.257	19.77
18	55.34	4	1921.53	40.2	1.38	0.266	20.46
19	71.23	2	2473.26	103.4	0.69	0.323	24.85
20	71.23	3	2473.26	68.9	1.03	0.323	24.85
21	71.23	4	2473.26	51.7	1.38	0.323	24.85
22	71.23	5	2473.26	41.4	1.72	0.336	25.85
23	71.23	10	2473.26	20.7	3.45	0.312	24
24	71.34	20	2477.08	10.4	6.89	0.235	18.08
25	71.34	30	2477.08	6.9	10.34	0.164	12.62
26	71.34	40	2477.08	5.2	13.78	0.141	10.85
27	71.34	50	2477.08	4.1	17.23	0.107	8.23
28	97.37	3	3380.9	94.2	1.03	0.461	35.46
29	97.37	4	3380.9	70.7	1.38	0.461	35.46
30	97.37	5	3380.9	56.5	1.72	0.459	35.31
31	108.34	3	3761.81	104.8	1.03	0.499	38.38
32	108.34	4	3761.81	78.6	1.38	0.515	39.62
33	108.34	5	3761.81	62.9	1.72	0.497	38.23
34	108.34	10	3761.81	31.4	3.45	0.483	37.15
35	108.34	20	3761.81	15.7	6.89	0.368	28.31
36	108.34	30	3761.81	10.5	10.34	0.286	22
37	108.34	40	3761.81	7.9	13.78	0.22	16.92
38	108.34	50	3761.81	6.3	17.23	0.184	14.15
39	124.07	3	4307.99	120	1.03	0.575	44.23
40	124.07	4	4307.99	90	1.38	0.543	41.77
41	124.07	5	4307.99	72	1.72	0.57	43.85
42	150.83	3	5237.15	145.9	1.03	0.726	55.85
43	150.83	4	5237.15	109.5	1.38	0.735	56.54
44	150.83	5	5237.15	87.6	1.72	0.725	55.77
45	150.83	10	5237.15	43.8	3.45	0.71	54.62
46	150.83	15	5237.15	29.2	5.17	0.618	47.54
47	150.83	20	5237.15	21.9	6.89	0.498	38.31
48	150.83	30	5237.15	14.6	10.34	0.387	29.77
49	150.83	40	5237.15	10.9	13.78	0.315	24.23
50	150.83	50	5237.15	8.8	17.23	0.25	19.23
51	150.83	60	5237.15	7.3	20.67	0.208	16
52	150.83	70	5237.15	6.3	24.12	0.182	14

this indicates that as the fluid oscillation frequency increase beyond 5 Hz, $\%VAR$ will decrease as f further increases for any Re_o value.

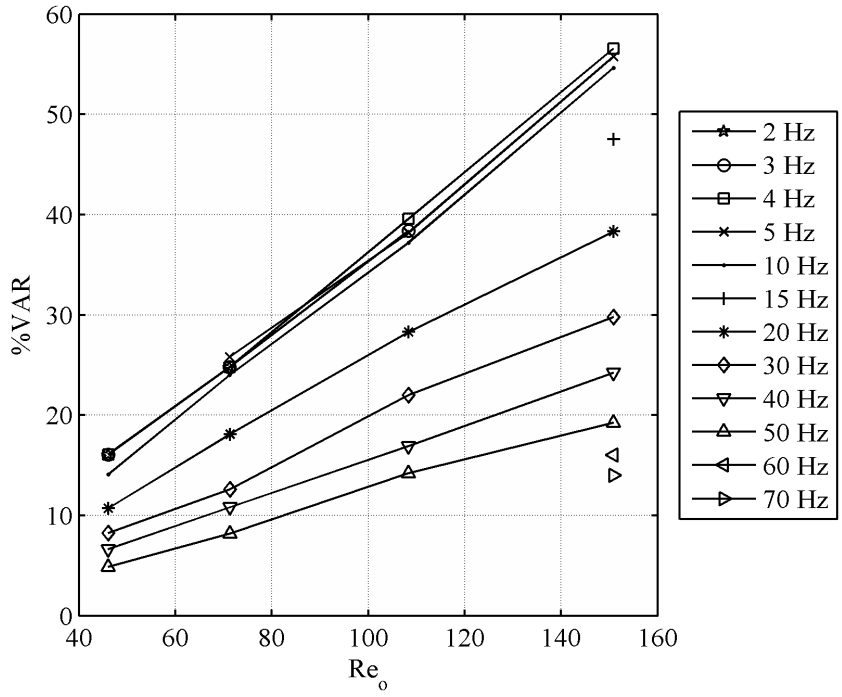

Figure 4.15: $\%VAR$ as function of Re_o at different fluid oscillation frequency.

One way to investigate this observation is to use the Stockes number (Sto) which is used to indicate the establishment of fully developed flow, see Eq. 4.4. Sto is the ratio between the characteristic time scale to establish fully developed flow and the superimposed oscillation characteristic time scale . Figure 4.16 shows the $\%VAR$ as function of Re_o, f and Sto, here for any combination of Re_o and f, $\%VAR$ started to decrease noticeably when Sto value is greater than 5. This is because as Sto values increased above unity, flow will have less time to be fully developed i.e. as oscillation frequency become higher the time for each oscillation cycle will become smaller, $t = 1/f$, and therefore vortices will have less time to be fully developed and reach its maximum size.

In these CFD simulations, it is clear that the $\%VAR$ were relatively remain constant for any Re_o value providing that Sto values ranging from 1 to 3. This behaviour is in total agreement with the work of Horner et al. (see Glasgow et al., 2004) as they indicated that maximum flow separation i.e. maximum $\%AVR$, can be achieved at Sto ranged from 1 to 3. Figure

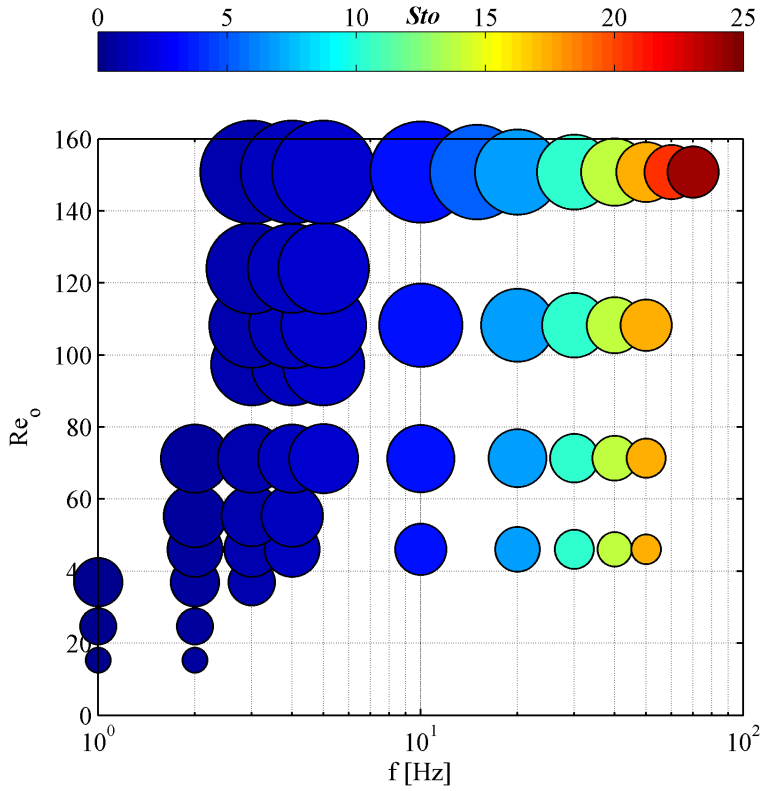

Figure 4.16: Normalised $\%VAR$ as function of Re_o, f and Sto.

4.17 shows the $\%VAR$ as a function of Sto for different Re o values. At this graph, that maximum $\%VAR$ achieved at Sto ranged from 1 to 3.

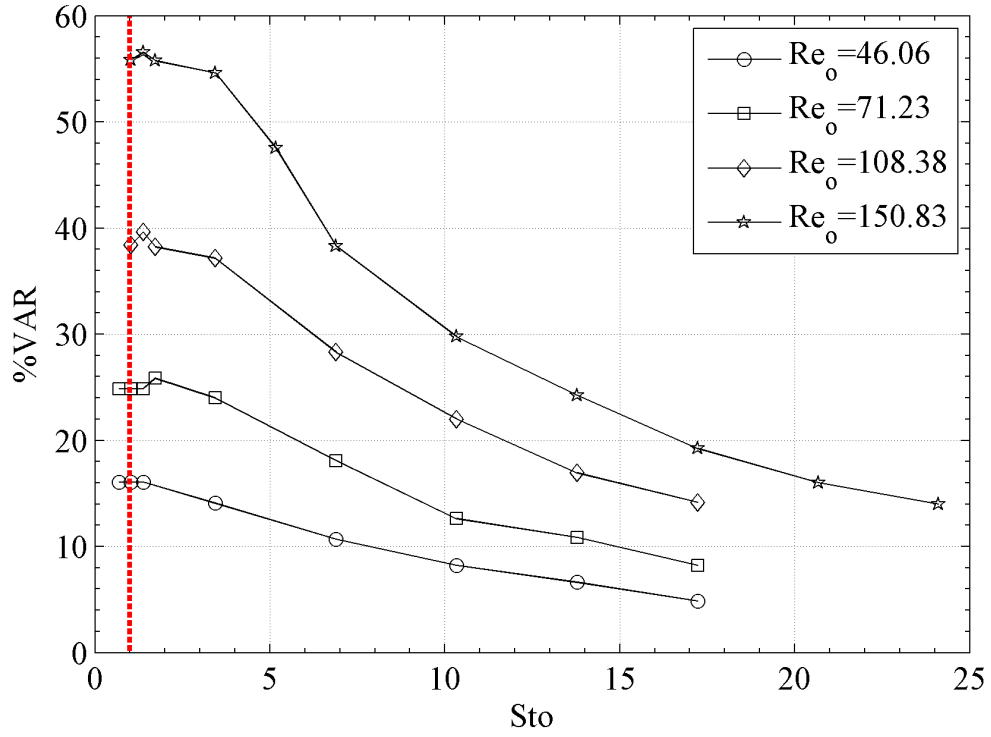

Figure 4.17: $\%VAR$ as function of Sto for different values of Re_o. The red vertical dotted line represent unity value for the Sto.

As a conclusion for this section, it will be a good idea to ensure that any later experimentation on OBM should be done with a Sto values varied from 1 to 3 to ensure maximum vortices evolution and to achieve maximum non axial mixing degree. As for Re_o, it is recommended to use as higher as possible to ensure maximum vortices area evolution as well.

4.4 Particle-based flow visualisation

With the intention to validate results obtained from the CFD study presented in §5.3 and inspired by the work of Khodaparast et al. (2013), a particle-based flow visualization (PV) experiment was conducted to track flow pattern within the OBM. This experiment was carried through tracking, using an inverted microscope equipped with high-speed camera, movements of three-micrometre-sized suspended particles at different oscillatory flow amplitude and frequency.

4.4.1 Experiment setup

The PV system used for this work consisted of an inverted light microscope (Olympus IX51) with Halogen light source, tracer particles (SIGMA LB-30, Polystyrene Latex Beads with 3.0 micrometre mean particle size), high-speed CMOS camera (Phantome Miro M110). The tracer particles used were 3.0 micrometre white styrene particles with 1.05 specific density. These particles were chosen to be large enough to be seen in the above mentioned optical setup. The tracer particle suspension was prepared by suspending 0.032 g of the tracer particles in 10 g of water/glycerin solution having the same density as the tracer particles. Oscillatory flow was generated by using CAVRO XE-1000 syringe pump. Figure 4.18 shows a schematic of the experiment setup described above.

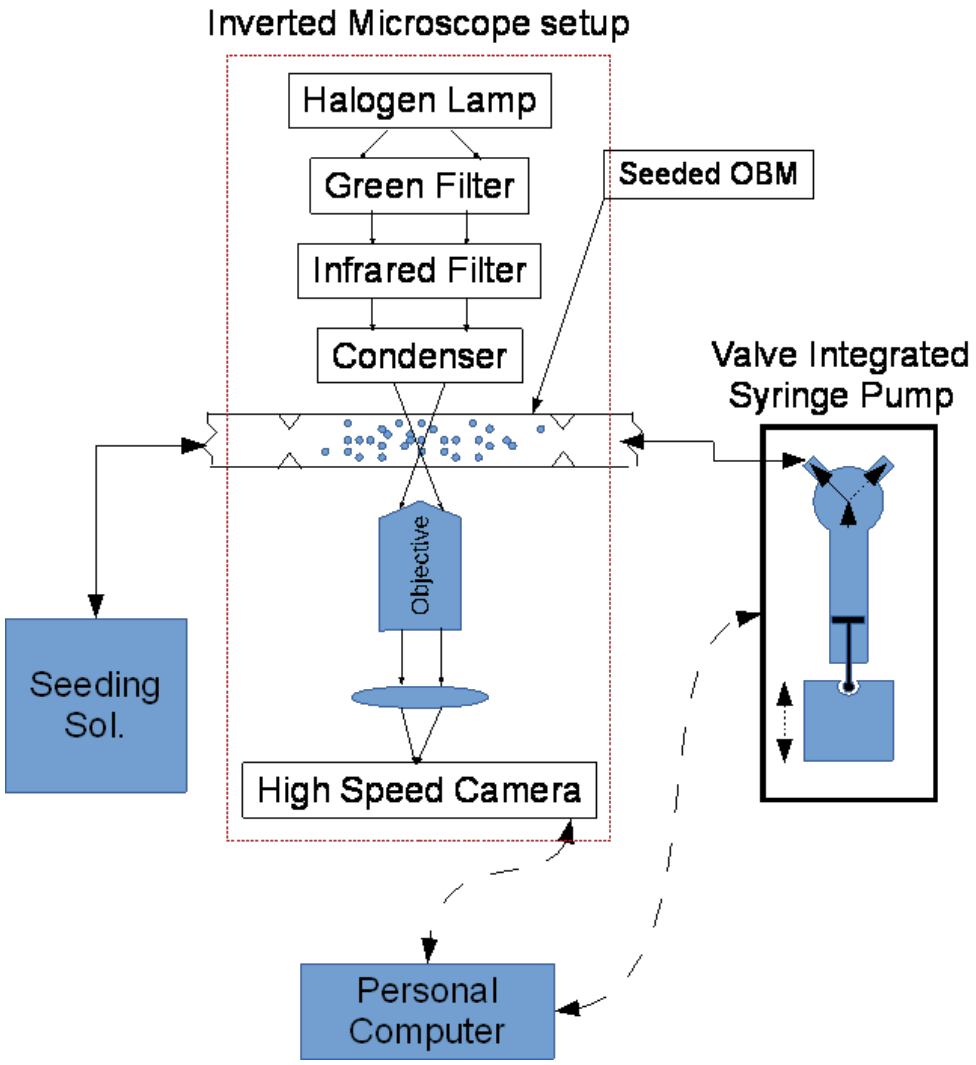

Figure 4.18: Drawing of the particle-based flow visualization experiment.

4.4.2 Methodology

The following methodology was used for the acquisition of 2D particle movement pattern:

1. Once the system filled with tracer solution and the optical setup was focused, syringe pump was programmed and then run to deliver the required Re_o and f (see Figure 4.19).

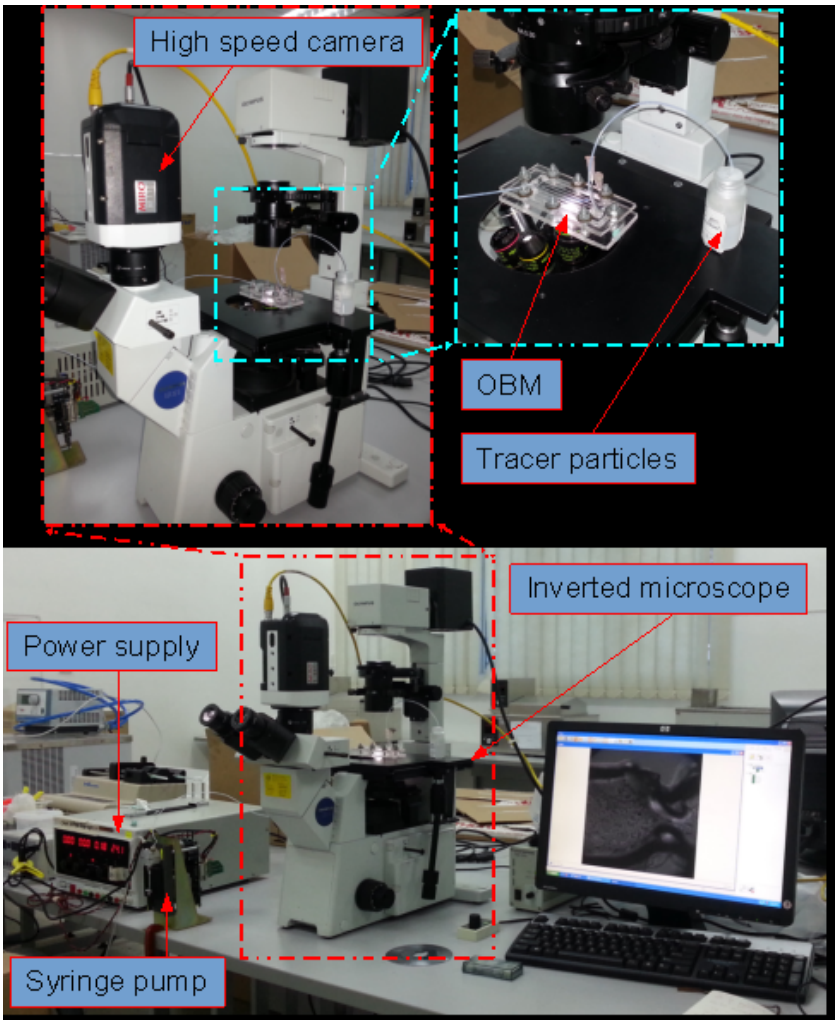

Figure 4.19: Particle-based flow visualisation experiment.

2. High-speed camera was then triggered to acquire images of a single inter-baffle cavity at a rate of 5000 frames per second for a period of two seconds. Figure 4.20 shows an example of an acquired image. Raw images acquired here were about 10,000 images with total storage size about 200 Giga Byte for each Re_o and f combination.

3. Image sequences representing half oscillation cycle were then selected, stacked and processed using image processing software (Abramoff

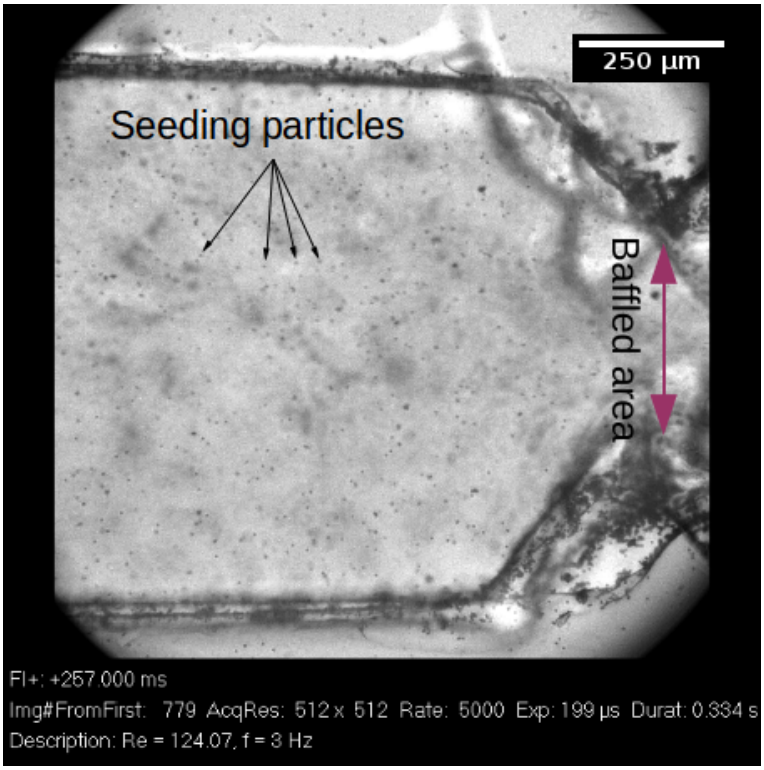

Figure 4.20: Instantaneous raw image acquired at a rate of 5000 fps with exposure time of 199 micro second.

et al., 2004) to produce a single image shows the oscillatory flow pattern behind the baffled area. Image processing techniques involved were background subtracting followed by standard deviation projection. Figure 4.21 shows the resulted flow pattern for an arbitrary oscillatory flow.

4. Image produced in the previous step was then spatially calibrated followed by vortex areas identification and measurement in similar manner listed in 3rd paragraph of §5.3.5. Figure 4.22 shows the final results.

5. Steps (a) to (d) were repeated for 29 times for each combination of Re_o and f.

4.4.3 Results and discussions

Table 4.5 shows results obtained from the particle-based flow visualisation experiment at different combinations of Re_o and f. These results were obtained from the images produced from step (d) in the previous section.

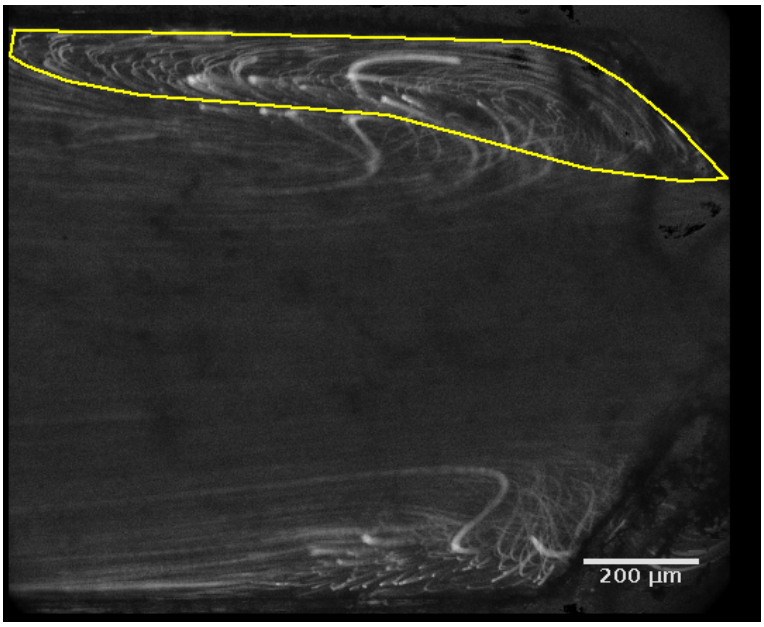

Figure 4.21: Standard deviation projection for image stacks representing half oscillating cycle. Here, vortices were visualised, selected and measured.

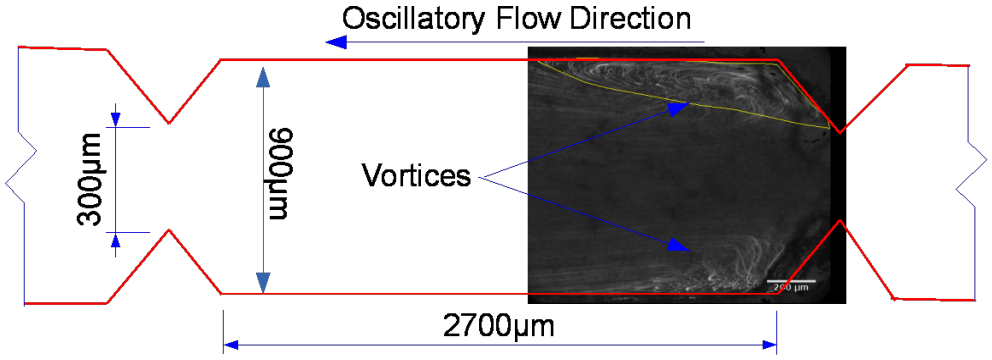

Figure 4.22: Result from flow visualisation experiment showing seeded particles flow pattern. Boundaries of one vortex area are highlighted here (top). Resulted image was superimposed by the geometry of single OBM cavity to visualised vortices shapes, sizes and locations.

Table 4.5: Percentage vortex area ratio obtained from the particle-based flow visualisation experiment at different combinations of Re_o and f.

#	Re_o	f [**Hz**]	Sto	VA [**m2**]	$\%VAR$
1	15.38	1	0.31	4786	0.36
2	15.38	2	0.63	5223.15	0.4
3	24.65	1	0.31	12155.18	0.92
4	24.65	2	0.63	10026.18	0.76
5	36.98	1	0.31	26030.6	1.97
6	36.98	2	0.63	27177.42	2.06
7	36.98	3	0.94	21409.25	1.62
8	46.06	2	0.63	26297.43	1.99
9	46.06	3	0.94	23873.21	1.81
10	46.06	4	1.26	31724.97	2.41
11	55.34	2	0.63	48200.61	3.65
12	55.34	3	0.94	27336.39	2.07
13	55.34	4	1.26	21346.8	1.62
14	71.23	2	0.63	67401.37	5.11
15	71.23	3	0.94	46991.34	3.56
16	71.23	4	1.26	60543.14	4.59
17	71.23	5	1.57	43800.67	3.32
18	97.37	3	0.94	76144.47	5.77
19	97.37	4	1.26	64108.51	4.86
20	97.37	5	1.57	50738.38	3.85
21	108.34	3	0.94	122096.85	9.26
22	108.34	4	1.26	94908.08	7.2
23	108.34	5	1.57	71415.25	5.41
24	124.07	3	0.94	107205.19	8.13
25	124.07	4	1.26	80067.51	6.07
26	124.07	5	1.57	77671.68	5.89
27	150.83	3	0.94	160589.21	12.18
28	150.83	4	1.26	149898.78	11.37
29	150.83	5	1.57	133695.66	10.14

A complete list of these processed images for different combinations of Re_o and f were listed in Appendix C.

As seen from Figure 4.23 which shows a normalised comparison between total vortex area obtained from the CFD study and from the particle-based flow visualization experiment. The $\%VAR$ values obtained from the particle-based flow visualisation were significantly smaller than the $\%VAR$ obtained from the CFD study. The main reason for this considerable reduction in VA is due to that the Re_o produced by the syringe pump did not reach the desired amplitude because the syringe pump did not have enough time to accelerate to the required plunger speed during an oscillatory movement which required a reciprocating movement. The reduction

in VA obtained from the particles-based visualisation experiment at any Re_o level with increasing f is in favour of the previous statement, as with higher f syringe pump will have less time to reach the desired pumping speed. Another possible reason for such bias in VA is may be due to the large size of the tracer particle used. Usually in flow visualisation experiment, the smaller tracer particle is better in order to depict the actual flow dynamics. Furthermore and as can be seen from Figure 4.24 which shows the normalised $\%VAR$ as function of Re_o, f and Sto obtained from the particle-based flow visualisation experiment. This reduction in VA were unrelated to not fully developed flow as Sto values ranged from 0.32 to 1.57 which is within the 1–3 range discussed earlier in this section.

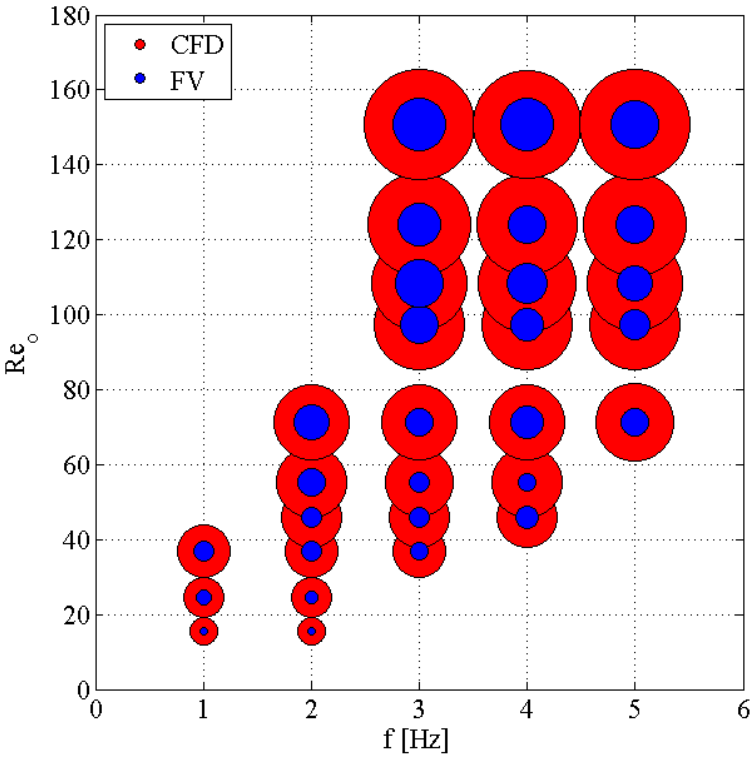

Figure 4.23: A comparison between total vortex area obtained from the CFD study and from the particle-based flow visualisation experiment (FV). Circles size represents the normalized VA values

Figure 4.25 shows the relation between $\%VAR$ andRe_o at different fluid oscillation frequencies for the particle-based flow visualisation experiment - which were best fitting with power law i.e. $\%VAR = aRe_o^b$ to show deviation from linearity. This deviation from linearity which resulted from the CFD study (see Figure 4.15) mainly related to the poor performance of the syringe pump. Another observation which can be seen from this figure is the low $\%AVR$ values at low Re_o for any fluid oscillation frequency. This is

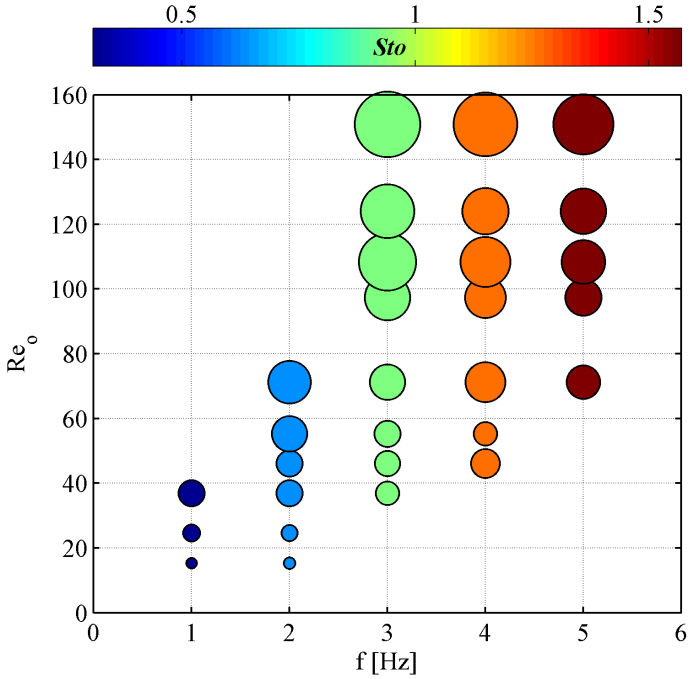

Figure 4.24: Normalized $\%VAR$ as function of Re_o, f and Sto obtained from the particle-based flow visualisation experiment.

again related to poor performance of the syringe pump as discussed previously in §4.2.3 for low Re_o. Despite that, generally the behaviour between the Re_o and $\%VAR$ obtained from PV experiment agreed with the one obtained from the CFD simulation as $\%VAR$ decreases as the Sto value increase.

4.5 Conclusions

As a conclusion to this chapter, the usability of OBM was investigated by means of pressure drop trend, computational fluid dynamics and micro-flow visualisation to identify the workable operation variables margins for the Re o and f. Therefore, as the CFD study and FV experiment shown, in order to achieve maximum non-axial mixing in an OBM, any combination of Re_o and f need to be having a Sto value ranging from 1 to 3 which produced the largest possible vortices. Furthermore, in order to operate within the good performance region of the syringe pump, Re_o need to be set from 100 to 385 and f need to be set from 1–30 Hz.

Thus, in order to use the OBM, it is recommended to balance between these operation variable such that to avoid operating in high fluid oscillating

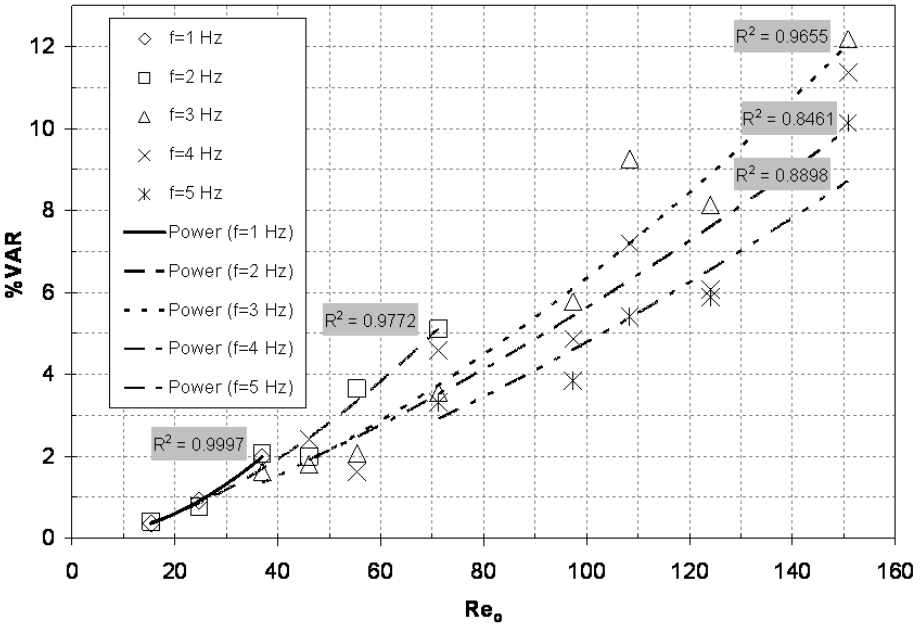

Figure 4.25: $\%VAR$ as function of oscillatory Reynolds number at different oscillation frequencies.

frequencies and to avoid low fluid oscillating amplitudes as they led to a low degree of mixing. In order to achieve that, it is recommended also to use design of experiment methodologies to identify the optimal operation condition for any future experimentation using the OBM device. This will be discussed in chapter 6.

References

M.D. Abramoff, P.J. Magalhaes, and S.J. Ram. Image processing with imagej. *Biophotonics International*, 11(7):36–42, 2004. 69, 76

C. R. Brunold, J. C. B. Hunns, M. R. Mackley, and J. W. Thompson. Experimental observations on flow patterns and energy losses for oscillatory flow in ducts containing sharp edges. *Chemical Engineering Science*, 44 (5):1227–1244, 1989. U4289 Times Cited:100 Cited References Count:12. 54

C. M. Chew, R. I. Ristic, R. D. Dennehy, and J. J. De Yoreo. Crystallization of paracetamol under oscillatory flow mixing conditions. *Crystal Growth & Design*, 4(5):1045–1052, 2004. 851VL Times Cited:11 Cited References Count:33. 53

Ian Glasgow, Samuel Lieber, and Nadine Aubry. Parameters influencing pulsed flow mixing in microchannels. *Analytical chemistry*, 76(16):4825–4832, 2004. 72

Ahmad Azahari Hamzah, Nurul Hasan, Mohd Sobri Takriff, Siti Kartom Kamarudin, Jaafar Abdullah, Isa M Tan, and Wah Keng Sern. Effect of oscillation amplitude on velocity distributions in an oscillatory baffled column (obc). *Chemical Engineering Research and Design*, 90(8):1038–1044, 2012. 64

A. P. Harvey, M. R. Mackley, and P. Stonestreet. Operation and optimization of an oscillatory flow continuous reactor. *Industrial & Engineering Chemistry Research*, 40(23):5371–5377, 2001. 490XP Times Cited:15 Cited References Count:7. 53

H. Jian and X. Ni. A numerical study on the scale-up behaviour in oscillatory baffled columns. *Chemical Engineering Research and Design*, 83 (10):1163–1170, 2005. 64

Sepideh Khodaparast, Navid Borhani, Giulia Tagliabue, and John Richard Thome. A micro particle shadow velocimetry (psv) technique to measure flows in microchannels. *Experiments in fluids*, 54(2):1–13, 2013. 74

S. Lawton, G. Steele, P. Shering, L. H. Zhao, I. Laird, and X. W. Ni. Continuous crystallization of pharmaceuticals using a continuous oscillatory baffled crystallizer. *Organic Process Research & Development*, 13

(6):1357–1363, 2009. 521CE Times Cited:12 Cited References Count:43. 53

N. Reis, A. P. Harvey, M. R. Mackley, A. A. Vicente, and J. A. Teixeira. Fluid mechanics and design aspects of a novel oscillatory flow screening mesoreactor. *Chemical Engineering Research and Design*, 83(4):357–371, 2005. 64, 67

I.J. Sobey. Oscillatory flows at intermediate strouhal number in asymmetric channels. *Journal of Fluid Mechanics*, 125(1):359–373, 1982. 54

M. Z. Zheng and M. Mackley. The axial dispersion performance of an oscillatory flow meso-reactor with relevance to continuous flow operation. *Chemical Engineering Science*, 63(7):1788–1799, 2008. 53, 64

Chapter 5

Crystallisation in continuous oscillatory baffled microchannel

5.1 Introduction

This chapter continues the theme of using periodically baffled with superimposed oscillatory flow in microchannels to manipulate flow to create non-axial movement. While Chapter five focused upon their use for investigating the mixing effects of oscillatory flow in baffled microchannels, this chapter looks to develop a practical use as a continuous crystallisation unit. Work carried out by Ristic (2007) identified the process by which Paracetamol crystals are formed and, using an oscillatory mixer, demonstrated how crystal quality could be increased by carefully controlling the hydrodynamics surrounding the crystals as they grow. Another work carried out by Lawton et al. (2009) highlight the advantages of using continuous baffled crystalliser such as lower operational cost and shorter production time compare with batch processes. Moreover and in the mesoscale, works carried out by Zheng and Mackley (2008) and Phan et al. (2011) show the suitability and the usability of oscillatory baffled meso-reactors for product screening and biodiesel production respectively. On the microscale domain, current works on particle crystallisation or precipitation were either using oscillatory flow in straight microchannels (Parambil et al., 2011) or steady flow in baffled microchannel (Chung et al., 2011). In this chapter, the effects of oscillatory flow amplitude and frequency on particle production were investigated in an oscillatory baffled microchannel.

It is shown experimentally using a novel oscillatory baffled microchannel design that a continuous microchannel crystalliser is feasible under a range of operating parameters. The oscillatory flow and supersaturation degree influences on various properties of the produced crystals under these conditions are investigated using design of experiment methodology to determine the optimum operation conditions required for the crystalliser to produce particle with minimal particle size and particle size distribution.

5.2 Experiment setup

In this experiment a 250-mm-long oscillatory baffled microchnnel (OBM) was used with 400 micrometre channel height, see Figure 5.1. The fluid oscillating unit using a valve integrated syringe pump (CARVO XE-1000) connected to the oscillation port by means of 1.8 mm internal diameter Teflon tube. Fluid oscillation amplitude and frequency were achieved by programming the syringe pump using CAVRO pump protocol. Fluid oscillation frequencies, f, between 0 and 30 Hz and amplitudes between $Re_o = 100$ and $Re_o = 385$ were possible. Another two set of valve integrated syringe pumps (Kloehn V3) were used to dispense Paracetamol Ethanol/Water saturated solution and water (antisilvent) into ports (A) and (B) of the OBM, see Figure 5.1. An inline 0.2 micrometre syringe-type filter was installed into the section line after the Paracetamol Ethanol/Water reservoir to prevent any Paracetamol crystals and/or dirt to be introduced into the OBM which may cause a secondary or heterogeneous nucleation. Figure 5.2 shows the experiment setup where all interconnection tubes were Teflon tubes with 1.8 mm internal diameter.

5.3 Experiment Methodology

At this experiment, the flowing methodology was used to investigate continuous antisolvent crystallisation using OBM:

1. Prepare Paracetamol saturated solution in (8:2) volume ratio of Ethanol/Water mixture. This was achieved by dissolving 250 g of Paracetamol in one litter of 0.8 Ethanol volume fraction in Ethanol/Water system, see Figure 5.3. After mixing overnight to achieve equilibrium, the mixture was filtered using 0.2 micrometre filter paper to remove any excess non dissolved Paracetamol and any other contamination. The

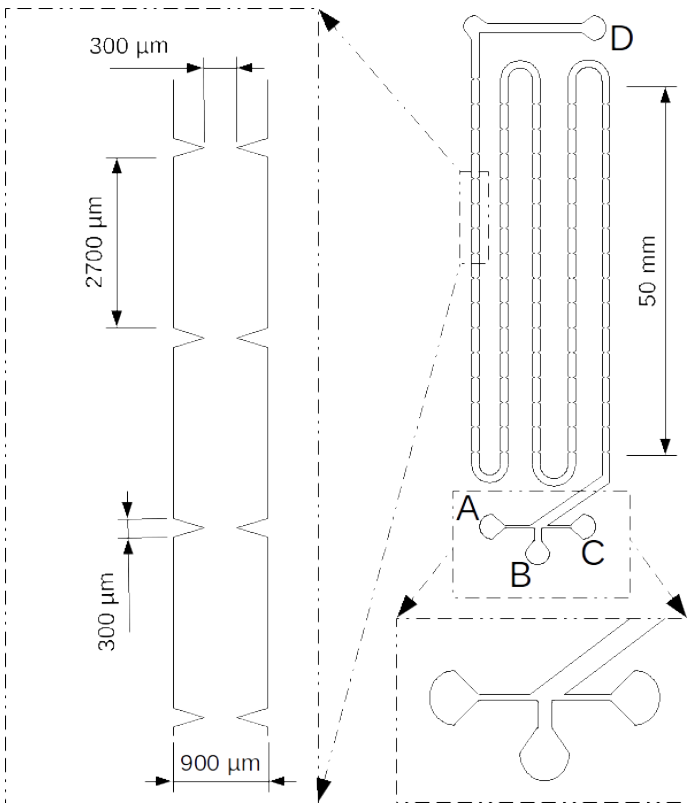

Figure 5.1: The OBM used in this antisolvent crystallisation experiment. This OBM has Dh equivalent to 0.55386 mm. A: Paracetamol-Ethanol/Water solution inlet port; B: Oscillatory fluid port; C: Antisolvent (Water) inlet port; D: product outlet.

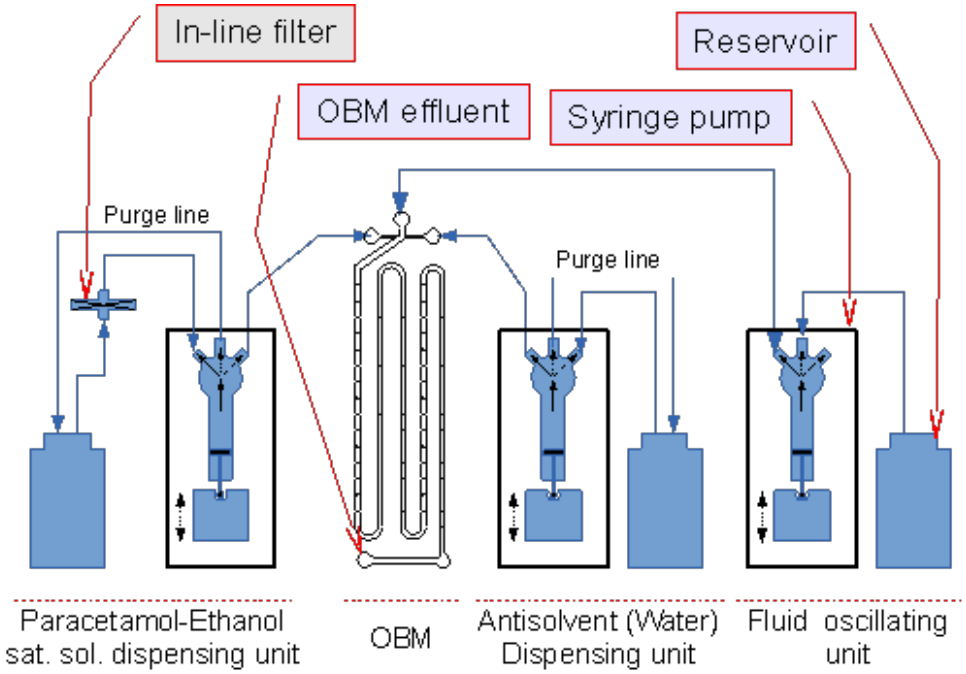

Figure 5.2: Experiment setup. Product collected at the OBM outlet was analysed for particle size and particle size distribution within 5 to 10 minutes after sample collection.

concentration of the final saturated solution was 244 g/l of Paracetamol in 0.8 Ethanol volume fraction of ethanol/water mixture.

2. Set the fluid oscillation unit to deliver the required nominated Re_o and f.

3. Set the Paracetamol saturated solution and antisolvent dispensing units to deliver the required flow rates witch satisfied the required antisolvent fraction (ASF). Also, the total flow rate need to be equivalent to Re_n of 9.23 as this experiment designed to run on a constant net flow rate.

4. Run the experiment on the settings provided in step 2 and 3 for ten times the residence time to achieve steady state, here the estimated residence time is 15 s.

5. Collect product sample and then analyse it for particle size and particle size distribution.

6. Stop the experiment and clean the OBM with water prior to the next run to prevent cross contamination which may lead to seeded crystallization.

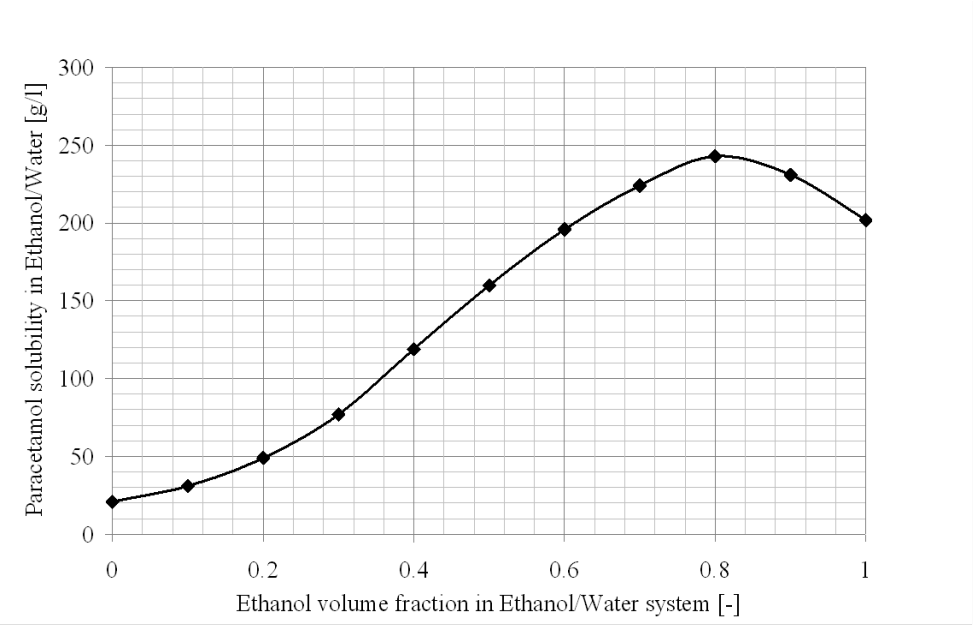

Figure 5.3: Paracetamol solubility in Ethanol/Water system at 30℃ (see Yalkowsky et al.).

7. Repeat each experiment run for minimum of three times to examine repeatability.

As mentioned in the previous chapter, there was a trade-off between the Re_o and f which affects the delivered oscillatory flow quality and hence the non axial mixing in the OBM. Therefore, in this chapter, response surface methodology (RSM) will be used to quantify this trade-off and its affects on the produced particle size and its size distribution.

5.3.1 Design of experiment

In this experiment a custom computer-generated RSM experiment design was used instead of the commonly used designs such as PlackettBurman design, BoxBehnken design or central composite design. This is because there were certain combinations of Re_o and f, due to pump performance, need to be avoided as it produced a poor oscillatory flow, see §5.2.3. Here the custom design of experiment comes in handy as it allows constraining the factors combinations as required. The design of experiment software used was JMP with I-Optimal optimisation routine which is a mathematical optimality criterion as it is more appropriate for response prediction rather than parameters estimations.

5.3.1.1 Factors and factor constraints

Factors chosen for this experiment were Re_o, f and ASF as the first two related to the non axial mixing in the OBM and the third factor related the crystallisation process. All of these factors were continuous and their ranges were chosen based on initial experimentations. The range for each factor is listed below:

1. Re_o, with a range spans from 100 to 385,
2. f, with a range spans from 5 Hz to 30 Hz, and
3. ASF, with a range spans from 0.90 to 0.98.

As for constrains, the design was constrained to avoid any combinations of Re_o and f that produced a pulse volume ratio (PVR) less than 3.75 or greater than 20. PVR is the ratio between the oscillatory volume dispensed in one direction at any Re_o and f and the volume of a single inter-baffle cavity ($v_{inter-baffle}$) of the OBM, see Equation 5.1 (Glasgow et al., 2004). The $v_{inter-baffle}$ for the OBM used, Figure 5.1, is 1.04 mm^3.

$$PVR = \frac{\text{pulse volume}}{\text{inter-baffle volume}} = \frac{Q_o}{120 f v_{inter-baffle}} \tag{5.1}$$

Figure 5.4 shows a contour plot representing the PVR values as function of Re_o and f with the feasible region shaded in red. At this figure and by using the PVR, it is possible to avoid any combination of Re_o and f that leads to poor syringe pump performance.

5.3.1.2 Interaction terms

In order to obtain a response surface for this experiment, interaction terms that need to be estimated were:

1. Main effect for each factor,
2. Second-order degree for each factor, and
3. Second-order degree interactions between factors.

Equation 5.2 shows the response surface equation with all required parameters including the lack of fit, $\bigtriangledown$, and the pure error, ϵ.

$$y = \beta_1 Re_o + \beta_1 f + \beta_3 ASF + \beta_4 Re_o^2 + \beta_5 f^2 + \beta_6 ASF^2 + \beta_7 Re_o f + \beta_8 Re_o ASF + \beta_9 f ASF + \bigtriangledown + \varepsilon \tag{5.2}$$

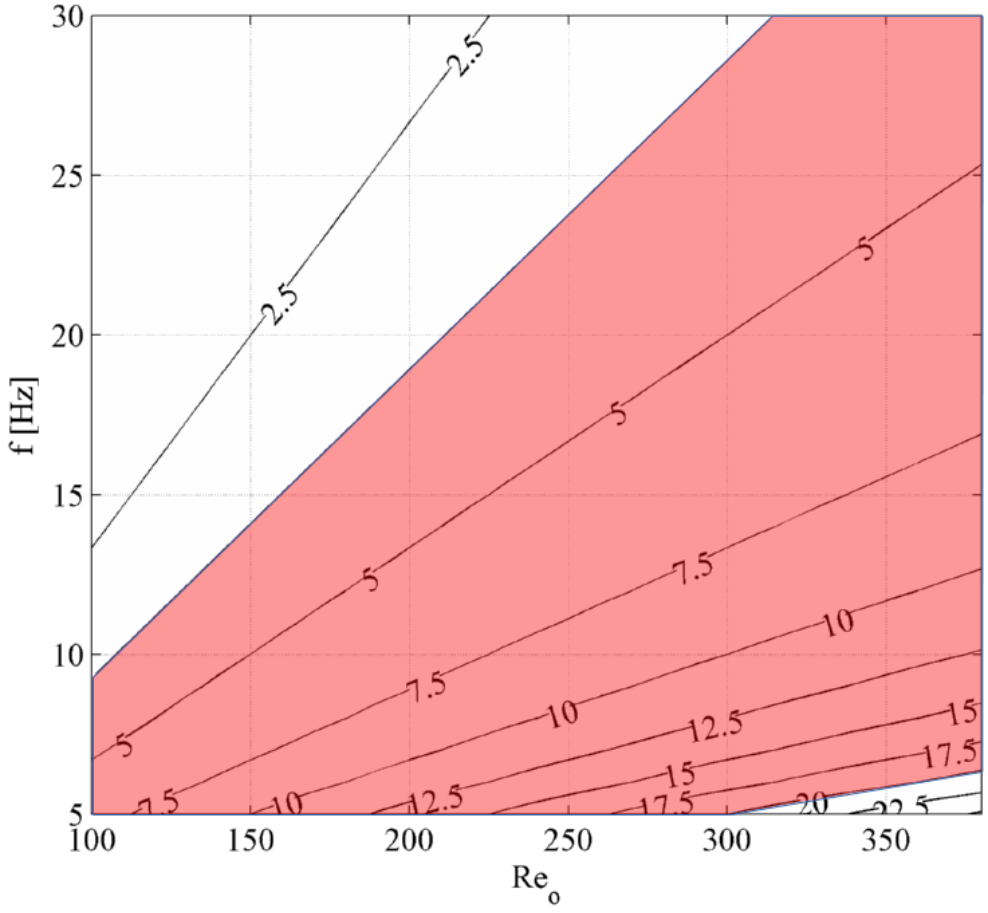

Figure 5.4: PVR contour curves as function of Re_o and f. Red shaded area represents the feasible region for experimentation.

5.3.1.3 Response

The response chosen for this experiment was the average particle size as it is the main measurement required in any crystallisation processes. The particle size measurement will be done using dynamic light scattering (DLS) which is a non-invasive technique for measuring the size and size distribution of molecules and particles typically in the submicron region. Particle size measurement produced from this technique is known as Z-Ave which is a hydrodynamic average particle size based on the intensity of scattered light. Alongside the Z-Ave, it is provides a measurement on the polydispersity of the measured sample which known as polydispersity index (PDI) which ranged from zero to unity. The lower the PDI indicates low polydispersity i.e. narrow particle size distribution. Another version of the PDI is the PDI width, which gives a sense for the width of the particle size distribution in a measurable units e.g. nm.

5.3.1.4 Number of runs

The number of runs required to estimate the required parameters with a statistical significance was 16. Another four runs representing centre point were added in order to estimate the lack of fitness and the pure error of the system which is associated with experiment error. The total number of runs and its corresponded factors levels were listed in Table 5.1 while Figure 5.5 shows the distribution of these runs on the Re_o and f matrix.

5.4 OBM design modification

Initially, antisolvent crystallisation of paracetamol experiment using the OBM showed in Figure 5.1 was not successful due to OBM blockage and high degree of unrepeatability in the obtained results. OBM blockages were mostly appeared at ASF setting of 0.90 at the cross-junction area which indicate a non perfect mixing situation. After reviewing the used OBM design, it is appears that non perfect mixing may occurs at the area before the cross-junction toward the fluid oscillation port where fluids enters the connection tube at the reverse phase of the fluid oscillation cycle. These could lead to a non perfect and slow mixing of the fluids which promote the formation and growth of larger Paracetamol crystals which eventually block the OBM passage.

A modification has been done to the OBM design to include a 50 mm long baffled microchannel before the cross-junction area. This will help to

Table 5.1: Randomised list of the computer-generated experiment runs. Experiment runs were executed in the same order as listed.

Run #	Factor 1	Factor 2	Factor 3
	Re_o^*	f^* [Hz]	ASF
1	385	21.25	0.9
2	242.5	17.5	0.94
3	299.5	13.75	0.948
4	242.5	17.5	0.94
5	242.5	20.99	0.9
6	385	21.25	0.944
7	204.67	17.5	0.948
8	256.75	8.75	0.9
9	319.78	27.5	0.92
10	320.09	27.5	0.98
11	242.5	17.5	0.94
12	114.25	9.69	0.98
13	157	13.44	0.944
14	385	6.35	0.968
15	199.75	5	0.932
16	242.5	17.5	0.94
17	370.75	18.75	0.98
18	370.75	6.25	0.904
19	214	5	0.98
20	100	7.5	0.9

* Nominal (set) value

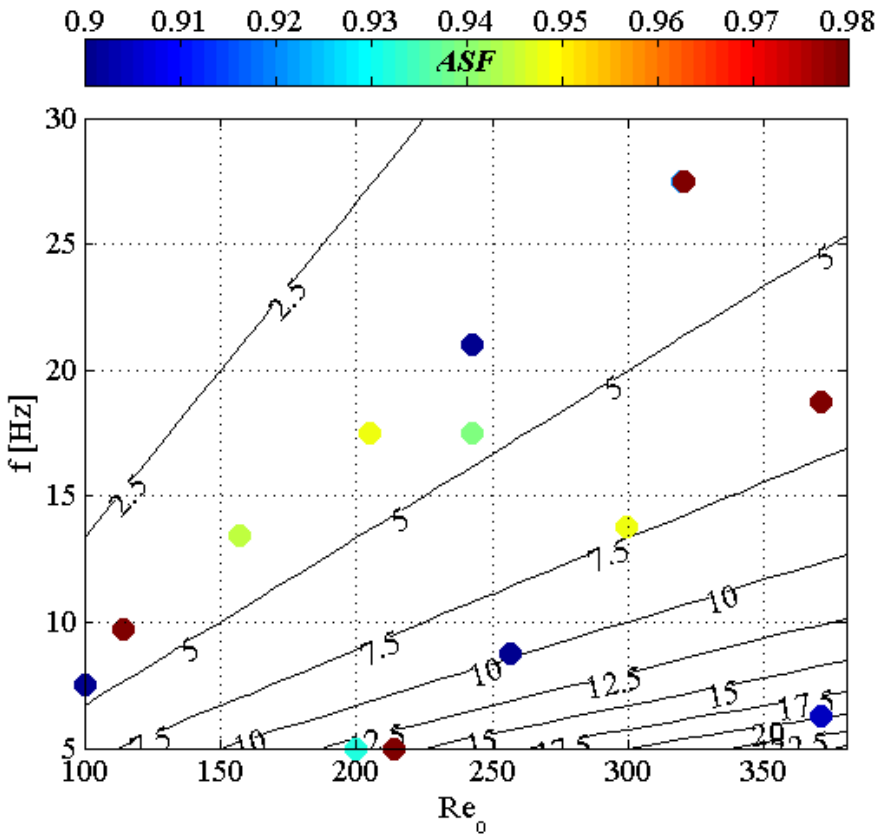

Figure 5.5: Distribution of the computer-generated experiment runs with respect to Re_o and f. The contour curves represent the PVR levels and the dot colour represents the ASF levels.

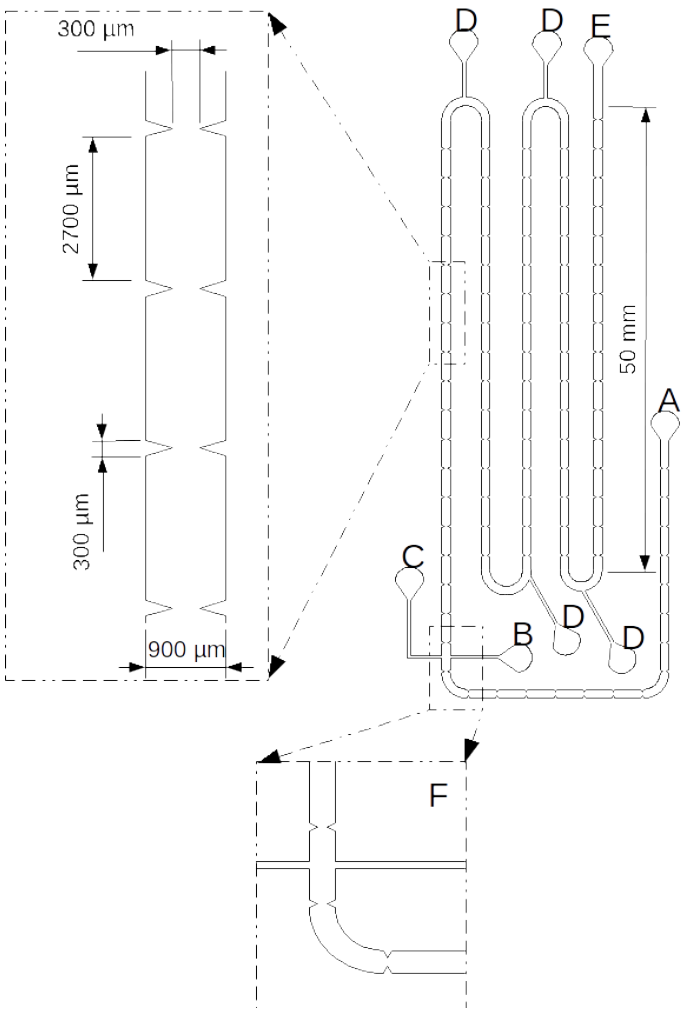

Figure 5.6: Drawing of the modified OBM. A: Oscillatory fluid port; B: Paracetamol-Ethanol/Water solution inlet port; C: Antisolvent (Water) inlet port; D: utility ports used for cleaning and purging; E: product outlet; F: cross-junction area.

promote the same degree of mixing after and before the cross-junction area at the forward and reverse phases of the fluid oscillation cycles.

5.5 Results and discussions

5.5.1 Experiment results

Figure 5.7 shows a photo of the Paracetamol antisolvent crystallisation in OBM experiment using the modified OBM shown in Figure 5.8. Each experiment run was repeated three to five time in order to examine the operability of the experiment and the repeatability of the obtained results. The experiment was successful and it was running smooth without any

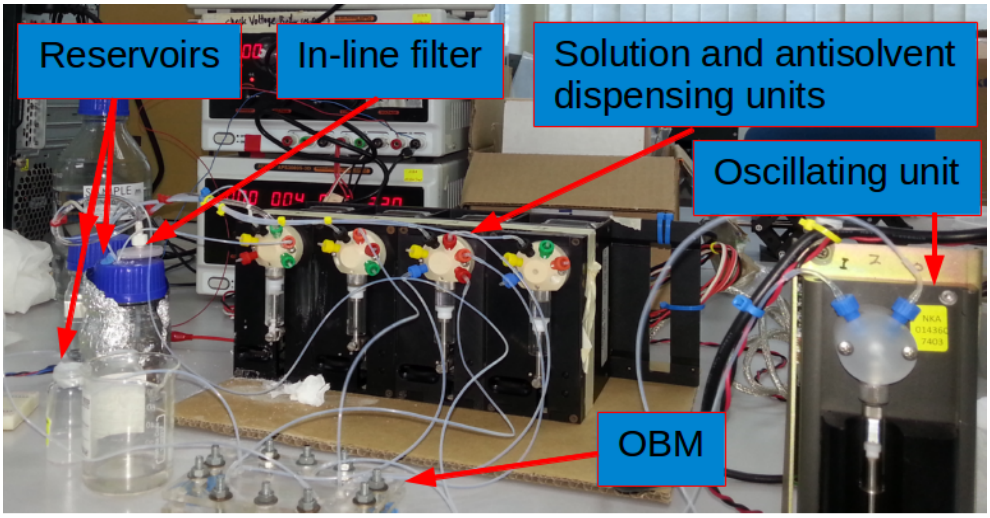

Figure 5.7: Photo of the antisolvent crystallisation in OBM experiment.

channel blockage for 1–2 hours. This indicate that the modification made on the OBM design was effectively sorted the problem of channel blockage and enhanced the non axial mixing in the OBM which indicated by the repeatability of the results obtained. Table 5.2 and Figure 5.9 list and illustrate the obtained results obtained from the experimental runs suggested by the design of experiment methodology which are tabulated in Table 5.1. Columns 2, 3 and 4 in Table 5.2 stated the experimental levels for the Re_o, f and ASF respectively. Columns 5 and 6 of the same table stated the obtained Z-Ave and the standard deviation from repeated experimental runs, while columns 7 and 8 stated the PDI and its standard deviation value. Further statistical analysis for the results obtained in this section will be discussed in the following sections to determine a statistical model and its goodness.

5.5.2 Response surface and response prediction

Fitting analysis for the suggested response model stated in Equation 5.2 shows a good degree of fitness with $R^2 = 0.87$, and $p = 0.0024$, see Figure 5.10 shows the experimental Z-Ave values (actual) vs predicted values from the proposed model. Here, most of the points are placed near the diagonal line in a random manner, which gives a visual sense for the model goodness to predict response values. A complete list of the actual particle size (Z-Ave), the model predicted particle size and the residual values are tabulated in. A complete list of the actual particle size (Z-Ave) and the model predicted particle size is tabulated in Table 5.3.

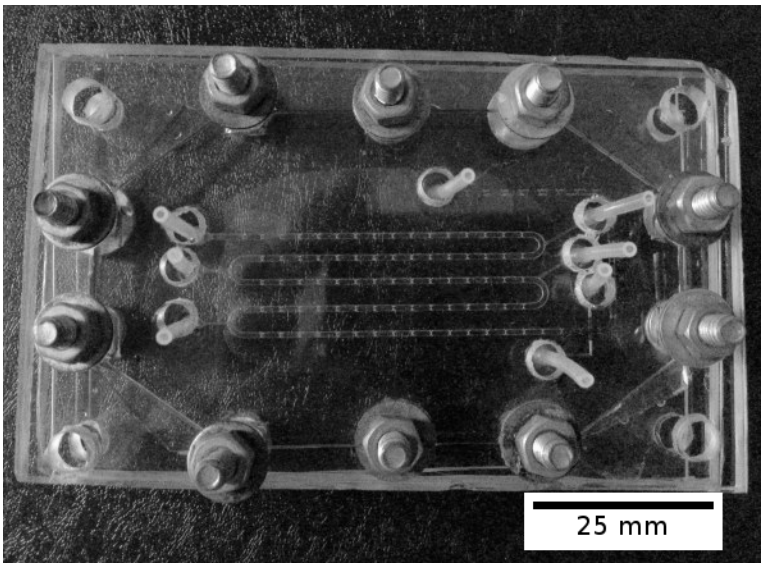

Figure 5.8: Photo shows the modified OBM device used in this experiment.

Table 5.2: Summary of the results obtained from the Paracetamol antisolvent crystallisation in the OBM experiment.

#	Re_o	**f [Hz]**	ASF	**Z-Ave [d. nm]**		**PDI width [d. nm]**	
				Ave.	**SD**	**Ave.**	**SD**
1	385	21.25	0.9	159.4	1.45	51.63	3.52
2	242.5	17.5	0.94	148.9	1.22	44.48	2.34
3	299.5	13.75	0.948	175.6	0.85	47.72	6.28
4	242.5	17.5	0.94	120.62	1.83	37.22	2.69
5	242.5	20.99	0.9	169.28	1.15	56.26	3.96
6	385	21.25	0.944	164.7	0.68	36.92	6.27
7	204.67	17.5	0.948	148.44	1.64	42.02	5.62
8	256.75	8.75	0.9	174.3	1.83	55.22	5.34
9	319.78	27.5	0.92	165.64	0.91	49.71	4.8
10	320.09	27.5	0.98	129	0.2	22.7	6.29
11	242.5	17.5	0.94	129.48	1.7	36.61	3.6
12	114.25	9.69	0.98	127	0.36	31.3	1.45
13	157	13.44	0.944	231.6	1.67	106.37	3.47
14	385	6.35	0.968	203.1	1.21	52.32	6.13
15	199.75	5	0.932	191.36	2.02	53.09	8.13
16	242.5	17.5	0.94	130.46	2.18	39.19	4.96
17	370.75	18.75	0.98	129.9	0.54	31.21	6.31
18	370.75	6.25	0.904	301.74	2.82	139.96	4.61
19	214	5	0.98	109.34	0.94	28.24	5.24
20	100	7.5	0.9	273.26	2.4	130.34	3.68

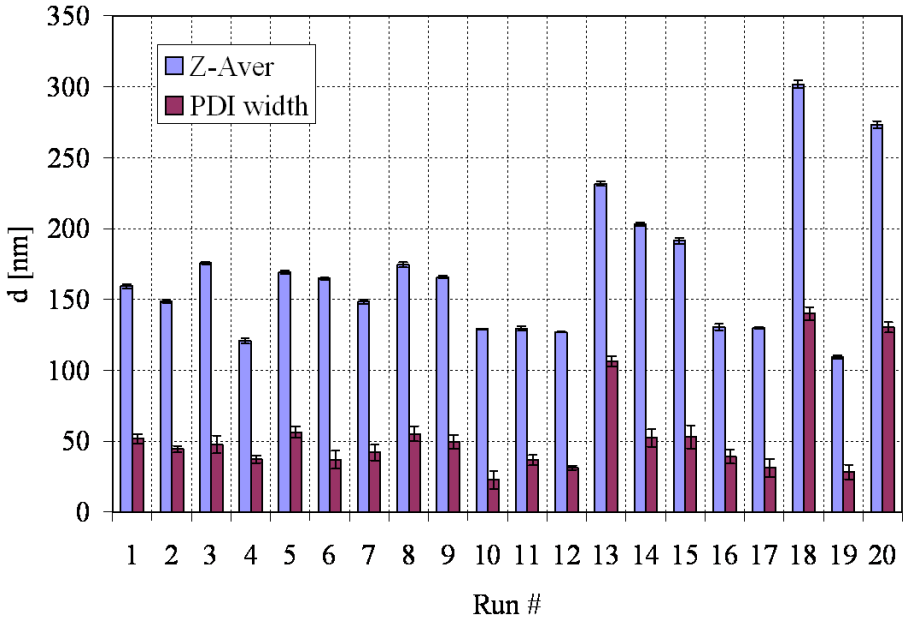

Figure 5.9: Average particle size and particle size distribution width obtained from the Paracetamol antisolvent crystallisation in the OBM experiment. The total number of samples analysed was 91.

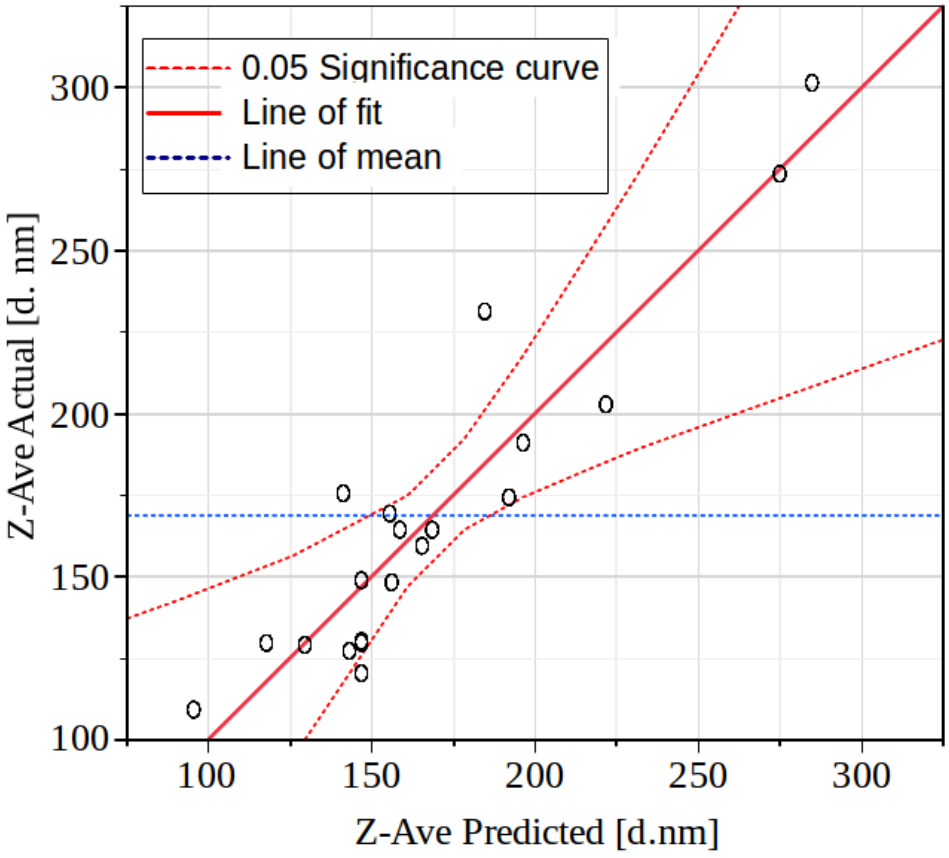

Figure 5.10: Actual vs. predicted Particle size, Z-Ave.

Table 5.3: Actual particle size vs. the model predicted.

Run #	Z-Ave	Predicted Z-Ave	Residual
	[d. nm]		
1	159.4	165.9	-6.5
2	148.9	147.1	1.8
3	175.6	142.1	33.5
4	120.6	147.1	-26.5
5	169.3	156	13.3
6	164.7	168.8	-4.1
7	148.4	156.4	-8
8	174.3	192.6	-18.3
9	164.6	158.9	5.7
10	129	129.9	-0.9
11	129.5	147.1	-17.7
12	127	143.9	-16.9
13	231.6	184.8	46.8
14	203.1	222.4	-19.3
15	191.4	196.7	-5.4
16	130.5	147.1	-16.7
17	129.9	118.1	11.8
18	301.7	285.2	16.5
19	109.3	96.2	13.1
20	273.3	275.4	-2.1

Effect Tests

Source	Nparm	DF	Sum of Squares	F Ratio	Prob > F
Reo(100,385)	1	1	3409.714	5.2050	0.0457*
f(5,30)	1	1	287.948	0.4396	0.5223
ASF(0.9,0.98)	1	1	7406.347	11.3059	0.0072*
Reo*Reo	1	1	11491.249	17.5416	0.0019*
Reo*f	1	1	4188.623	6.3940	0.0299*
f*f	1	1	3538.374	5.4014	0.0425*
Reo*ASF	1	1	119.032	0.1817	0.6789
f*ASF	1	1	2583.322	3.9435	0.0751
ASF*ASF	1	1	1778.576	2.7150	0.1304

Figure 5.11: Effect tests result. Effects with (Prob¿F) value less than 0.05 were statistically significant.

5.5.2.1 Model effects test

In order to test the statistical significance of each effect in the model proposed in §5.3.1.2, an effect tests was done using the JMP statistical software. Any effect that has (Prob¿F) value bigger than the confidence value (0.05) is considered a non-significant effect (Goupy and Creighton, 2007). Figure 5.11 shows the results of this test where five out of nine effects were statistically significant. These statically significant effects were Re_o, ASF, Re_o^2, Re_o, f and f^2.

5.5.3 Lack of fit

In order to test the fitness of the suggested model, a lack of fit test was carried out too to determine whether the scattering of the predicted valued is related the model or it is a resulted from the pure error associated with this experiment. The p-value resulted from this test was greater that the significance level () of 0.05, (Goupy and Creighton, 2007). Thus, the suggested model for this experiment did not show a lack of fitness and it is sufficient to represent the experiment.

5.5.4 Parameters estimation

As the mathematical model was statistically significant and without Llack of fit, the model parameters can be then estimated using the JMP software. Table 5.4 shows the estimated parameters alongside with its significant level. The next step is to use the model to optimise the operation parame-

Lack Of Fit

Source	DF	Sum of Squares	Mean Square	F Ratio
Lack Of Fit	7	6127.5379	875.363	6.2038
Pure Error	3	423.3035	141.101	**Prob > F**
Total Error	10	6550.8414		0.0809
				Max RSq
				0.9914

Figure 5.12: Lack of fit test results. Here, the Prob¿F (p-value) is greater than 0.05.

Table 5.4: stimation of the mathematical model parameters. Parameters with P-value less than 0.05, marked with asterisks, were statically significant.

Parameter	Estimate	Std Error	P-value
Intercept	147.14316	9.680512	<.0001*
Re_o(100,385)	-43.71496	19.16106	0.0457*
f(5,30)	13.714188	20.68528	0.5223
ASF(0.9,0.98)	-33.20174	9.874325	0.0072*
Re_o*Re_o	79.090062	18.88369	0.0019*
Re_o*f	-67.63049	26.74579	0.0299*
f*f	51.608144	22.20572	0.0425*
Re_o*ASF	5.4767101	12.84805	0.6789
f*ASF	28.735498	14.47032	0.0751
ASF*ASF	-24.16659	14.66654	0.1304

ters in order to achieve a produced particle with minimum size. This Will be discussed in the next section.

5.5.5 Operation condition optimization

As the mathematical model was established, it is possible to optimise the operation conditopns (effects) in order to the find factors levels that meet an operational target. Figure 5.13 shows the response (Z-Ave) as function of Re_o, f and ASF. The lower row of this graph depicted the desirability for each effect where all of them were set to one (black horizontal line) as an indication of high desirability. As can be seen from Figure 5.13 the factors levels that lead to minimum produced particle size, Z-Ave=80.568 ±40.57 nm, were $Re_o = 255.3$, $f = 13.1$ Hz and $ASF = 0.98$. The blue continuous lines in the upper row of the graph represent the 95% confidence region. For a wider prospective, Figure 5.14 shows the effect of Re_o and f on the produced particle size which represented as the red contour at ASF level

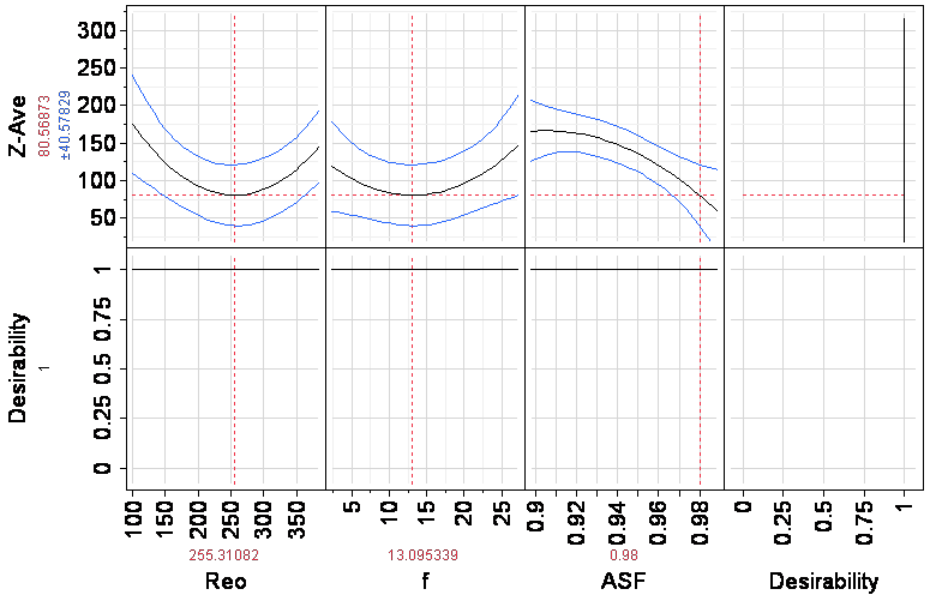

Figure 5.13: Factors values for minimum response.

fixed to 0.98. Here, in order to achieve minimum particle size (Z-Ave = 80.568 nm) the OBM need to be operated at $Re_o = 255.31$ and $f = 13.09$ Hz.

In order to check the accuracy of the optimised factors levels, a series of experimental runs were executed at the factors levels suggested by the optimisation study and results of these experiment runs were tabulated in Table 5.5.

Figure 5.15 shows a plot of the produced particle sized at the optimised factors levels alongside the predicted Z-Aver value (red dotted line) and the prediction margine of 95% confidence (blue dashed lines). As can be seen from Figure 5.15, the produced Paracetamol particle sizes at the optimised factors levels were relatively above the minimum predicted particle size and all of them were falling within the upper 95% confidence interval. Furthermore, the majority of produced particles having a particle size distribution width within the predicted 95% confidence interval. This is a good indication that the model and the optimisation process were successfully agreed with the experimental results obtained from 12 experimental runs.

5.5.6 Result verification

In attempt to verify results obtained in the previous section, produced Paracetamol particles were examine using an environmental scanning elec-

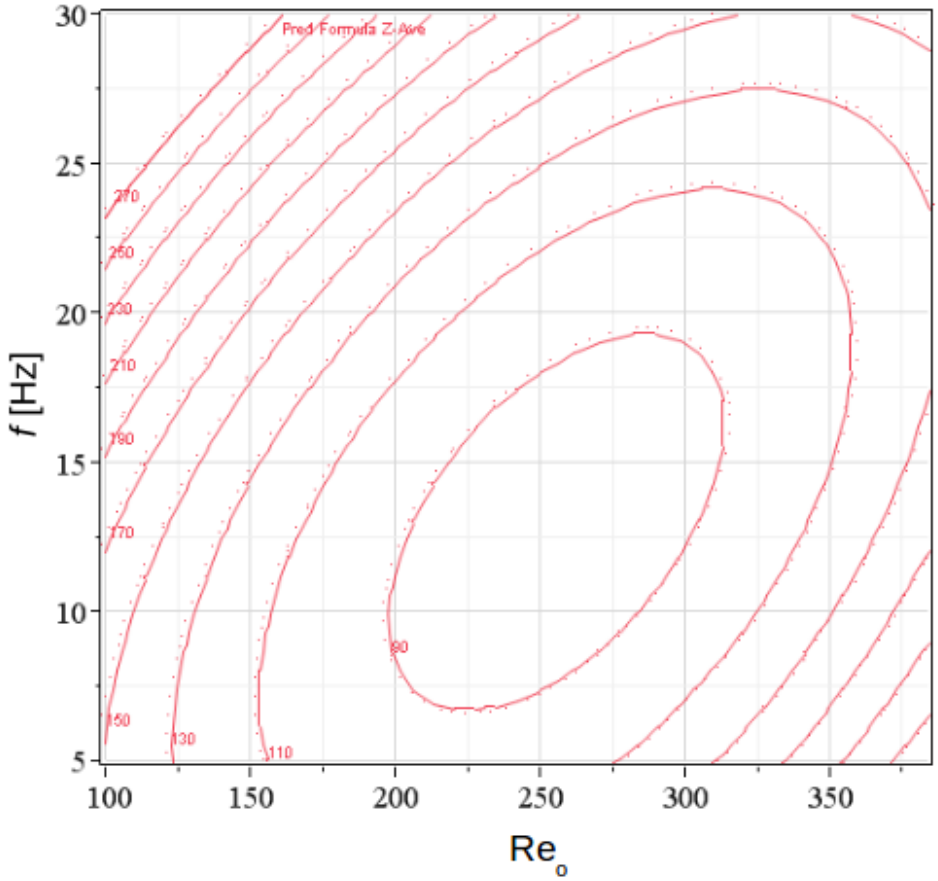

Figure 5.14: Contour curves show the predicted particle size, Z-Ave, as function of Re_o and f at ASF level equal to 0.98.

Table 5.5: Particle size and size distribution of the produced Paracetamol particle at the optimum operating conditions.

Run #	**Z-Ave (d.nm)**	**PdI**	**PdI Width (d.nm)**
1	101.2	0.045	21.55
2	102.6	0.044	21.53
3	102.9	0.056	24.37
4	98	0.046	20.95
5	98.91	0.063	24.84
6	99.49	0.072	26.62
7	88.88	0.037	17.05
8	89.33	0.083	25.8
9	89.18	0.098	27.9
10	109.1	0.071	29.03
11	109.1	0.043	22.71
12	110	0.052	24.99
Average	***99.89***	***0.0591***	***23.945***
Standard deviation	***7.315***	***0.0178***	***3.211***

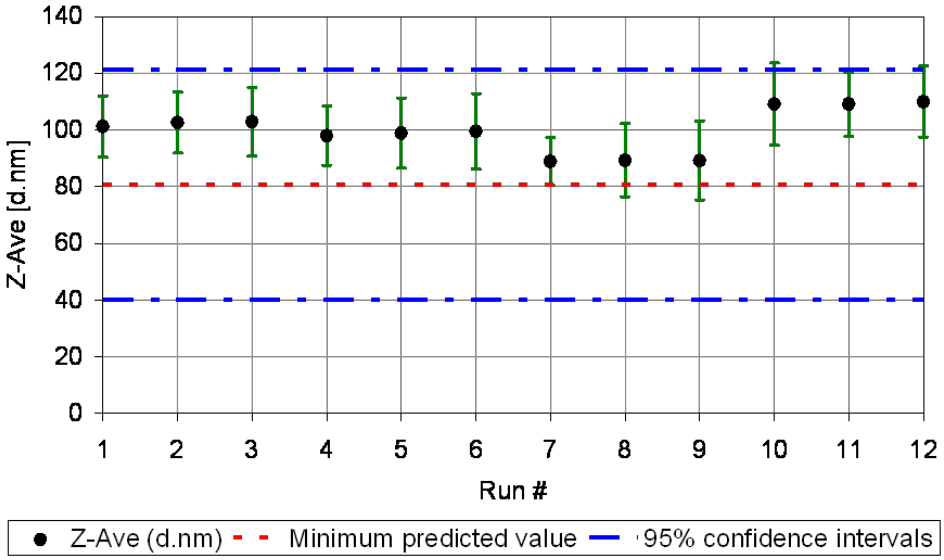

Figure 5.15: Produced Paracetamol particle size at the optimised operating condition; $Re_o = 255.31$, $f = 13.09$ Hz and $ASF = 0.98$. Here, the green vertical bars represent the PDI width in nm.

tron microscope (ESEM). Unfortunately, the available ESEM (FEI Quanta 400F FESEM) was not equipped with wet sample holder thus produced samples were need to be undergo for sample preparation for ESEM scan.

Sample preparation steps were:

1. Filtering of 1 ml of the sample using 50 micrometre pore filter paper (Whatman Nuclepore). Figure 5.16 shows the filtration setup.

2. Filter papers were then oven-dried at 60℃ overnight in closed containers with side vents to prevent contamination with airborne particles.

3. Finally, filter paper were stickled to the ESEM examine stubs using carbon tape.

Figure 5.17 shows a sample photo of the produced Paracetamol particles using ESEM. Here the individual particles were agglomerated as a result of sample preparation steps taken (Washington, 2005). From this figure, it appeared that individual particles were originally spherical in shape and then agglomerated. As for the particle sizes which measured manually and directly from this image using an image processing software(ImageJ), most of the particles were under 100 nm in diameter which agreed with the results obtained from the DLS measurement tabulated in Table 5.5. A

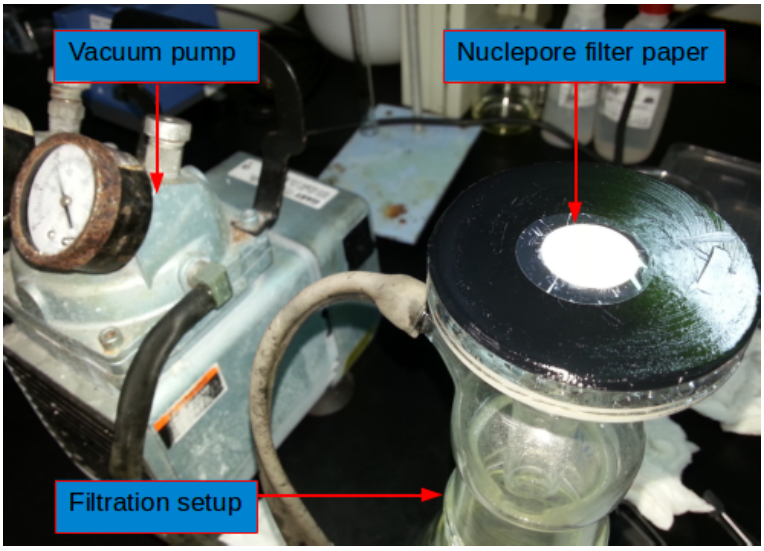

Figure 5.16: Sample filtration setup using Whatmans Nuclepore filter paper.

complete set of the successful ESEM images were included in Appendix D for the samples produced in §5.5.6.

5.6 Conclusion

The feasibility of growing crystals in micro-scale devices on a continuous basis has been proved using a periodically baffled microchannel with superimposed oscillatory flow. The net flow rate in this devise was equivalent to Reynolds number of 9.23 i.e. a residence time of 15 second. The superimposed oscillatory flow has a nominally oscillatory magnitude equivalent to 100–385 Reynolds number and oscillation frequency ranged from 5 to 30 Hz.

Produced crystals size in OBM were in tens of nanometre with a very narrow particle size distribution e.g. average Z-Ave=99.89 nm with standard deviation equivalent to 7.315 nm. This was achieved without using any surfactant which is usually used in nano-particle syntheses processes. In addition to that and with a appropriate OBM design, microchannels blockage did not occurs even with long operation time e.g. 1–2 hours.

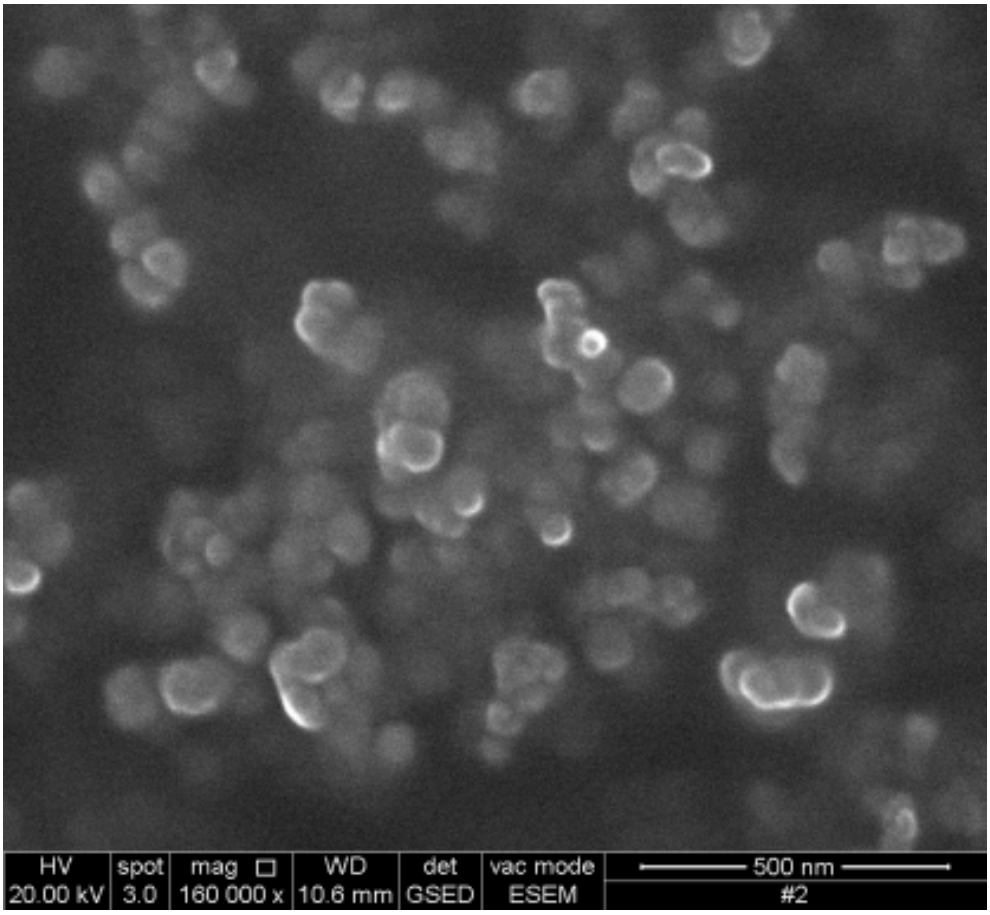

Figure 5.17: ESEM image of the produced Paracetamol particle at the optimum factors levels.

References

CK Chung, TR Shih, CK Chang, CW Lai, and BH Wu. Design and experiments of a short-mixing-length baffled microreactor and its application to microfluidic synthesis of nanoparticles. *Chemical Engineering Journal*, 168(2):790–798, 2011. 85

Ian Glasgow, Samuel Lieber, and Nadine Aubry. Parameters influencing pulsed flow mixing in microchannels. *Analytical chemistry*, 76(16):4825–4832, 2004. 90

J. Goupy and L. Creighton. *Introduction to Design of Experiments with JMP Examples*. SAS Institute, 2007. 100

S. Lawton, G. Steele, P. Shering, L. H. Zhao, I. Laird, and X. W. Ni. Continuous crystallization of pharmaceuticals using a continuous oscillatory baffled crystallizer. *Organic Process Research & Development*, 13 (6):1357–1363, 2009. 85

Jose V Parambil, Marc Schaepertoens, Daryl R Williams, and Jerry YY Heng. Effects of oscillatory flow on the nucleation and crystallization of insulin. *Crystal Growth & Design*, 11(10):4353–4359, 2011. 85

Anh N Phan, Adam P Harvey, and Martin Rawcliffe. Continuous screening of base-catalysed biodiesel production using new designs of mesoscale oscillatory baffled reactors. *Fuel Processing Technology*, 92(8):1560–1567, 2011. 85

RI Ristic. Oscillatory mixing for crystallization of high crystal perfection pharmaceuticals. *Chemical Engineering Research and Design*, 85(7):937–944, 2007. 85

C. Washington. *Particle Size Analysis In Pharmaceutics And Other Industries: Theory And Practice: Theory And Practice*. Taylor & Francis, 2005. 104

Samuel H. Yalkowsky, Yan He, and Parijat Jain. *Handbook of aqueous solubility data*. CRC Press, Boca Raton, FL, 2 edition. xiii, 89

M. Z. Zheng and M. Mackley. The axial dispersion performance of an oscillatory flow meso-reactor with relevance to continuous flow operation. *Chemical Engineering Science*, 63(7):1788–1799, 2008. 85

Chapter 6

General conclusions and suggestions for future work

6.1 General conclusions

The design and operation of continuous micro-scale crystallizers was achieved successfully. The novel design consists of a periodically baffled microchannel operated by superimposing a fully reversed oscillatory flow on the net flow of the micro crystalliser. The superimposed oscillatory flow has a nominal oscillatory Reynolds number and frequency ranging from 100–385 and 5–30 Hz respectively. Under optimized operation conditions, the micro-scale crystalliser can produce crystalline particles in tens of nanometres with particle distribution size width in order on one nanometre. In addition to that, the operation of such design was smooth and without any microchannel blockages.

Two modes of crystallisation were investigated in this thesis, namely; cooling and antisolvent. The former crystallisation mode (chapter 3) was not promising in micro-scaled application as it was very hard to maintain different parts of the experiment setup at different temperatures. The latter (chapter 5), on the other hand, was very successful in driving crystallisation in micro-164 scaled devices as it was operated in ambient temperature and do not require any thermally controlled environment.

Analyses of the performance of the oscillatory baffled microchannel in term of mixing with the absent of net flow were preformed utilizing computational fluid dynamics simulations and then compared with experimental micro flow visualisation outcomes (chapter 4). The comparison outcomes between the two methods were conceptually agreed with each other in terms of behaviour; however, in terms of results magnitude the experimental re-

sults were all less compared with the simulation studies. The reason for such behaviour was related to the performance of the syringe bumps used in this study.

To conclude, at this thesis, the objectives stated in §1.5 were addressed successfully throughout original academic research. The key objectives addressed are listed below:

1. The usability of continuous crystallisation by cooling in a micro-scale crystalliser was investigated. Results were not consistence, did not show any degree of repeatability and the experimentation were very hard to carry out due to (i) the difficulties in maintaining different parts of the microfluidic setup at different temperature levels and (ii) microchannels blockage by uncontrolled crystal growth. This led to use the antisolvent crystallisation mode, which operated at constant temperature. The use of the antisolvent to drive continuous crystallisation required to develop a mechanism to promote non-axial mixing within the microcrystalliser to achieve fast mixing which is essential for this kind of crystallisation mode.

2. Achievement of a novel design and operation mechanism to promote non-axial mixing within a continuous antisolvent microcrystalliser to achieve fast mixing. That was achieved by utilizing baffled microchannel with superimposed oscillatory flow and antisolvent crystallisation mode.

3. Non-axial mixing within the proposed oscillatory baffled microchannel has been quantified by measuring the total vortices area generated behind the baffles using computational fluid dynamics simulations and then compared with results obtained experimentally utilising micro-flow visualisation technique. There was significant drop in the total vortices area measured from the micro-flow visualisation experiment compared with the CFD simulation results. That was because the poor performance of the syringe pump used at higher140 oscillation frequencies. However, the non-axial mixing within the baffled microchannels was observed as a proof of concept.

4. By means of design of experiment, the performance of the proposed oscillatory baffled microchannel as a continuous microcrystalliser has been modelled and optimised at different operation conditions; namely oscillatory Reynolds number, oscillation frequency and antisolvent ratio. Results of the optimisation process were particles with tens of

nanometre in size and have very narrow particle size distribution. Crystallisation process was continuous without any blockage in the microchannels.

6.2 Recommendations for future work

The following are some recommendations for future development on the micro scale continuous crystalliser using the oscillatory baffled microchannel crystalliser:

1. Study the effects of different baffled geometry such as smooth and curvature baffles on the produced particle size and size distribution. Using smooth and curvature baffled area will reduce the shear stress level within the baffle area which eventually effect the nucleation rate and the produced particle sized and distribution frequency.

2. Utilizing pressure-vacuum-driven microfluidics flow instead of positive displacement flow to generate oscillatory flow will eliminate the problems related to the poor performance of the syringe pumps. Using such technology will enable oscillatory flow with a fast acceleration, very short response time and higher flow resolution such that the achieved magnitude and oscillation frequency will be very closes to the desired ones.

3. Studying the influence of using surfactants on the performance of the oscillatory baffle microchannel crystalliser. As with the usage of surfactants in this setup, it is expected to produce smaller particles with narrower particle size distribution because surfactants will prevent particles from agglomeration.

Appendix A: Pressure drop trend results

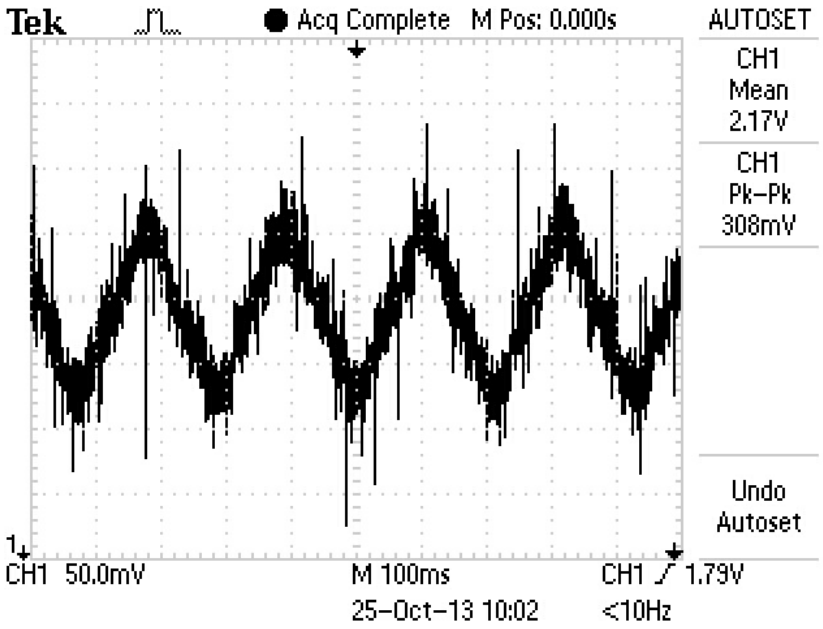

Figure A.1: Captured oscilloscope screen represent pressure drop trend across OBM for programmed Re_o of 100 and f of 5 Hz. Here x-axis represent time trend of 1 s and y-axis represent pressure drop measured in mV.

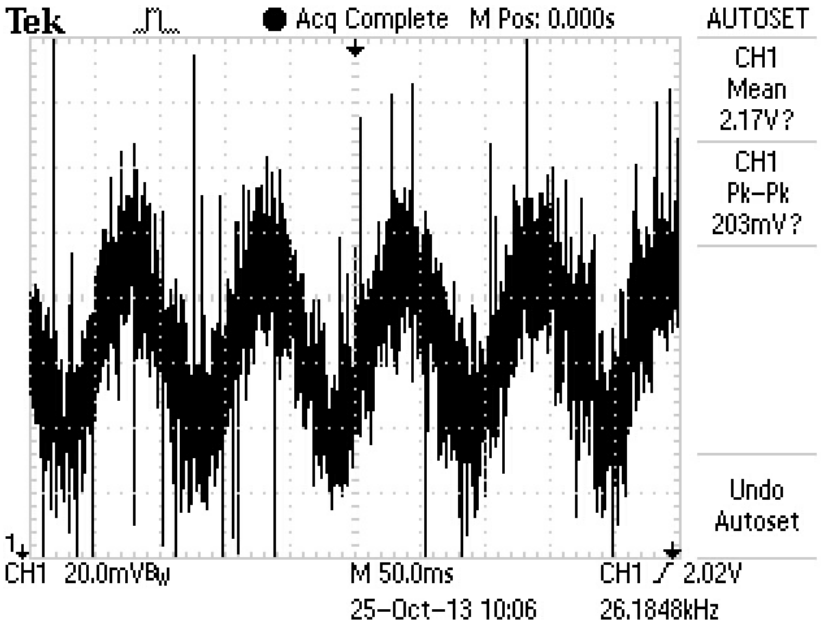

Figure A.2: Captured oscilloscope screen represent pressure drop trend across OBM for programmed Re_o of 100 and f of 10 Hz. Here x-axis represent time trend of 0.5 s and y-axis represent pressure drop measured in mV

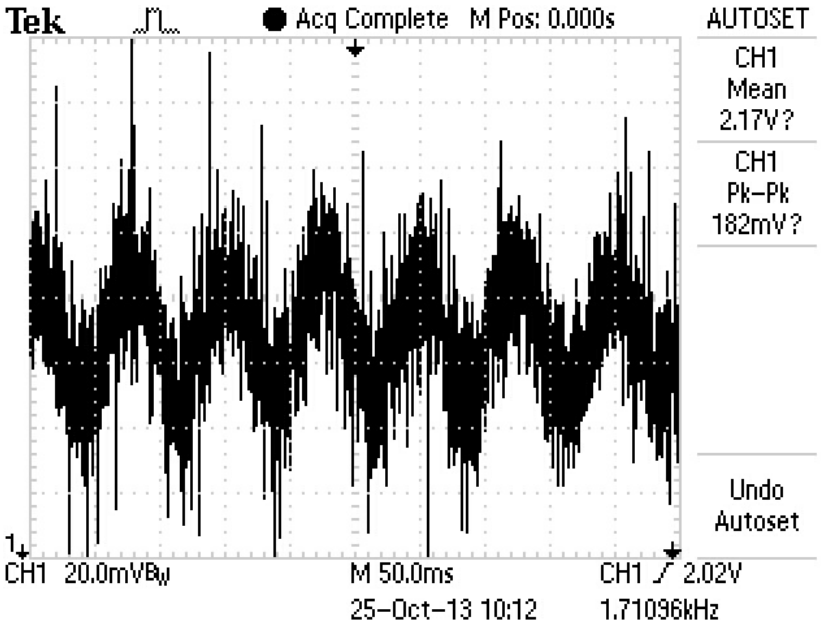

Figure A.3: Captured oscilloscope screen represent pressure drop trend across OBM for programmed Re_o of 100 and f of 15 Hz. Here x-axis represent time trend of 0.5 s and y-axis represent pressure drop measured in mV.

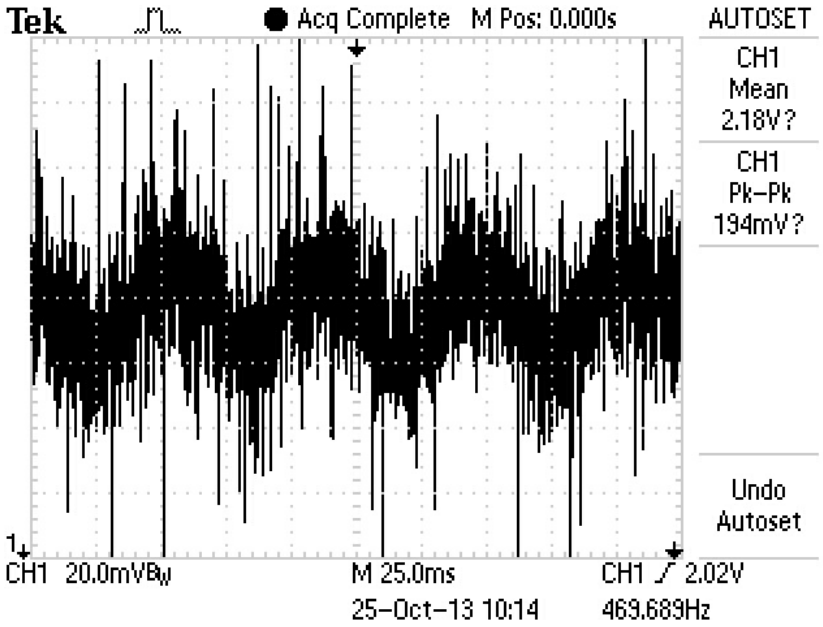

Figure A.4: Captured oscilloscope screen represent pressure drop trend across OBM for programmed Re_o of 100 and f of 20 Hz. Here x-axis represent time trend of 0.25 s and y-axis represent pressure drop measured in mV.

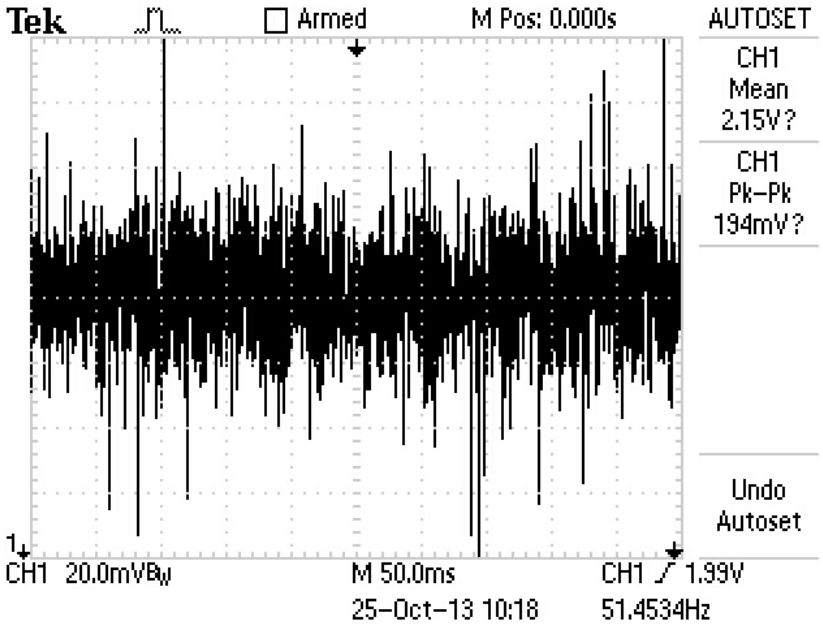

Figure A.5: Captured oscilloscope screen represent pressure drop trend across OBM for programmed Re_o of 100 and I of 25 Hz. Here x-axis represent time trend of 0.5 s and y-axis represent pressure drop measured in mV.

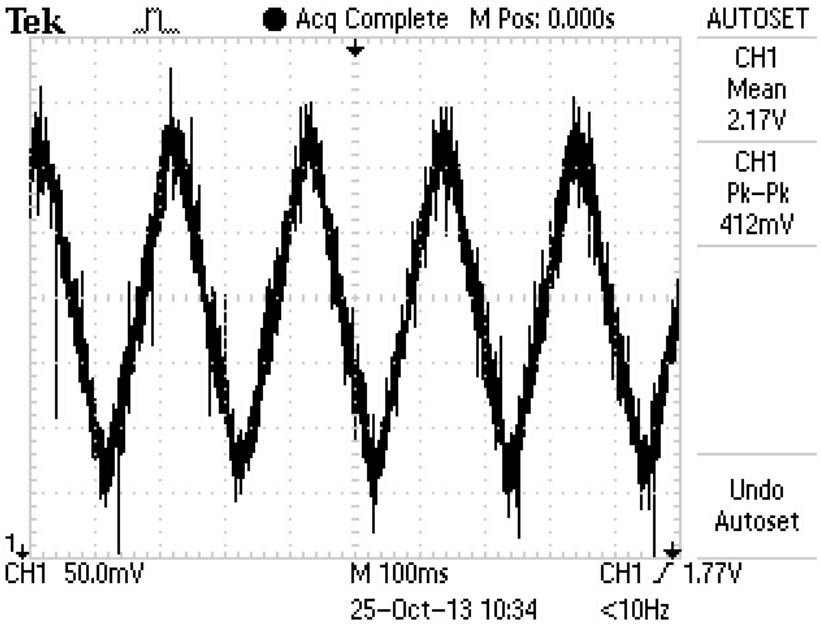

Figure A.6: Captured oscilloscope screen represent pressure drop trend across OBM for programmed Re_o of 200 and f of 5 Hz. Here x-axis represent time trend of 1 s and y-axis represent pressure drop measured in mV.

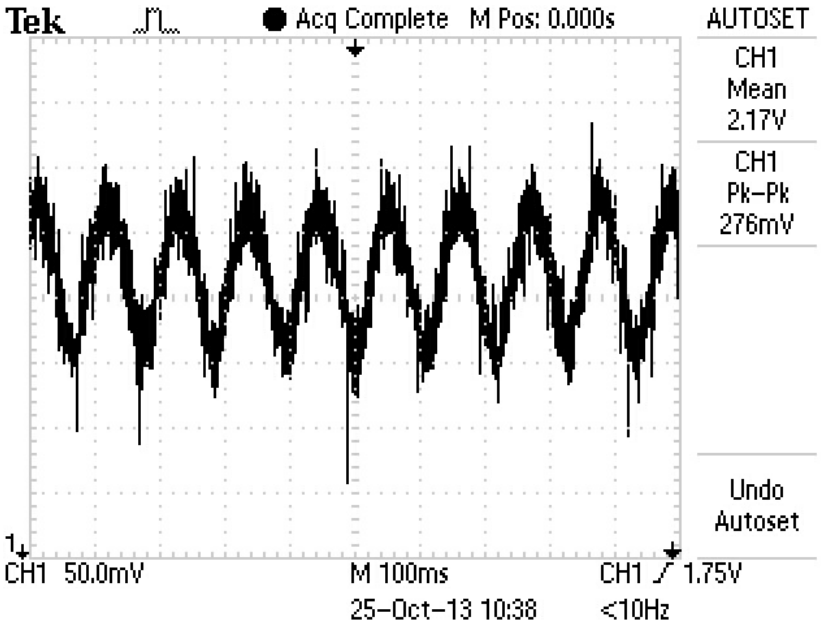

Figure A.7: Captured oscilloscope screen represent pressure drop trend across OBM for programmed Re_o of 200 and f of 10 Hz. Here x-axis represent time trend of 1 s and y-axis represent pressure drop measured in mV.

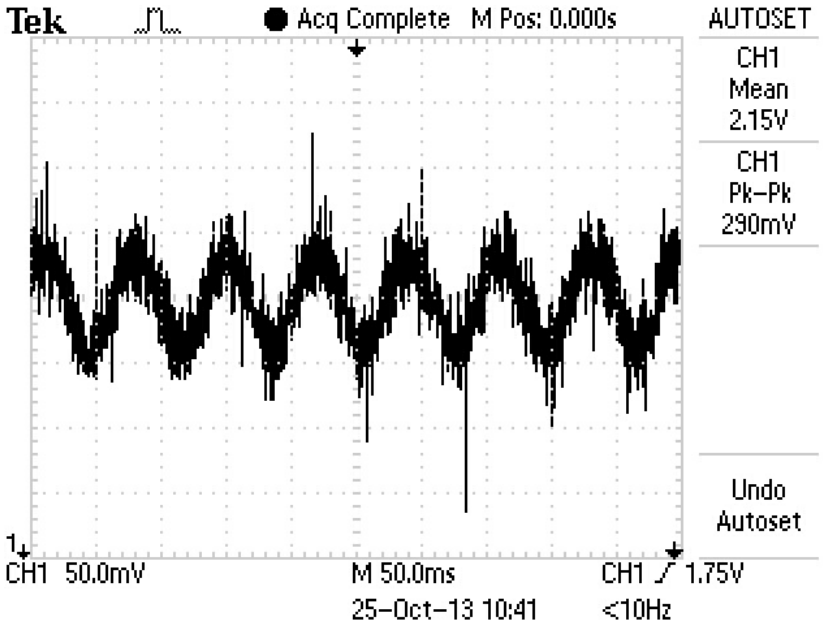

Figure A.8: Captured oscilloscope screen represent pressure drop trend across OBM for programmed Re_o of 200 and f of 15 Hz. Here x-axis represent time trend of 0.5 s and y-axis represent pressure drop measured in mV.

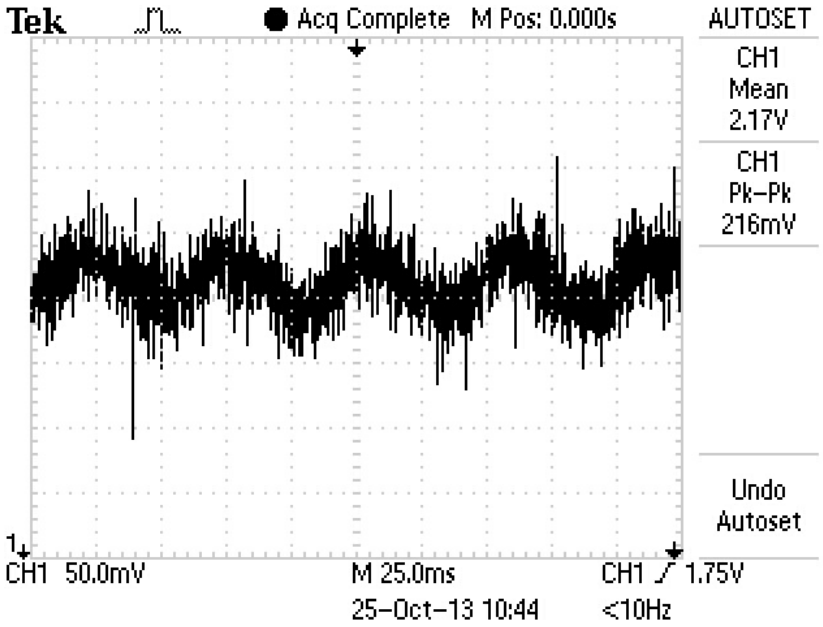

Figure A.9: Captured oscilloscope screen represent pressure drop trend across OBM for programmed Re_o of 200 and f of 20 Hz. Here x-axis represent time trend of 0.25 s and y-axis represent pressure drop measured in mV.

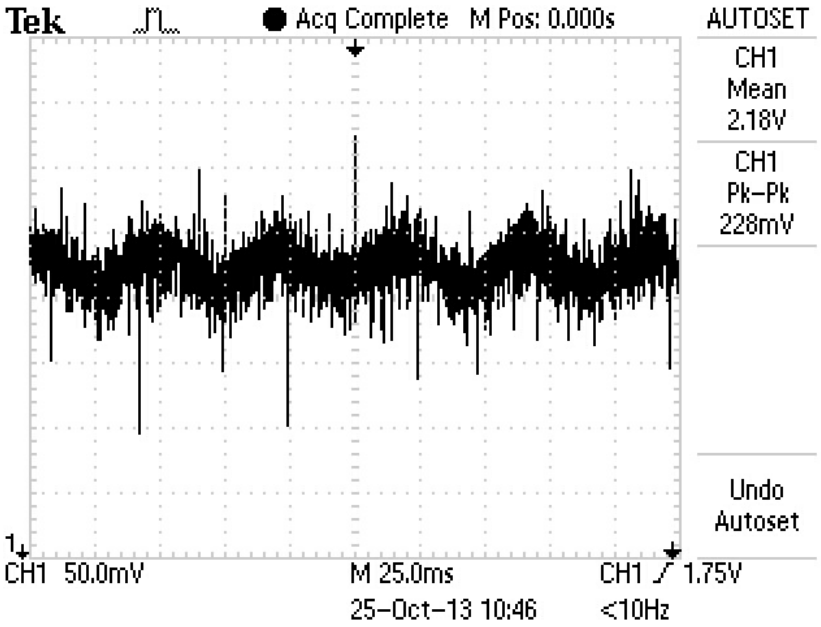

Figure A.10: Captured oscilloscope screen represent pressure drop trend across OBM for programmed Re_o of 200 and f of 25 Hz. Here x-axis represent time trend of 0.25 s and y-axis represent pressure drop measured in mV.

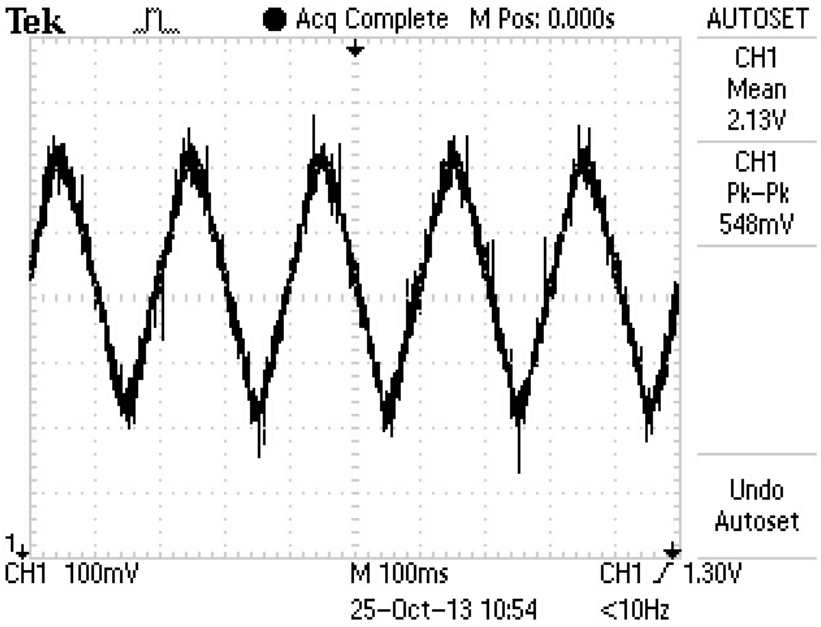

Figure A.11: Captured oscilloscope screen represent pressure drop trend across OBM for programmed Re_o of 300 and f of 5 Hz. Here x-axis represent time trend of 1 s and y-axis represent pressure drop measured in mV.

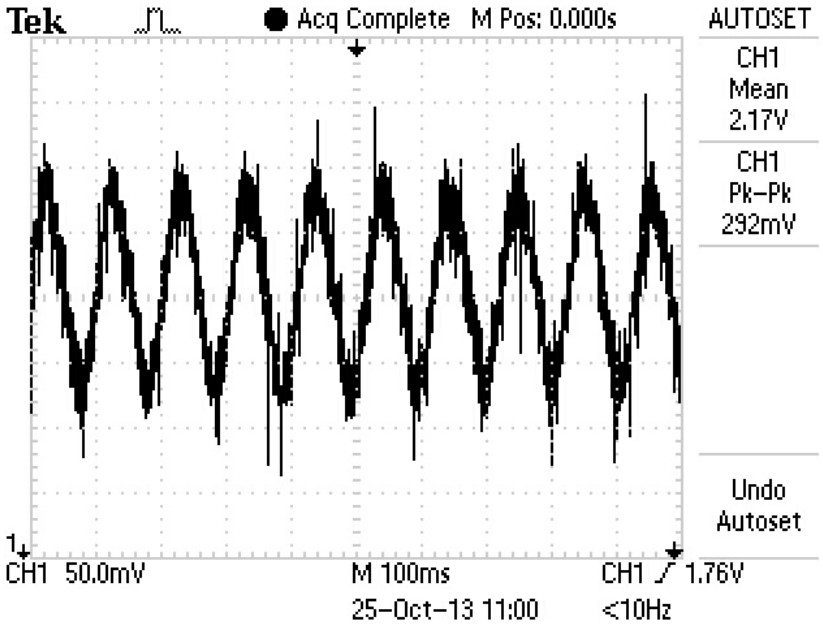

Figure A.12: Captured oscilloscope screen represent pressure drop trend across OBM for programmed Re_o of 300 and f of 10 Hz. Here x-axis represent time trend of 1 s and y-axis represent pressure drop measured in mV.

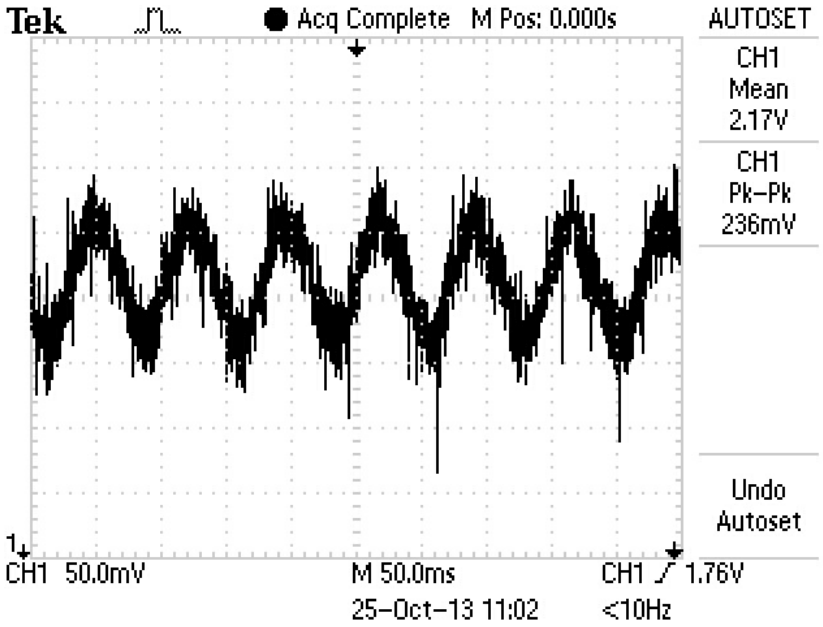

Figure A.13: Captured oscilloscope screen represent pressure drop trend across OBM for programmed Re_o of 300 and f of 15 Hz. Here x-axis represent time trend of 0.5 s and y-axis represent pressure drop measured in mV.

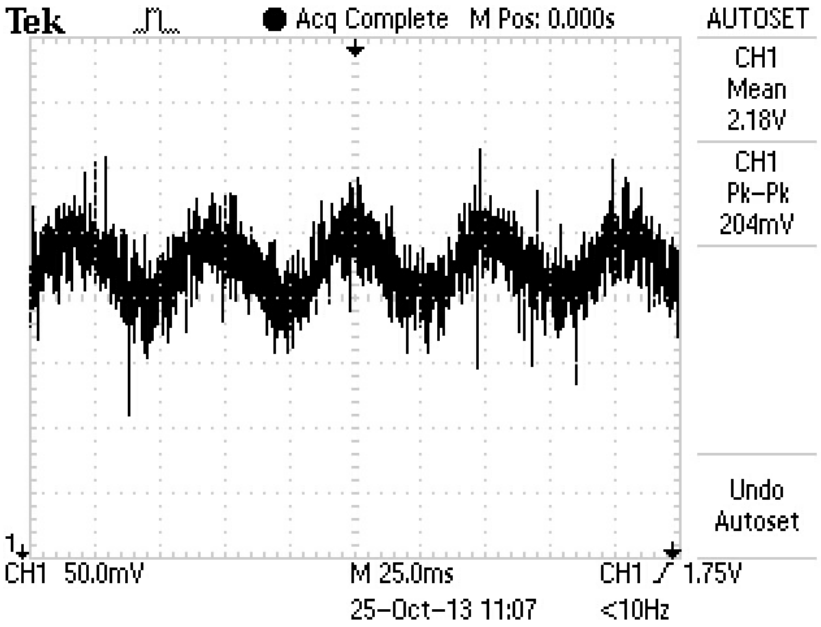

Figure A.14: Captured oscilloscope screen represent pressure drop trend across OBM for programmed Re_o of 300 and f of 20 Hz. Here x-axis represent time trend of 0.25 s and y-axis represent pressure drop measured in mV.

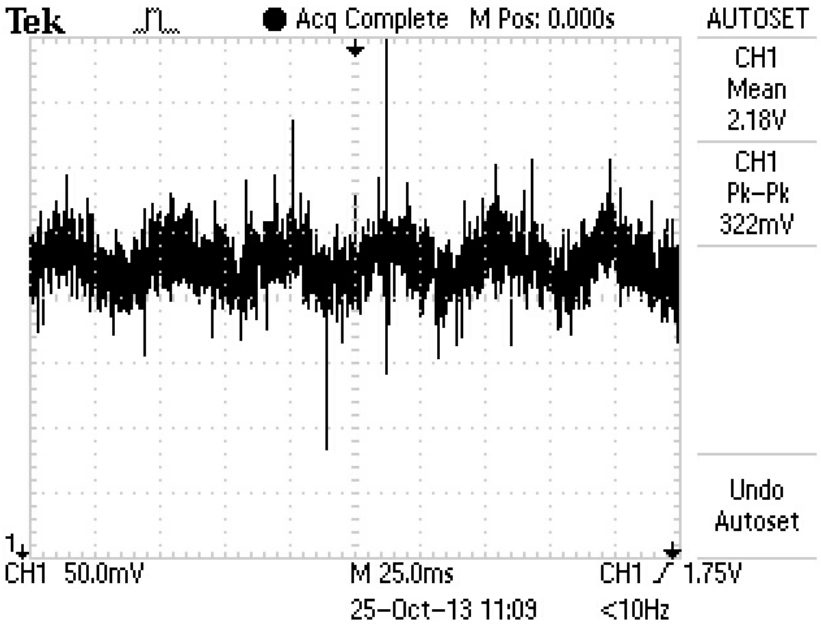

Figure A.15: Captured oscilloscope screen represent pressure drop trend across OBM for programmed Re_o of 300 and f of 25 Hz. Here x-axis represent time trend of 0.25 s and y-axis represent pressure drop measured in mV.

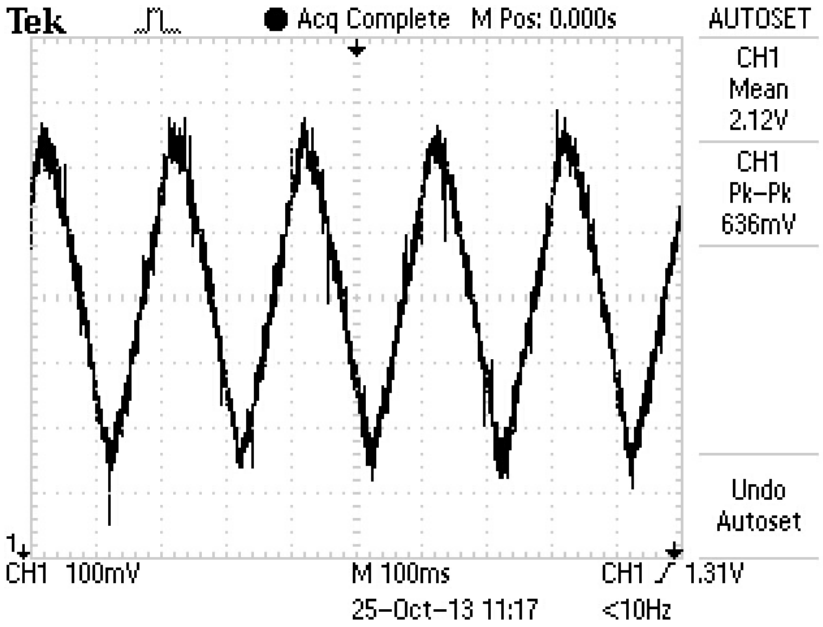

Figure A.16: Captured oscilloscope screen represent pressure drop trend across OBM for programmed Re_o of 385 and f of 5 Hz. Here x-axis represent time trend of 1 s and y-axis represent pressure drop measured in mV.

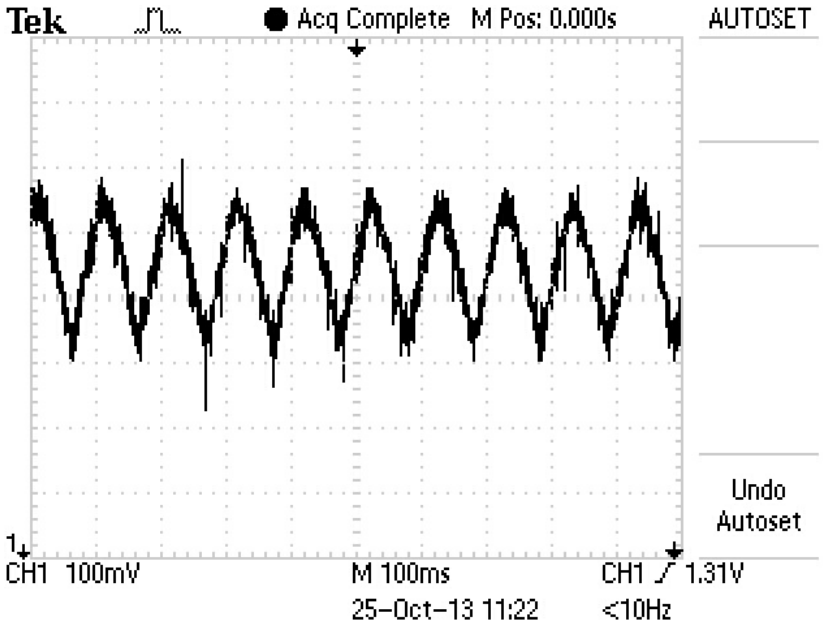

Figure A.17: Captured oscilloscope screen represent pressure drop trend across OBM for programmed Re_o of 385 and f of 10 Hz. Here x-axis represent time trend of 1 s and y-axis represent pressure drop measured in mV.

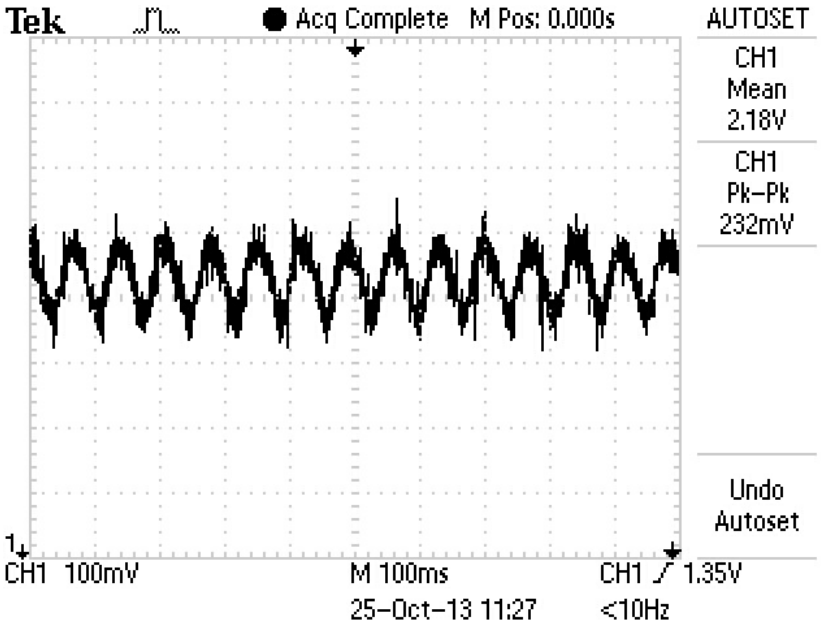

Figure A.18: Captured oscilloscope screen represent pressure drop trend across OBM for programmed Re_o of 385 and f of 15 Hz. Here x-axis represent time trend of 1 s and y-axis represent pressure drop measured in mV.

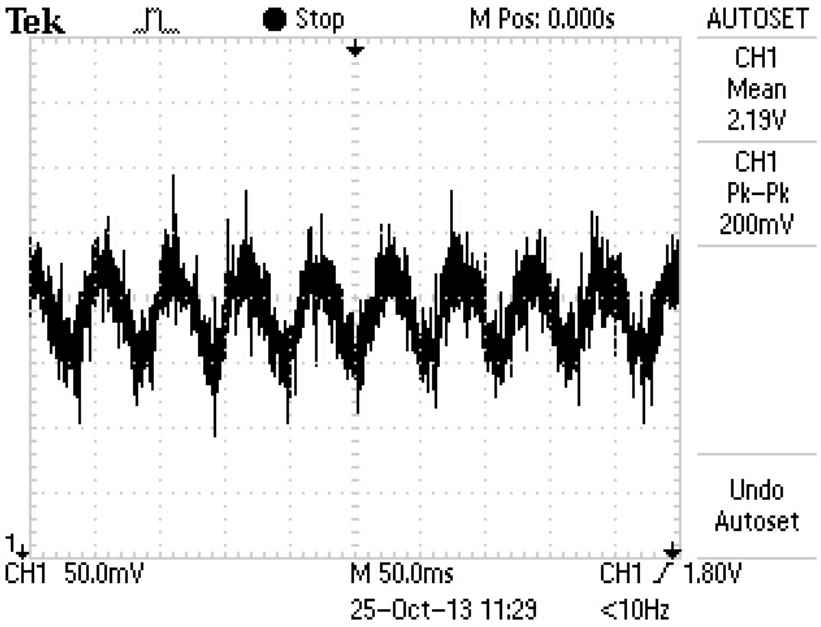

Figure A.19: Captured oscilloscope screen represent pressure drop trend across OBM for programmed Re_o of 385 and f of 20 Hz. Here x-axis represent time trend of 0.5 s and y-axis represent pressure drop measured in mV.

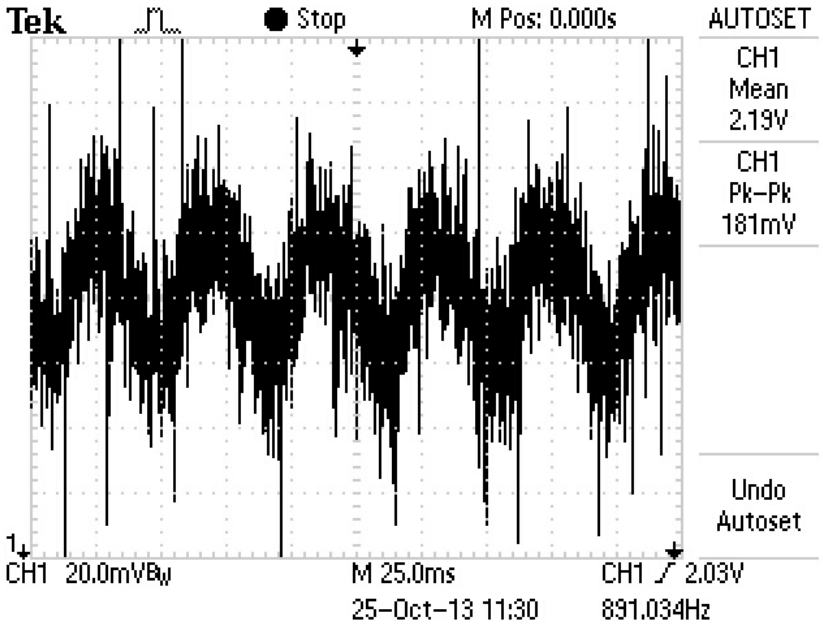

Figure A.20: Captured oscilloscope screen represent pressure drop trend across OBM for programmed Re_o of 385 and f of 25 Hz. Here x-axis represent time trend of 0.25 s and y-axis represent pressure drop measured in mV.

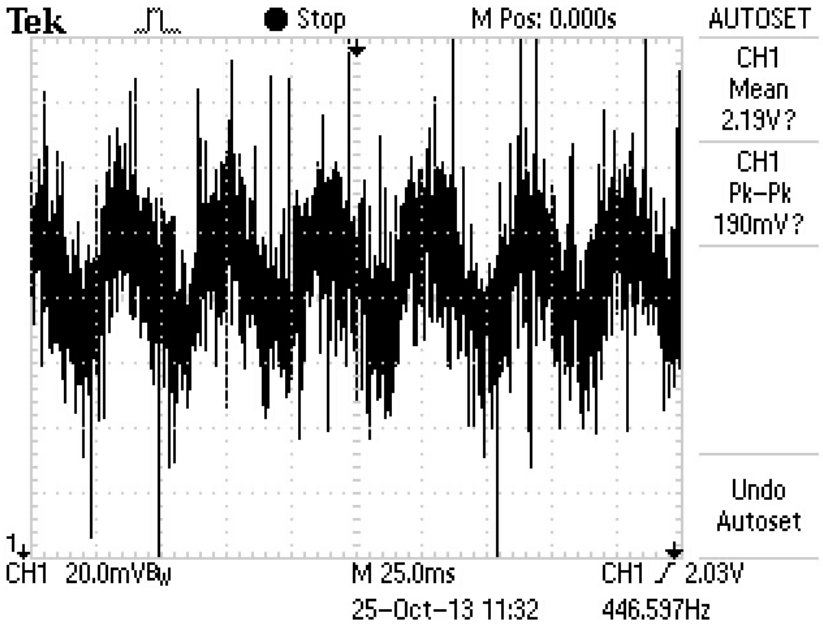

Figure A.21: Captured oscilloscope screen represent pressure drop trend across OBM for programmed Re_o of 385 and f of 30 Hz. Here x-axis represent time trend of 0.25 s and y-axis represent pressure drop measured in mV.

Appendix B: Computational fluid dynamic simulation results

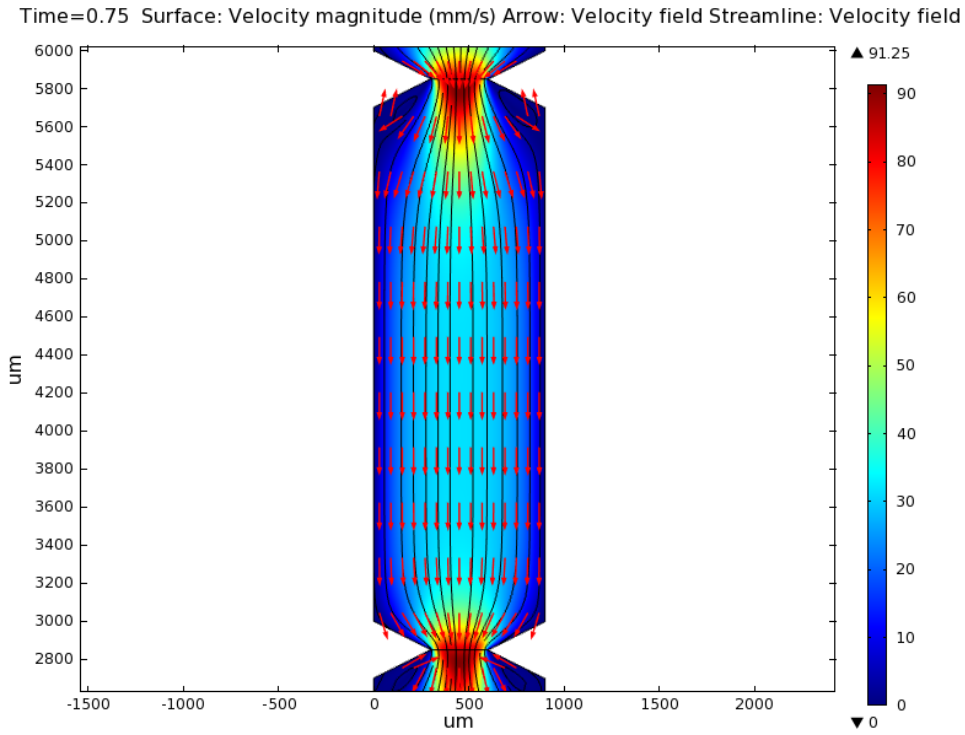

Figure B.1: Simulated vortices formation after a baffled area generated by sinusoidal oscillating flow at Re_o of 15 and f of 1 Hz.

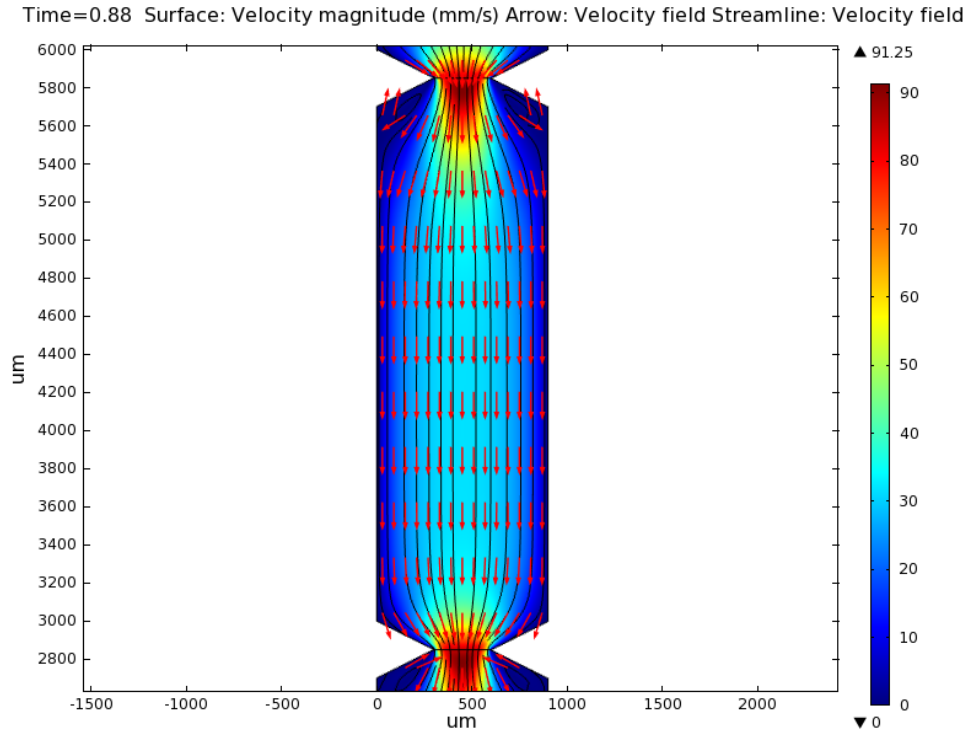

Figure B.2: Simulated vortices formation after a baffled area generated by sinusoidal oscillating flow at Re_o of 15 and f of 2 Hz.

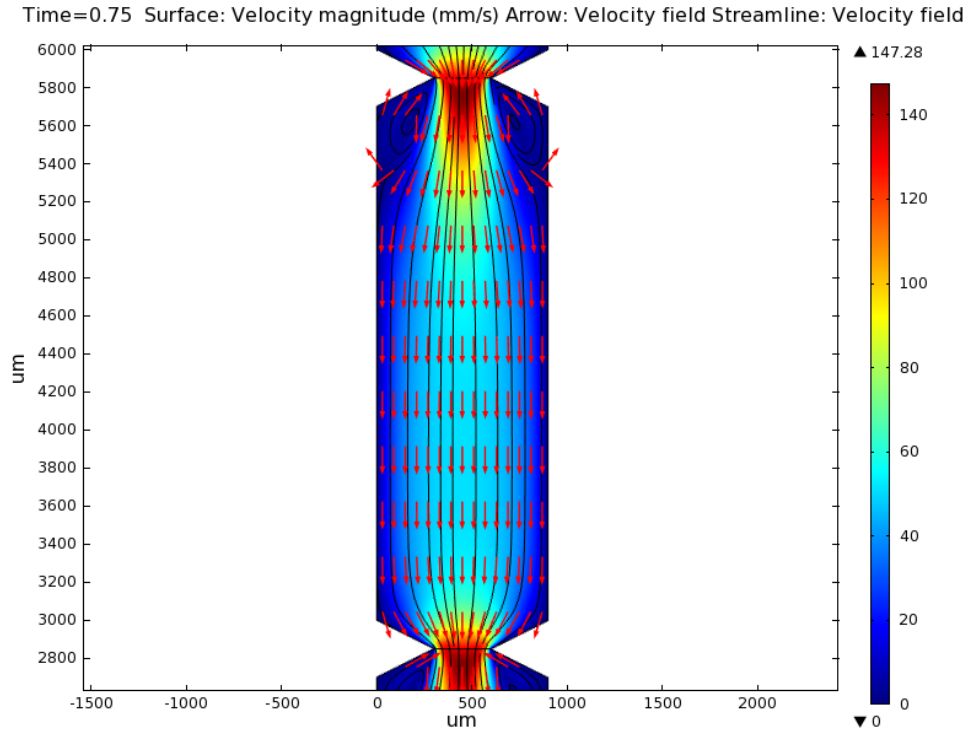

Figure B.3: Simulated vortices formation after a baffled area generated by sinusoidal oscillating flow at Re_o of 24 and f of 1 Hz.

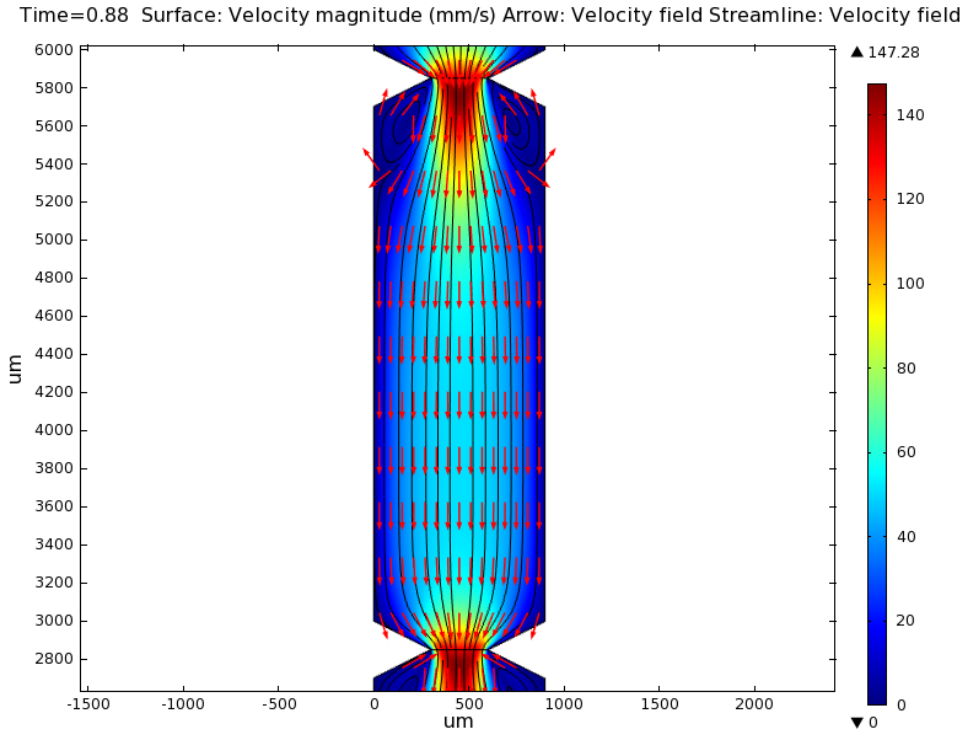

Figure B.4: Simulated vortices formation after a baffled area generated by sinusoidal oscillating flow at Re_o of 24 and f of 2 Hz.

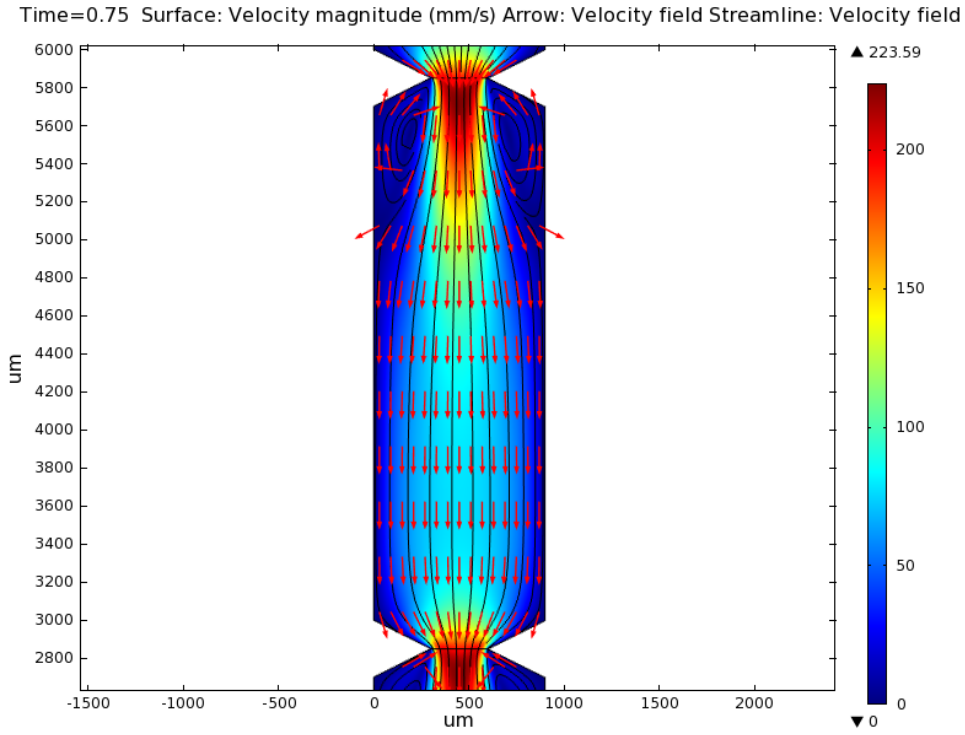

Figure B.5: Simulated vortices formation after a baffled area generated by sinusoidal oscillating flow at Re_o of 36 and f of 1 Hz.

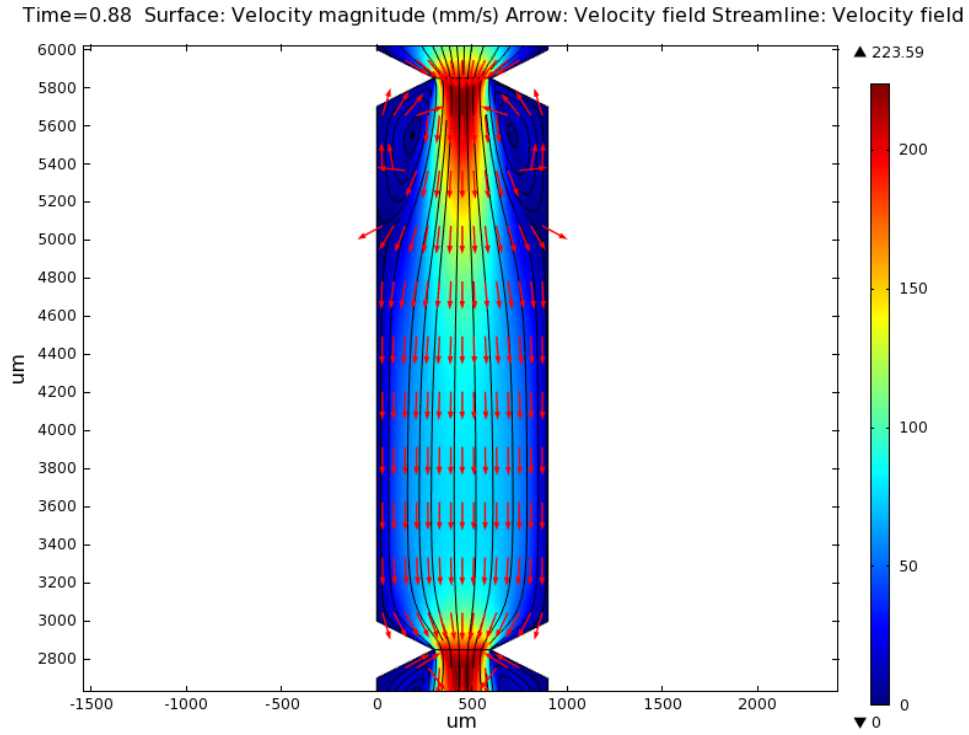

Figure B.6: Simulated vortices formation after a baffled area generated by sinusoidal oscillating flow at Re_o of 36 and f of 2 Hz.

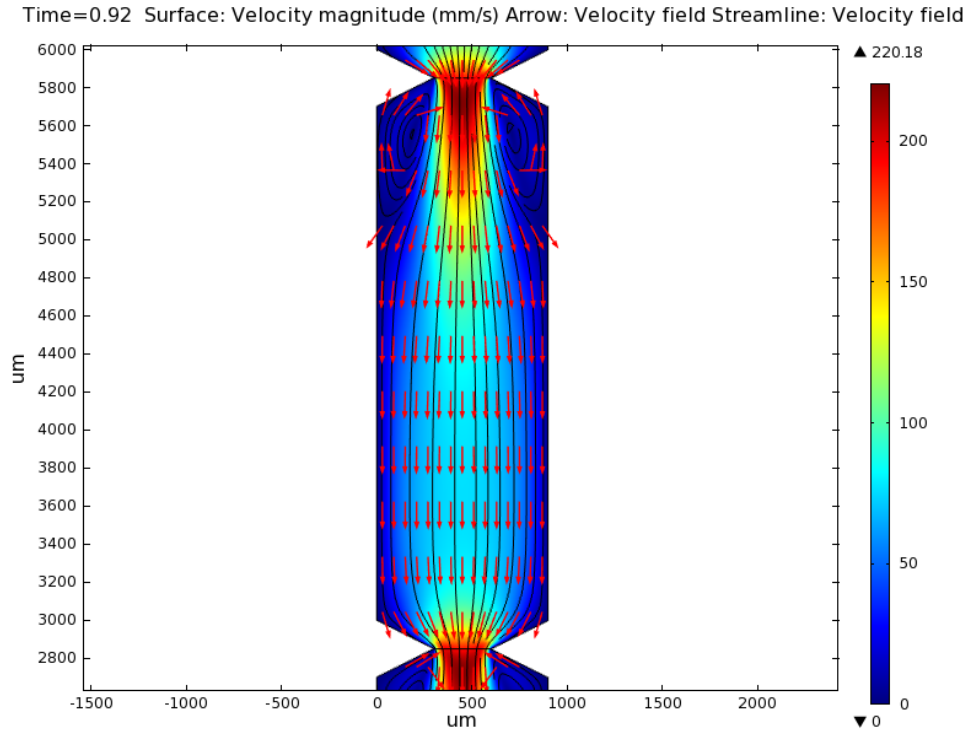

Figure B.7: Simulated vortices formation after a baffled area generated by sinusoidal oscillating flow at Re_o of 36 and f of 2 Hz.

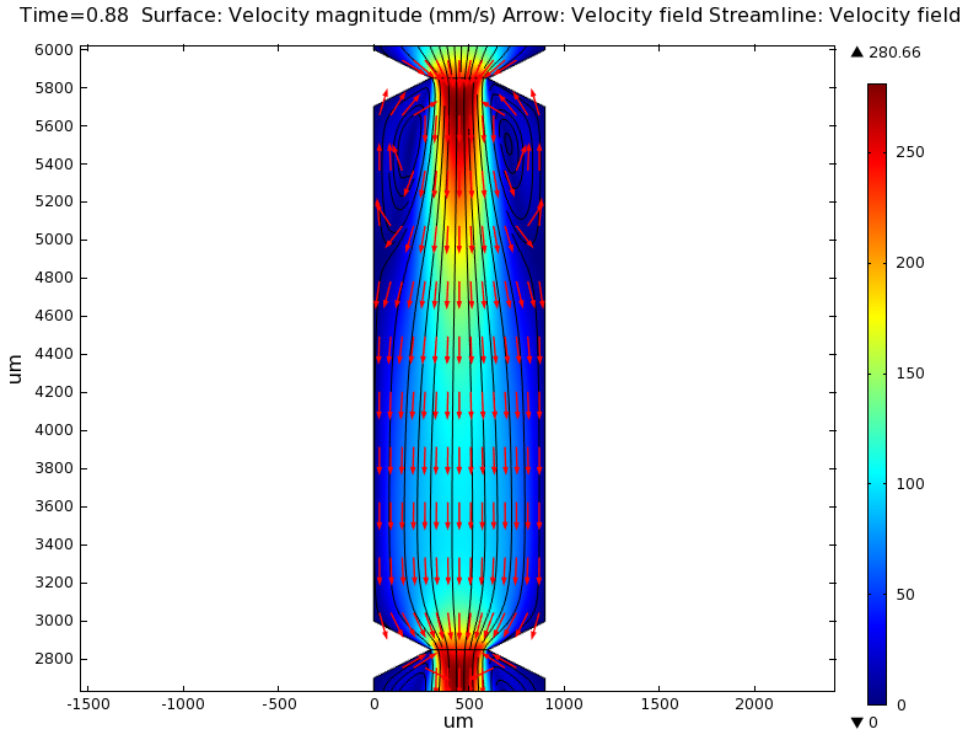

Figure B.8: Simulated vortices formation after a baffled area generated by sinusoidal oscillating flow at Re_o of 46 and f of 2 Hz.

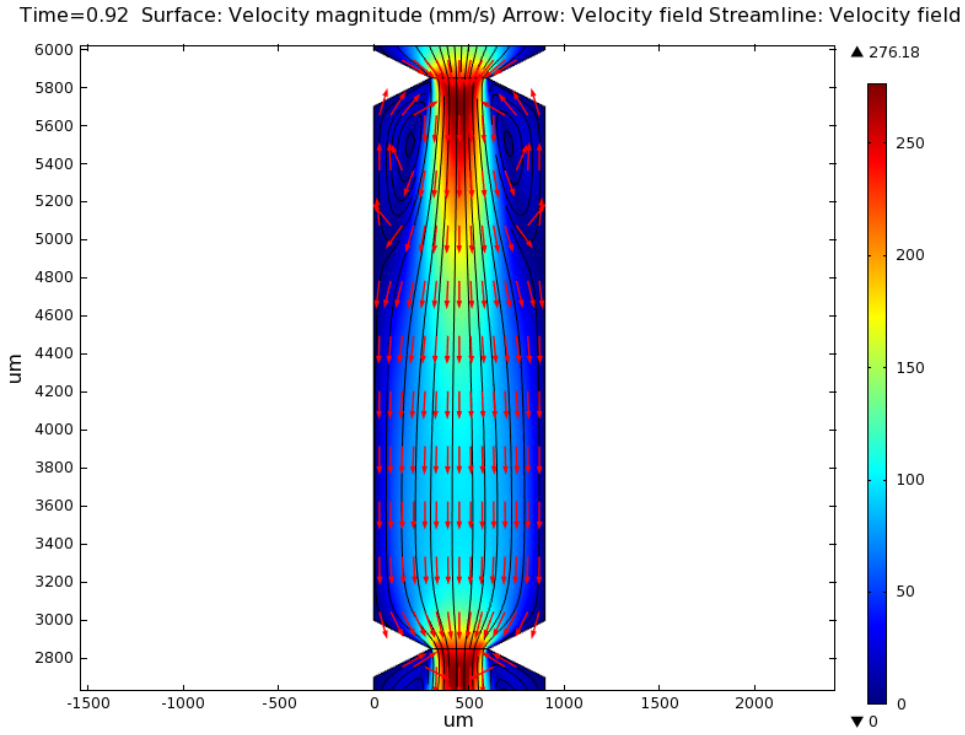

Figure B.9: Simulated vortices formation after a baffled area generated by sinusoidal oscillating flow at Re_o of 46 and f of 3 Hz.

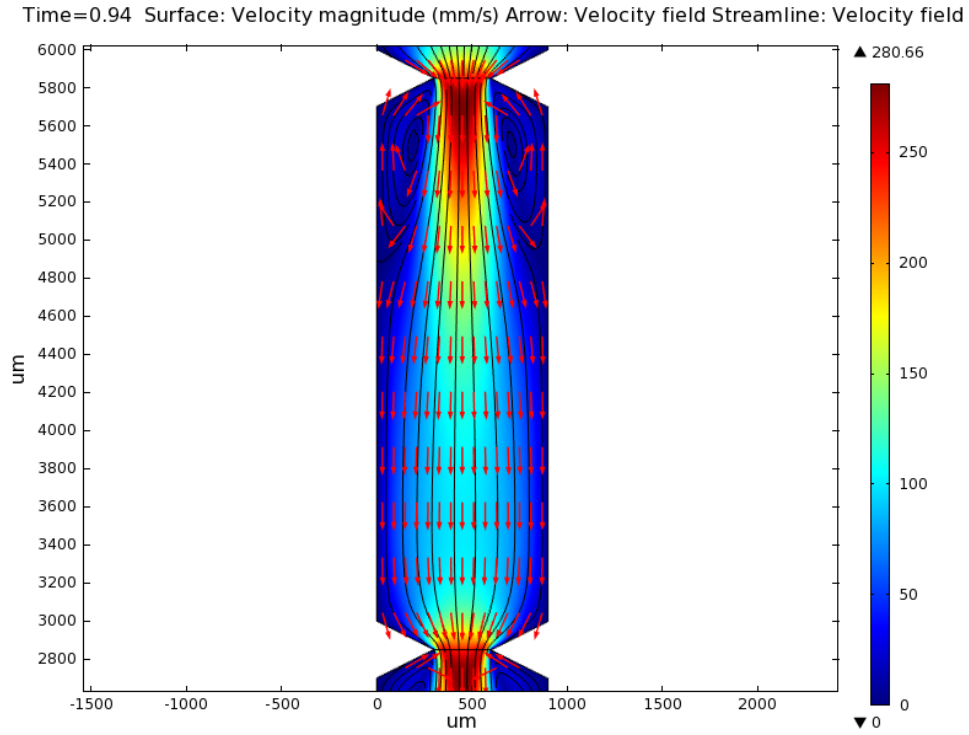

Figure B.10: Simulated vortices formation after a baffled area generated by sinusoidal oscillating flow at Re_o of 46 and f of 4 Hz.

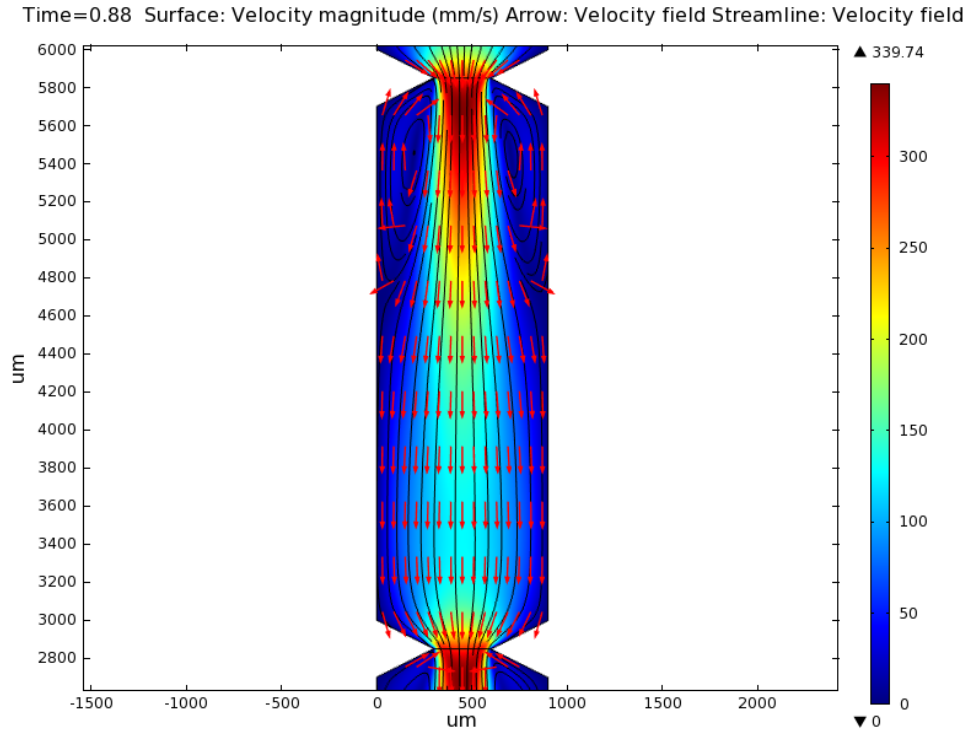

Figure B.11: Simulated vortices formation after a baffled area generated by sinusoidal oscillating flow at Re_o of 55 and f of 2 Hz.

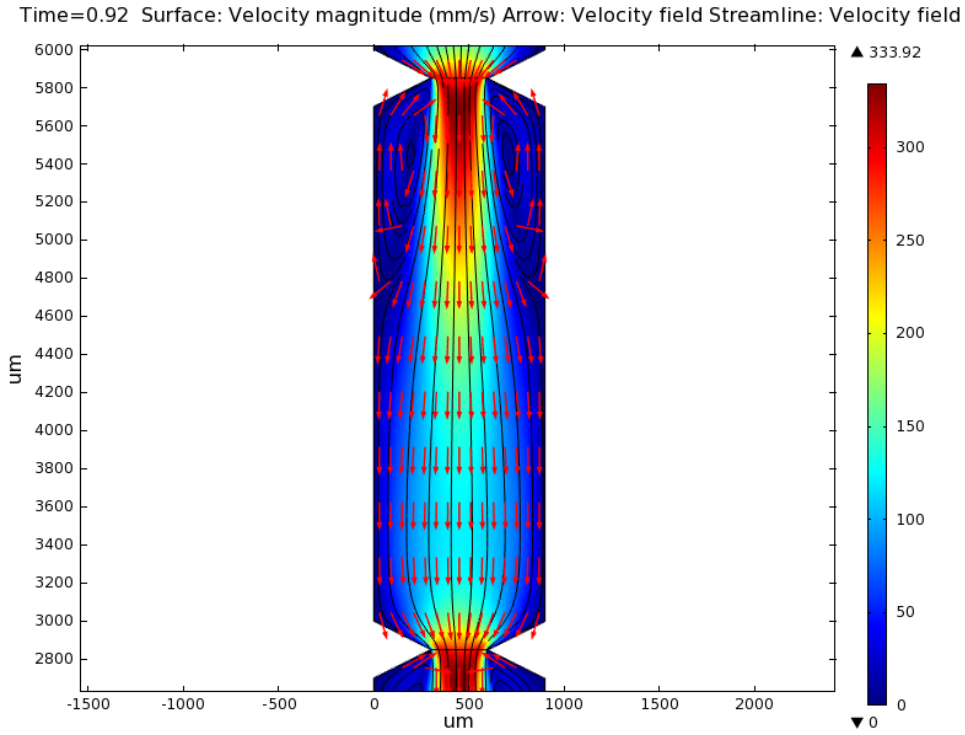

Figure B.12: Simulated vortices formation after a baffled area generated by sinusoidal oscillating flow at Re_o of 55 and f of 3 Hz.

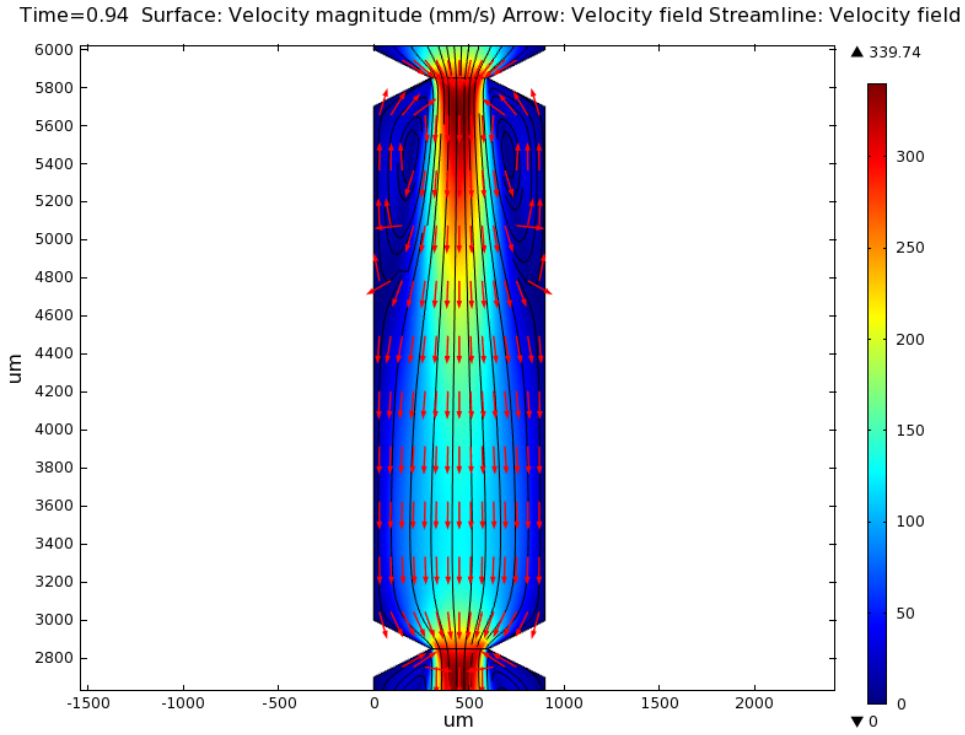

Figure B.13: Simulated vortices formation after a baffled area generated by sinusoidal oscillating flow at Re_o of 55 and f of 4 Hz.

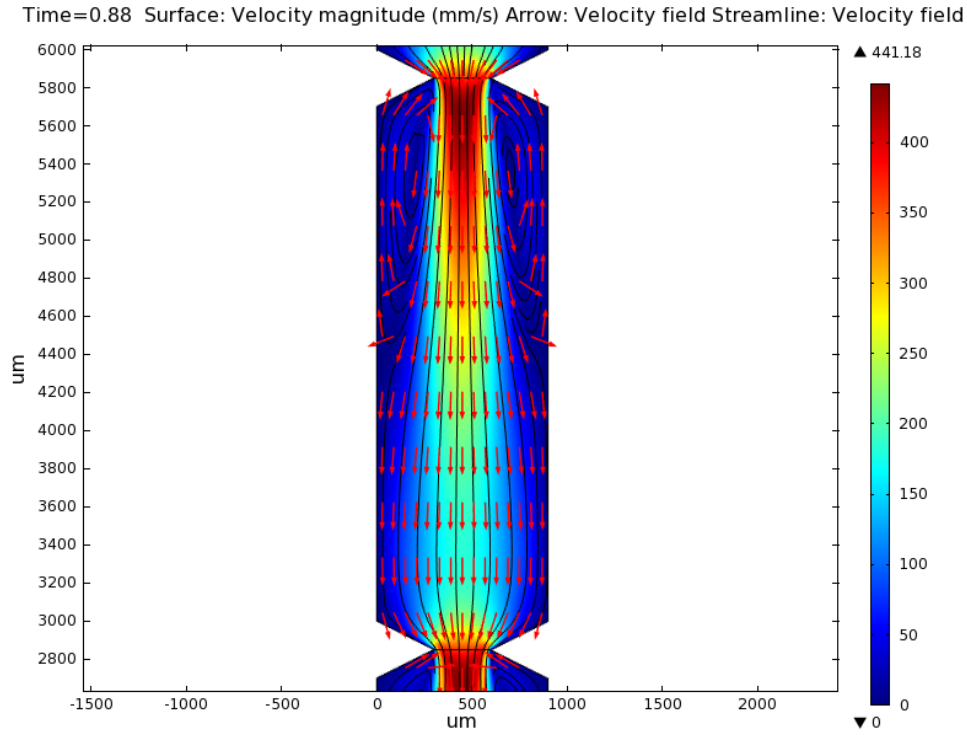

Figure B.14: Simulated vortices formation after a baffled area generated by sinusoidal oscillating flow at Re_o of 71 and f of 2 Hz.

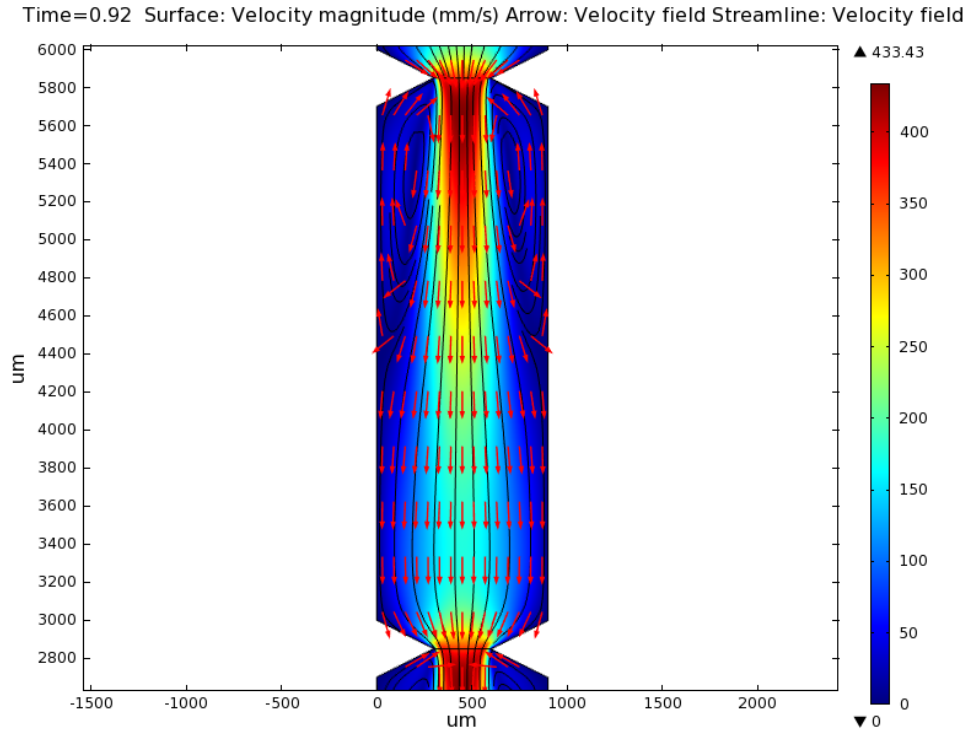

Figure B.15: Simulated vortices formation after a baffled area generated by sinusoidal oscillating flow at Re_o of 71 and f of 3 Hz.

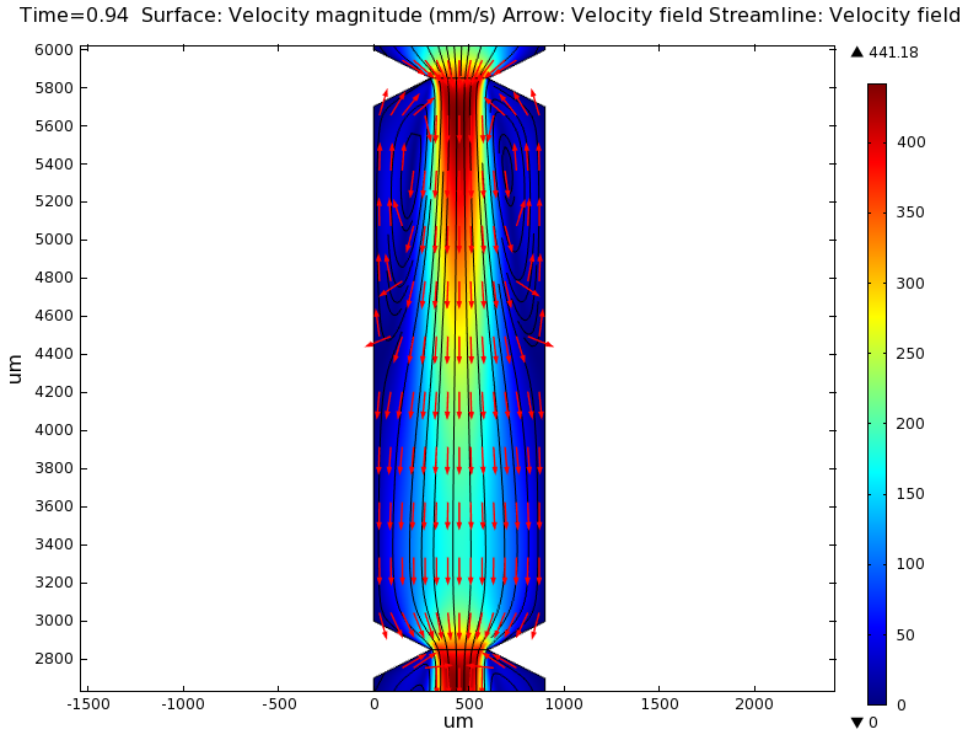

Figure B.16: Simulated vortices formation after a baffled area generated by sinusoidal oscillating flow at Re_o of 71 and f of 4 Hz.

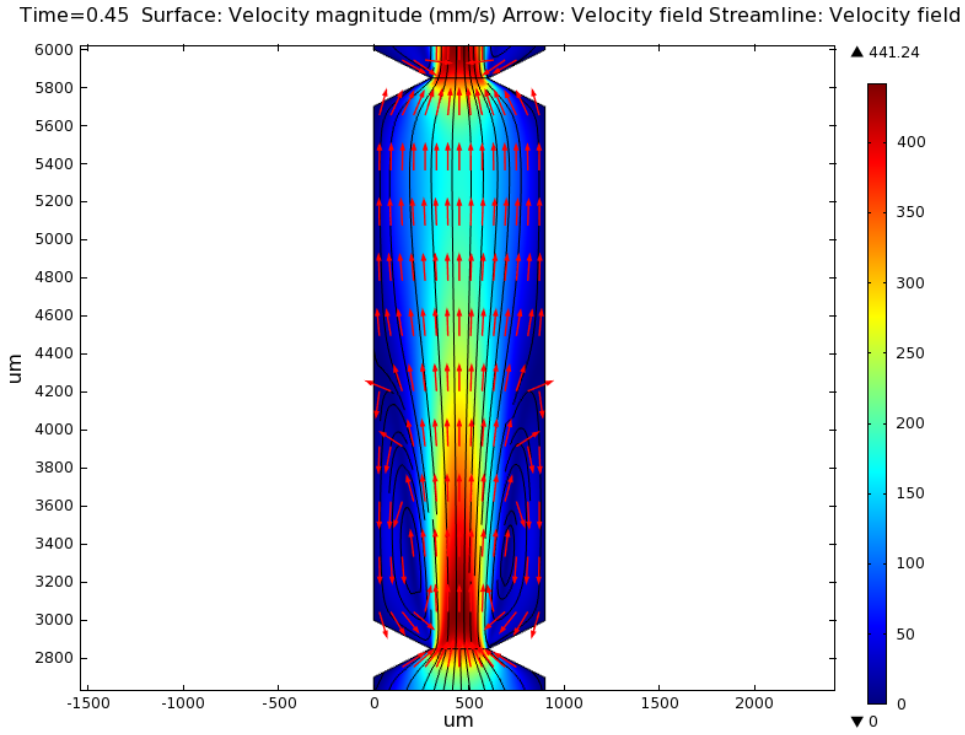

Figure B.17: Simulated vortices formation after a baffled area generated by sinusoidal oscillating flow at Re_o of 71 and f of 5 Hz.

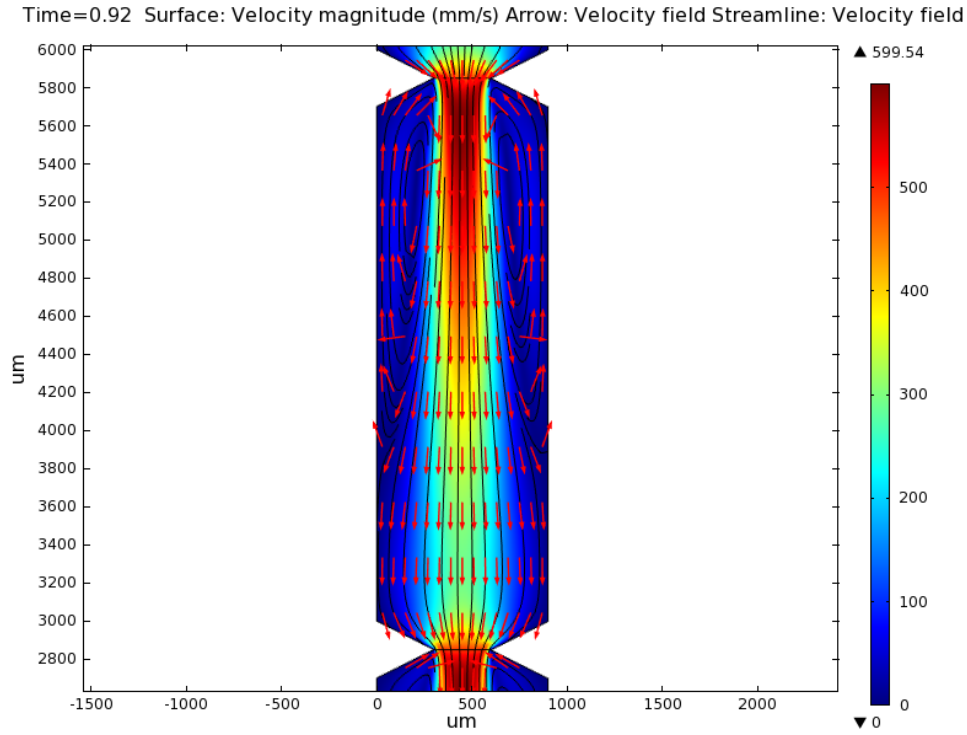

Figure B.18: Simulated vortices formation after a baffled area generated by sinusoidal oscillating flow at Re_o of 97 and f of 3 Hz.

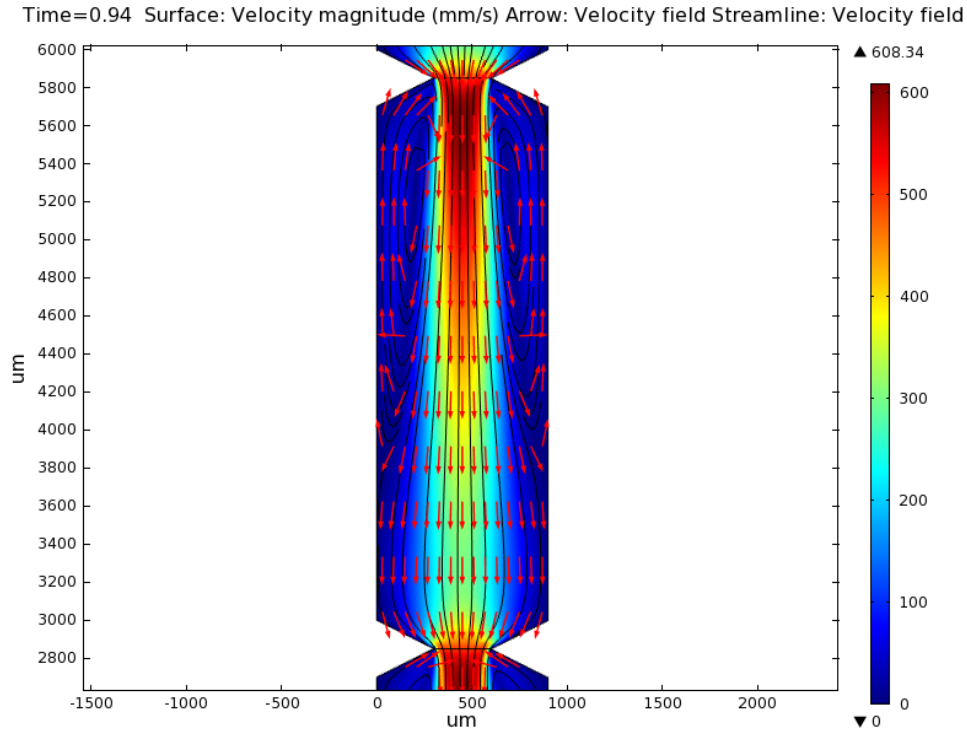

Figure B.19: Simulated vortices formation after a baffled area generated by sinusoidal oscillating flow at Re_o of 97 and f of 4 Hz.

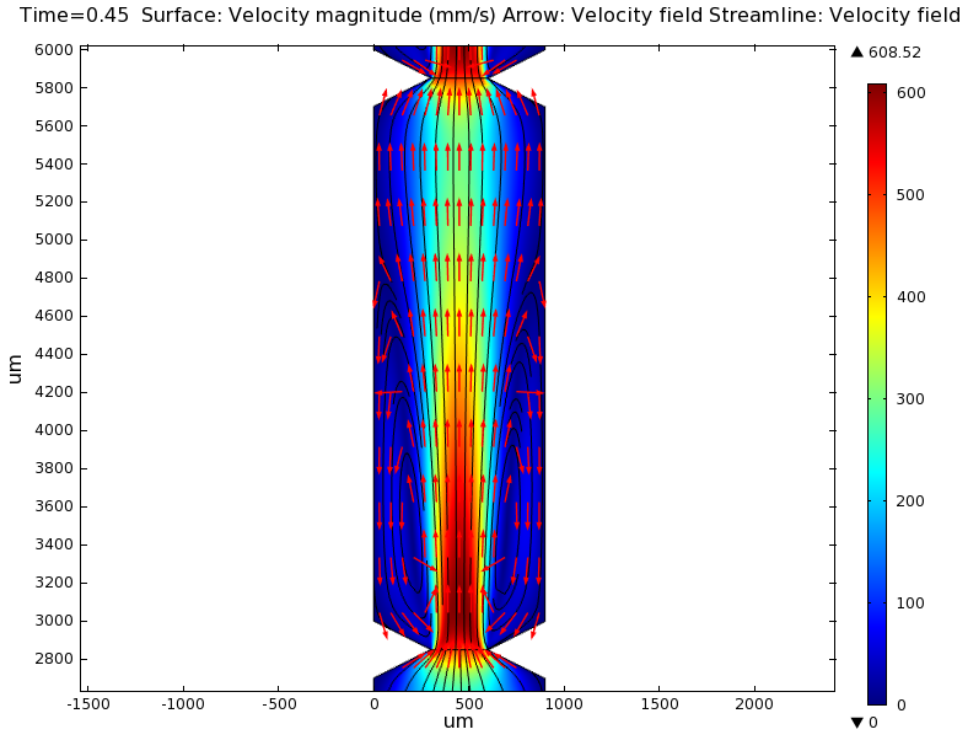

Figure B.20: Simulated vortices formation after a baffled area generated by sinusoidal oscillating flow at Re_o of 97 and f of 5 Hz.

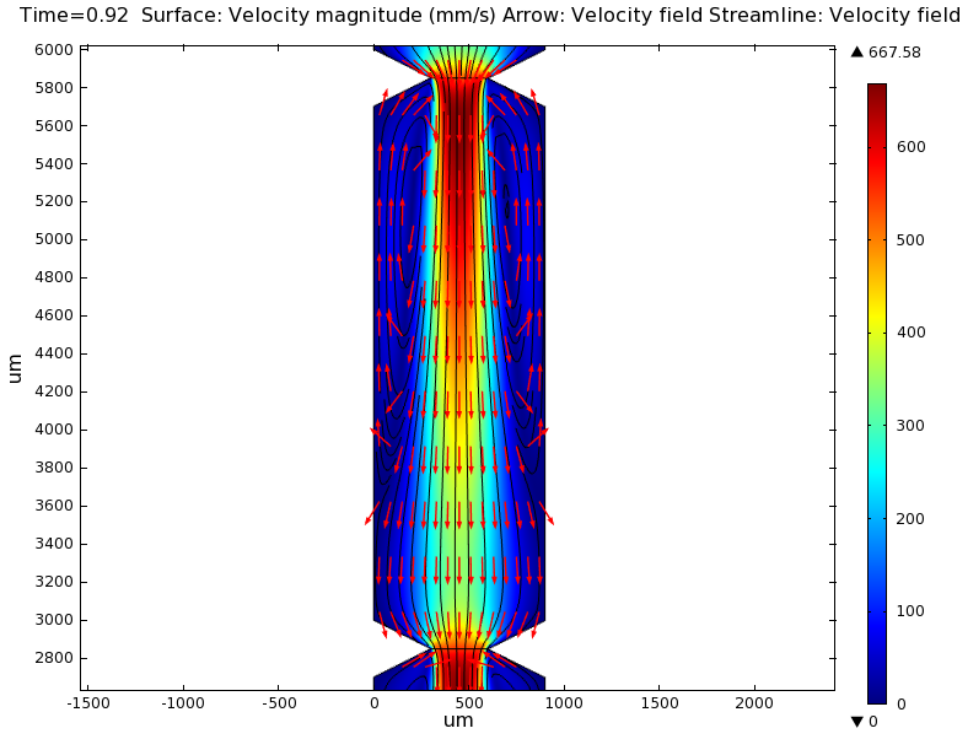

Figure B.21: Simulated vortices formation after a baffled area generated by sinusoidal oscillating flow at Re_o of 108 and f of 3 Hz.

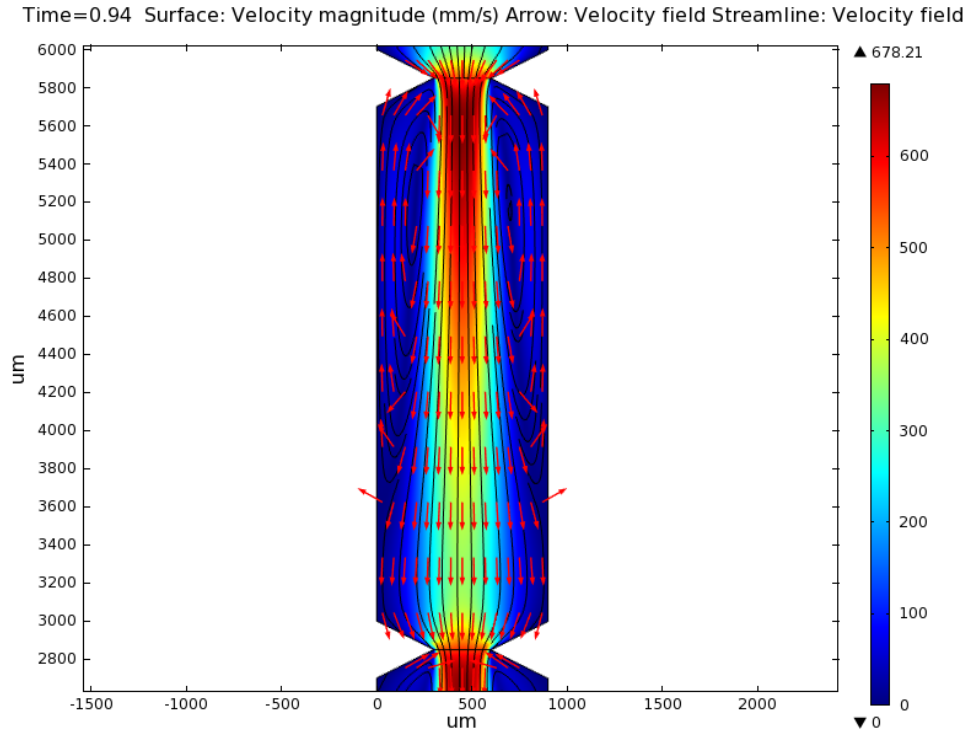

Figure B.22: Simulated vortices formation after a baffled area generated by sinusoidal oscillating flow at Re_o of 108 and f of 4 Hz.

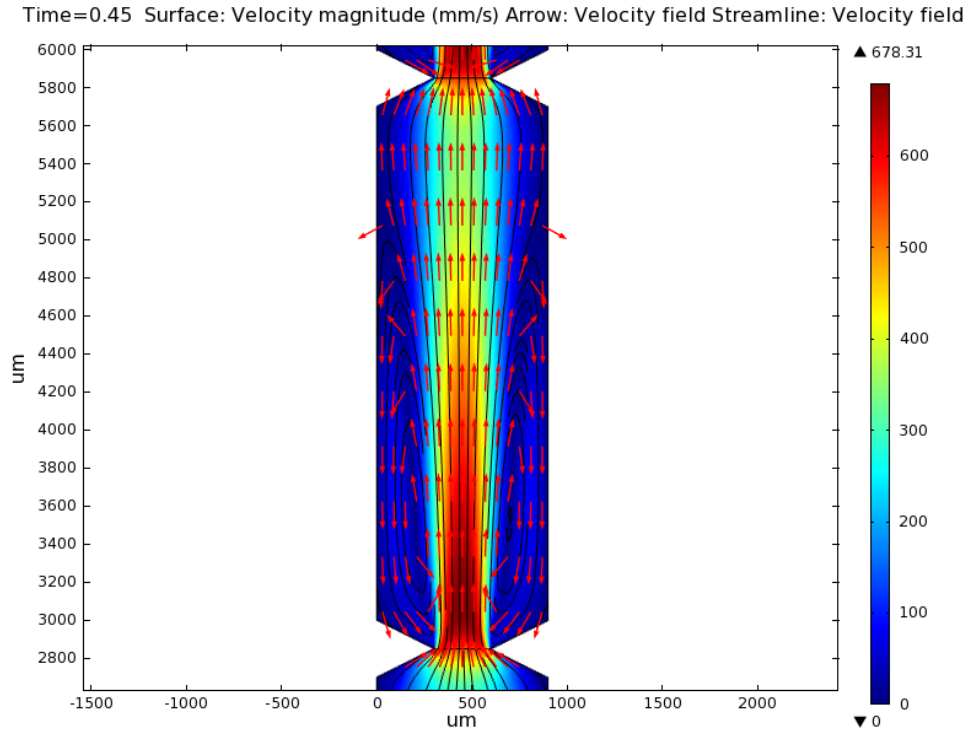

Figure B.23: Simulated vortices formation after a baffled area generated by sinusoidal oscillating flow at Re_o of 108 and f of 5 Hz.

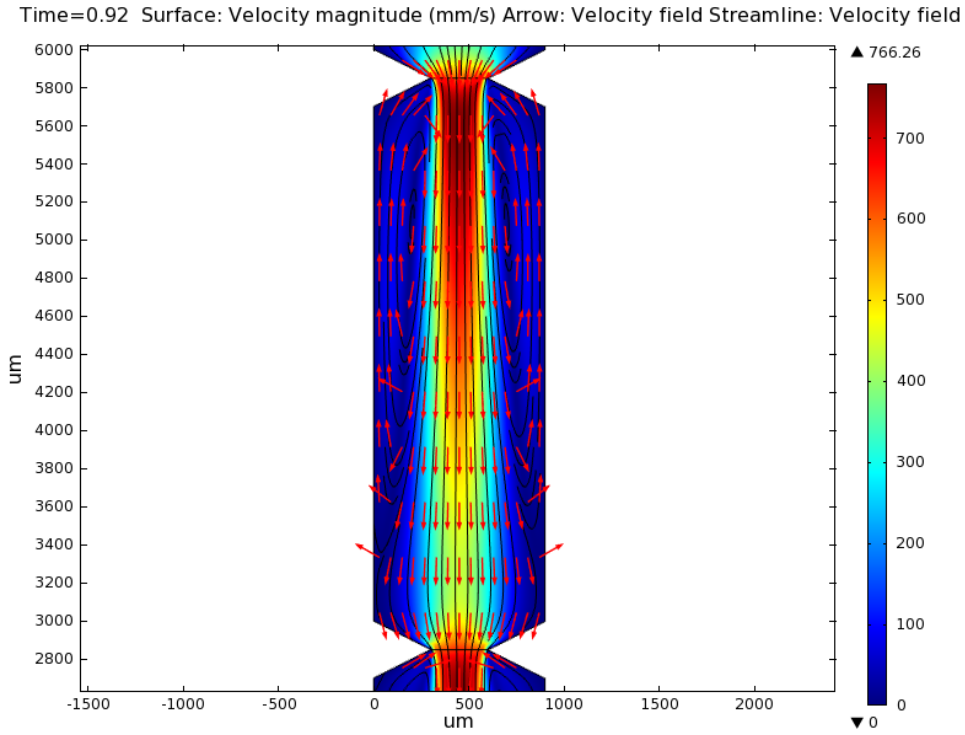

Figure B.24: Simulated vortices formation after a baffled area generated by sinusoidal oscillating flow at Re_o of 124 and f of 3 Hz.

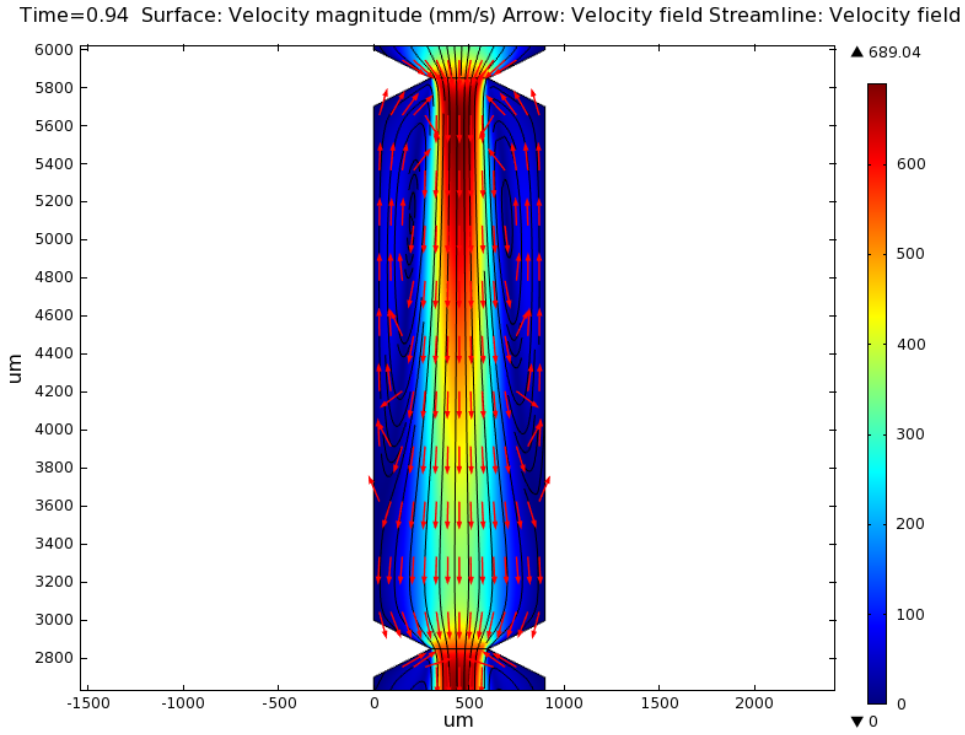

Figure B.25: Simulated vortices formation after a baffled area generated by sinusoidal oscillating flow at Re_o of 124 and f of 4 Hz.

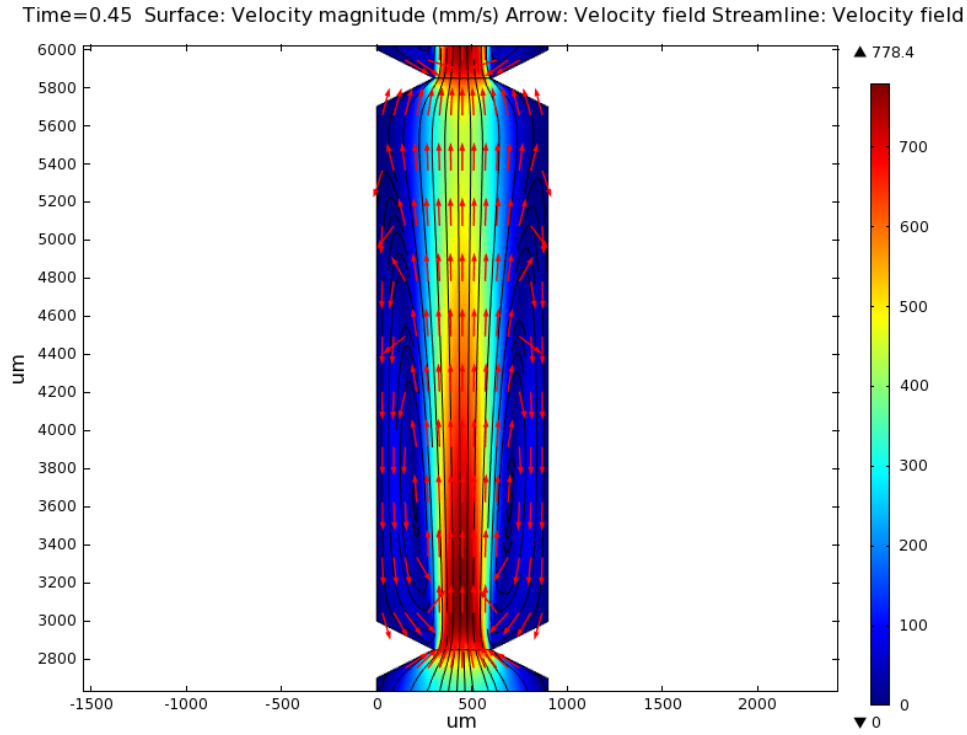

Figure B.26: Simulated vortices formation after a baffled area generated by sinusoidal oscillating flow at Re_o of 124 and f of 5 Hz.

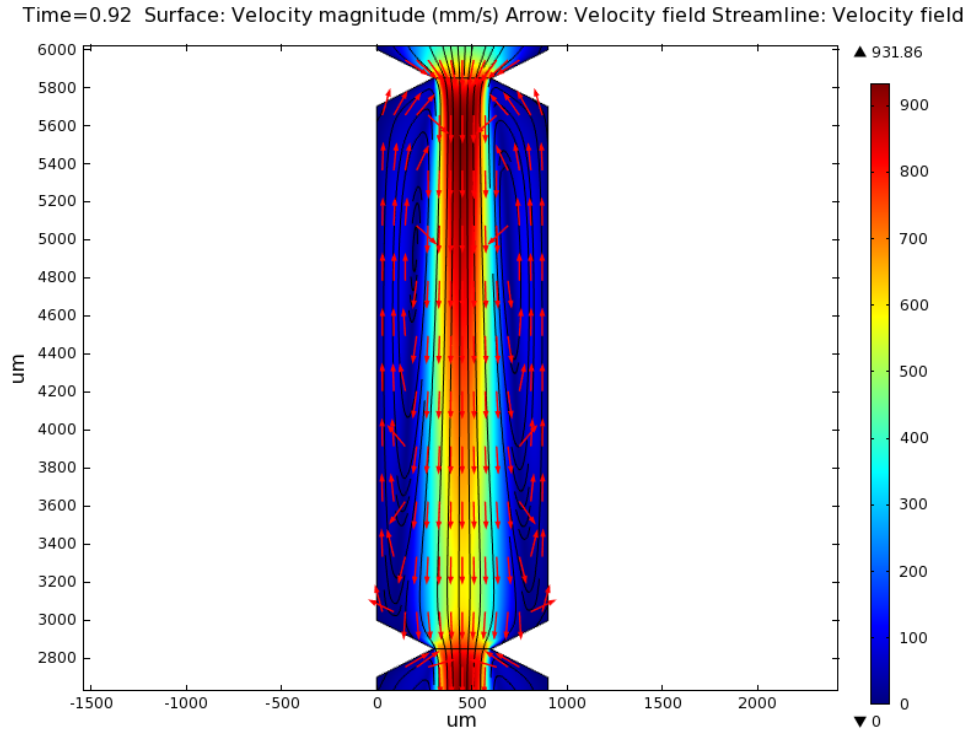

Figure B.27: Simulated vortices formation after a baffled area generated by sinusoidal oscillating flow at Re_o of 150 and f of 3 Hz.

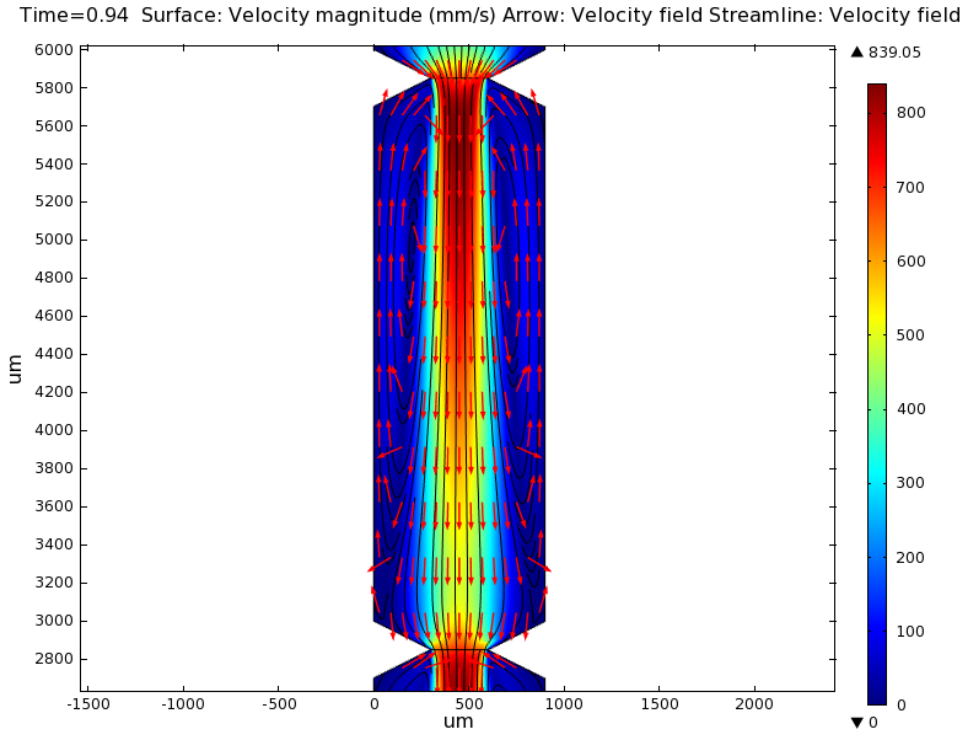

Figure B.28: Simulated vortices formation after a baffled area generated by sinusoidal oscillating flow at Re_o of 150 and f of 4 Hz.

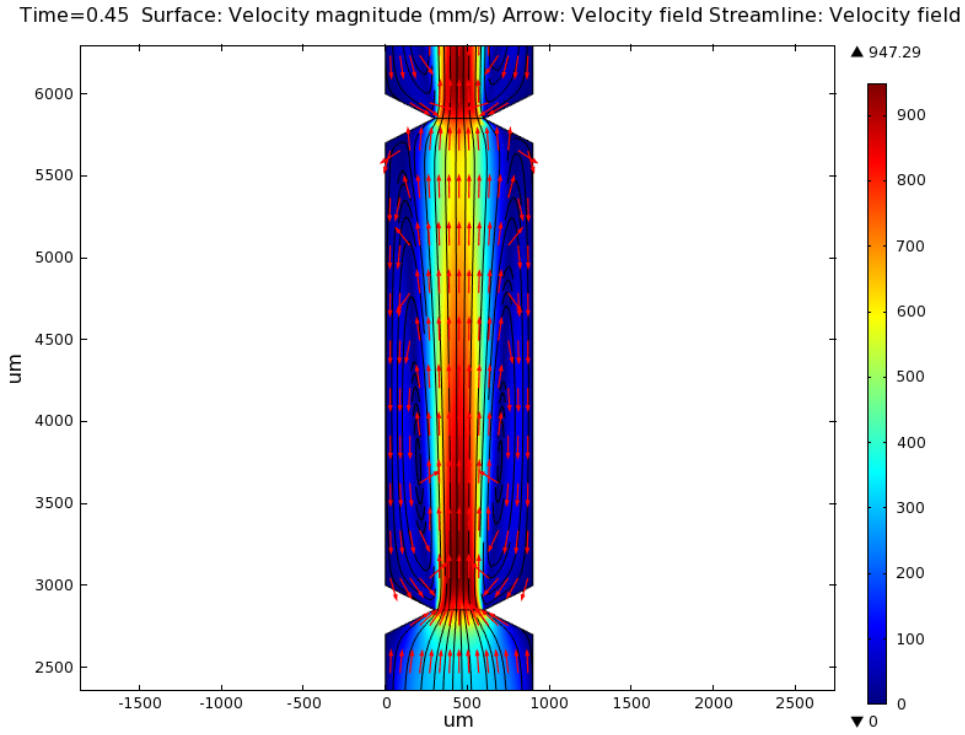

Figure B.29: Simulated vortices formation after a baffled area generated by sinusoidal oscillating flow at Re_o of 29 and f of 5 Hz.

Appendix C: Micro flow visualisations results

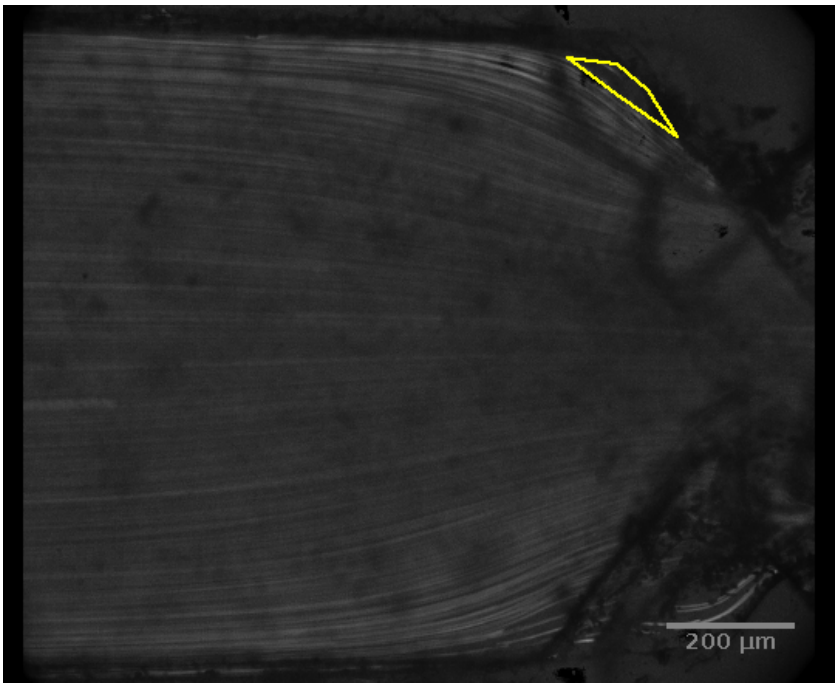

Figure C.1: Standard deviation projection for image stacks representing half oscillating cycle. Here, $Re_o = 15.38$, $f = 1$ Hz.

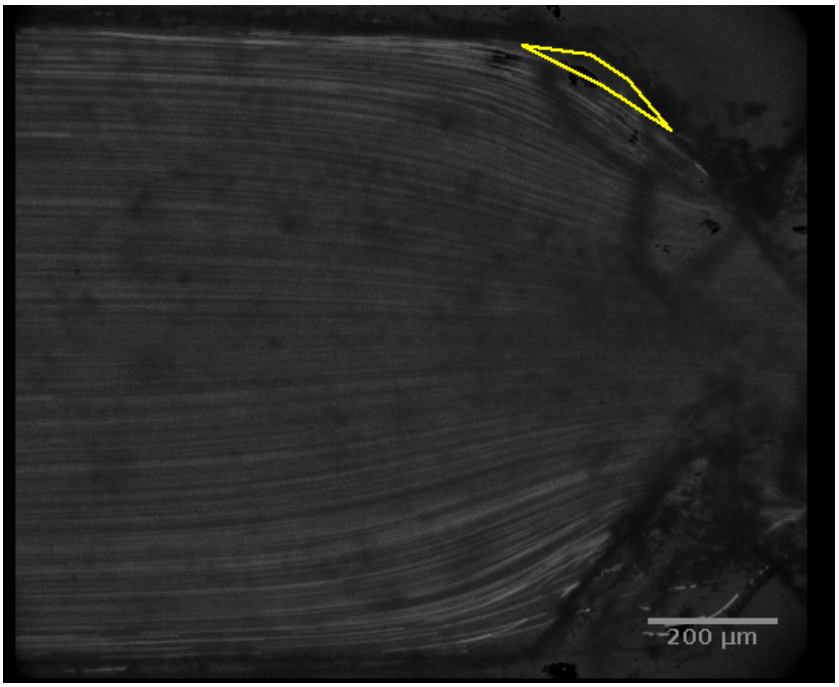

Figure C.2: Standard deviation projection for image stacks representing half oscillating cycle. Here, $Re_o = 15.38$, $f = 2$ Hz.

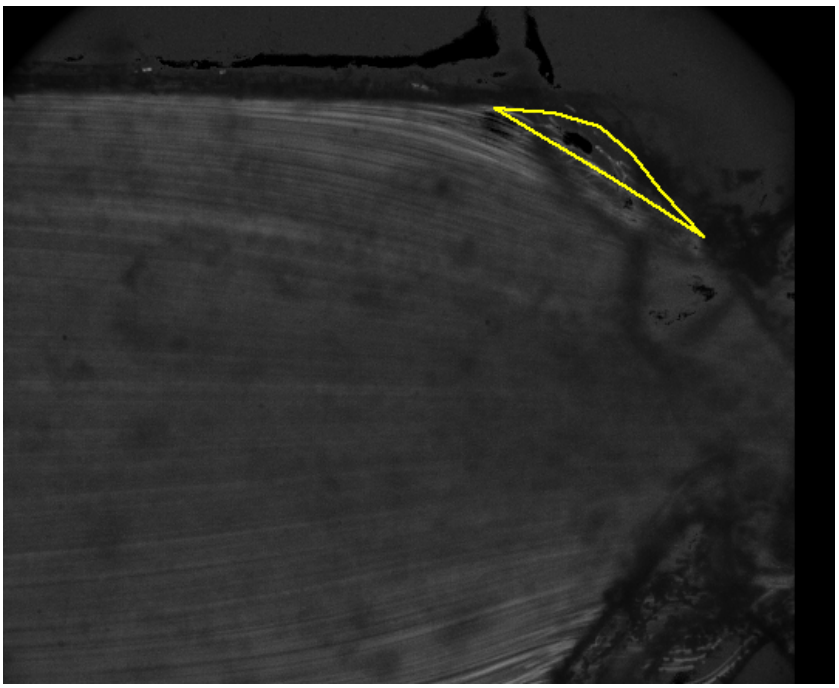

Figure C.3: Standard deviation projection for image stacks representing half oscillating cycle. Here, $Re_o = 24.65$, $f = 1$ Hz.

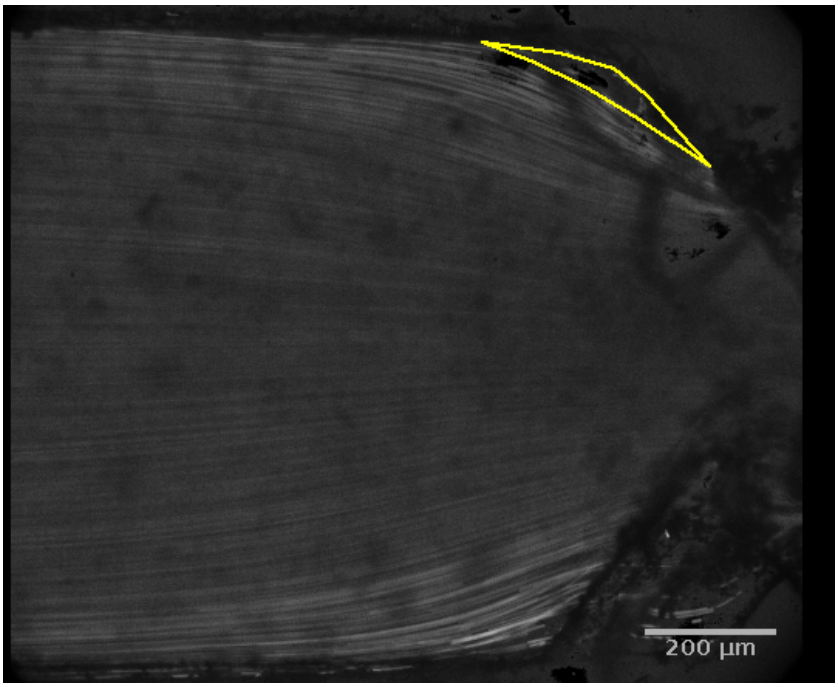

Figure C.4: Standard deviation projection for image stacks representing half oscillating cycle. Here, $Re_o = 24.65$, $f = 2$ Hz.

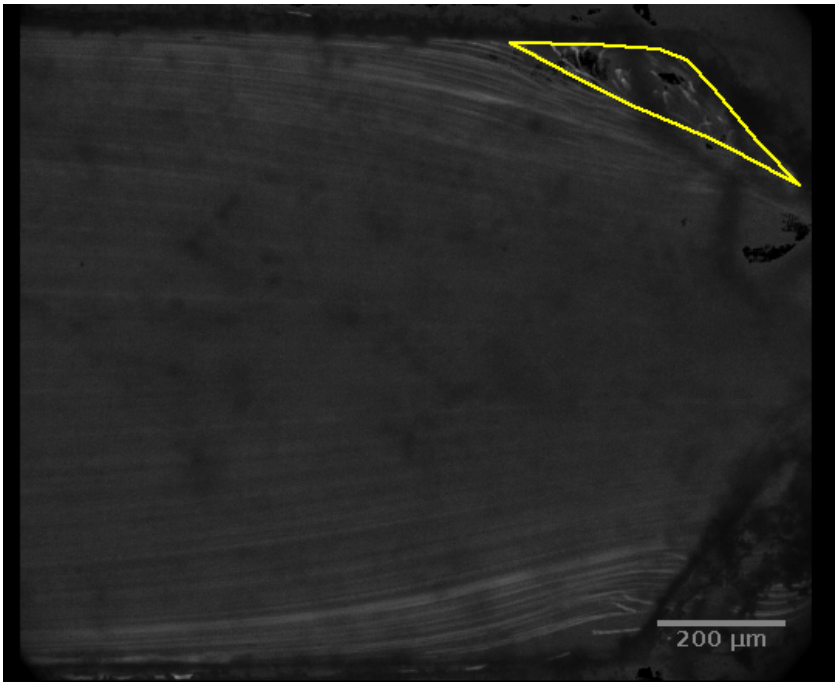

Figure C.5: Standard deviation projection for image stacks representing half oscillating cycle. Here, $Re_o = 36.98$, $f = 1$ Hz.

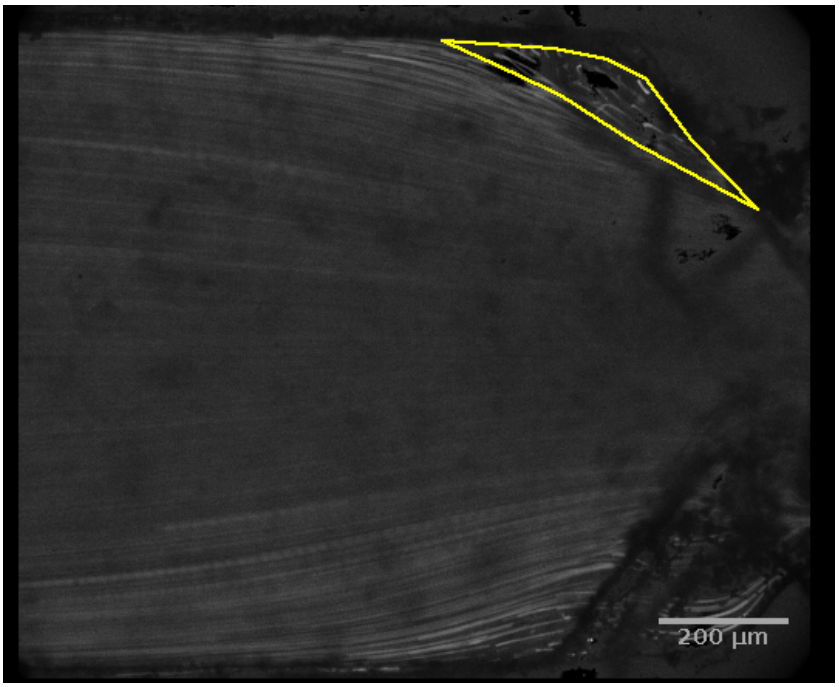

Figure C.6: Standard deviation projection for image stacks representing half oscillating cycle. Here, $Re_o = 36.98$, $f = 2$ Hz.

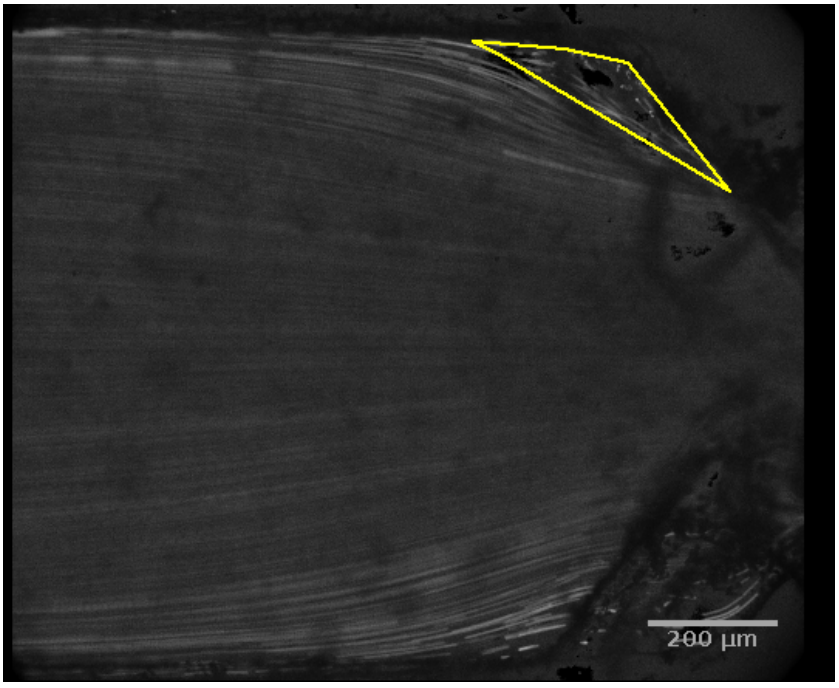

Figure C.7: Standard deviation projection for image stacks representing half oscillating cycle. Here, $Re_o = 36.98$, $f = 3$ Hz.

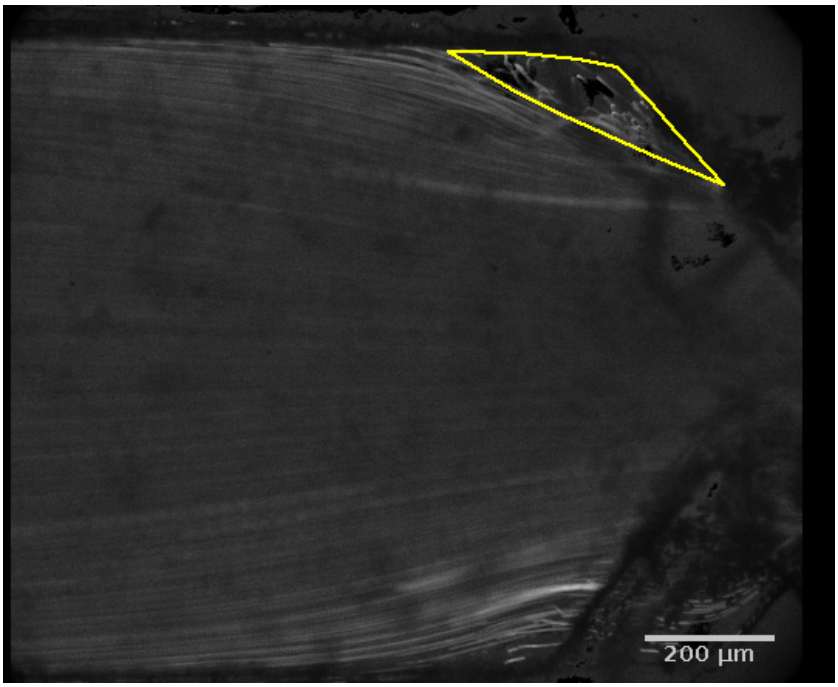

Figure C.8: Standard deviation projection for image stacks representing half oscillating cycle. Here, $Re_o = 46.06$, $f = 2$ Hz.

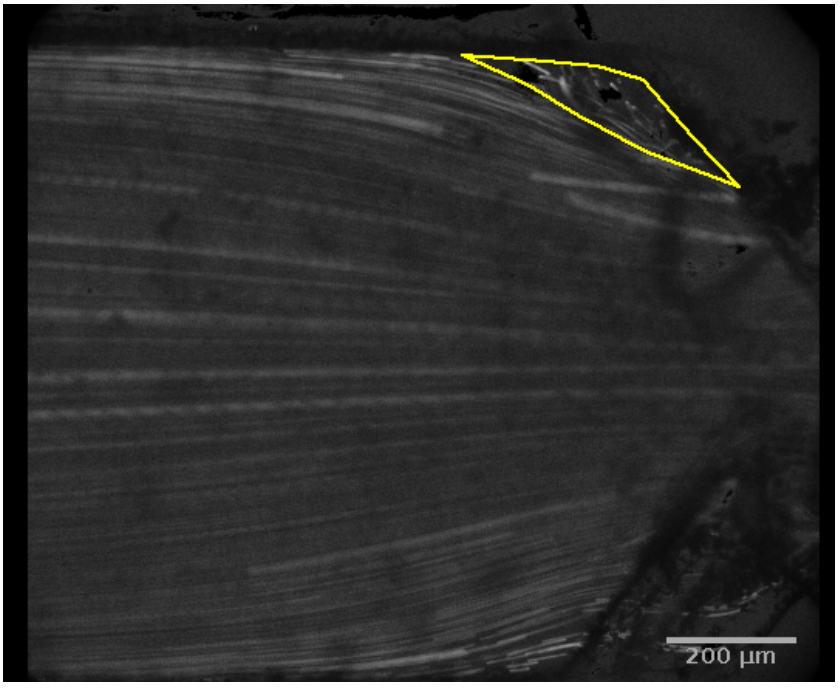

Figure C.9: Standard deviation projection for image stacks representing half oscillating cycle. Here, $Re_o = 46.06$, $f = 3$ Hz.

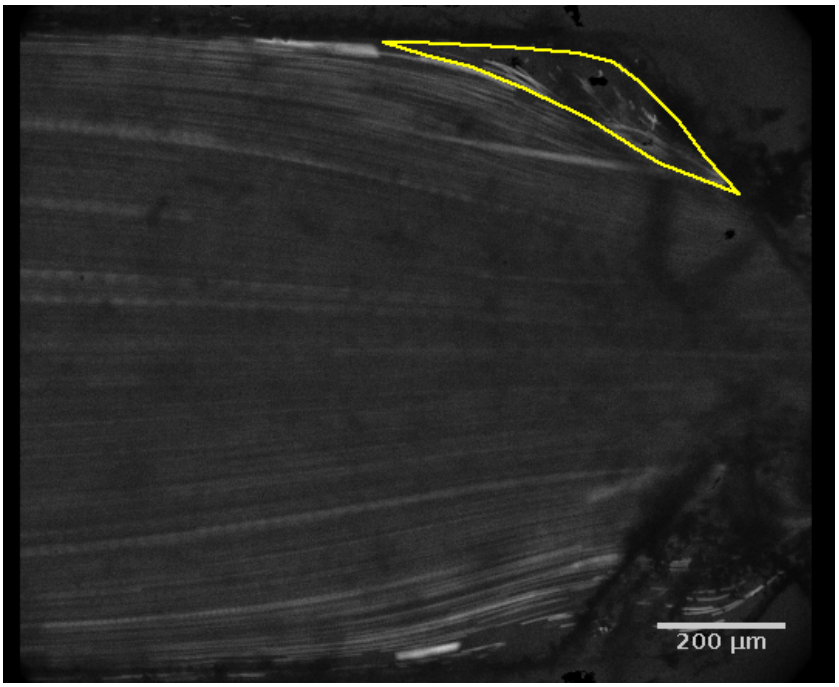

Figure C.10: Standard deviation projection for image stacks representing half oscillating cycle. Here, $Re_o = 46.06$, $f = 4$ Hz.

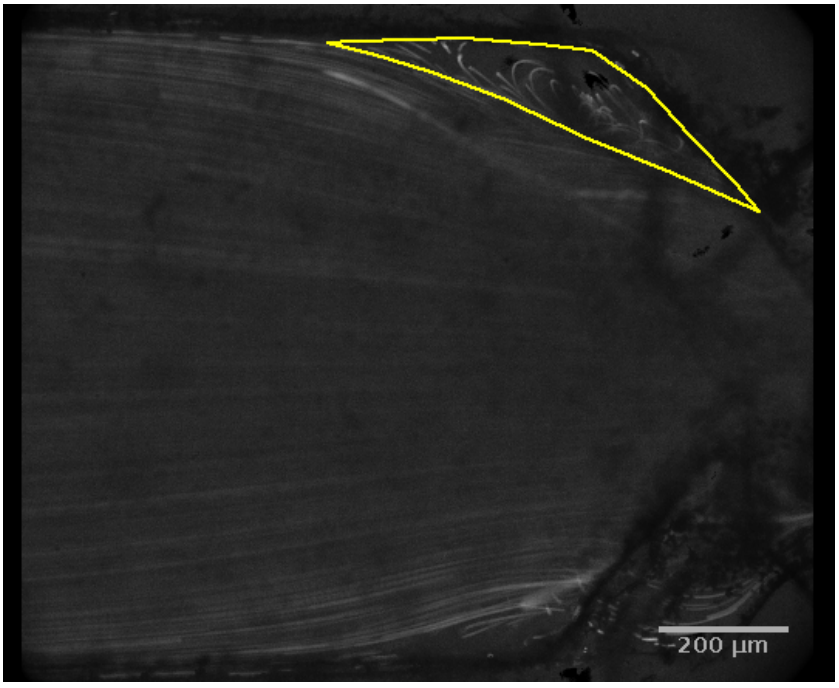

Figure C.11: Standard deviation projection for image stacks representing half oscillating cycle. Here, $Re_o = 55.34$, $f = 2$ Hz.

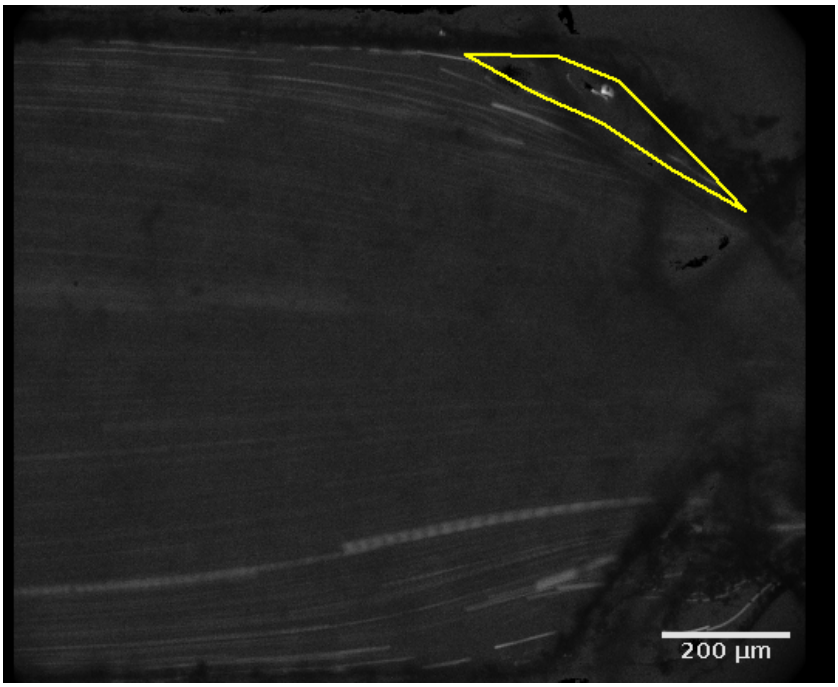

Figure C.12: Standard deviation projection for image stacks representing half oscillating cycle. Here, $Re_o = 55.34$, $f = 3$ Hz.

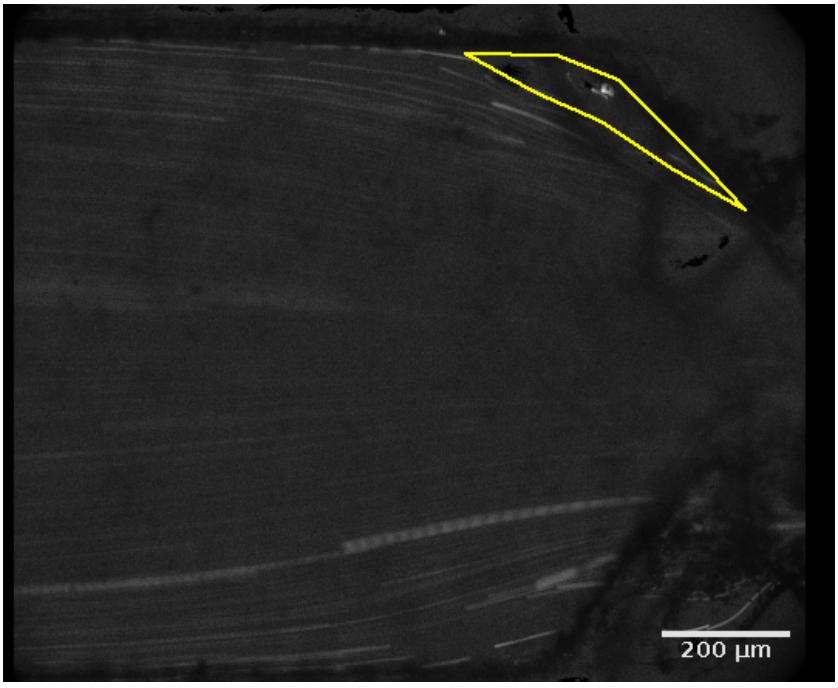

Figure C.13: Standard deviation projection for image stacks representing half oscillating cycle. Here, $Re_o = 55.34$, $f = 4$ Hz.

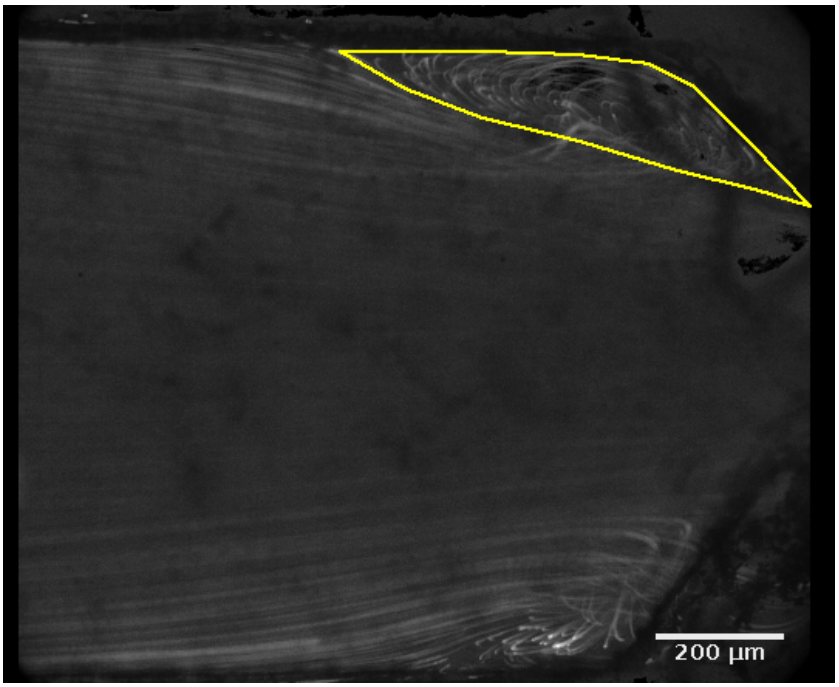

Figure C.14: Standard deviation projection for image stacks representing half oscillating cycle. Here, $Re_o = 71.23$, $f = 2$ Hz.

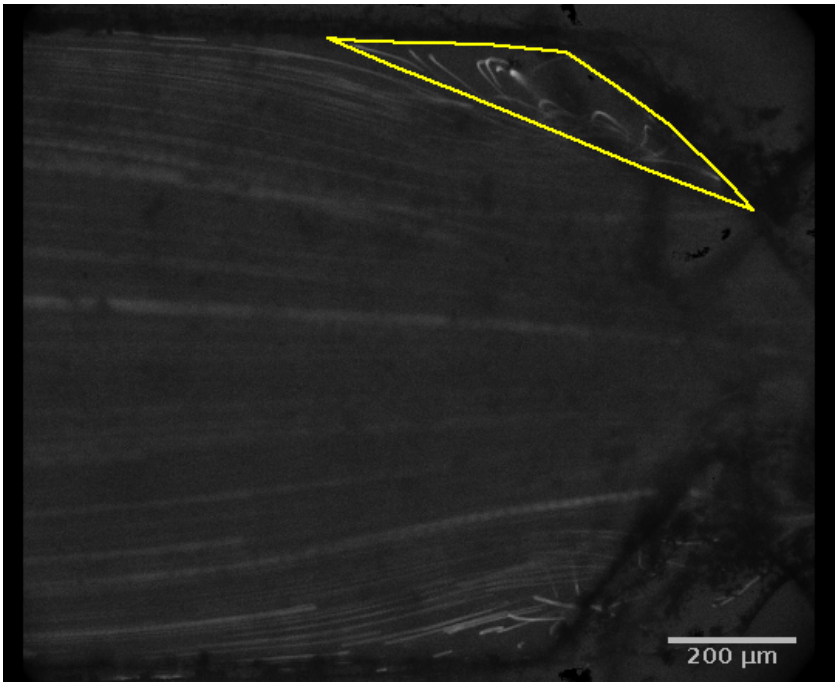

Figure C.15: Standard deviation projection for image stacks representing half oscillating cycle. Here, $Re_o = 71.23$, $f = 3$ Hz.

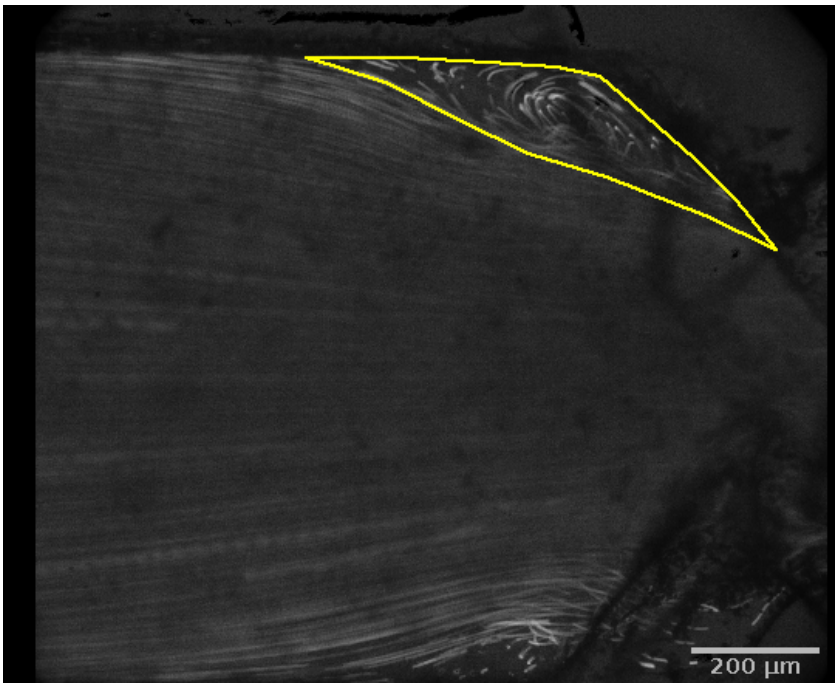

Figure C.16: Standard deviation projection for image stacks representing half oscillating cycle. Here, $Re_o = 71.23$, $f = 4$ Hz.

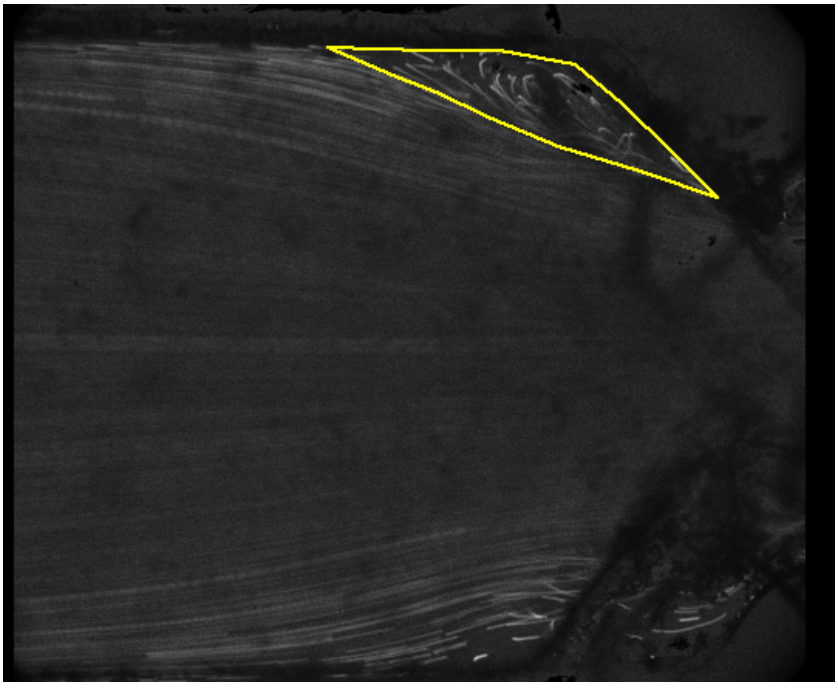

Figure C.17: Standard deviation projection for image stacks representing half oscillating cycle. Here, $Re_o = 71.23$, $f = 5$ Hz.

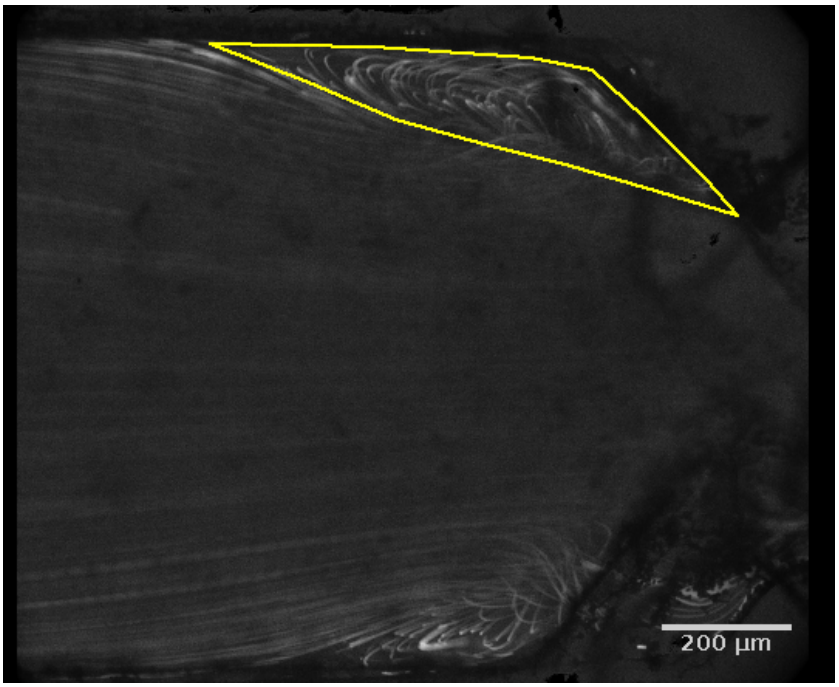

Figure C.18: Standard deviation projection for image stacks representing half oscillating cycle. Here, $Re_o = 97.37$, $f = 3$ Hz.

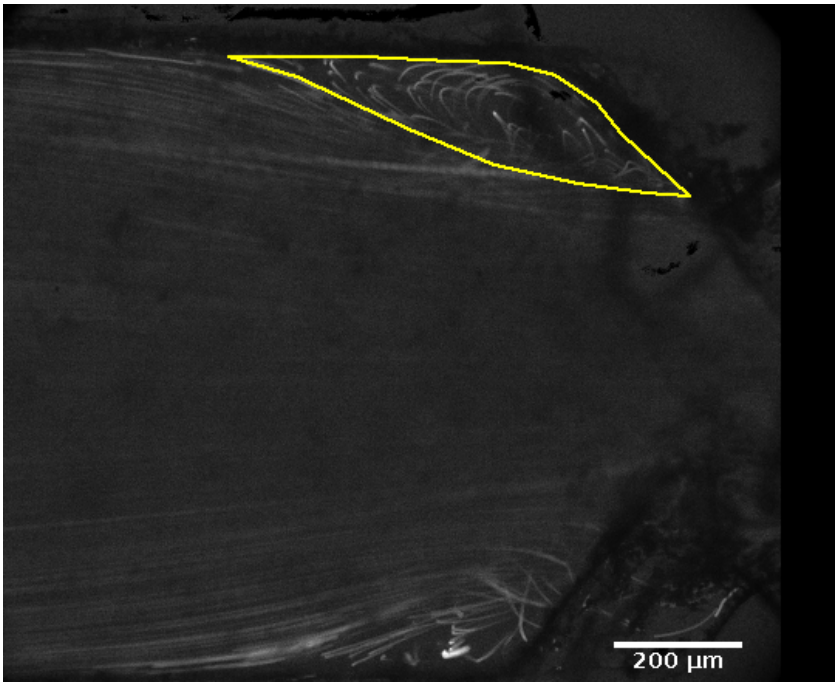

Figure C.19: Standard deviation projection for image stacks representing half oscillating cycle. Here, $Re_o = 97.37$, $f = 4$ Hz.

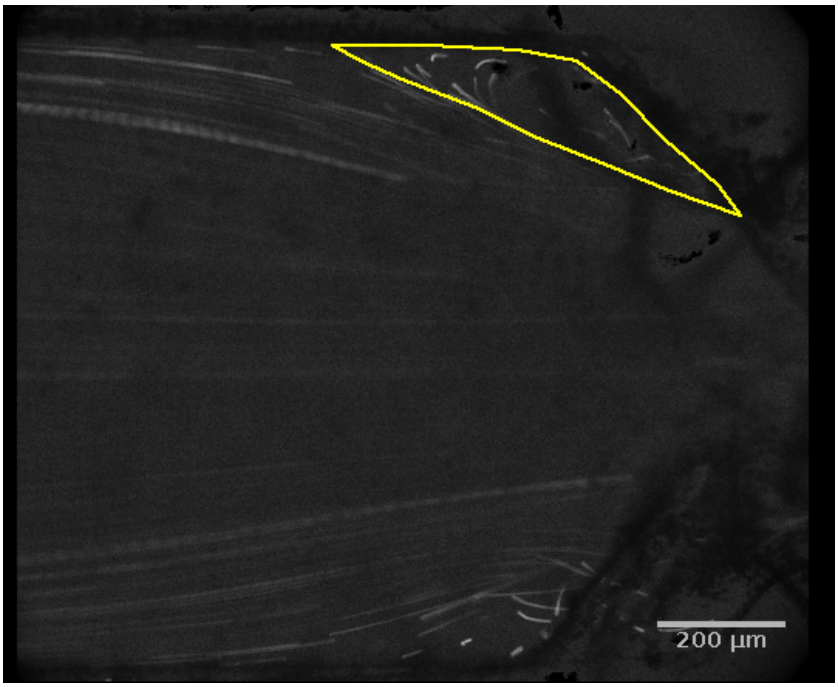

Figure C.20: Standard deviation projection for image stacks representing half oscillating cycle. Here, $Re_o = 97.37$, $f = 5$ Hz.

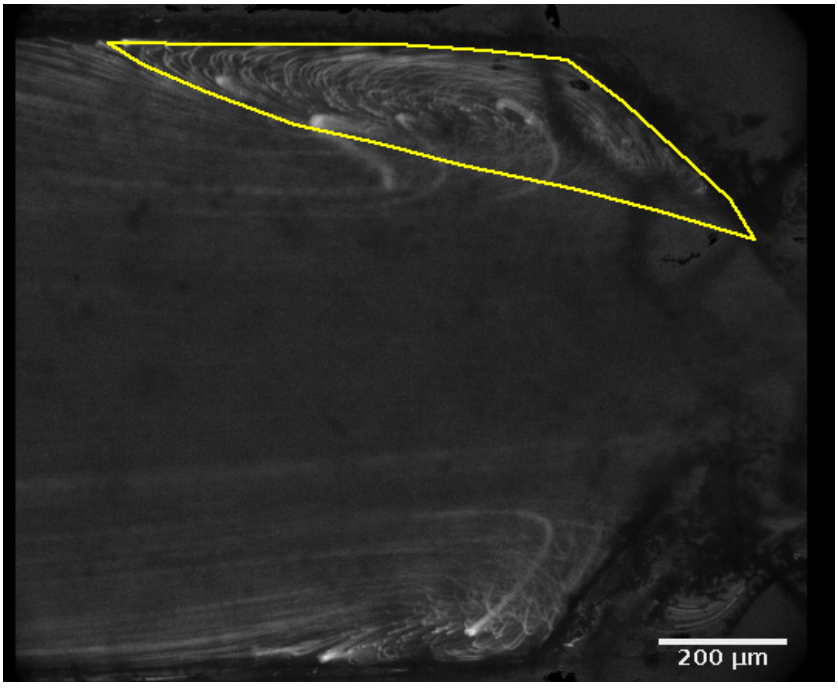

Figure C.21: Standard deviation projection for image stacks representing half oscillating cycle. Here, $Re_o = 108.34$, $f = 3$ Hz.

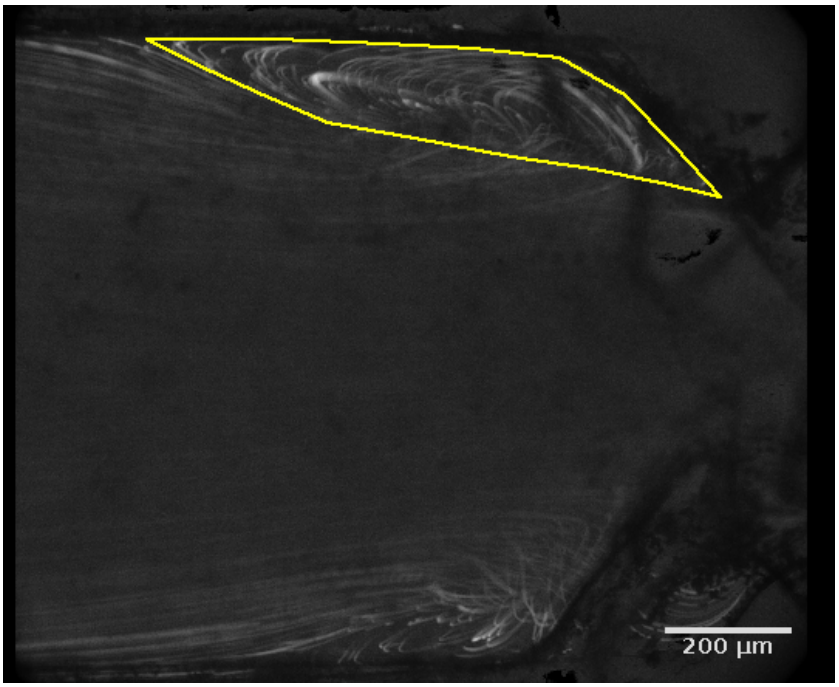

Figure C.22: Standard deviation projection for image stacks representing half oscillating cycle. Here, $Re_o = 108.34$, $f = 4$ Hz.

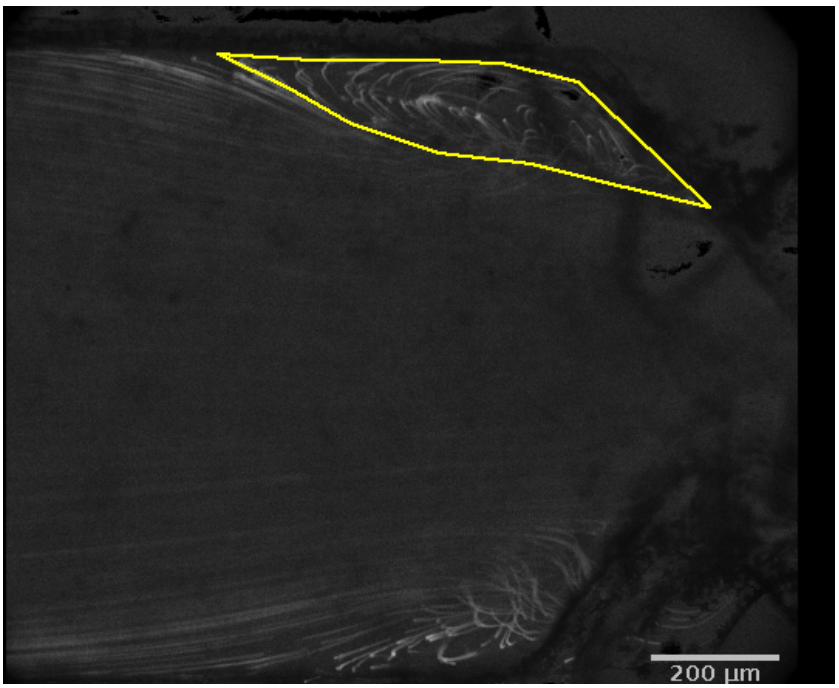

Figure C.23: Standard deviation projection for image stacks representing half oscillating cycle. Here, $Re_o = 108.34$, $f = 5$ Hz.

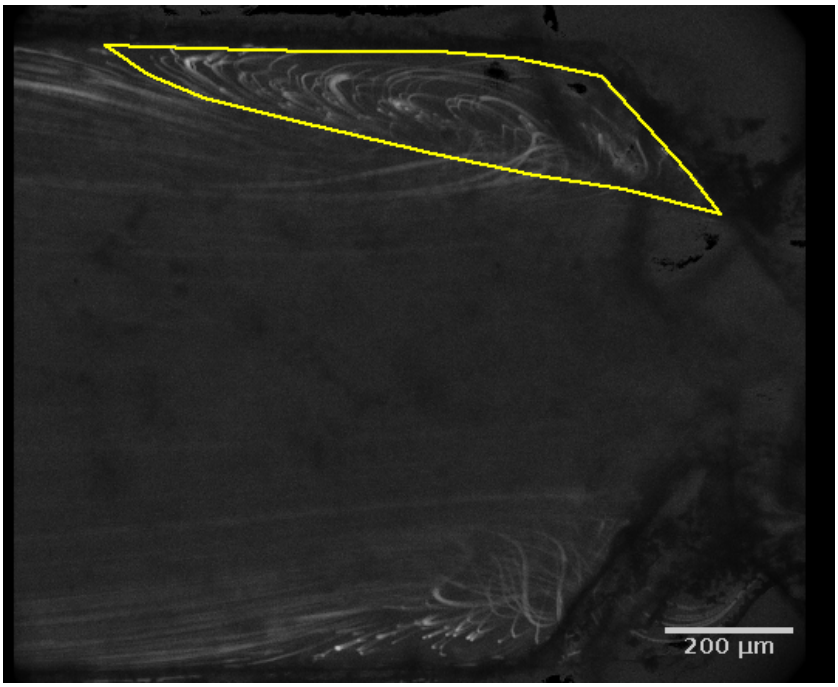

Figure C.24: Standard deviation projection for image stacks representing half oscillating cycle. Here, $Re_o = 124.07$, $f = 3$ Hz.

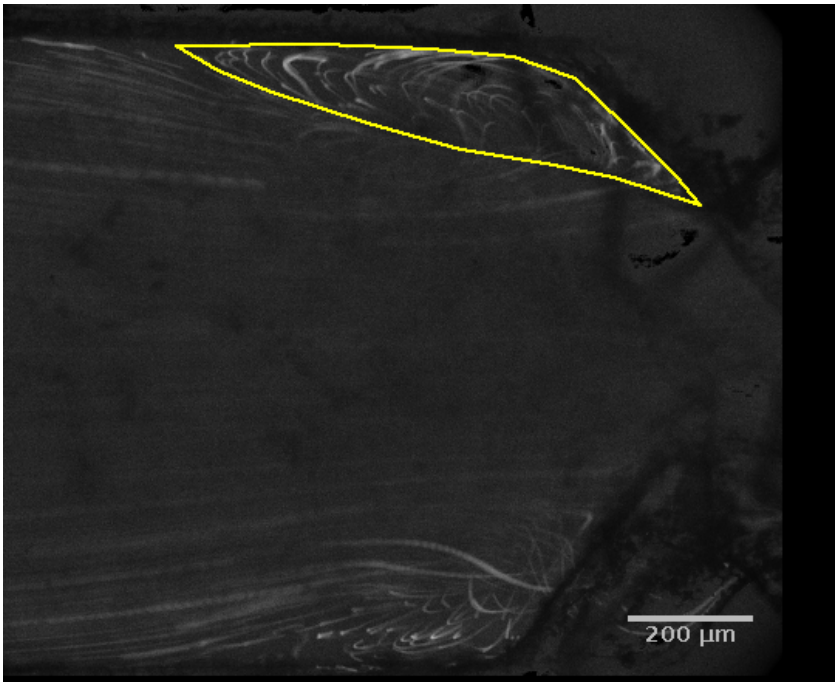

Figure C.25: Standard deviation projection for image stacks representing half oscillating cycle. Here, $Re_o = 124.07$, $f = 4$ Hz.

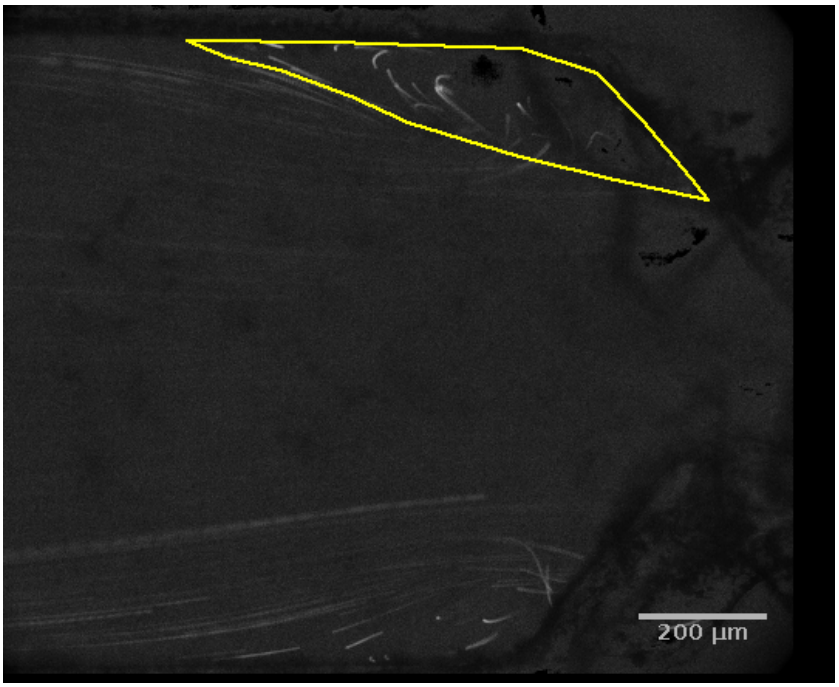

Figure C.26: Standard deviation projection for image stacks representing half oscillating cycle. Here, $Re_o = 124.07$, $f = 5$ Hz.

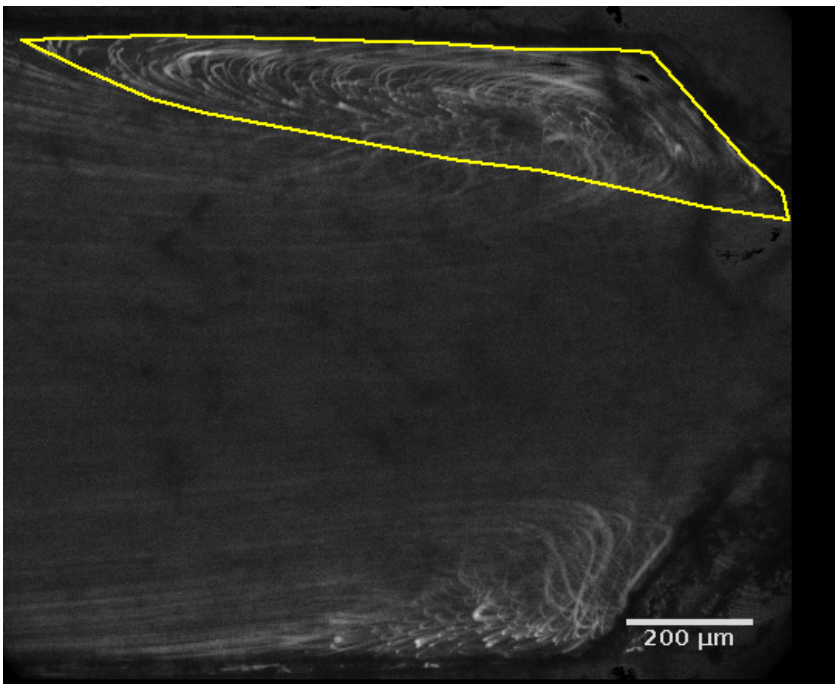

Figure C.27: Standard deviation projection for image stacks representing half oscillating cycle. Here, $Re_o = 150.83$, $f = 3$ Hz.

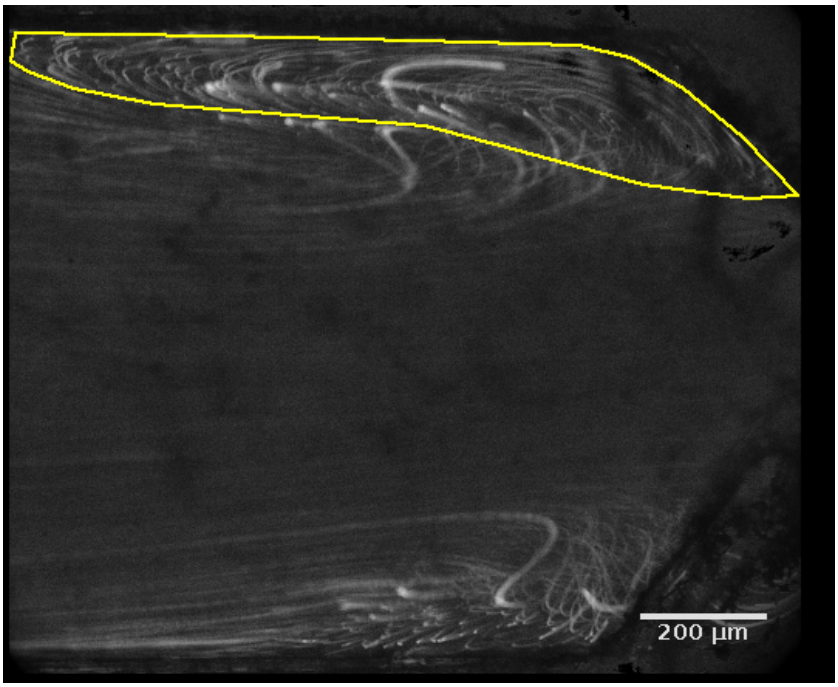

Figure C.28: Standard deviation projection for image stacks representing half oscillating cycle. Here, $Re_o = 150.83$, $f = 4$ Hz.

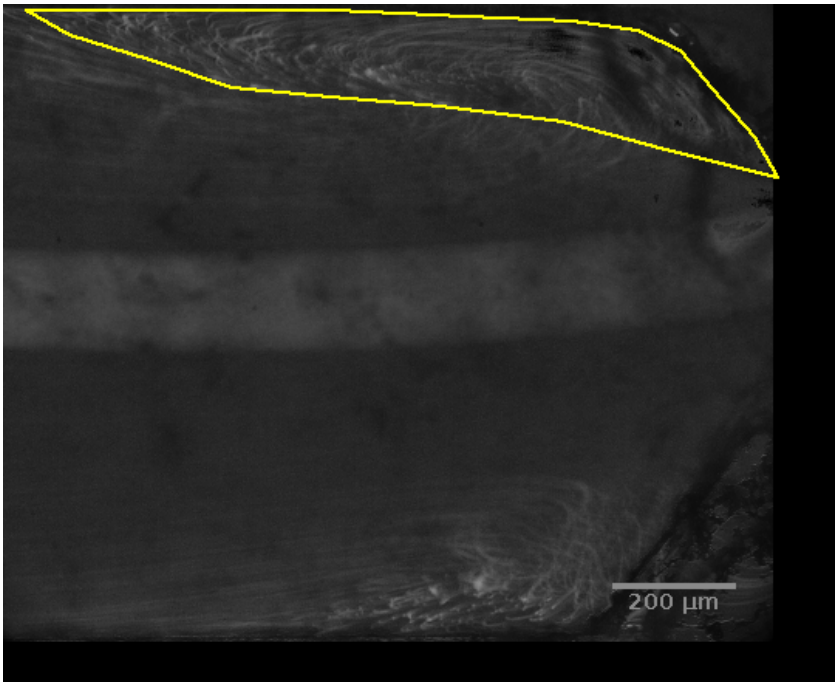

Figure C.29: Standard deviation projection for image stacks representing half oscillating cycle. Here, $Re_o = 150.83$, $f = 5$ Hz.

Appendix D: ESEM images of the produced Paracetamol particle

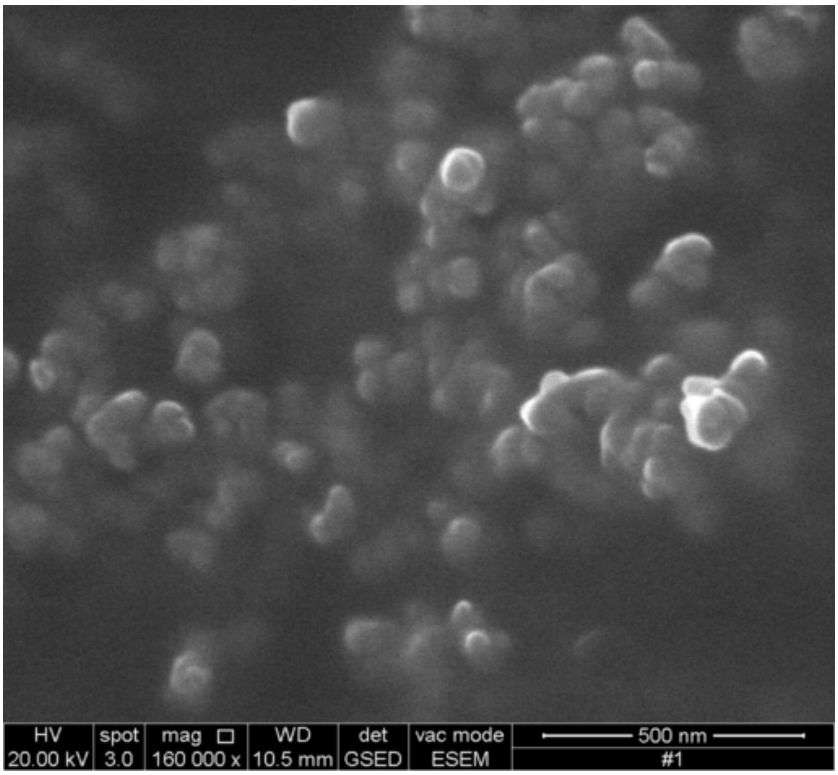

Figure D.1: ESEM image of the produced Paracetamol particle at the optimum factors levels, run #1.

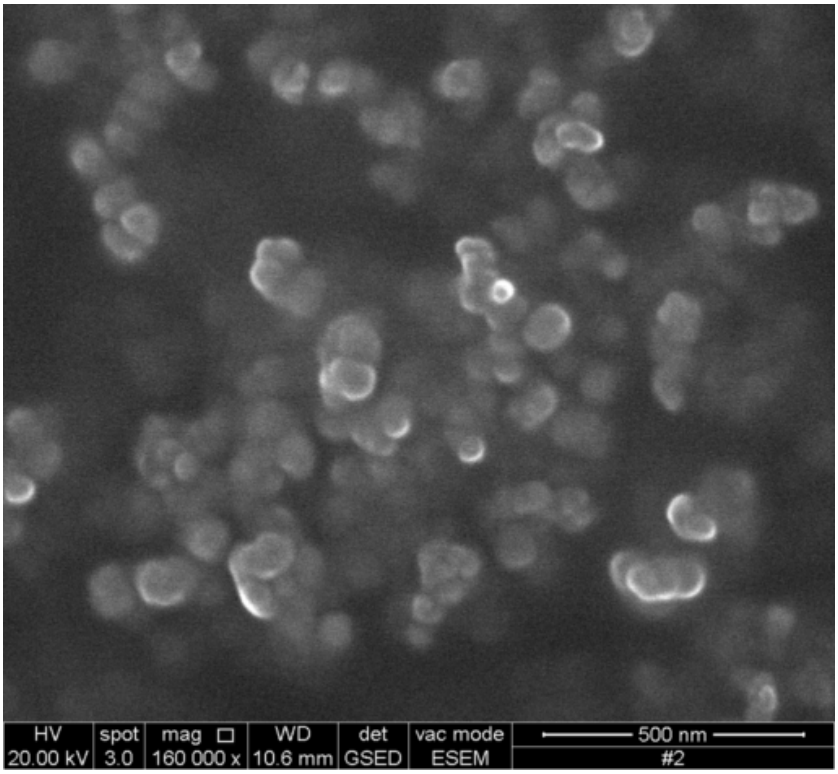

Figure D.2: ESEM image of the produced Paracetamol particle at the optimum factors levels, run #2.

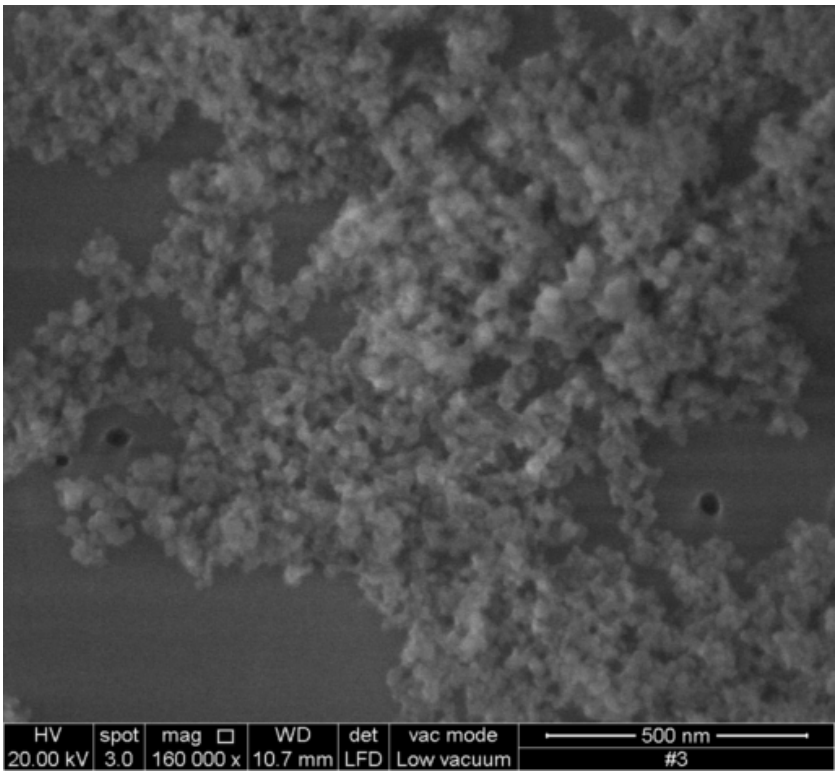

Figure D.3: ESEM image of the produced Paracetamol particle at the optimum factors levels, run #3.

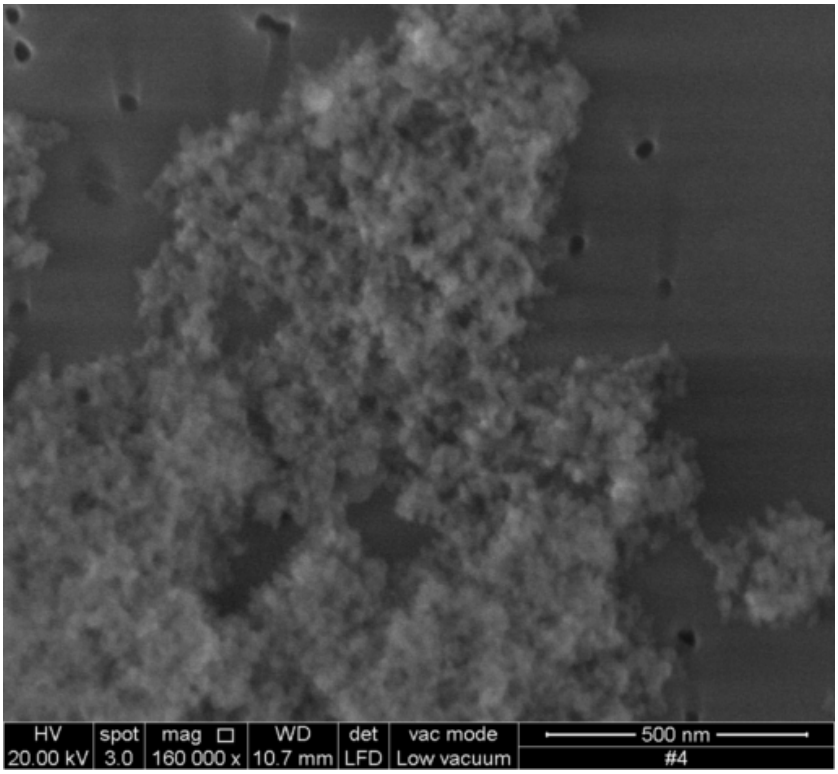

Figure D.4: ESEM image of the produced Paracetamol particle at the optimum factors levels, run #4.

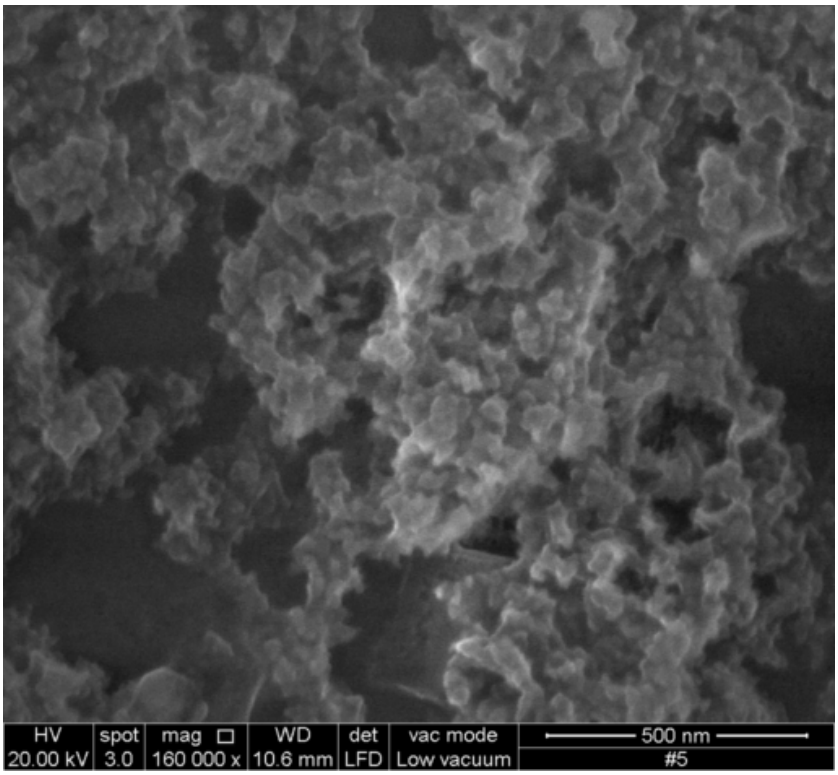

Figure D.5: ESEM image of the produced Paracetamol particle at the optimum factors levels, run #5.

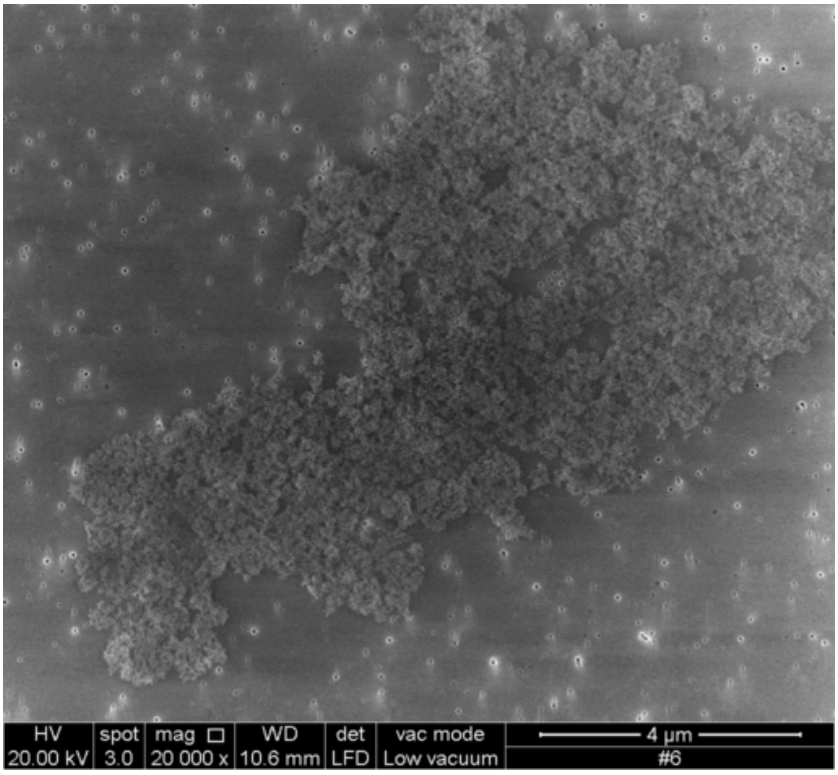

Figure D.6: ESEM image of the produced Paracetamol particle at the optimum factors levels, run #6.